A Search for Dark Matter Interactions in the DEAP 3600 Detector Using Fiducial Masses Ranging from 1433 to 2966 kg

by

Sina Safarabadi Farahani

A thesis submitted in partial fulfillment of the requirements for the degree of

Doctor of Philosophy

Department of Physics

University of Alberta

Abstract

The DEAP-3600 detector is a single-phase direct-detection Dark Matter (DM) experiment located 2 km underground at SNOLAB in Sudbury, Canada. The detector consists of 3279 kg of liquid Argon contained in a spherical acrylic vessel. DEAP-3600 was specifically designed to search for direct detection of dark matter candidates known as Weakly-Interacting Massive Particles (WIMPs).

Radioisotope surface activity is a major source of background in dark matter experiments, and most experiments use a fiducial volume to remove these events, which reduces signal acceptance. The second result of DEAP-3600 published in 2019, used a fiducial radius of 630 mm reducing the detector volume by nearly 60%. Instead of only relying on position reconstruction algorithms and using a strict fiducial volume to remove surface background events, we designed a new veto algorithm to identify these events. This approach will enable us to tag and veto surface events and expand the fiducial volume up to 820 mm to increase signal acceptance and improve the limits we can set on the WIMP-nucleus cross-section. Using 386 live-days of physics data and a WIMP mass of 100 GeV/c^2, the 820 mm fiducial volume showed an improvement of the spin-independent WIMP-nucleon cross-section by more than 30% compared to a fiducial volume of 720 mm, an updated limit actively being considered by the DEAP-3600 collaboration. We set an upper limit on the WIMP-nucleon spin-independent cross-section of 3.8×10^{-45}cm^2 (1.4×10^{-44}cm^2) for a WIMP mass of 100 GeV/c^2 (1 TeV/c^2) at 90% confidence level.

Dedication

To my dear mother, though miles may separate us, your love and encouragement have carried me through the toughest of times. This achievement is as much yours as it is mine, and I dedicate it to you with all my heart.

To my beloved father, who left this world too soon but whose unwavering support and guidance has stayed with me every step of the way. I dedicate this achievement to you and I hope I have made you proud. Thank you for being the foundation of my life, and for always believing in me.

"All that is good in me, began with you, father."

Acknowledgements

First and foremost, I would like to express my deep gratitude to my supervisor, Professor Aksel Hallin, for his unwavering support, invaluable guidance, and constructive criticism throughout my PhD studies. Having him as my supervisor was the main source of making the Ph.D. life bearable. He was always available when his students had questions or needed help, no matter if it was late in the evening and during the weekend, he would always be there to help.

I am grateful to the whole DEAP collaboration, and the group at the University of Alberta, for providing a collaborative and supportive environment for my research. Their expertise and resources have been indispensable in advancing my work. I would like to thank Simon Viel and Andrew Erlandson for always being available to answer any question I had

I would like to thank my dear friend Danial, my TA and friend during my undergraduate studies, and my roommate and colleague the last two years of my studies. Thanks for lending me your ear to listen to my rants and being my second set of eyes when I needed sanity checks for my codes.

Last and definitely not the least, I would like to express my heartfelt thanks to my lifelong and closest friend Mina. Her unwavering love, support, and understanding have been my rock through and through. Having a friend like you that can make you feel calm and happy even when thousands of miles away is a gift of life I will not take for granted and I will forever cherish our friendship.

Contents

Abstract ii

Acknowledgements iv

1 Review of Theory and Model 1
- 1.1 The Standard Model of Particle Physics 1
- 1.2 General Relativity 5
- 1.3 ΛCDM 7
  - 1.3.1 Thermal History 8
  - 1.3.2 Λ, The Cosmological Constant 11
  - 1.3.3 Hot, Warm, and Cold Dark Matter 11
- 1.4 Standard Halo Model 13

2 Dark Matter and Observational Evidence 19
- 2.1 Rotation Curves 19
- 2.2 Bullet Cluster 22
- 2.3 Cosmic Microwave Background 24
- 2.4 Structure Formation 27

3 Dark Matter Candidates and Detectors 29
- 3.1 Modified Gravity 29
  - 3.1.1 Modified Newtonian Dynamics 29
  - 3.1.2 Tensor-Vector-Scalar Gravity 31
- 3.2 Particle Candidates 32
  - 3.2.1 WIMPs 32
  - 3.2.2 Axions 33
- 3.3 Previous Searches for WIMPs 34
  - 3.3.1 Particle Colliders 35
  - 3.3.2 Indirect Detection 35
  - 3.3.3 Direct Detection 36
- 3.4 Detectors and Detection Techniques 37
- 3.5 WIMP Properties 40

4 DEAP-3600 43
4.1 Why Liquid Argon? 43
4.2 Liquid Argon Scintillation 44
4.3 Light Yield 46
4.4 Argon Pulse-Shape Discrimination 47
4.5 SNOLAB Underground Science Laboratory 50
4.6 DEAP-3600 Design 51
  4.6.1 Photomultiplier Tubes 54
  4.6.2 Veto Systems 58
  4.6.3 Data Acquisition System 59
  4.6.4 Data Reduction 64
4.7 Pulse-Shape Discrimination in DEAP-3600 65
4.8 Backgrounds in DEAP 66
  4.8.1 ^{39}Ar β Decays 68
  4.8.2 Cherenkov Radiation 68
  4.8.3 Radiogenic and Cosmogenic Neutrons 69
  4.8.4 Alphas 71

5 Analysis 79
5.1 DEAP Analysis Variables 80
  5.1.1 Non-Physics Event Removal Variables 80
  5.1.2 Pile-Up Event Removal Variables 81
  5.1.3 Calculated Variables 84
5.2 Position Fitters 85
  5.2.1 TimeFit2 85
  5.2.2 MBLikelihood 86
5.3 Recombination Model Tuning 87
5.4 Scintillation Likelihood Processor 95
5.5 Late Light and PMT Saturation 103
5.6 Use of Late Light in DEAP-3600 108
  5.6.1 Late Light MBL 113
  5.6.2 Alpha Quenching Factors 116
5.7 Surface Tagging Algorithm 128
  5.7.1 MC-Driven Tagging Performance 132
  5.7.2 Data-Driven Tagging Performance 139
5.8 Double Charge Clusters 145

6 Dark matter Analysis Results 147
6.1 New Cutflow 147
6.2 Background Expectation Sources 152
  6.2.1 Neck α 153
  6.2.2 Dust α 153
  6.2.3 Cherenkov 154

6.2.4 Neutron . . . 156
6.2.5 Surface α . . . 157
6.3 MC Background Uncertainty . . . 160
6.4 Expected Background & Observed Data . . . 162
6.5 Signal Acceptance & Model Parameters . . . 164
6.6 Exclusion Curve . . . 166
6.7 Future Steps . . . 170

7 Conclusions **171**

References **173**

A WIMP Miracle **189**
A.1 Boltzmann Equation . . . 189
A.2 Dark Matter Relic and WIMP Miracle . . . 191

B nSCBayes Saturation and Late Light **195**

C Monte Carlo Quenching Factor **201**

D Event Leakage **203**

E Background Expectation Material **204**
E.1 Neck & Dust Rates . . . 204
E.2 Cherenkov Charge Cluster 3D View . . . 205
E.3 Background Uncertainty . . . 206
E.4 Total Background . . . 212

F Extra Exclusion Curves **215**
F.1 Upper, Median, and Lower Curves . . . 215
F.2 Tagged Events . . . 217

List of Tables

1.1 A brief history of the evolution of the universe and the key events [3]. . . 10
1.2 The free parameters of the Standard Halo Model (SHM) and the refined version. Note that the SHM^{++} introduces two new free parameters. See Ref. [55] for more details on the SHM^{++}. 18

4.1 Comparing some of the properties of argon and Xenon relevant to Dark Matter (DM) searches. It is also important to have multiple isotopes and multiple technologies and systematic uncertainties. The average cost is taken from [132]. 44
4.2 The four lowest excited states and the ground state of argon atom. Energies taken from [140], converted to eV for convenience. 47

5.1 Different trigger types used in Dark matter Experiment using Argon Pulse-shape discrimination (DEAP). 81
5.2 A list of different calcut flags used in DEAP. Smart QT (SQT) is an algorithm used in the front-end software of the V1720 digitizers to encode waveforms. 82
5.3 A summary of low-level cuts applied to data. 84
5.4 Liquid Argon (LAr) optical parameters used in the recombination model as described by Equation 5.3. We show the parameters that were found by fitting to data from Ref. [169] and values we tuned for our simulations. Note that, unlike the time constants, the weights are energy-dependent and the values in the table show the range of these values in our MC. . . 90
5.5 The cutflow used for selecting ^{39}Ar events in data. 91
5.6 The fit parameters, their description and fit values as described by Equation 5.9. All the time constants are in units of ns. 98
5.7 The alpha energy of the three main isotopes used in our study. The decay mode of ^{222}Rn and ^{214}Po are 100% to an α daughter particle. α decay of ^{218}Po is at 99.98%. All data is taken from NNDC database. 104
5.8 Position resolution of regular MBL and late light MBL for X, Y, Z, and R, variables measured as the RMS of their corresponding histograms. . . 116
5.9 Results of the Gaussian fit to the three alpha lines with three different MBLR ranges for data. The late light qPE mean and its uncertainty come directly form the Gaussian fit and the late light Light Yield (LY) variable is the fitted qPE divided by the corresponding alpha energy. 122

5.10 The alpha peak energies found from the late light calculation explained in the text for data and the corresponding Quenching Factors (QFs). We have used $LY_R = 0.16$ and $F_{\text{prompt}} = 0.71$ for best agreement to data. For QF uncertainties, we have assumed a 2% uncertainty in LY_R and F_{prompt}. 125
5.11 Livetime of each detector setting based on the number of dead PhotoMultiplier Tubes (PMTs) during the 231-days exposure. Note that we never had three dead PMTs during the first-year dataset, but this condition did happen in the future runs of our three-year dataset. 132
5.12 The activity of each surface α event type measured by the DEAP collaboration. Note that the unreasonable number of digits were copied from another document. These values are probably accurate to the 10 to 20%. 133
5.13 Measuring the performance of the Surface Tagging Algorithm (STA) in different regions of qPE and F_{prompt}. The fiducial cut is based on the reconstructed position and not the truth MC position. 135
5.14 The cutflow used for selecting ^{39}Ar events in data for measuring the leakage and the surface tagging performance. 141

6.1 The low-level cuts applied in the DM search analysis to remove non-physics and pile-up events. 149
6.2 The background removal cuts applied in the DM search analysis in order to reduce background events in the Weakly Interacting Massive Particle (WIMP) Region of Interest (ROI). 150
6.3 Number of neutron background events per live-year for no radial cut and two fiducial cuts at 800 and 550 mm in the qPE range of 120 to 240. Results courtesy of Eric Vazquez. 157
6.4 Expected number of background events from each source at different fiducial volume cuts and the updated cutflow. The first row, 630*, corresponds to the original cutflow used by DEAP. 163
6.5 Total number of expected background and the observed data in the one-year and three-year open datasets corresponding to 222.9 and 386.2 live-days. 163
6.6 The free astrophysical parameters supported by the Maxpatch framework used to calculate the WIMP event rate. 164
6.7 The free parameters supported by the Maxpatch framework to model the detector response in detecting PhotoElectrons (PEs). 165

C.1 Results of the Gaussian fit to the three alpha lines with three different MBLR ranges for MC off_off. The late light LY variable is the fitted qPE divided by the corresponding alpha energy. 201
C.2 Results of the Gaussian fit to the three alpha lines with three different MBLR ranges for MC on_off. The late light LY variable is the fitted qPE divided by the corresponding alpha energy. 202

E.1 Neck alpha trigger rates for each of the Inner Flowguide Inner Surface (IFIS), Inner Flowguide Outer Surface (IFOS), and Outer Flowguide Inner Surface (OFIS) for the 15 systematic variations and the nominal sample. Data courtesy of DEAP collaboration. 204
E.2 Dust alpha trigger rates for each of the dust particulate size. The dust samples are not coated with any TetraPhenyl Butadiene (TPB). Data courtesy of DEAP collaboration. 205

List of Figures

1.1 Elementary particles of the Standard Model of Particle Physics (SM). Image copyright from MissMJ Cush under Creative Commons Attribution, taken from Wikipedia. 4
1.2 Rotation curve of the spiral galaxy NGC 3198 taken from [68]. See Ref [68] for more information on the different possible fits for the halo and the disk contribution to the orbital velocity. 18

2.1 The rotation curve of 21 Sc galaxies showing the mean velocities in the plane of the galaxy versus distance from the core. Image taken from [73]. 21
2.2 The right panel shows the artificially coloured image from the Chandra X-ray observatory with a 500 ks exposure time. The intensity shows the mass distribution derived from the X-ray emission of the gas. The green contours show the mass distribution reconstructed from weak lensing. The blue +s on the left panel, an image from the Magellan IMACs telescope, show the centre of mass of the baryonic matter. Image taken from [75]. . 23
2.3 The anisotropies of the Cosmic Microwave Background (CMB) map as measured by the Planck satellite [76]. 24
2.4 The magnitude of the CMB temperature anisotropies as a function of the multipole l in Equation 2.3. The lower x-axis is the multipole l which is logarithmic for $l < 30$ and linear for higher orders. The upper x-axis is the angular resolution with similar behaviour for logarithmic and linearity. The data are from the latest results of the experiments mentioned in the legend. Some data points with large error bars were removed by the authors. The plotted curve is from Planck's best fit of the ΛCDM model. Image is taken from [1]. 26

3.1 A schematics representation of the different approaches for detecting DM where n is a particle in the SM and χ represents the DM. Graph courtesy of Pietro Giampa. 34
3.2 A schematic drawing of different signal detection techniques and technologies used in direct detection experiments. Image taken from [111] . . 37
3.3 The 90% confidence limit for Spin-Independent (SI) WIMP-nucleus cross section as a function WIMP mass set by the LUX-ZEPLIN experiment (LZ) collaboration [121]. 39

4.1 A graphical representation showing the two mechanisms in argon producing Vacuum UltraViolet (VUV) photons. Image taken from [134]. 46
4.2 A Schematic diagram of argon energy levels where the VUV photon emitted from Ar_2^* is also illustrated. Image taken from [140]. 49
4.3 A plot of the muon flux per cm^2 per second as a function of kilometre water equivalent for different underground laboratories. Image taken from [146] where the solid line is the parameterization and taken from [147]. 50
4.4 A map of the underground section of SNOLAB where the Cube Hall that houses DEAP-3600 is highlighted in the top left. Image taken from [149]. 51
4.5 A schematic view of the DEAP detector and its components. Image taken from [150]. 52
4.6 The spectra of the wavelength re-emitted by the TPB for waves with four different incident wavelengths. Image taken from [151]. 53
4.7 The quantum efficiency, in percentage and the photocathode radiant sensitivity, defined as photoelectric current over the incident (mA/W), of R5912-High Quantum Efficiency (HQE) PMT. Image taken from [152]. . 54
4.8 A schematic view of the inner components of the DEAP-3600 highlighting the Light Guide (LG), PMT, and filler blocks. Image taken from [150]. . 55
4.9 A collection of photos showing the DEAP detector in various stages. From top to bottom and left to right: assembling the Acrylic Vessel (AV); bonding the LGs to the AV; applying the reflector to the LGs; installing the PMTs, their shielding and the filler blocks; installing the detector inside the water tank; the final steel shell enclosing the AV inside the water tank where the muon veto PMTs are also visible. Image taken from [154]. 56
4.10 A schematic view from Hamamatsu PMT, linear-focused type, showing the process of multiplication of a single electron to many electrons using a chain of dynodes [155]. 57
4.11 The neck region of DEAP, before installing the neck filler blocks, showing the wavelength shifting fibres wrapped around the bottom 10 cm of the neck. Image taken from [150]. 59
4.12 A schematic drawing of the Data AcQuisition (DAQ) system used in DEAP where the hardware components and software programs are shown as shaded and white boxes, respectively. Image taken from [150]. 60
4.13 An Single PhotoElectron (SPE) pulse saved in Zero Length Encoding (ZLE) mode on a V1720 channel where the baseline is at 3900 Analog-to-Digital Converter (ADC) and the time bins are 4 ns wide. Image taken from [150]. 62
4.14 The (E_{prompt}, F_{prompt}) phase space for an example taken using the physics trigger without applying any cut. The z-axis is indicative of the number of events. Image taken from [150]. 64

4.15 PE versus F_{prompt} distribution using 4.4 live-day dataset where the ElectroMagnetic (EM) and nuclear recoil bands are shown in blue and green respectively. The DM ROI highlighted with red lies in the region of 80-200 PE. 67

4.16 The ROI for DM search shown in black where the boundaries are defined by Electron Recoil (ER) (50% of the ER events are in the blue band and 0.05 events in the 223 days move the top boundary of the blue curve to the black region), nuclear recoil (green), and neck alpha (pink) backgrounds. Image taken from [162]. The 67

4.17 Top plot shows the spectrum of PE versus F_{prompt} for the dataset of 247.2 days after quality checks and a sequence of cuts. The bottom plot shows the contribution of different event types in the EM band. Since the ^{40}K and ^{208}TI energy range are well above the DM ROI, we won't discuss them in detail in this thesis. But ^{39}Ar β-decays can leak into the ROI. Image taken from [164]. 69

4.18 Probability of detecting an EM exceeding a specific F_{prompt} value in the WIMP ROI's lowest 1 keV_{ee} bin. Vertical lines depict the values above which 90% and 50% of Nuclear Recoil (NR)s are anticipated to be found. Image taken from [162]. 70

4.19 Decay chain diagrams of **(a)** ^{238}U and **(b)** ^{232}Th taken from Ref. [165]. . 72

4.20 Graphical breakdown of ^{210}Po surface alphas. The alpha-decays can happen **(a)** inside the LAr, **(b)** within the TPB layer, and **(c)** inside the AV inner surface. Image courtesy of the DEAP-3600 collaboration. 74

4.21 The diagram of the geometry of the neck region showing the inner and outer flow guides. Image courtesy of the DEAP-3600 collaboration. . . . 76

4.22 A schematic view of an α-decay happening within a dust particulate. The dust is in the LAr. The alpha particle loses most of its energy in the dust material before exiting to the LAr and creating scintillation light. A portion of the scintillation light will also get absorbed by the dust particulate. Image courtesy of DEAP-3600 collaboration. 78

5.1 An example of pile-up event with subeventN = 2. A second pulse happens within the integration window of the first trigger. This will add to the total charge of the event and change the pulse shape discrimination (PSD) variable. The prompt and late windows are shown as yellow and blue, respectively. The green area shows the overlap region. Image courtesy of Matthew Dunford. 83

5.2 Two examples of events with numEarlyPulses great than 3. The prompt and full integration windows are shown in yellow and blue, respectively. The green area is the overlap region of the prompt and late windows. Image courtesy of Matthew Dunford. 84

5.3 The waveform of ^{39}Ar obtained from data and those simulated with the double-exponential model and the Energy Dependant Recombination (EDR) model. **(a)** shows the waveform using MBLikelihood (MBL) for Time of Flight (ToF) calculations while **(b)** uses TimeFit2 (TF2) position. Since the number of events used in each sample could be different, the histograms are scaled such their integral equates to 1 so the shape can be easily. To compare the shapes of the waveforms, they are scaled such that their integral is equal to one. 92

5.4 The difference between the truth position of events found from MC samples minus the position found by the TF2 algorithm for **(a)** the X position, **(b)** Y position, and **(c)** the Z position. Since the EDR model captures the peak of the waveform better, TF2 also performs better with the updated model. 93

5.5 The mean $\mathrm{F_{prompt}}$ for different qPE energy bins. The error bars are purely statistical. The huge error bars at very high energies are due to lack of statistics at such energies. 94

5.6 The **(a)** qPE vs $\mathrm{F_{prompt}}$ and **(b)** event position plot of the events when the detector was filled with Gaseous Argon (GAr). 96

5.7 The position plot of the potential discharge events, after applying the cuts, using the **(a)** MBL and **(b)** TF2 fitter. **(c)** shows the qPE vs $\mathrm{F_{prompt}}$. 97

5.8 The simulated time responses using **(a)** only LAr scintillation, **(b)** LAr scintillation convolved with TPB response, and **(c)** both convolved with a Gaussian function. For a better comparison **(d)** shows all three within the same time window. The mean of the Gaussian is 0 and the standard deviation used here was set 5 to magnify the effect. 99

5.9 ^{39}Ar waveform and the fitted time-response function using the physics data. 100

5.10 All four PDFs used in the scintillation-likelihood processor. **(a)** shows the PDFs in linear-scale and up to 100 ns with bin width of 1 ns, **(b)** shows them in the log-scale and up to 500 ns in bin width of 5 ns, and **(c)** shows them in log-scale for the full 10 μs in bin width of 50 ns. Note that the Argon-TPB PDF shown here uses ^{39}Ar singlet and triplet factors, hence the lower prompt peak compared to other PDFs. 102

5.11 The distribution of qPE-$\mathrm{F_{prompt}}$ and qPE-MBLR for physics data processed with two different Reactor Analysis Tool (RAT) versions; 5.11 and 5.14. The three alpha lines starting at 30,000 qPE from left to right are ^{222}Rn, ^{218}Po, and ^{214}Po. Due to the effects of saturation and clipping, 5.11 shows curved lines caused by missing charges for events near the surface. Data processed with 5.14 corrects this missing charge and forms straight lines. The bulb around 20,000 to 25,000 are the ^{210}Po events. 105

5.12 qPE vs. $\mathrm{F_{prompt}}$ and qPE vs. MBLR for our two sets of MC with off_off setting and on_off. We have also included nSCBayes vs. MBLR for comparison. 107

5.13 Late light qPE vs. MBLR using different lower bounds (50, 100, 150, 200, and 250 ns) for charge integration. The fact that the time windows below 200 ns are wider implies this cut does not remove all saturation. This is the MC samples with both clipping and Pulse-Level Saturation Correction (PLSC) turned off. 110

5.14 Late light qPE vs. MBLR using different lower bounds for charge integration. This is the MC sample with clipping enabled but PLSC disabled. 111

5.15 Late light qPE vs. MBLR with different lower bounds for charge integration. This is data with rat version 5.11 which does not include PLSC. . . 112

5.16 Truth position minus regular MBL (red) and late light MBL (blue) using the MC sample. The left column is with clipping and PLSC both enabled and the right column is with both processors disabled. Row 1 to 3 are the X, Y, and Z positions. 115

5.17 Truth radius minus the fitted radius found by the regular MBL (red) and late light MBL (blue). 116

5.18 Alpha quenching factors found by DEAP collaboration based on nSCBayes and full energy events using DEAP data corrected with the PLSC. Image courtesy of David Gallacher. 120

5.19 **(a)** the SRIM electronic stopping power, **(b)** Lindhard quenching factors from SRIM, and **(c)** the QF using Birk's law, both instantaneous and track averaged, with a Birk's constant of $kB = 7.4 \times 10^{-4}$ MeV^{-1} g cm^{-2} as a function of energy. 121

5.20 Late light qPE projected with three different MBLR ranges for both data (RAT 5.11) and MC sample (off_off setting). The vertical lines show the range used for the Gaussian fits to find the energy peak. 126

5.21 Comparing the quenching factor of the combined Birk's QF and Lindhard QF with Birk's constant $kB = 7.4 \times 10^{-4}$ MeV^{-1} g cm^{-2} [175] with DEAP data, and the current QF array used in our MC. $LY_R = 0.16$ and $\mathrm{F}_{\mathrm{prompt}} = 0.71$ were used for achieving the best agreement. For QF uncertainties, we have assumed a 2% uncertainty in LY_R and $\mathrm{F}_{\mathrm{prompt}}$. . . 127

5.22 Map of the PMT positions in $\cos\theta$ and ϕ space. The numbers in the box represent the PMT id. The pentagonal gaps are highlighted with red numbers. Note that there is a pentagonal caused by the spring support gap at the bottom of the detector that covers the full ϕ range at $\cos\theta = -1$, number 10 in this figure. The top of the detector could also be a pentagonal gap but it is the neck region. 129

5.23 The charge distribution of the four different event types used in the surface tagging algorithm where **(a)** shows all the 255 PMTs while **(b)** only shows the first 40 bins to highlight the difference in the closest PMTs to the event location. 136

5.24 The blinding strips and the ROI used in our 2019 paper. 137

5.25 **(a)** A plot of the MC surface events inside the blinding strip 3 and fiducial cut of $R < 800$ mm after each event is tagged by our algorithm. The black squares show the region around pentagonal gaps, where the gap at the bottom of the detector is not shown (expands the full ϕ range). The three red circles show the location of the dead PMTs. Neither the dead PMTs nor the pentagonal gap regions are drawn to scale. To better show the performance of our algorithm, the angular position of the events is based on their MC truth position and not the reconstructed position. **(b)** The bottom plot is the same as **(a)**, except we only plot the 144 events that are mistagged as ^{40}Ar-like events. The distribution is not uniform in cosθ and needs to be studied more. But it could be due to the pentagonal gap at the bottom of the detector and the dead PMTs at ϕ>1. 138

5.26 The leakage percentage (solid lines) of the pseudo-events using the two golden runs. The dashed lines show the percentage of events tagged as ^{40}Ar events. Note that we want to minimize the dashed lines before the solid lines take off too much; i.e. maximum surface veto with minimal leakage. 143

5.27 **(a)** The leakage percentage using the two golden physics runs. Run 21399 has two dead PMTs and clearly shows an enhanced leakage compared to run 18831. **(b)** Relative difference of leakage between the two runs where we have taken the average leakage between the two pseudo-events. Run 21399 with two dead PMTs and can have up to 30% more leakage at lower radii. 144

6.1 Expanding the upper bound of the WIMP ROI to have a 5% signal loss instead of the 30% loss used in previous studies. 151

6.2 PE distribution of two runs where the detector was filled with LAr. The red curve had the ^{232}U calibration source deployed. Plot courtesy of Jie Hu. 155

6.3 **(a)** shows the number of expected neutron background events within any fiducial volume before applying any STA cut. **(b)** shows the effect of applying the STA cut on ^{40}Ar MC. **(c)** shows the expected neutron background after applying the STA cut. 159

6.4 The acceptance curves for different fiducial volumes using the updated cutflow in each PE bin, except for the black curve, which uses the original cutflow. 165

6.5 The upper 90% Confidence Level (CL) for the 6 fiducial volumes studied with the updated cutflow. The results from the original cutflow are also shown for comparison. **(a)** and **(b)** show the results using the 223 and 386 live-days datasets. 169

A.1 . Image taken from [3]. 193

B.1 Late light qPE vs. MBLR with different lower bound for charge integration. This is data with rat version 5.14 which includes the PLSC. 196
B.2 Late light nSCBayes vs. MBLR with different lower bound for charge integration. This is data with rat version 5.11 which does not include PLSC. 197
B.3 Late light nSCBayes vs. MBLR with different lower bound for charge integration. This is data with rat version 5.14 which includes the PLSC. 198
B.4 Late light nSCBayes vs. MBLR with different lower bound for charge integration. This is the MC samples with clipping turned on and PLSC turned off. 199
B.5 Late light nSCBayes vs. MBLR with different lower bound for charge integration. This is the MC samples with both clipping and PLSC turned off. 200

D.1 Event leakage using the SplitEvent procedure for different fiducial volume cuts broken into different energy bins. As expected, lower energy events, due to their low charge information, have a higher leakage. Top row uses run 18831 and bottom row uses run 21399. The non-smooth behaviour is due to lower statistics at lower energies and lower fiducial volume cut, but the general trend remains the same; higher leakage probability for lower energy events. 203

E.1 A regular Cherenkov event with a single bright PMT. 205
E.2 Four examples of Cherenkov events where we have two or three cluster of bright PMTs. These event would not happen very often if the detector was filled with LAr. This is an indication of the electron leaking inside the detector and hitting another LG causing a second Cherenkov event. . 206
E.3 Expected number of neck and dust background events using afterpulsing_DOWN, afterpulsing_UP, and pmt_204_OFF systematic variations. 207
E.4 Expected number of neck and dust background events using pmt_efficiency_DOWN, pmt_efficiency_UP, and pmt_efficiency_SMEAR systematic variations. 208
E.5 Expected number of neck and dust background events using quenching_factor_DOWN, quenching_factor_UP, and refractive_index_DOWN systematic variations. 209
E.6 Expected number of neck and dust background events using refractive_index_UP, tpb_ly_DOWN, and tpb_ly_UP systematic variations. 210
E.7 Expected number of neck and dust background events using tpb_scattering_length_DOWN and tpb_scattering_length_UP systematic variations. 211
E.8 Total number of expected background events **(a)** assuming the first-year dataset and the **(b)** the three-year dataset using the original cutflow used by DEAP. The fiducial volume is 630 mm 212
E.9 Total number of expected background events with the updated cutflow proposed in this thesis and assuming the first-year dataset for different fiducial volume cuts. 213

E.10 Total number of expected background events with the updated cutflow proposed in this thesis and assuming the three-year dataset for different fiducial volume cuts. 214

F.1 From top row to the bottom row, the upper, median, and lower 90% CL for the 6 fiducial volumes studied with the updated cutflow. The left column uses the 223 live-days dataset and the right column uses the 386 live-days dataset. 216

F.2 The events that survive the full cutflow and the events that were tagged and removed by the STA and the Double Charge Cluster (DCC) cut for different fiducial volumes are shown in the nSCBayes-$R_{\mathrm{prompt60Bayes}}$ space using the 223 live-days dataset. The numbers in parenthesis in the legend show the number of events in each category. The black box is the WIMP ROI used in this thesis. 218

F.3 The events that survive the full cutflow and the events that were tagged and removed by the STA and the Double Charge Cluster (DCC) cut for different fiducial volumes are shown in the spacial ρ-Z space (MBL fitter) using the 223 live-days dataset. The numbers in parenthesis in the legend show the number of events in each category. The green line highlights the fiducial boundary. 219

F.4 The events that survive the full cutflow and the events that were tagged and removed by the STA and the Double Charge Cluster (DCC) cut for different fiducial volumes are shown in the nSCBayes-$R_{\mathrm{prompt60Bayes}}$ space using the 386 live-days dataset. The numbers in parenthesis in the legend show the number of events in each category. The black box is the WIMP ROI used in this thesis. 220

F.5 The events that survive the full cutflow and the events that were tagged and removed by the STA and the Double Charge Cluster (DCC) cut for different fiducial volumes are shown in the spacial ρ-Z space (MBL fitter) using the 386 live-days dataset. The numbers in parenthesis in the legend show the number of events in each category. The green line highlights the fiducial boundary. 221

Glossary

Symbols | **A** | **B** | **C** | **D** | **E** | **F** | **G** | **H** | **L** | **M** | **N** | **P** | **Q** | **R** | **S** | **T** | **V** | **W** | **Z**

Symbols

ΛCDM Λ Cold Dark Matter, or Standard Model of Cosmology.

A

ADC Analog-to-Digital Converter.

ADMX Axion Dark Matter eXperiment.

AmBe AMericium-BEryllium.

AP AfterPulsing.

ArDM Argon Dark Matter.

ASUM Analog SUM.

AV Acrylic Vessel.

B

BBN Big Bang Nucleosynthesis.

BH Black Hole.

BSM Beyond the Standard Model.

C

CDM Cold Dark Matter.

CDMS Cryogenic Dark Matter Search.

CL Confidence Level.

CMB Cosmic Microwave Background.

CP Charge-Parity.

CPT Charge-Parity-Time reversal.

CR Control Region.

D

DAQ Data AcQuisition.

DEAP Dark matter Experiment using Argon Pulse-shape discrimination.

DM Dark Matter.

DN Dark Noise.

DTM Digitizer and Trigger Module.

E

EDR Energy Dependant Recombination.

EFE Einstein Field Equations.

EIR Energy Independant Recombination.

EM ElectroMagnetic.

ER Electron Recoil.

F

Fprompt Ratio of Prompt Charge.

G

GADMC Global Argon Dark Matter Collaboration.

GAr Gaseous Argon.

GR General Theory of Relativity.

GVT Gauge Vector-Tensor gravity.

H

HDM Hot Dark Matter.

HQE High Quantum Efficiency.

L

LAr Liquid Argon.

LET Linear Energy Transfer.

LG Light Guide.

LHC Large Hadrons Collider.

LHS Left-Hand Side.

LSR Local Standard of Rest.

LXe Liquid Xenon.

LY Light Yield.

LZ LUX-ZEPLIN experiment.

M

MACHO Mssive Astrophysical Compact Halo Object.

MBL MBLikelihood.

MC Monte Carlo.

MDM Mixed Dark Matter.

MoND Modified Newtonian Dynamics.

MS Million Sample.

MVA Multi-Variable Analysis.

MWE Metre Water Equivalent.

N

NEWS-G New Experiments with Spheres-Gas.

NFW Navarro–Frenk–White.

NLL Negative Log Likelihood.

NR Nuclear Recoil.

nSCBayes Number of Scintillation Photons.

P

PBH Primordial Black Hole.

pC picoCoulomb.

PDF Probability Distribution Function.

PDG Particle Data Group.

PE PhotoElectron.

PLR Profile Likelihood Ratio.

PLSC Pulse-Level Saturation Correction.

PMT PhotoMultiplier Tube.

PPG Pulse Pattern Generator.

PSD pulse shape discrimination.

Q

QCD Quantum ChromoDynamics.

QF Quenching Factor.

QFT Quantum Field Theory.

R

RAT Reactor Analysis Tool.

RHS Right-Hand Side.

RMS Root Mean Squared.

ROI Region of Interest.

S

SCB Signal Conditioning Board.

SD Spin-Dependent.

SHM Standard Halo Model.

SHV Safe High Voltage.

SI Spin-Independent.

SM Standard Model of Particle Physics.

SNO Sudbury Neutrino Observatory.

SPE Single PhotoElectron.

SSB Spontaneous Symmetry Breaking.

STA Surface Tagging Algorithm.

T

TeVeS Tensor-Vector-Scalar gravity.

TF2 TimeFit2.

ToF Time of Flight.

TPB TetraPhenyl Butadiene.

TPC Time Projection Chamber.

V

VUV Vacuum UltraViolet.

W

WDM Warm Dark Matter.

WIMP Weakly Interacting Massive Particle.

Z

ZLE Zero Length Encoding.

Chapter 1

Review of Theory and Model

In this chapter, I review the theories and models related to our study. We first take a look at the Standard Model of Particle Physics (SM) [1], then the General Theory of Relativity (GR) [2] and lastly, we take a close look at the ΛCDM (Λ Cold Dark Matter) model [3], also referred to as the standard model of cosmology. We also will cover the Standard Halo Model (SHM).

1.1 The Standard Model of Particle Physics

The SM has been extremely successful in explaining three of the four fundamental forces: the electromagnetic, weak, and strong forces. A theory is considered successful if it can explain the observations that are already made and make predictions that can be verified. The SM for many years did the same. In a single framework, it was capable to explain the observations related to the three fundamental forces and made extremely important predictions, among which are the prediction of the top and charm quarks, gluons, W and Z bosons, and the Higgs boson that was discovered last in 2012 to complete the SM picture [1].

The elementary particles in the SM are divided into two categories: Fermions and Bosons. Fermions are particles with a half-integer spin that obey the Fermi-Dirac statistics. Bosons follow Bose-Einstein statistics and have full integer spins. Fermions themselves are sub-divided into two groups: leptons and quarks. Both leptons and quarks come in three generations. All particles in the SM come with an antiparticle. Antiparticles have the same mass as their partner but some quantum numbers are reversed, such as the electric charge and lepton number. Some particles, such as photons and gluon, are their own antiparticle [1].

The three generations of charged leptons are electron(e), muon (μ), and tau (τ). They all have an electric charge of -1q_e[1] but the mass increases from each generation to the next. Each generation include a corresponding neutrino; i.e electron-neutrino (ν_e), muon-neutrino (μ_e), and tau-neutrino (τ_e). Neutrinos carry no electric charge and there has not been an exact measurement of their mass, only upper limit bounds have been measured [1].

Similar to leptons coming in pairs, quarks also come in pairs that are up-type quarks and down-type quarks. The up-type quarks, in the order of increasing mass, are up (u), charm (c), and top (t) which all carry a fractional charge of +2/3. The corresponding down-type quarks are down (d), strange (s), and bottom (b), all carrying an electric charge of $-1/3$. Another major difference between leptons and quarks is that due to the colour confinement phenomenon, quarks cannot be observed in isolation but are always contained in particles called hadron. Hadrons, based on their quark content are divided into two groups, baryons and mesons. Baryons are made of three quarks while mesons constituents are a quark and an anti-quark. The most common hadrons, baryons to be explicit, are protons and neutrons. A proton is made up of two up quarks and a down quark leading to an electric charge of +1 and a neutron is made of two down quarks and an up quark making it electrically neutral [1].

Bosons are divided into two groups. The four gauge bosons are the force carriers: the photon (γ) being the force carrier of the electromagnetic force, $W^{\pm}$ and Z bosons are the force carrier of weak interactions, and gluon (g) is the force carrier of the strong force. All of the gauge bosons are vector bosons with spin 1. The Higgs boson is a scalar boson, spin 0, which is responsible for giving the particles their mass through the Higgs mechanism. See Figure 1.1 for the full picture of SM elementary particles [1].

The SM is a gauge theory with a symmetry group of $SU(3)_C \otimes SU(2)_L \otimes U(1)_Y$ where

---

[1] $q_e = 1.60 \times 10^{-19}$ Coulombs (C). q_e, sometimes also denoted as e, is the unit elementary charge carried by a proton. In this thesis, we set $q_e = 1$.

the subscripts C, L, and Y stand for colour, left-handedness, and the weak hypercharge, respectively. The $SU(3)$ group is responsible for explaining the strong interaction and the eight massless gluon fields. The $SU(2) \otimes U(1)$ group, plus using the Higgs mechanism, explains the electroweak interaction and the massive $W^{\pm}$ and Z bosons, along with the massless photon γ [1]. In 2012, two of the CERN detectors (ATLAS[4, 5] and CMS[6]) confirmed the existence of a Higgs particle with a mass of 125 GeV/c^2 and completed the SM picture.

Although the SM has had significant success in explaining the interactions of the elementary particle and three forces of nature, there have been important questions and observations that it has not been capable of explaining. To name a few such important issues: matter-antimatter asymmetry, strong Charge-Parity (CP) violation, neutrino oscillations, the hierarchy problem, and proposing no candidates for the dark energy and the dark matter. The shortcoming of the SM in these areas has made physicists look into theories Beyond the Standard Model (BSM) [7], for a better model or extend the current model to address these problems. The two questions most interesting to us are dark matter and CP violation. The latter is of interest to us because a proposed solution can also give rise to a Dark Matter (DM) candidate.

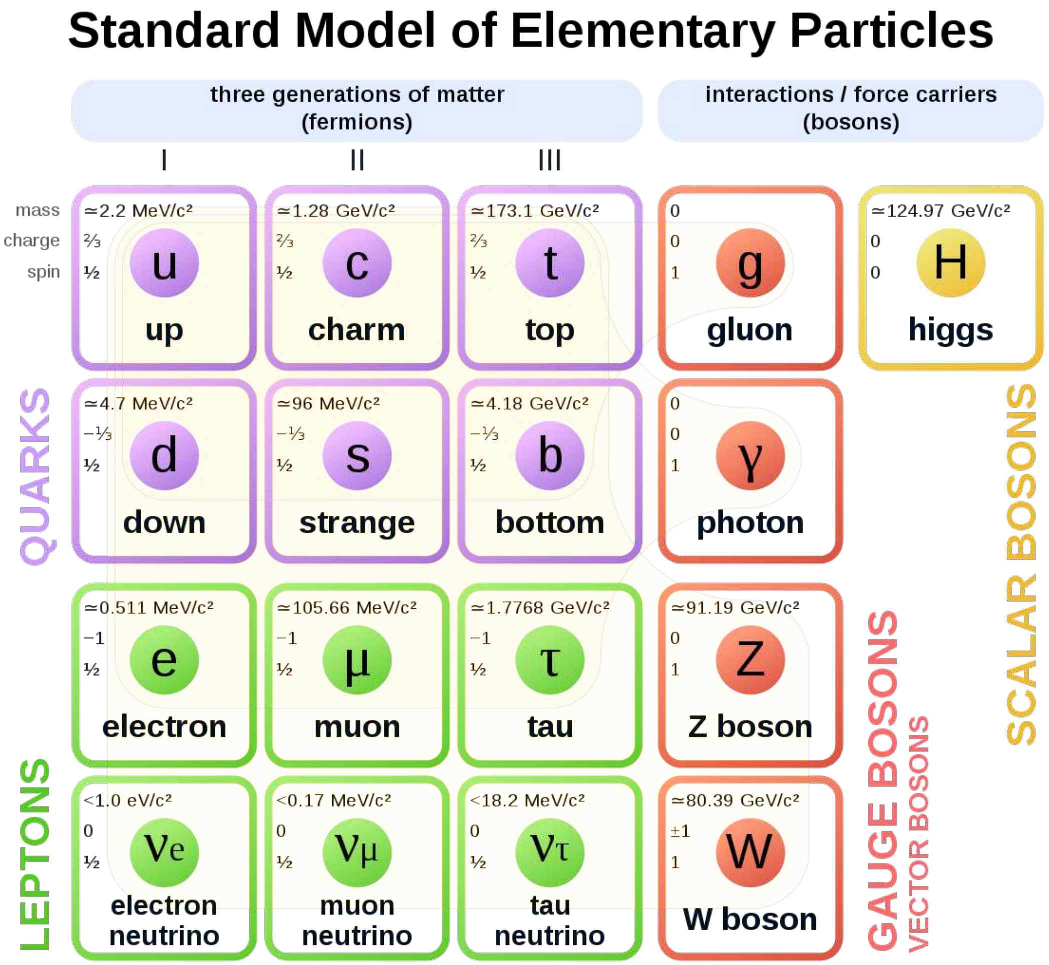

Figure 1.1: Elementary particles of the SM. Image copyright from MissMJ Cush under Creative Commons Attribution, taken from Wikipedia.

1.2 General Relativity

The fourth force of nature, gravity, is described by GR. Unlike SM which is a quantum theory, GR is a classical theory and we still do not have a consistent quantum theory for it. GR was first proposed by Albert Einstein back in 1915 [2] in an attempt to generalize his special relativity and Newton's law of universal gravitation. His work, as he mentioned in his paper, greatly relied on the work of great mathematicians and physicists such as Minkowski, Gauss, Riemann, Christoffel, and Grassmann. Einstein viewed the gravitational force as the curvature or the geometric properties of the spacetime governed by the matter distribution. GR is described by the Einstein Field Equations (EFE):

$$R_{\mu\nu} - \frac{1}{2} R g_{\mu\nu} + \Lambda g_{\mu\nu} = \frac{8\pi G}{c^4} T_{\mu\nu}, \tag{1.1}$$

where $R_{\mu\nu}$ and R are the Ricci curvature tensor and the Ricci scalar (also known as scalar curvature), respectively. $g_{\mu\nu}$ is the metric tensor and Λ is the cosmological constant, G is the newton's gravitational constant, c is the speed of light, and $T_{\mu\nu}$ is the stress-energy tensor. μ and ν are free parameters running from 0 to 3. Equation 1.1 is usually written in the form:

$$G_{\mu\nu} + \Lambda g_{\mu\nu} = \frac{8\pi G}{c^4} T_{\mu\nu}, \tag{1.2}$$

where $G_{\mu\nu} = R_{\mu\nu} - \frac{1}{2} R g_{\mu\nu}$ is the Einstein tensor. The Left-Hand Side (LHS) describes the curvature of the spacetime and the Right-Hand Side (RHS) is the description of the matter-energy content of the spacetime. In a rather well-known quote, John Wheeler described EFE "Spacetime tells matter how to move; matter tells spacetime how to curve."

EFE are a set of non-linear partial differential equations, thus making it very hard to solve. There are in fact very few exact solutions to these equations. A trivial solution is the Minkowski metric which describes the case of the flat spacetime; i.e no matter content and setting $T_{\mu\nu} = 0$:

$$\eta_{\mu\nu} = \mathrm{diag}(-1, +1, +1, +1). \tag{1.3}$$

Since the Minkowski metric is a special case of the metric tensor $g_{\mu\nu}$, it is often denoted by $\eta_{\mu\nu}$. There is always a degree of freedom in choosing the metric signature; i.e the sign of spatial and time coordinates. So, both $(-1, +1, +1, +1)$ and $(+1, -1, -1, -1)$ describe the same physics. What matters is that the spatial coordinates have the same sign and are opposite to that of time coordinate. In GR, the most convenient way to describe a physical system is to use the Lorentz invariant spacetime interval ds:

$$ds^2 = g_{\mu\nu} ds^{\mu} dx^{\nu} \tag{1.4}$$

where dx is an infinitesimal coordinate displacement, and the component of $g_{\mu\nu}$ specify the solutions to the EFE. The first non-trivial solution of the EFE was found by Karl Schwarzschild in 1915 which described an electrically neutral, non-rotating, and spherically symmetric object with a mass M. This was the metric that first hinted at the existence of Black Holes (BHs); also known as the Schwarzschild Black Hole [8].

There is a historic and important point about Equation 1.2, the Λ term specifically. The original EFE did not include this term. Einstein realized that the equations without this term do not allow a static universe. The belief at that time was that our universe was static. So two years later in 1917, he added the constant term. But it came to light that there is a chance of expanding the universe using GR. The first person to find this was Alexander Friedmann in 1922. The equations came to be known as Friedmann equations. A few years later in 1927, Georges Lemaître came to the same conclusion, independently. In 1929 Edwin Hubble's observations confirmed the expansion of the universe using the redshift of distant galaxies. The observation was then called Hubble's law and then renamed to Hubble–Lemaître law [9, 10, 11, 12]. Einstein then accepted these observations and removed the term from his field equations, going back to his original proposal. Einstein, probably, thinking that he sacrificed the beauty of his theory for the sake of observations which later on were observed to be wrong, called this his biggest blunder[1]. The main twist came in 1998. Although the physics community had accepted the notion of the expanding universe, the expectation was that the rate of expansion should be decreasing due to the gravitational pull of all the matter in the universe. Observations of Type-Ia supernovae in 1998 showed that the rate of acceleration is increasing [13, 14]. So, once again the second term in Equation 1.2 was added to the EFE, this time to explain the accelerating expansion of the universe.

GR has been tested for decades on different fronts and every time has come out successful. One of the first tests of the theory was calculating the correct amount of perihelion precession of Mercury done by Einstein himself [15]. Although this was a good validation for the theory, the first and most important observation was the deflection of light by the Sun. This was known but only GR ended up calculating the correct amount of deflection. The total solar eclipse that happened on May 29, 1919 gave scientists a great opportunity to test the theory by measuring the change in the position of stars where their light was passing near the Sun. The measurements done by Arthur Eddington and his collaborators [16, 17] confirmed the calculated values by GR and made headlines. Some other observations that made GR successful are: gravitational redshift of light, gravitational lensing, direct detection of gravitational waves [18], and the latest confirmation being the direct observation and an image of a black hole [19].

1.3 ΛCDM

Since most of the evidence of DM comes from cosmological observations, it is useful to briefly discuss this model. The most successful model describing the universe is the Big Bang model. In this model, the universe was born from an initial singularity with an infinite density about 13.799 ± 0.021 billion years ago [20]. As time passed, the universe expanded and as a consequence, cooled down. Let's first take a look at the thermal history of the universe.

---

[1] Although there are not many exact references to this.

1.3.1 Thermal History

For studying the thermal history of the universe, we need two key parameters; the rate of particle interaction Γ and the rate of expansion H which is the Hubble parameter. Then we can define the time characteristics as:

$$t_c \equiv \frac{1}{\Gamma}, \qquad t_H \equiv \frac{1}{H}. \tag{1.5}$$

When $\Gamma \gg H$, it means that the particle interactions are much faster than the expansion of the universe. Typically, at high energies, the rate of interaction is much bigger than the rate of expansion but as the universe cools down, Γ decreases faster than H. When $t_c \sim t_H$ the particles decouple from the thermal bath. Since different particle species have different interaction rates, they decouple at different times throughout the expansion of the universe [3].

The first major event after the Big Bang is Baryogenesis. The universe at the present is filled with matter and no antimatter. There can only be two explanations for this observation. One could simply assume that the universe was initially born with more matter and see it as an initial condition. The other scenario is to assume the universe was symmetric but there are processes that can break the symmetry of matter and antimatter. Baryogenesis refers to such processes that create matter asymmetry. There are models for Baryogenesis but we still do not have observational evidence to pick a model.

The next major event happened at around 100 GeV or 20 ps after the Big Bang where the electroweak phase transition happened; when particles received their mass through the Higgs mechanism. At around 150 MeV the Quantum Chromodynamics (QCD) phase transition happened. This was the time that quarks and gluons combined to create mesons and baryons such as protons and neutrons. We still have not discussed DM but somewhere between 150 MeV to 1 MeV, DM freeze-out took place[1]. One second after the Big Bang, the energy dropped to around 1 MeV and the neutrinos decoupled

---

[1] Under certain assumptions and DM models.

with the thermal bath. Up to this point, photons, electrons, and positrons have been in equilibrium. Five seconds later, at 500 keV, electron-positron annihilation happened which caused the temperature of photons to decrease to less than that of neutrinos. Big Bang Nucleosynthesis (BBN) is the formation of light elements and happened about 3 minutes later at energies around 100 keV. The universe kept expanding and cooling down and 60,000 years after the Big Bang it transitioned from radiation dominance to matter dominance.

Probably one of the most important incidents in the history of the universe is recombination. Recombination happened around 260–380 thousand years after the Big Bang. When the temperature (or energy density) of the universe dropped to around 0.3 eV, neutral hydrogen started forming because the reverse reaction of $e^- + p^+ \rightarrow H + \gamma$ would happen less frequently has the universe cooled down and there were less energetic photons causing the reverse reaction. So far, the photon has been coupled to the thermal bath through the Thomson scattering $e^-\gamma \rightarrow e^-\gamma$. The formation of neutral hydrogen meant a drastic reduction of free electrons, thus the photon decoupled from the thermal bath. From the Big Bang until around 380 thousand years no photons could not escape and the universe was opaque. After the recombination and photon decoupling, the first photons were released and created the Cosmic Microwave Background (CMB). That's why the CMB map is extremely important in modern cosmology: it contains the oldest information about our universe. Note that the "re" prefix is a misleading name, there had not been any combination before this era.

After more than 100 million years after the Big Bang, the first stars began to form. These stars could produce high-energy photons to ionize the neutral hydrogen in the universe. This epoch is known as reionization. And the last major incident happened about 4 billion years ago when the universe transitioned from matter dominant to dark energy-dominant era causing the accelerated expansion of the universe. Table 1.1 summarizes the thermal history of the universe.

Event	time t	redshift z	temperature T
Singularity	0	∞	∞
Quantum gravity (Planck epoch)	$\lesssim 10^{-43}$s	-	$\gtrsim 10^{19}$ GeV
Grand unification	$\lesssim 10^{-36}$s	-	$\gtrsim 10^{16}$ GeV
Inflation	$\lesssim 10^{-34}$s	-	$10^{15} \sim 10^{9}$ GeV
Baryogenesis	$\lesssim$ 20ps	$> 10^{15}$	$>$ 100 GeV
EW phase transition	20 ps	10^{15}	100 GeV
QCD phase transition	20 μs	10^{12}	150 MeV
Dark matter freeze-out	?	?	?
Neutrino decoupling	1 s	6×10^{9}	1 MeV
Electron-positron annihilation	6 s	2×10^{9}	500 keV
Big Bang nucleosynthesis	3 min	4×10^{8}	100 keV
Matter-radiation equality	60 kyr	3400	0.75 eV
Recombination	260–380 kyr	1100–1400	0.26 - 0.33 eV
Photon decoupling	380 kyr	1100	0.26 eV
Reionization	100–400 Myr	10 - 30	2.6–7.0 meV
Dark energy-matter equality	9 Gyr	0.4	0.33 meV
Present	13.8 Gyr	0	0.24 meV

Table 1.1: A brief history of the evolution of the universe and the key events [3].

1.3.2 Λ, The Cosmological Constant

The first part of the ΛCDM model is, of course, the Λ or the cosmological constant which represents the dark energy. As we discussed earlier in this chapter, Λ was added to the EFE, Equation 1.2, after the discovery of accelerating expansion of the universe [21]. Nine billion years after the Big Bang, the Universe had another transition and became dark energy dominant and the expansion of the universe started accelerating. Dark energy is an unknown form of energy that instead of causing the matter content to collapse under gravitational force, it repels them away from each other. The density of dark energy stays constant as the universe expands and does not dilute. We can formulate Λ in a way that would be equivalent to the vacuum energy of space. The nature of the cosmological constant is an active research area. In fact, the disagreement between the observed value of the cosmological constant and the suggested value from Quantum Field Theory (QFT) is referred to as the cosmological constant problem or vacuum catastrophe. The discrepancy can be as high as 120 orders of magnitude [22] where the authors mention that this is "the largest discrepancy between theory and experiment in all of science". There are also other models such as the inhomogeneous cosmology where physicists argue that the observed acceleration expansion can be just an observational artifact and there is no need for dark energy. See [23, 24, 25] for more details.

1.3.3 Hot, Warm, and Cold Dark Matter

The second part of the ΛCDM model is the Cold Dark Matter. DM candidates are often divided into three categories: Hot, warm, and cold DM. To the authors' knowledge, these terms were first used in 1983 [26, 27]. In this section, we talk about these different candidates and why the cold DM is usually conceived as a better candidate.

Hot Dark Matter (HDM) HDMs are a form of DM that travel at ultra-relativistic velocities. HDM was mainly discarded after the observations made of the CMB. When it comes to the structure formation in the observable universe[1], the small fluctuations in the CMB combined with HDM cannot explain the formation of galaxies. Any fluctuation with a scale smaller than super-clusters will be washed out by the HDM [27]. It also contributes to top-down structure formation which does not agree with the observed data; DM is not hot, or at least not dominantly. An example of HDM is neutrinos.

Cold Dark Matter (CDM) CDM particles are typically heavier than HDM and travel much slower. However axions which are very light can form a different type of CDM. The free streaming of CDM does not have any impact on the CMB fluctuations and can explain the structure formation much better than HDM; therefore it has been the more favourable model for the past few decades. The CDM was first proposed in 1982 by three independent groups [28, 29, 30] and the theory was further developed in 1984 [31]. CDM contributes to the bottom-up structure formation and are the focal point in this thesis. We will discuss them in more detail in section 3.2.

Warm Dark Matter (WDM) WDMs land somewhere between the hot and cold DM. They can cause a bottom-up (or hierarchical) structure formation from above their free-streaming scale and top-down (or fragmentation) below their free-streaming scale. WDM also have trouble with explaining the oldest observed large structures. Although the CDM is the best model yet, it is not safe from problems. Some have suggested that the inclusion of a fraction of WDM, even so very little, can reduce or completely solve these issues [32, 33]. Two of the most common WDM candidates are sterile neutrinos [34] and gravitinos[2] [35, 30, 29].

Mixed Dark Matter (MDM) One other category is MDMs which is not a new type but rather the combination of the first two categories, cold and hot DM. There are also

---

[1] We will have some reference to the structure formation in this section which will be discussed in section 2.4.

[2] In this thesis we won't talk about gravitinos anywhere else. These particles arise from the combination of GR and supersymmetry, and are the supersymmetric partner of the graviton which are the hypothesized quanta of gravity.

studies where MDM refers to the combination of cold and warm DM; e.g see [36]. A combination of hot and cold DM was of interest in the early 1990s but with the discovery of accelerating expansion of the universe in 1998 [21], the limits on the fraction of HDM became ever more stringent and the CDM gained more interest.

1.4 Standard Halo Model

Later in this thesis, we will concentrate more on the SHM for modelling DM in our universe and galaxy. In this section, we will cover the basics of this model.

An important observational evidence of DM was the galactic rotational curves. As can be seen from Figure 1.2, the disk of visible matter cannot alone explain galactic rotation. The SHM model was proposed based on such observations. The dark matter decouples from the cosmic expansion and clutters in regions that are called dark matter halo; the basic unit of cosmological structure. The ΛCDM model proposes that these halos themselves can contain subhalos [37]. Given we have halos, the question would be what is the DM distribution function?

One of the first and among the famous distribution profiles is the pseudo-isothermal halo distribution introduced in 1972 [38]:

$$\rho(r) = \frac{\rho_0}{1 + (r/r_c)^2}, \tag{1.6}$$

where ρ_0 is the finite central density and r_c is the core radius[1]. One of the main problems of this profile is that the total mass of the halo does not converge to a finite value as the radius goes to infinity. The most commonly used profile for the spatial mass distribution of DM in the SHM model is the Navarro–Frenk–White (NFW) profile. This profile was obtained by Julio Navarro, Carlos Frenk, and Simon White in 1995 by performing a fit to DM halos identified in N-body simulations [39]. The density of DM can be written as a function of radius:

$$\rho(r) = \frac{\rho_{crit}\ \delta_c}{(r/r_s)\,(1 + r/r_s)^2}, \tag{1.7}$$

---

[1] A measure of size of the central region.

where $\rho_{crit} = \frac{3H}{8\pi G}$ is the usual critical density of the universe, $r_s = r_{200}/c$ is a characteristic or scale radius in which r_{200} is referred to as the virial radius[1], and δ_c is dimensionless and is the characteristic over-density related to concentration c as follows:

$$\delta_c = \frac{200}{3} \frac{c^3}{(\ln(1+c) - c/(1+c))}. \tag{1.8}$$

This profile still results in mass divergence so the edge of the halo is often taken as the virial radius to avoid this issue. The NFW is a universal density profile [41] because it was shown that this profile can work for a variety of halos including dwarf galaxies and galaxy clusters and with masses spanning four orders of magnitude [39].

DM halos can be observed from their gravitational effects. For halos with lower masses, the gravitational lensing becomes too noisy and it is harder to extract useful information. But the recent and more accurate measurements, and by averaging the profiles of similar systems, show that the predictions of NFW profile remains valid even for small halos where these halos can be as small as the ones that surround isolated galaxies, such as the Milky Way [43]. It is up to debate if the NFW profile is compatible with observations when it comes to inner regions of bright galaxies such as the Milky Way or M31 [44]. But when it comes to the inner regions of low-surface-brightness galaxies that have less than predicted central mass, the NFW profile cannot describe the observations [45, 46]. This shortcoming is known as the cuspy halo problem[2]. It is still not clear what is the source of this discrepancy; it can be due to the nature of the DM, or caused by dynamical processes during galaxy formation, or the dynamical modelling of the observational data has shortcomings [51].

In the SHM, the velocity distribution of DM in the halo is a Maxwellian distribution,

---

[1] In Ref [39], r_{200} is the radius where the average density within this radius is 200 times the critical or mean density of the universe. A more general equation would be $R_\delta = cR_s$ where the average density within the radius is δ times the critical density. The virial radius is usually between R_{200} to R_{500} but even values of R_{100} are used in X-ray astronomy caused by higher concentrations [40].

[2] The lack of consistency between the inferred DM density profile of low-mass galaxies and the density profile that cosmological N-body simulations predict is referred to as the cuspy halo problem or core-cusp problem. See Ref. [47, 48, 49, 50] for some of the proposed solutions to the cuspy halo problem

modelled as an isothermal sphere [52]:

$$f(\mathbf{v}) = \frac{1}{(2\pi)^{3/2}\sigma^3} \exp\left(-\left(\mathbf{v}-\mathbf{v}_{\mathrm{lag}}\right)^2/2\sigma^2\right), \tag{1.9}$$

where $\sigma \approx 156$ km/s is the velocity dispersion in the Milky Way where the typical value is chosen such that it would match the peak speed of the local rotational speed of $v_0 = \sqrt{2}\sigma \approx 220$ km/s[1]. $\mathbf{v}_{\mathrm{lag}}$ contains the information on the motion of the Earth with respect to the Galactic halo which is the contribution of the motion of the Sun within the galaxy and the Earth's orbital motion around the sun. $\mathbf{v}_{\mathrm{lag}}$ is time dependant but in simple models, a constant value of $|\mathbf{v}_{\mathrm{lag}}| \approx 230$ km/s is chosen [53], which is to say, to first order, we can ignore the Earth's motion around the Sun. Since the DM is gravitationally bound to the galaxy, the velocity distribution is truncated and can't extend to any arbitrary high value. So we calculate that distribution up to the gravitational escape velocity of $v_{\mathrm{esc}} \approx 544$ km/s [54].

There is a more elegant way to rewrite Equation 1.9 as a Gaussian in the Galactic frame [55]:

$$f_R(\mathbf{v}) = \frac{1}{(2\pi\sigma_v^2)^{3/2} N_{\mathrm{R,esc}}} \exp\left(-\frac{|\mathbf{v}|^2}{2\sigma_v^2}\right) \times \Theta\left(v_{\mathrm{esc}} - |\mathbf{v}|\right), \tag{1.10}$$

where the truncation is achieved through the use of the Heaviside function Θ. After the truncation, we need to renormalize the distribution using the constant $N_{\mathrm{R,esc}}$ defined as:

$$N_{\mathrm{R,esc}} = erf\left(\frac{v_{\mathrm{esc}}}{\sqrt{2}\sigma_v}\right) - \sqrt{\frac{2}{\pi}}\frac{v_{\mathrm{esc}}}{\sigma_v} \exp\left(-\frac{v_{\mathrm{esc}}^2}{2\sigma_v^2}\right). \tag{1.11}$$

In the SHM model, to fully describe the velocity distribution we only need to have the values of v_0 and v_{esc}. There have been updates to these parameters throughout the years and although the SHM remains a good model, it has some shortcomings.

In light of recent data from the Gaia Sausage, the SHM has been refined and referred to as SHM^{++} [55]. The main problem that was seen through the data from Gaia was that the observations were showing that our local halo has two components rather than

---

[1] v_0 is also called Local Standard of Rest (LSR)

one [56, 57, 58, 59]. One region is the more metal-poor stars that form a weakly-rotating almost-spherical structure. The weak rotation in the former region is probably due to having many dwarf galaxies with low masses heading in random directions such that the net angular momentum is almost zero. The second region is the more metal-rich stars where their structure is more flattened and are highly radially anisotropic. This is known as the "Gaia Sausage" created by the merger of a large dwarf galaxy around 8-10 billion years ago with a mass of approximately $10^{10} - 10^{11} M_\odot$ [56, 60, 61], where a stream of DM would have followed such accretion. So, given the Gaia data, we can rewrite the velocity distribution as the sum of two terms where we add a Sausage term [55]:

$$f(\mathbf{v}) = (1-\eta)\, f_R(\mathbf{v}) + \eta f_S(\mathbf{v}), \tag{1.12}$$

where $f_R(\mathbf{v})$ is Equation 1.10 describing the velocity distribution of a DM halo that is smooth and nearly round, dominating the gravitational potential of the most inner region, ≈ 20 kpc and $f_S(\mathbf{v})$ encodes the velocity distribution of the Gaia Sausage. Lastly, η is a constant determining the fraction of DM in the Sausage. The new velocity distribution has apparently three parameters but there is an extra hidden parameter when we expand $f_S(\mathbf{v})$. Using the galactocentric spherical coordinates, we can write the dispersion tensor as $\sigma^2 = \mathrm{diag}\left(\sigma_r^2, \sigma_\theta^2, \sigma_\phi^2\right)$ and since the gravitational potential is close to being spherical [62, 63], we have $\sigma_\theta^2 = \sigma_\phi^2$. The radial anisotropy of the Sausage term can be parameterized by:

$$\beta = 1 - \frac{\sigma_\theta^2 + \sigma_\phi^2}{2\sigma_r^2}. \tag{1.13}$$

Note that $\beta = 0$ is for an isotropic dispersion tensor. $\beta = 1$ means fully radial orbits, while $\beta = -\infty$ corresponds to a fully circular orbit. The Gaia Sausage shows $\beta = 0.9$ [56, 58] and based on the Globular Clusters, we have $\beta \sim 0.95$ [64], which shows a very radially anisotropic distribution. Thus, the full form of $f_R(\mathbf{v})$ is [65]:

$$f_R(\mathbf{v}) = \frac{1}{(2\pi)^{3/2}\sigma_r \sigma_\theta^2 N_{\mathrm{S,esc}}} \exp\left(-\frac{v_r^2}{2\sigma_r^2} - \frac{v_\theta^2}{2\sigma_\theta^2} - \frac{v_\phi^2}{2\sigma_\phi^2}\right) \times \Theta\left(v_{\mathrm{esc}} - |\mathbf{v}|\right), \tag{1.14}$$

where the velocity dispersion components can be written in terms of the amplitude of the rotation curve [65]:

$$\sigma_r^2 = \frac{3v_0^2}{2(3-2\beta)}, \qquad \sigma_\theta^2 = \sigma_\phi^2 = \frac{3v_0^2(1-\beta)}{2(3-2\beta)}, \tag{1.15}$$

where v_0 is regular LSR. Lastly, we need to write $N_{\mathrm{S,esc}}$ which is the renormalization factor similar to $N_{\mathrm{R,esc}}$:

$$N_{\mathrm{S,esc}} = \mathrm{erf}\left(\frac{v_{\mathrm{esc}}}{\sqrt{2}\sigma_r}\right) - \left(\frac{1-\beta}{\beta}\right)^{1/2} \exp\left(-\frac{v_{\mathrm{esc}}^2}{2\sigma_\theta^2}\right) \times \mathrm{erfi}\left(\frac{v_{\mathrm{esc}}}{\sqrt{2}\sigma_r}\frac{\beta^{1/2}}{(1-\beta)^{1/2}}\right), \tag{1.16}$$

where erfi is the imaginary error function. This is the full description of the SHM^{++} model, a fully analytic model describing a roundish dark halo and the new highly radially anisotropic Sausage term.

The last free parameter is the canonical value of the local density of DM within the SHM model. Using Particle Data Group (PDG) [1, 66], it is often taken as:

$$\rho_0 = 0.3 \text{ GeV cm}^{-3}. \tag{1.17}$$

Different assumptions can yield slightly different values which are still usually within a factor of 2 to 3 of the above value [66]. Table 1.2 summarizes the free parameters of the original SHM model and the refined version where the new model updates the three original free parameters and introduces two new ones.

Model	ρ_0 [GeV cm^{-3}]	v_0 [km/s]	v_{esc} [km/s]	β	η	$f(\mathbf{v})$
SHM	0.3	220	544	NA	NA	$f_R(\mathbf{v})$ Equation 1.10
SHM^{++}	0.55±0.17	233±3	528^{+24}_{-25} [67]	0.9 ± 0.05	0.2±0.1	$f_R(\mathbf{v})$ Equation 1.12

Table 1.2: The free parameters of the SHM and the refined version. Note that the SHM^{++} introduces two new free parameters. See Ref. [55] for more details on the SHM^{++}.

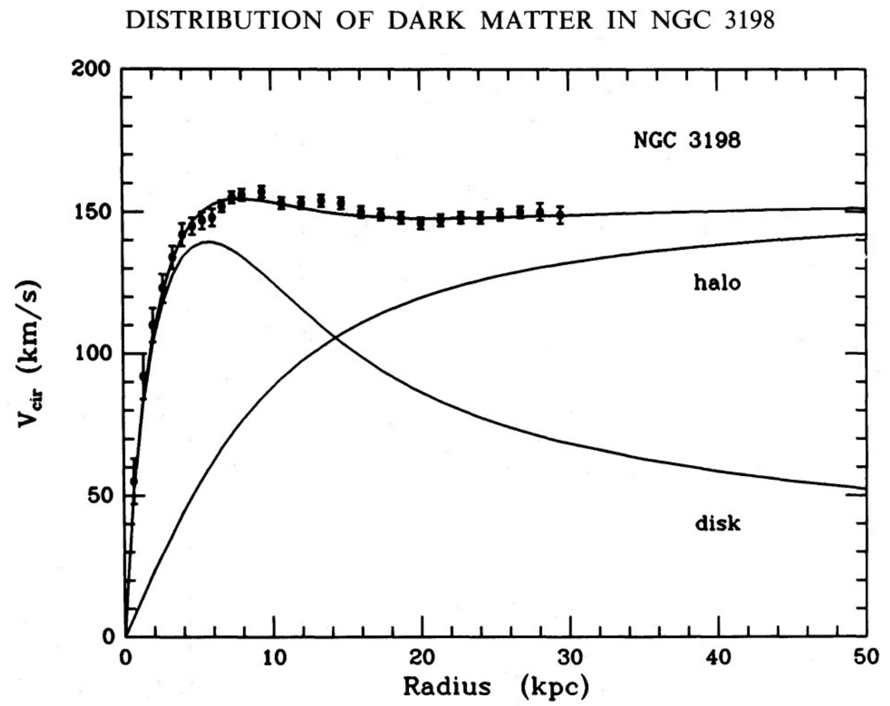

Figure 1.2: Rotation curve of the spiral galaxy NGC 3198 taken from [68]. See Ref [68] for more information on the different possible fits for the halo and the disk contribution to the orbital velocity.

Chapter 2

Dark Matter and Observational Evidence

In this chapter, I will cover some of the most important observational evidence for the existence of DM.

2.1 Rotation Curves

Fritz Zwicky was a Swiss astronomer who for the first time used the term “dunkle Materie” or dark matter in English. In 1933, Fritz Zwicky was studying the Coma galaxy cluster and used the virial theorem which for the first time showed a gravitational anomaly [69]. In a stable system with discrete particles, the virial theorem relates the total potential energy of the system to its averaged-over-time kinetic energy. Zwicky’s observations showed that the galaxies near the edge of the cluster are moving too fast to be gravitationally bound. He estimated that for the system to be stable, there should be about 400 times more unseen mass which he referred to as DM. His estimates were far off today’s observations, mostly from the value of the Hubble constant he was using. In 1930, the Hubble constant was believed to be around 500 km/s/Mpc while recent measurements, such as Planck’s 2018 result [70], show that the Hubble constant is closer to 70 km/s/Mpc. Although this observation started the consideration of the missing matter, it did not gain significant attention until the 1970s.

In 1970, following the work of Australian astronomer Kenneth Charles Freeman [71], Vera Rubin, Kent Ford, and Ken Freeman showed more evidence of the existence of DM using galaxy rotation curves [72]. Their observation of the rotation curve was far from what they expected. For a bound star, in a simplified model, if the mass of a galaxy within a radius r is $M(r)$, the centrifugal and gravitational force should balance:

$$\frac{mv^2}{r} = \frac{GmM(r)}{r^2}. \tag{2.1}$$

For most galaxies, most of the visible mass of the galaxy is close to the centre and we can model the galaxy as a point mass, assuming all the mass is the luminous mass. For the objects that are far enough from the centre, one can approximate $M(r)$ to be constant which would mean that the rotation curve should fall as:

$$v \approx 1/\sqrt{r}. \tag{2.2}$$

Rubin and Ford published their paper [73] in 1980 showing that for their sample of 21 Sc galaxies, shown in Figure 2.1, the rotation curve kept increasing or stayed constant, in disagreement with Equation 2.2. For 13 samples, they used the Hydrogen line[1] to expand their measurements to include gas. As more samples were collected in the following years, this behaviour was seen in other galaxies as well. Such behaviour would mean that the mass of the galaxy should increase linearly as a function of distance, or a mass density proportional to r^{-2}. This missing mass is called DM.

---

[1] Hydrogen line, or 21-cm line, or HI line, is the electromagnetic radiation caused by the spin-flip transition in hydrogen atom. The 1s ground state of hydrogen has two hyper-fine levels and when the electron's spin flips such that its spin is anti-aligned with the proton's spin and the emitted photon has a wavelength of $\lambda = 21$ cm.

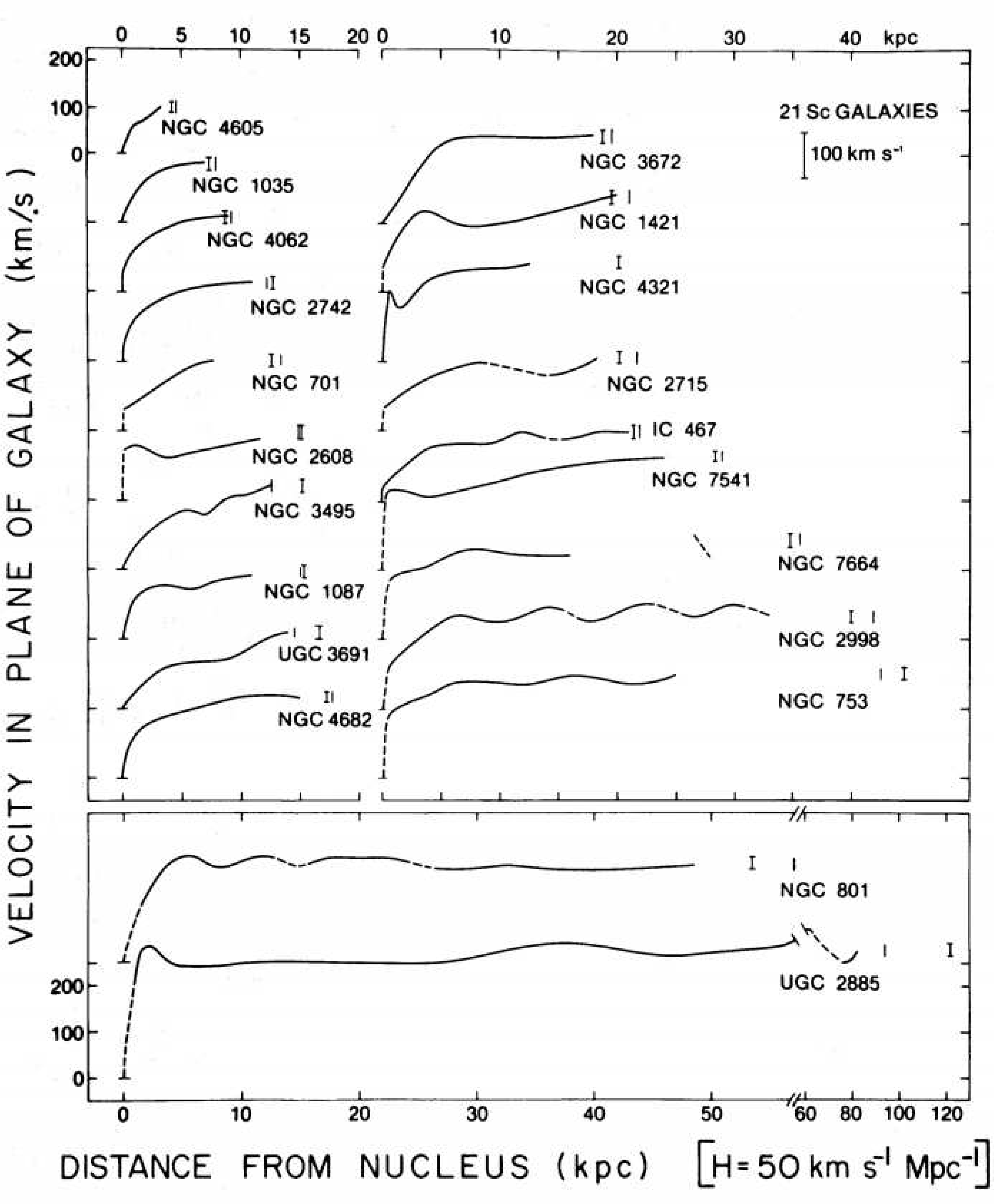

Figure 2.1: The rotation curve of 21 Sc galaxies showing the mean velocities in the plane of the galaxy versus distance from the core. Image taken from [73].

2.2 Bullet Cluster

The discrepancy observed in rotation curves was not enough to persuade the physics community about the existence of a new type of matter and attempts were made to solve the problem by modifying the theory of gravity, which will be discussed in the next chapter. The observation that made modified gravity theories face trouble explaining it was the Bullet cluster.

To better understand the Bullet cluster observation, we need to know about gravitational lensing. From GR, we know that any mass in the universe bends the space-time fabric. The path of light that travels through the space will be affected and bent by the curvature of space-time. In 1937, Fritz Zwicky postulated that this effect will make galaxy clusters behave as gravitational lenses. Gravitational lensing was observed for the first time in 1979 from the Twin Quasar [74]. In this observation, the galaxy YGKOW G1 was in the line of sight of the earth and a quasar. The distortion and lensing caused by the galaxy made the quasar appear as two different quasars. Gravitational lensing is also a powerful method for finding black holes where a source image is distorted while no visible mass is observed.

The Bullet cluster refers to the observation of the collision of two galaxy clusters that happened 150 million years ago at a distance of 1.14 Gpc away. Assuming DM exists, you can divide the constituents of a galaxy into three parts based on their behaviour during a collision. Due to the vast empty space between them, the galaxy distributions in the two clusters pass through each other during a collision and are only affected by the gravitational force. The stars can be observed in visible light. The hot gas of the two galaxies makes up most of the baryonic matter which during the collision interacts via electromagnetic force and is slowed down much more than the stars. The gas is observed in the X-ray range of the electromagnetic spectrum. Another way to find the mass distribution of the collision is through the gravitational lensing of the background objects. Without the existence of DM, it would be expected that the lensing would be strongest near the gas regions since it makes most of the visible matter but the results published in 2006 showed something different. Figure 2.2 shows the Bullet cluster from the Chandra X-ray observatory with an exposure time of 500 ks. The image is artificially coloured to show the intensity of the X-ray emission while the green contours show the mass distribution using gravitational lensing. The study done in [75] showed that the centre of the total mass is displaced from the baryonic mass peaks with a statistical significance of 8σ that cannot be explained by modifying the gravitational force law. To explain this discrepancy, you would need a large amount of non-luminous non-interacting matter that can pass through each other and shift the centre of the mass.

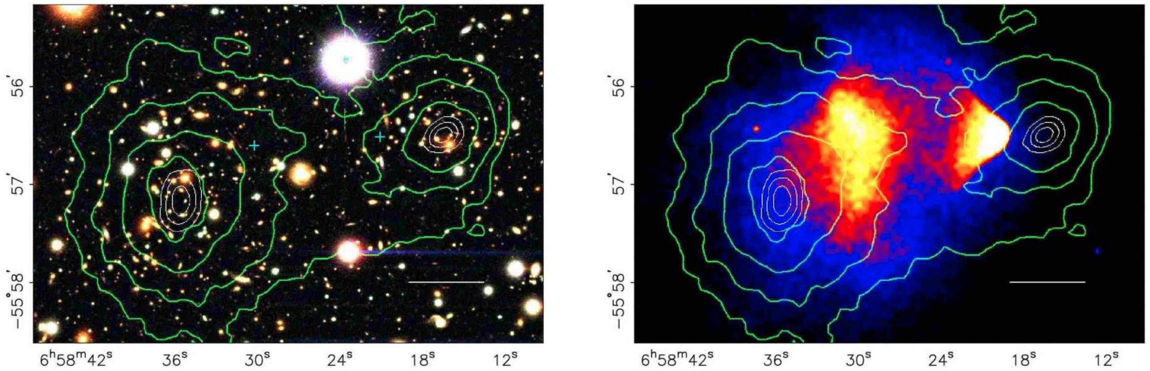

Figure 2.2: The right panel shows the artificially coloured image from the Chandra X-ray observatory with a 500 ks exposure time. The intensity shows the mass distribution derived from the X-ray emission of the gas. The green contours show the mass distribution reconstructed from weak lensing. The blue +s on the left panel, an image from the Magellan IMACs telescope, show the centre of mass of the baryonic matter. Image taken from [75].

2.3 Cosmic Microwave Background

In modern cosmology, the CMB map is the most important piece of data from which many physical parameters can be derived and/or constrained and produces strong evidence for dark matter. The CMB encodes the information about 380 thousand years after the Big Bang when the universe became transparent to photons. The CMB has a thermal black body spectrum with a temperature of $T = 2.7255\ K$. The temperature is uniform up to orders of $10^{-5} K$. Figure 2.3 shows the anisotropies of the CMB collected by the Planck satellite [76].

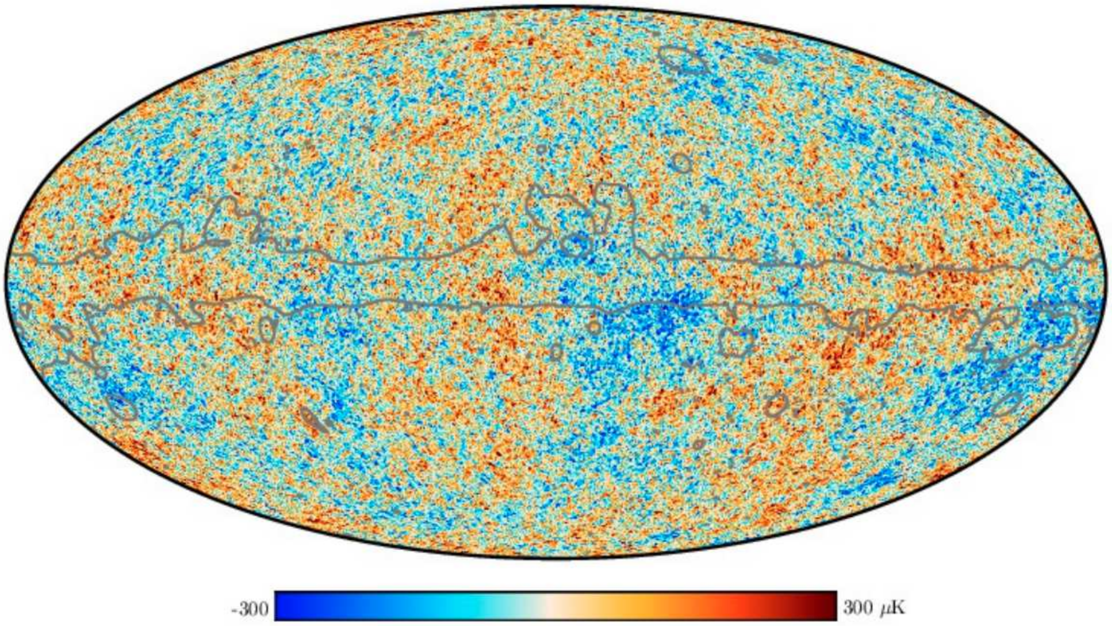

Figure 2.3: The anisotropies of the CMB map as measured by the Planck satellite [76].

Although the deviations from the mean temperature in CMB are small, they contain important information about the universe. The anisotropies can be described using a spherical harmonic expansion [1]:

$$T\left(\theta, \phi\right) = \sum_{lm} a_{lm} Y_{lm}\left(\theta, \phi\right), \tag{2.3}$$

where a_{lm} are the coefficients and Y_{lm} is the spherical harmonic. Figure 2.4 shows the temperature anisotropy in the CMB map. This figure only shows some of the latest results from a few experiments where data points with huge error bars have been removed [1].

The monopole component of the CMB map reduces to a_{00} that corresponds to the mean temperature of $T_\gamma = 2.7255 \pm 0.0006\ K(1\sigma)$ [77, 1]; the CMB spectrum can be described as a black body function with $T = 2.7255\ K$. This temperature can only be measured by absolute temperature instruments; like FIRAS on the COBE satellite [78, 1]. But this mean temperature is not important since most mappings deal with differences and are not sensitive to this average temperature.

The dipole term ($l = 1$) has the largest anisotropy, an amplitude of $3362.08 \pm 0.99\ \mu K$ [70]. This anisotropy is believed to correspond to the motion of the Solar System causing the monopole component to get Doppler shifted. The measurements of the radial velocities of local galaxies supports this interpretation [79, 1]. The higher-order multipoles are also important for cosmologists since they encode the density perturbation of the early universe. But the more important features of the CMB map are in acoustic peaks happening in the $100 \lesssim l \lesssim 1000$ range.

These acoustic peaks, in the angular scales less than 1°, have the highest constraining power. Fitting the ΛCDM model to the CMB temperature anisotropies can give us the density of DM, normal matter, and dark energy. The Planck 2018 results were fit assuming the total density $\Omega_{\text{tot}} = 1$, and found that $\Omega_b h^2 = 0.02237 \pm 0.00015$, $\Omega_c h^2 = 0.1200 \pm 0.00012$, and $\Omega_\Lambda = 0.6847 \pm 0.0073\ (= 1 - \Omega_m)$ [76, 1]. More than 68% of the total mass-energy of the universe is dark energy, more than 26% is made up of DM and less than 5% is baryonic matter.

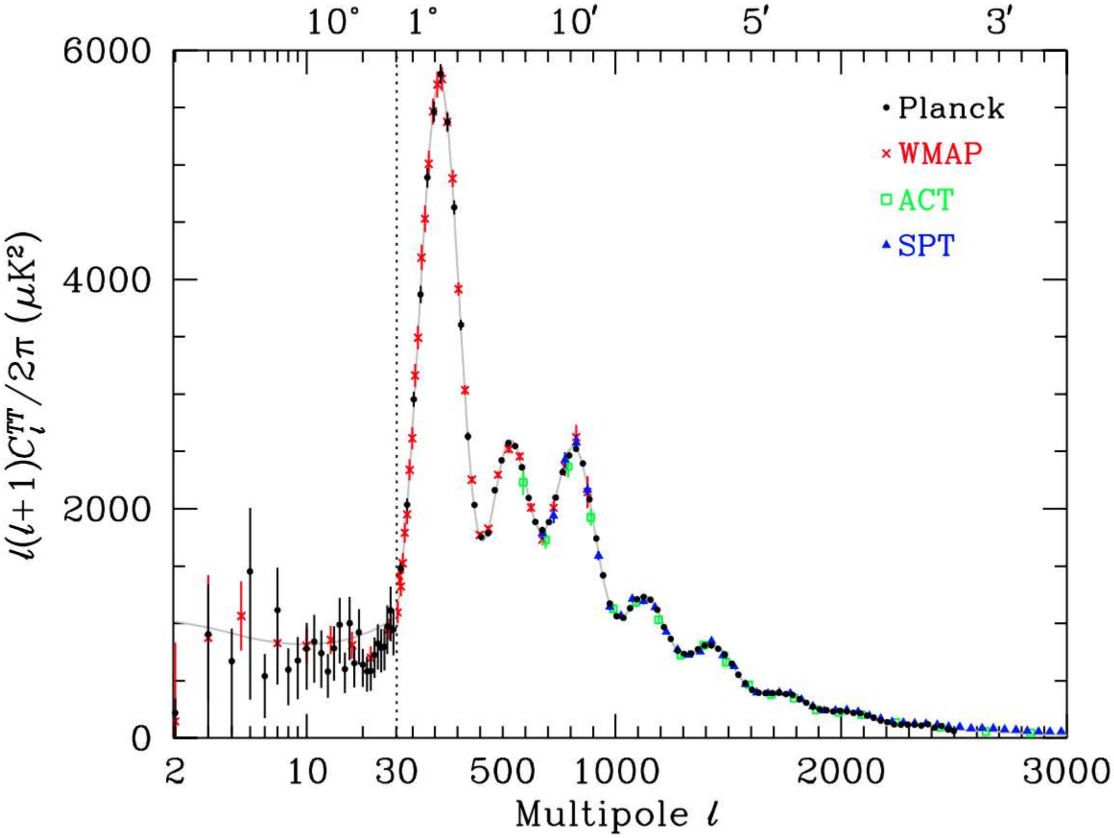

Figure 2.4: The magnitude of the CMB temperature anisotropies as a function of the multipole l in Equation 2.3. The lower x-axis is the multipole l which is logarithmic for $l < 30$ and linear for higher orders. The upper x-axis is the angular resolution with similar behaviour for logarithmic and linearity. The data are from the latest results of the experiments mentioned in the legend. Some data points with large error bars were removed by the authors. The plotted curve is from Planck's best fit of the ΛCDM model. Image is taken from [1].

2.4 Structure Formation

Another observational evidence for DM is the structure formation of the universe. Structure formation refers to the galaxies, galaxy clusters, and other larger structures that are formed from the small perturbation in the early energy-matter density distribution. Without DM it is hard to explain the existence of some of the oldest galaxies we observe, such as the GN-z11 galaxy [80]. The fluctuations in the CMB map are too small and it would take the gravitational force much longer to make the gas collapse and create such structures. For the first 50,000 years, the universe was in a radiation-dominated state and ordinary matter could not collapse to form gravitational wells. But the dark matter does not interact with the radiation and has enough time to create attractive potential wells from the small density fluctuations and speed up the structure formation process. When the matter decouples from the thermal bath, it can fall into these wells that already exist at this time.

There are two models for structure formation: bottom-up or hierarchical structure formation and top-down or fragmentation formation. The top-down theory was first proposed in 1962 [81]. This model begins from the matter fluctuations of the early universe. These clumps which were mostly made of DM would give each other some angular momentum through the tidal torques caused by their gravitational interaction. As time passes and the baryonic matter cools down, most of the mass would become concentrated in the centre. Since the angular momentum should remain conserved, the rotation of mass as it nears the centre would speed up which in return would form a tight disk. Once the disk cools down, the gas will no longer be gravitational stable and cannot remain as a single homogeneous cloud and thus breaks into smaller clouds. The stars are then formed from these smaller patches of gas. That's why the top-down model is also called the fragmentation model. Meanwhile, since the DM only interacts with the baryonic matter via gravity and does not dissipate, it remains outside the disk. This region of DM is also known as the dark halo. The problem though is that we have observations of stars outside the disk which does not agree with this model and this model is rejected these days.

The bottom-up model works in the opposite direction. Instead of clumps attracting and joining each other to form galaxies and galaxy clusters, in these models matter starts from these small clumps. Then these smaller structures join each other to form galaxies. Consecutively, the gravitational attraction of these galaxies brings them together to form galaxy clusters. With the same reasoning as above, the baryonic matter still ends up with disk-like distributions with the dark halo encompassing it. But the advantage of this approach is that it predicts more smaller galaxy populations compared to large ones which agrees with the observations.

Although the existence of DM solves some issues, there are still other astronomical problems with explaining other details of the galaxy formation and evolution. These problems are outside the scope of this thesis and they do not contradict the need of DM, but only suggest more refinement to the ΛCDM to better explain the observations.

Chapter 3

Dark Matter Candidates and Detectors

In the previous chapter, we talked about the observational evidence for the existence of DM. In this chapter, we will talk about some of the most promising or historically important candidates. We will also cover different detection methods of DM and the properties of DM based on the best current models.

3.1 Modified Gravity

Due to the inconsistency between observations and the gravitational model, some physicists started to question Newtonian gravitational law and proposed a modified version of the theory. Later on, such a proposition was taken into the GR model too. Although these approaches are not completely ruled out, most of them face a lot of trouble to explain all the observational evidence within a single model.

3.1.1 Modified Newtonian Dynamics

Chronologically, the first observed discrepancy that lead to the proposal of DM was the velocity distribution of galaxies in a galaxy cluster. One of the physicists that found an alternative to this approach was Mordehai Milgrom. In his 1983 paper [82], Milgrom proposed a modification to the Newtonian dynamics as a "possible alternative to the hidden mass hypothesis". Even in the 1980s, Newtonian gravity had been tested extensively but mainly in high-acceleration cases such as the Solar System or on the Earth. Milgrom suggested a modified version that would reduce to the Newtonian model in high-acceleration environments but would differ at low-acceleration, such as the stars in the outer parts of a galaxy. The gravitational force would be written as:

$$F = \frac{GMm}{\mu\left(\frac{a}{a_0}\right)R^2}. \tag{3.1}$$

This force differs from the Newtonian version by the function $\mu(x)$, also called the interpolating function. a_0 is a new fundamental constant marking the high and low acceleration regimes. All the models that take this approach are collectively known as the Modified Newtonian Dynamics (MoND) [82]. The high acceleration regime is referred to as the Newtonian regime while the low acceleration environment is called the deep-MOND regime. The interpolating function can take almost any form as long as it has the following two asymptotic behaviour:

$$\begin{cases} \mu(x) \to 1 & \text{for } x \gg 1, \\ \mu(x) \to x & \text{for } x \ll 1. \end{cases} \tag{3.2}$$

The two most common choices are:

$$\begin{aligned} \mu\left(\frac{a}{a_0}\right) &= \frac{1}{1+\frac{a}{a_0}}, && \text{simple interpolating function,} \\ \mu\left(\frac{a}{a_0}\right) &= \sqrt{\frac{1}{1+\left(\frac{a}{a_0}\right)^2}}, && \text{standard interpolating function.} \end{aligned} \tag{3.3}$$

Milgrom in his paper chose the standard interpolating function. For these functions to behave properly, we should have $a \ll a_0$. Taking the same simple assumption in Equation 2.1, in the deep-MOND regime, this time we have:

$$\frac{mv^2}{r} = \frac{GMm}{\frac{a}{a_0}r^2} = \frac{GMm}{\frac{v^2/r}{a_0}r^2} \quad \Rightarrow \quad v^4 = GMa_0, \tag{3.4}$$

which shows that the velocity is constant and independent of its radial distance, given it is sufficiently away from the centre to be in the deep-MOND regime. Milgrom fitted his model to the rotation curve and found $a_0 \approx 1.2 \times 10^{-10}$ ms^{-2} [82]. Note that, for example, the acceleration of the Earth around the Sun is approximately 6×10^{-3}ms^{-2}.

MoND is a classical modification to the Newtonian model. Before talking about the problems that these models face, let's first talk about relativistic generalization.

3.1.2 Tensor-Vector-Scalar Gravity

The Tensor-Vector-Scalar gravity (TeVeS) was developed in 2004 by Jacob Bekenstein [83]. This model is the relativistic generalization of the MoND paradigm. In this model, a scalar and a vector Lagrangian are added to the Einstein–Hilbert action:

$$S_{\text{TeVeS}} = \int \left(\mathcal{L}_g + \mathcal{L}_s + \mathcal{L}_v\right) d^4x, \tag{3.5}$$

where $\mathcal{L}_g = -\frac{1}{16\pi G} R\sqrt{-g}$ is the Einstein–Hilbert Lagrangian (the tensor part), while $\mathcal{L}_s$ and $\mathcal{L}_v$ are the newly added scalar and vector Lagrangians. We mention a few important points. First of all, this is not the only relativistic generalization, see Gauge Vector-Tensor gravity (GVT) [84], for example. Since these models are derived from the action principle, they respect conservation laws. Being a relativistic model, they can accommodate gravitational lensing too. Also, the MoND formula can be reproduced in the weak-field approximation of the spherically symmetric and static solutions.

Despite their success in explaining the rotation curve or even gravitational lensing to some degree, there are still observations that these models fail to explain. One of the most important ones is the Bullet Cluster we discussed earlier. Models proposing a modification to gravity predict that most of the mass would remain in the centre of the visible mass which contradicts the observations. On the other hand, models proposing DM predict the behaviour correctly. Other observations, including the CMB and structure formation, also pose difficulties for these modified gravity models.

3.2 Particle Candidates

One promising solution is to introduce new particles. Two of the most promising candidates are Weakly Interacting Massive Particles (WIMP) and Axions. There are other plausible candidates which we will not cover in detail in this section. Among these candidates are the Massive Astrophysical Compact Halo Objects (MACHOs) [85, 86], Sterile Neutrinos [87], Primordial Black Holes (PBHs) [88], dark photon [89], and so on. But in short, a suitable DM candidate is a massive particle that interacts via gravity and has no electromagnetic charge.

3.2.1 WIMPs

As mentioned before, WIMP is one the most promising DM candidates and many different collaborations and detectors around the world are trying to directly or indirectly observe them. Although there is not a clear definition of WIMP particle, a few properties are agreed upon; it's a new elementary particle that doesn't exist in the current SM, it only interacts via gravity and another force that is as weak as or weaker than the weak nuclear force but non-vanishing. WIMP candidates can cover a mass range of orders of 1 GeV to 10^3 GeV but the most favourable mass range is around 100 GeV. The main reason that WIMPs are a prime candidate is a phenomenon known as WIMP Miracle.

There are two points of view for the WIMP miracle that point to the same fact. A particle physics point of view is that some BSM scenarios can already predict new particles with masses around 100 GeV that happen to have the same required self-annihilation cross-section to explain the current abundance of DM. This coincidence that the properties of DM matches the properties of particles in the supersymmetric model is known as the WIMP miracle [90]. But the main point of view comes from cosmology which is independent of any specific model in particle physics. Since this involves more math but points to the same fact, we will cover this in more detail in Appendix A.

Since WIMPs are the topic of this thesis, I will cover them in more detail in section 3.5

3.2.2 Axions

Axions are another well motivated DM candidate. This candidate was proposed to solve the strong CP problem. In short, there is no reason for the strong interaction not to violate the CP symmetry but it apparently preserves this symmetry. For this preservation of symmetry, an input parameter in the SM has to be fine-tuned to zero without having a mechanism to explain it.

The fundamental symmetry of the SM is the Charge-Parity-Time reversal (CPT) symmetry but in 1976, Gerard't Hooft showed that the QCD part of the SM has a non-trivial vacuum structure that can conserve the CP symmetry [92]. The SM has 18 input parameters[1] one of which is an effective periodic term (θ ranging from 0 to 2π) describing the strong CP-violating terms. If the CP-violating terms were to survive, they would create a measurable electric dipole moment for neutrons. The experimental limit on the electric dipole moment is about 10^9 less than what the theory would expect [94]. Physicists have been looking at possible mechanisms that can explain why θ ends up being so close to zero without having to fine-tune its value.

The simplest way to solve the strong CP problem would be to have a massless quark but all of the six quarks are measured to have mass. Another approach was introduced by Roberto Peccei and Helen Quinn in 1977 where they employed properties of Spontaneous Symmetry Breaking (SSB). The idea was to introduce a new $U(1)$ global symmetry and promote θ to a field. Frank Wilczek [95] and Steven Weinberg [96], independently, showed that when the symmetry spontaneously breaks by the Higgs mechanism, it would produce a new particle that would play the role of θ. This will lead to a zero CP-violation parameter without needing to fine-tune any parameter, thus avoiding the naturalness problem.

Different axion models can cover a huge mass range. In 1983, using a lower bound set by the cosmological observations [97], Laurence Frederick Abbott and Pierre Sikivie showed that there is still a huge parameter space in which axions can have a major

---

[1] Note that the SM assumed massless neutrinos but now we know they are in fact massive particles [93] which will add 7 more input parameters to the SM.

contribution to the mass-energy content of the universe [98]. In the same year, other physicists argued that the axions can play the role of DM if they are massive enough [99, 100], usually more massive than 10^{-11} the mass of electron[1]. See [101] for more details on how the mass range can be expanded to include axions as a DM candidate, their production channels, and their impact on the inflationary cosmological model.

3.3 Previous Searches for WIMPs

Physicists have been searching for WIMPs and other DM candidates for decades. Although some experiments have published results of possible WIMP signals [52, 102, 103], no experiment has reached the statistical significance and calculated background models to establish discovery of WIMP particles. Also, there is no consistency between different published results to persuade the scientific community of a discovery. See [104] for a review.

The search for DM can be conducted in three ways; Particle production, direct direction and indirect detection, Figure 3.1. I will briefly cover each method below.

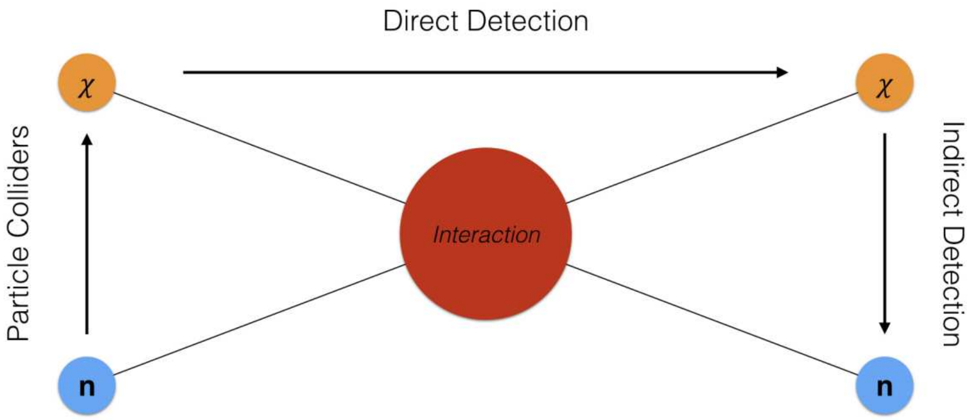

Figure 3.1: A schematics representation of the different approaches for detecting DM where n is a particle in the SM and χ represents the DM. Graph courtesy of Pietro Giampa.

---

[1] order of μeV to meV.

3.3.1 Particle Colliders

One method of identifying DM is to collide SM particles at super high energies (orders of TeV), the bottom to top path in Figure 3.1. The two SM particles will collide and change into DM particles, similar to what might have happened in the early universe. The ATLAS and CMS experiments at the Large Hadrons Collider (LHC), the world's strongest particle collider, are trying to detect such interaction [105]. The produced DM particles cannot be detected directly by the experiments' components, but they will result in a missing transverse momentum. Right now, in most analyses, the missing transverse momentum is associated with neutrinos which also leave no trace behind in the detectors' components.

3.3.2 Indirect Detection

In another detection method, experiments look for signatures coming from DM particle decay or self-annihilation, the top-to-bottom path in Figure 3.1. We can search for this signature in different ways.

If we consider regions with high DM density, like the centre of our galaxy, the chances of two DM particles annihilating and producing gamma rays or other SM particle-antiparticle pairs is increased. Also, if DM is not stable, it can decay into SM particles. So, studying the local flux of gamma rays, positrons, or antiprotons can provide a tool to indirectly find hints of DM signal [106]. The main issue with this method is background removal; there are many astrophysical sources that can produce signals similar to that of DM. But a combination of multiple signals can lead to a discovery using this method [106, 107].

Another way is using the annihilation of DM in astrophysical bodies. When DM passes through an object, like the Sun, they might scatter of the atoms and lose energy. If this energy loss is high enough, they can get gravitational bound to the object and increase the local density of the DM, thus increasing the probability of annihilation. Although photons are not be able to escape these objects, neutrinos usually do. These high-energy neutrinos can provide a good DM signal and if found, a strong indirect proof of particle nature of DM [107]. The detection of gravitational waves by LIGO in 2015 [108] has opened another way for indirect detection of DM, especially if DM is in the form of primordial black hole [109].

3.3.3 Direct Detection

The last detection method is from direct detection where we search for the scattering of DM from atomic nuclei within a detector, the left-to-right path in Figure 3.1. When DM scatters off the nucleus of an atom there will be recoil energy transferred to the nucleus which can subsequently generate scintillation light. The goal of such experiments is to find such interactions. The main challenge in this method is to keep an extremely low background in the Region of Interest (ROI) which is why most of these detectors are placed in underground laboratories to minimize background from cosmic rays.

There are different types of detectors for direct detection. For example, cryogenic detectors try to detect the heat produced when DM hits an atom in a crystal absorber like germanium. On the other hand, the noble liquid detectors try to detect the scintillation light produced by the collision of DM and a noble gas atom such as xenon or argon. The advantage of these techniques lie in their ability to distinguish the signal from the background. The background is mostly scattering from electrons while the signal is produced by the scattering of the nuclei.

Another important point about direct detection is that the interpretation of the search is often conducted with either of the two assumptions: the interaction is spin-dependent or independent. In the case of Spin-Dependent (SD), the coupling of DM is to the spin of the nucleons through the axial term of the Lagrangian [90]. Detectors with lighter nuclei with odd atomic numbers and high spin moments are more favourable for setting SD limits. For Spin-Independent (SI) searches, scalar interaction, the DM couples to the mass of the nucleus [90]. This distinction was seemingly first published by Goodman and Witten in 1985 [90, 110]. Since each nucleon within the nucleus target contributes coherently to the cross-section, in SI searches, for heavy DM particles, nuclei with large atomic numbers are the preferred target. SI search will be the emphasis of this thesis.

3.4 Detectors and Detection Techniques

To observe DM, different experiments have developed different techniques and they can be classified based on their readout approach. The main ones are heat, acoustic, charge, and light. Some experiments also use a combination of them, such as light and charge [111]. Figure 3.2 shows a schematic representation of these techniques.

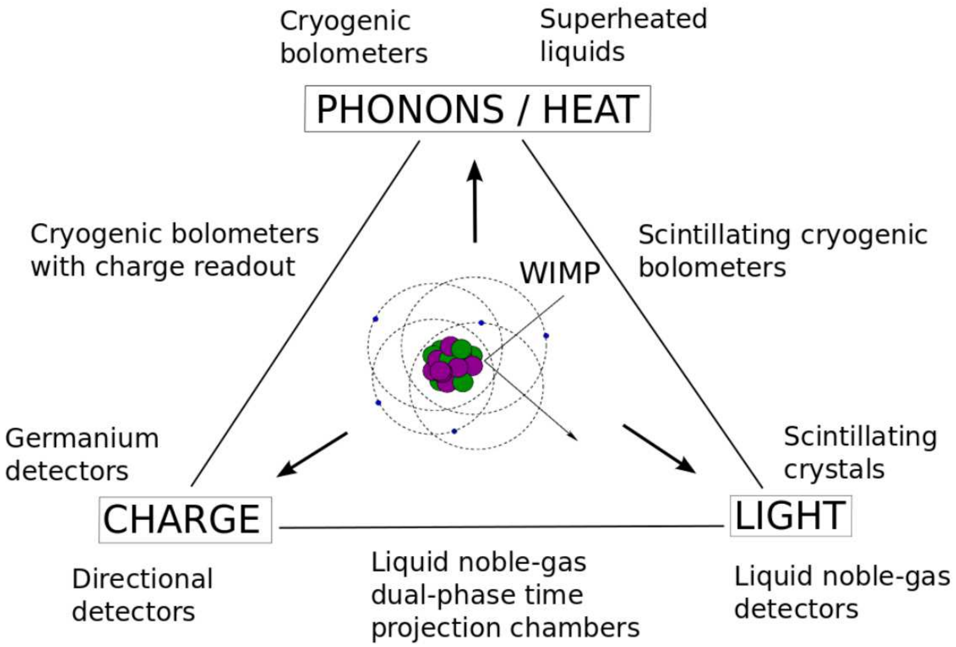

Figure 3.2: A schematic drawing of different signal detection techniques and technologies used in direct detection experiments. Image taken from [111]

Below, we cover a few of the most famous DM experiments. But there are many others that we have not covered here such as XENON, LUX, ZEPLIN, PICO, New Experiments with Spheres-Gas (NEWS-G), and others.

ADMX Axion Dark Matter eXperiment (ADMX), as the name suggests, is a DM experiment haunting for axions and unlike most of the other experiments that are located underground to be shielded from cosmic rays, ADMX is located at the University of Washington, in the Centre for Experimental Nuclear Physics and Astrophysics

(CENPA). The detector has a superconducting magnet which mostly operates just below 8 T. It also consists of a copper-plated cylindrical microwave cavity made of stainless steel with a length and diameter of approximately 1 m and 0.4 m, respectively [112]. This detector looks for the conversion of axions to microwave photons in the presence of a strong magnetic field. The ADMX, under the assumption that the all DM in the Milky Way is made up of axions, has ruled out one of the benchmark models of axion covering a mass range of 1.9-3.53 μeV [113]. A more recent exclusion result was published for axions in the mass range of 3.3-4.2 μeV [114] while it has the potential to set exclusion limits up to masses of around 20 μeV [115].

CDMS Cryogenic Dark Matter Search (CDMS) is an example of detectors that use the combination of heat and charge for their detection methodology where the active material is Silicon and Germanium crystals [116, 117]. CDMS is a series of detectors designed to search for WIMPs. The first experiment was called CDMS-I and was operated in a shallow underground tunnel under Stanford University from 1998-2002. The next detector was called CDMS-II operated from 2003 to 2009 in the Soudan Mine. The next instalment was called SuperCDMS Soudan which operated from 2011-2015 [118]. The latest in the series is the SuperCDMS SNOLAB which started its construction in 2018 and will operate in the SNOLAB facility Sudbury, Ontario in Canada [119].

LZ LUX-ZEPLIN experiment (LZ) was formed by the LUX and ZEPLIN collaborations making the next generation of DM detectors. LZ uses 10 tonnes of Liquid Xenon (LXe) as the target material. It is an example of using both charge and light for detection by using a dual phase Time Projection Chamber (TPC). It uses different types of PhotoMultiplier Tubes (PMTs) for different purposes. The top and bottom of the detector are equipped with two arrays of 494 PMTs[120]. In October 2022, the LZ collaboration published their first DM results and set the most stringent SI WIMP-nucleus cross-section limit, shown in Figure 3.3 [121].

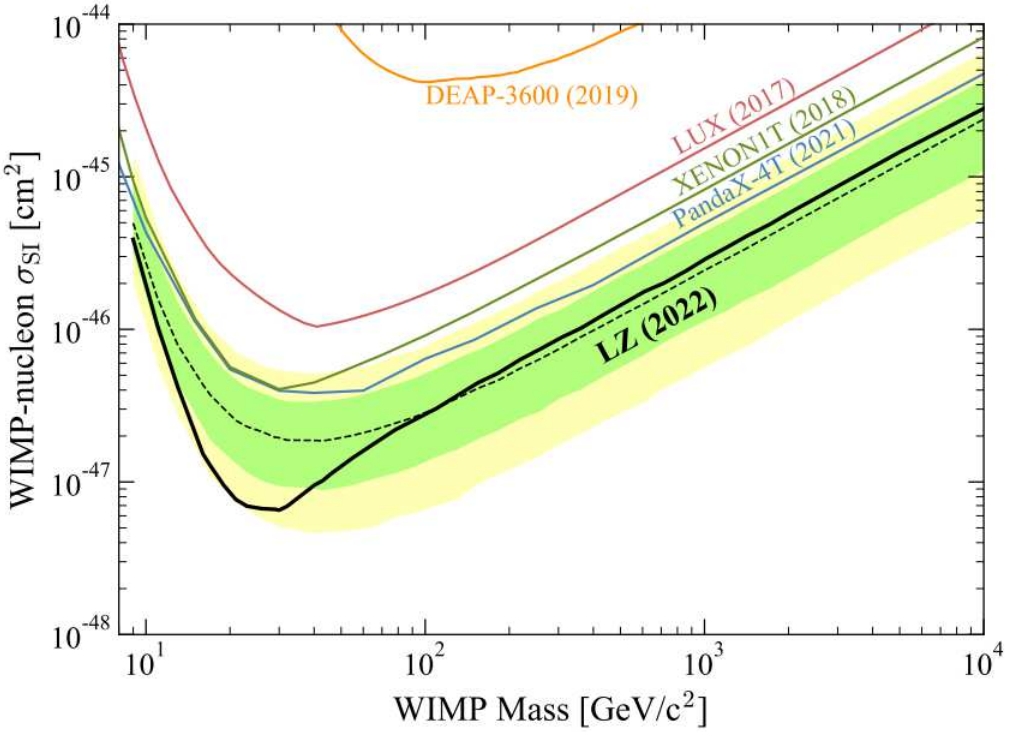

Figure 3.3: The 90% confidence limit for SI WIMP-nucleus cross section as a function WIMP mass set by the LZ collaboration [121].

DEAP The last detector we will talk about briefly here is the Dark matter Experiment using Argon Pulse-shape discrimination (DEAP) detector which is the emphasis of this thesis. We will cover the current generation of this detector, DEAP-3600, in more detail in the next chapter. Many DM detectors have been using LXe as the target material. DEAP, on the other hand, started using Liquid Argon (LAr) for its experiment. DEAP-1 was the first generation detector, or the prototype, with 7 kg of LAr and operated at the Queen's University in Canada. It was used to check the performance of LAr for pulse shape discrimination (PSD) at low recoil energies. It was later moved to SNOLAB in October 2007 and operated until 2011. It also only used two PMTs [122]. The detector was designed as a prototype and did not set any limits on DM cross-section.

After the success of DEAP-1, the next generation was built and called DEAP-3600. It was designed to use 3600 kg of LAr, hence the name and is operating at SNOLAB. The DEAP collaboration published their first result in 2017 using an exposure of 4.44 live days [123]. Their next improved result using 231-day exposure was published in 2019 and set a world-leading WIMP-nucleon SI upper limit cross-section among detectors using LAr target [124]. In 2022 they also published the first result of setting constraints on Planck-scale mass DM with multi-scattering signature [125].

In 2017, four collaborations, DEAP-3600, Argon Dark Matter (ArDM), MiniClean, and DarkSide-50, came together and formed the Global Argon Dark Matter Collaboration (GADMC). The collaboration expanded to 12 countries, 68 institutions, and 350 scientists. The first goal is to build a 20 tonnes LAr based detector called DarkSide-20k that can be considered the next-generation detector of DarkSide-50 and DEAP-3600. It will operate at the Gran Sasso Laboratory in Italy. Argo would be the future-generation detector, being designed to contain 300 tonnes or more of LAr and will operate at SNOLAB.

3.5 WIMP Properties

Event Rate & Kinematics For any detector, we need to first be able to compute the expected WIMP signal and test different theories. We assume the SHM model discussed in section 1.4. For a nuclear recoil energy of E_R, we can write the differential event rate per unit detector mass caused by the WIMP elastic scattering [52, 90] as:

$$\frac{dR}{dE_R} = \frac{\rho_0 \sigma_0}{2\mu_{\chi p}^2 m_\chi} F^2(E_R)\ \eta(v_{\min}), \tag{3.6}$$

where ρ_0 is the usual local WIMP density, σ_0 is the total cross-section without the form factor, m_χ is the mass of the WIMP, and $\mu_{\chi p} = (m_\chi m_p)/(m_\chi + m_p)$ is the reduced WIMP-proton mass. F is the form factor encoding the effects of the finite size of the nucleus which is often taken as the Helm form factor [126]. Lastly $\eta(v_{\min})$ is the mean inverse speed related to the velocity distribution $f(\mathbf{v})$ through:

$$\eta(v_{\min}) = \int_{v_{\min}}^{\infty} \frac{f(\mathbf{v})}{v} d^3\mathbf{v}, \tag{3.7}$$

where v_{min} is the minimum required WIMP speed to cause a recoil with energy E_R. For a detector with a nuclear target of m_N, the minimum speed can be written as [52]:

$$v_{\text{min}}(E_R, m_\chi, m_N) = \sqrt{\frac{m_N E_R}{2\mu_{\chi N}^2}}, \tag{3.8}$$

where $\mu_{\chi N}^2$ is the reduced WIMP-nucleon mass. Each detector, based on its ability to distinguish between signal and background, is sensitive to an energy range which can translate to a WIMP speed range $v \in [v_{\text{min}}(E_{\text{min}}), v_{\text{min}}(E_{\text{max}})]$ where the lower and upper limits of the signal window are defined as E_{min} and E_{max}. If a WIMP particle has a speed less than $v_{\text{min}}(E_{\text{min}})$, it cannot induce a nuclear recoil above the threshold energy of the detector. Also, if the WIMP has a speed above the $v_{\text{min}}(E_{\text{max}})$, the detector won't be sensitive to the exact form of the speed distribution above this speed because the contribution of these WIMPs to the nuclear recoil rate would be a constant offset [52].

Cross Section The total cross-section, σ_0 in Equation 3.6, takes two forms if the coupling of WIMP to nucleus is SD or SI. The simpler form is the SI case where we can write [90, 107]:

$$\sigma_0^{\text{SI}} = \left(\frac{4}{\pi}\right) \mu_{\chi N}^2 \left[Z f_p + (A - Z) f_n\right]^2, \tag{3.9}$$

where Z is the atomic number of the target nucleus (number of protons), A is the atomic mass number (number of protons and neutrons), and f_p and f_n are the effective scalar couplings of WIMP on protons and neutrons respectively. For WIMPs that primarily interact through Higgs exchange (scalar interaction), the two couplings are almost equal [127]. So, ignoring the small mass difference between proton and neutron, we can rewrite the pointlike σ_0^{SI} as [128]:

$$\sigma_0^{\text{SI}} \simeq \left(\frac{4}{\pi}\right) \mu_{\chi N}^2 A^2 |f_p|^2 = A^2 \left(\frac{\mu_{\chi N}}{\mu_{\chi p}}\right)^2 \sigma_{\chi p}^{\text{SI}}, \tag{3.10}$$

where

$$\sigma_{\chi p}^{\text{SI}} = \left(\frac{4}{\pi}\right) \mu_{\chi N}^2 |f_p|^2, \tag{3.11}$$

is the SI WIMP-nucleon cross-section. Note that we have ignored the form factor in the cross-section as it appears directly in the event rate, Equation 3.6.

The SD case which is the axial-vector interaction of WIMP with the spin of the target nuclei takes a bit more complicated form of [90, 107]:

$$\sigma_0^{\mathrm{SD}} = \left(\frac{32}{\pi}\right) G_F^2 \mu_{\chi N}^2 \left(\frac{J+1}{J}\right) \left[\langle S_p \rangle a_p + \langle S_n \rangle a_n\right]^2 , \tag{3.12}$$

where G_F is the Fermi constant, J is the total spin, $\langle S_p \rangle$ and $\langle S_n \rangle$ are the expectation values of the group spins of proton and neutron, and similarly, a_p and a_n are the effective SD couplings of WIMP to protons and neutrons. To a good approximation, only unpaired nucleons contribute to the cross-section since their spins in a nucleus are anti-aligned and we can rewrite the above equation as [128]:

$$\sigma_0^{\mathrm{SD}} = \left(\frac{32}{\pi}\right) G_F^2 \mu_{\chi N}^2 \left(\frac{J+1}{J}\right) \langle S_{p,n} \rangle^2 |a_{p,n}|^2. \tag{3.13}$$

For protons and neutrons we have $J = 1/2$ and $\langle S_p \rangle = \langle S_n \rangle = 1/2$. So:

$$\sigma_{\chi(p,n)}^{\mathrm{SD}} = \left(\frac{24}{\pi}\right) G_F^2 \mu_{\chi N}^2 |a_{p,n}|^2. \tag{3.14}$$

Chapter 4

DEAP-3600

In this chapter, I will cover the DEAP-3600[1] detector in more detail. But first, we will talk about the properties of argon which are necessary for understanding how the DEAP detector works.

4.1 Why Liquid Argon?

In this section and subsequent sections, I will cover the properties of LAr which makes it a candidate for current and future generations of DM detectors.

LAr has an atomic number of $Z = 18$ and an atomic mass of 40 U. Since it has an even nucleus, it only allows for SI DM searches. LAr is a scintillator with density of 1.398 g/L at a pressure of one atmosphere, and has a high photon yield per deposited energy which is approximately 40 photons per keV [129]. Another important property of LAr that makes it great for DM searches is that there are large time profile differences between nuclear recoils and ElectroMagnetic (EM) events that will allow the removal of all EM events but 1 event in 10^{+9} events [130]. So far, some of these properties are also present for LXe, to an even better degree for some properties. What puts LAr in advantage is its orders of magnitude better PSD power and the cost which is about 200 times less than that of LXe, making it ideal for future generations of detectors containing hundreds of tonnes of LAr. See Table 4.1 for a summary of comparing the two noble gases. The photon yield is also called Light Yield (LY) and will be covered later in this chapter.

---

[1] From now on, we will refer to the DEAP-3600 detector simply as DEAP.

Noble Gas	Z	Liquid Density (kg/L)	Photon Yield (photons/keV)	PSD Leakage Probability	Average Cost ($/100 g)
Argon	18	1.398	40	10^{-9}	0.5
Xenon	54	5.894	75	0.25 [131]	120

Table 4.1: Comparing some of the properties of argon and Xenon relevant to DM searches. It is also important to have multiple isotopes and multiple technologies and systematic uncertainties. The average cost is taken from [132].

4.2 Liquid Argon Scintillation

DEAP captures the light from interactions inside the detector. Understanding the properties of argon scintillation is crucial to better understanding the detector and how it operates and searches for WIMP. When an interaction happens with an argon atom, it will lead to scintillation photons that have a wavelength in the Vacuum UltraViolet (VUV) range. The peak is at 128 nm, corresponding to an energy of 9.7 eV, and has a spread of 6 nm [129]. Argon is transparent to these photons. The scintillation light can be produced in two ways, the process of excitons (excitation) and ions produced by ionizing radiation (ionization) [133]. Here we will consider argon, but note that a similar process can happen for other noble gases. For the case of excitation (Ar*), the following events take place [133]:

$$\begin{aligned} \chi + Ar &\rightarrow Ar^* + \chi, \\ Ar^* + Ar &\rightarrow Ar_2^*, \\ Ar_2^* &\rightarrow 2Ar + \gamma(128\ nm), \end{aligned} \tag{4.1}$$

where χ represents the WIMP. What happens in this scenario is we have an incident particle that excites many argon atoms, a process called atomic excitation. This excited argon atom will interact with a neighbouring argon atom that is at the ground state and form an excited pair often called excimers (excited dimer). This process is known as self-trapping. Finally, the excimer decays into two non-excited argon atoms and a

VUV photon. For ionization (Ar$^+$), we have: [133]

$$
\begin{aligned}
\chi + Ar &\rightarrow Ar^+ + e^- + \chi, \\
Ar^+ + Ar &\rightarrow Ar_2^+, \\
Ar_2^+ + e^- &\rightarrow Ar^{**} + Ar, \\
Ar^{**} &\rightarrow Ar^* + \text{heat}, \\
Ar^* + Ar &\rightarrow Ar_2^*, \\
Ar_2^* &\rightarrow 2Ar + \gamma(128\ nm),
\end{aligned}
\tag{4.2}
$$

where Ar^{**} is a highly excited state that is at least two energy levels higher than the ground state while Ar^* is only on the first excited energy level. In this case, the incident particle ionizes an argon atom causing an electron to be released. The ion will bond with a neutral atom creating a diatomic ion which will recombine with an electron to create the highly excited atom. Ar^{**} will de-excite in a non-radiative transition (no light is emitted). The rest of the process is the same as the excitation process. Note that in both cases, the excited dimer Ar_2^* is at the lowest excited level and will be de-excited to the ground state by emitting a single UV photon [133].

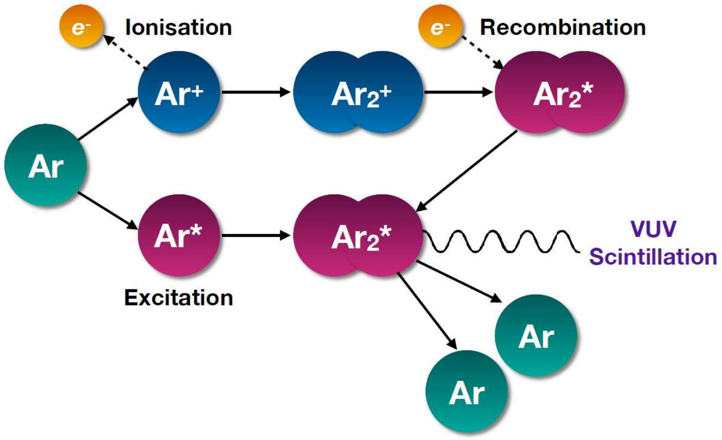

Figure 4.1: A graphical representation showing the two mechanisms in argon producing VUV photons. Image taken from [134].

4.3 Light Yield

Light Yield (LY) is the amount of light that is emitted by a scintillator per unit of the deposited energy. Argon has a high LY which for heavy ion collisions is measured to be 55 ± 8 γ/keV [135]. However, the LY at lower Linear Energy Transfers (LETs) is measured to be ≈ 40 γ/keV [129]. Having a lower LY is referred to as quenching and can be caused by different effects:

- Nuclear quenching: using the Lindhard theory, we can explain that some fraction of the energy is lost in the form of heat [136].
- Bi-excitonic quenching: the collision of two excited argon atoms with each other before they can form the excimer, will create an argon in the ground state plus an electron-ion pair, preventing the excimer to form ($Ar^*+Ar^* \rightarrow Ar+Ar^++e^-$) [129].
- Penning ionization: before emitting the VUV photon, two excimers can collide with each other and create two ground state argon atoms, an ionized dimer, and an electron ($Ar_2^* + Ar_2^* \rightarrow 2Ar + Ar_2^+ + e^-$) [137].

4.4 Argon Pulse-Shape Discrimination

An important feature of argon is its PSD capability. PSD is a method that explores the different reactions of the material, argon here, that enables the experiment to distinguish electromagnetic showers and nuclear recoils. The electron configuration of argon in its ground state can be written as:

$$[\mathrm{Ne}]\ 3s^2\ 3p^6. \tag{4.3}$$

Argon has many excited states, but we are only interested in the four lowest excited states. For these states, one electron from the $3p^6$ orbitals moves to the $4s^1$ orbital, but depending on the spin state, we can either get a singlet or triplet state. See Table 4.2 in which we have used the LS (also called Russell-Saunders) coupling notation ($^{2S+1}L_J$). Of these four states, only the $^3P_1$ and $^3P_2$ states can provide the necessary potential well for the formation of excimers. Accordingly, the excimer can be in one of two states, a singlet state $^1\Sigma_u$ (from $^3P_1 +^1 S_0$) and the triplet state $^3\Sigma_u$ (from $^3P_2 +^1 S_0$) [138]. See Figure 4.2 for an illustration of these states[1]. The peaks of the VUV photons from the singlet and triplet states cannot be resolved leading to the 6 nm width of the wavelength mentioned earlier.

configuration	State	LS	energy [eV]
[Ne] $3s^2$ $3p^6$	ground state	$^1S_0$	0.0
[Ne] $3s^2$ $3p^5$ $4s^1$	singlet state	$^1P_1$	11.82
[Ne] $3s^2$ $3p^5$ $4s^1$	triplet state	$^3P_0$	11.72
		$^3P_1$	11.62
		$^3P_2$	11.54

Table 4.2: The four lowest excited states and the ground state of argon atom. Energies taken from [140], converted to eV for convenience.

The characteristic differences between the singlet and triplet states are the source of the PSD capability of argon. The singlet state has a lifetime of 7 ± 1 ns while the triplet state lifetime is in the order of 1600 ± 100 ns [141]. The second feature is that

---

[1] See Ref [139] for a more original discussion of excimers in noble gases.

the ratio of the singlet to triplet states is highly dependent on the type of interaction that has happened in the argon. We can define the ratio as:

$$R = \frac{N_s}{N_t}, \tag{4.4}$$

where N_s and N_t are the number of excimers in the singlet and triplet states. The value of R is highly dependent on the LET, dE/dx [142, 129, 143], in a way that R increases as more energy is transferred (or lost) per unit track length. The lighter particles like electrons produce more of the triplet state excimers (EM) as they lose less energy, while heavier particles with large stopping powers such as alphas and argon recoils produce more of the singlet state excimers (Nuclear Recoil (NR)). The lifetimes of these two states are independent of the type of the particle which gives DEAP its great PSD power.

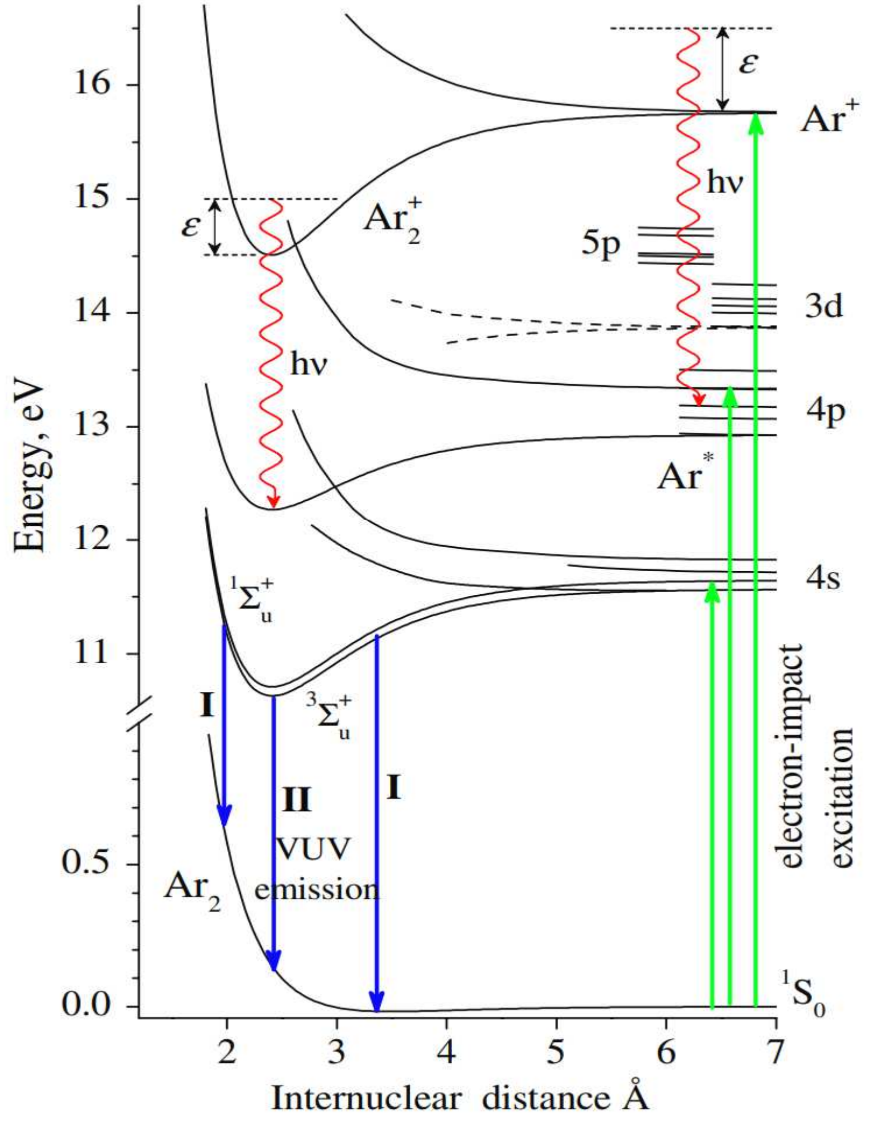

Figure 4.2: A Schematic diagram of argon energy levels where the VUV photon emitted from Ar_2^* is also illustrated. Image taken from [140].

4.5 SNOLAB Underground Science Laboratory

SNOLAB is located 2 km below the surface in Vale's Creighton nickel mine near Sudbury, Ontario in Canada [144]. After the success of Sudbury Neutrino Observatory (SNO) experiment which operated from May 1999 to November 2006, the SNOLAB facility was built. Since its initial construction, SNOLAB has gone through expansions and has been transformed into a multi-experiment laboratory. The SNOLAB facility provides great shielding from cosmic rays with a measure of 6010 Metre Water Equivalent (MWE) where MWE is a measure of muon flux. For SNOLAB, the muon flux is 0.286 μ/m^2/day [145]. For comparison, the muon flux is about 15 million μ/m^2/day on the surface. The 2 km of rock shielding reduces the cosmic rays by a factor of 50 million [144]. See Figure 4.3 for a comparison of muon flux for various underground laboratories.

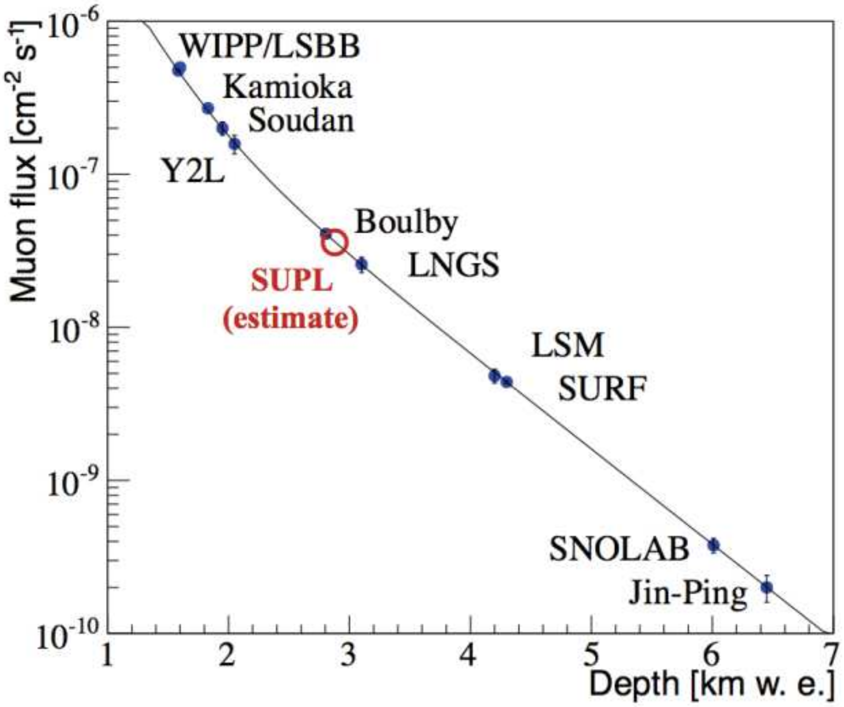

Figure 4.3: A plot of the muon flux per cm^2 per second as a function of kilometre water equivalent for different underground laboratories. Image taken from [146] where the solid line is the parameterization and taken from [147].

The SNOLAB facility has an excavated area of 7215 m^2 of which 4942 m^2 is for general infrastructure and 3055 m^2 is for laboratories [145, 148]. Although the main focus of SNOLAB is on astroparticle physics, mainly neutrino and dark matter experiments, it is also used for biology and geology studies [144].

Our detector, DEAP-3600, is located in the Cube Hall section of the SNOLAB facility, highlighted in Figure 4.4. This area is shared with miniCLEAN and NEWS-G.

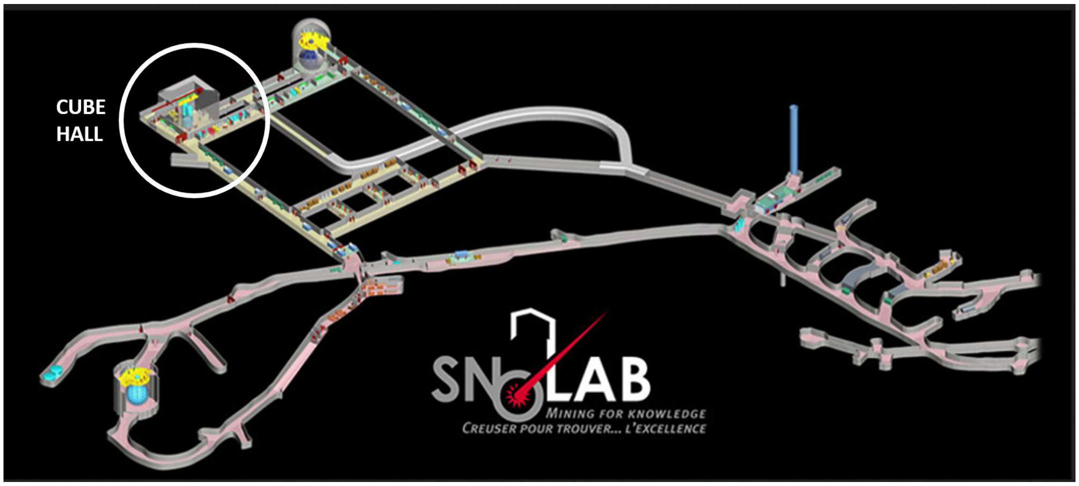

Figure 4.4: A map of the underground section of SNOLAB where the Cube Hall that houses DEAP-3600 is highlighted in the top left. Image taken from [149].

4.6 DEAP-3600 Design

The schematic of the DEAP detector is shown in Figure 4.5. In this section, we will cover the DEAP detector in more detail. This section and its subsequent subsections follow from Ref [150], unless stated otherwise.

The innermost part is an acrylic sphere which is known as Acrylic Vessel (AV). The AV has an inner radius of ≈ 851 mm at room temperature and a wall thickness of 50 mm that can contain 3600 kg of LAr. The inner surface of the AV is coated with a 3 μm layer of TetraPhenyl Butadiene (TPB) (1,1,4,4-Tetraphenyl-1,3-butadiene $C_{28}H_{22}$). TPB is a wavelength-shifting material that will shift the VUV light produced inside the detector into the visible part of the spectrum, from a peak distribution at 128 nm to 420 nm [151], as shown in Figure 4.6. There are 255 locations around AV where we have cylindrical acrylic Light Guides (LGs), each of which is 450 mm long with a diameter of 190 mm

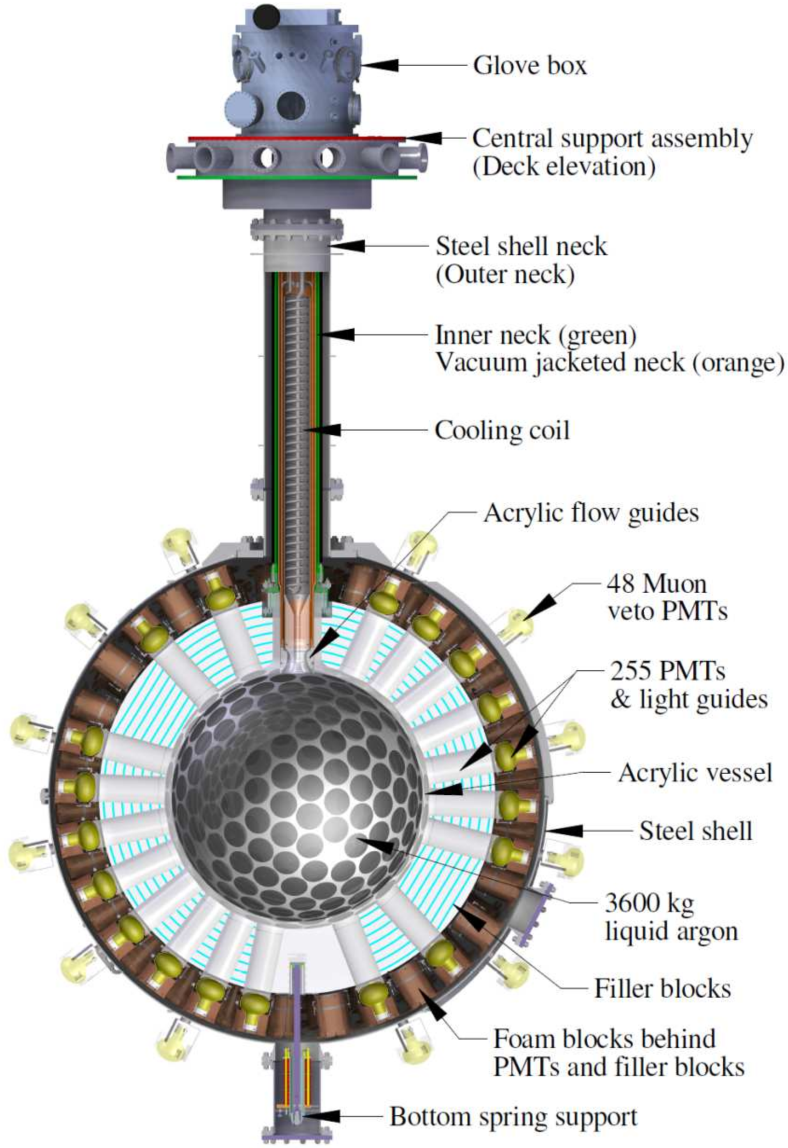

Figure 4.5: A schematic view of the DEAP detector and its components. Image taken from [150].

which together will cover 76% of the detector surface [150]. At the end of each LG, we have a Hamamatsu R5912-High Quantum Efficiency (HQE) Photo Multiplier Tube for detecting the visible light emitted from the TPB. These PMTs are sensitive to single photons with a nominal efficiency of 32% [150, 152]. See Figure 4.7 for the efficiency spectrum as a function of the incident wavelength.

To increase the light collection and to optically isolate the LGs, an additional 50 μm

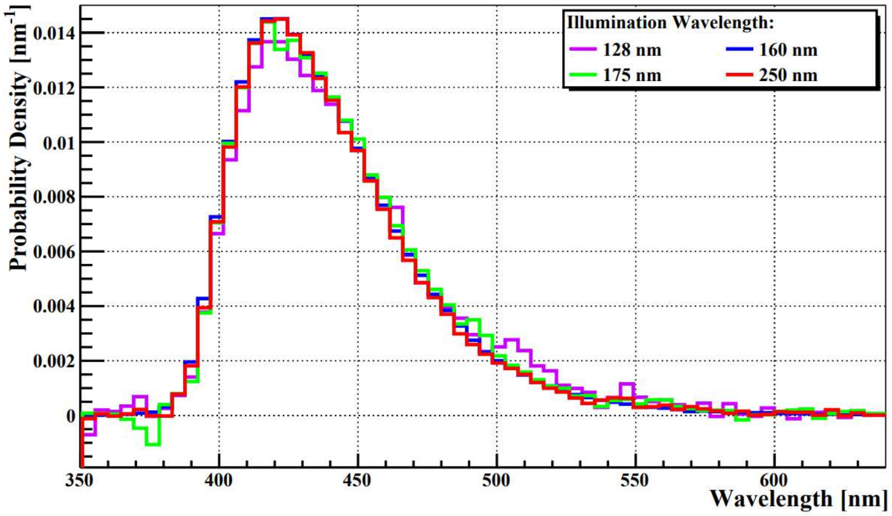

Figure 4.6: The spectra of the wavelength re-emitted by the TPB for waves with four different incident wavelengths. Image taken from [151].

layer of specular reflector made of Aluminized mylar is loosely wrapped around the LGs. This material was used because it has a high reflectance and no alpha-induced scintillation. The empty volume between the LGs is filled with 486 filler blocks which are made of alternating layers of high-density polyethylene and Styrofoam [153]. The combination of polyethylene and Styrofoam, on top of providing thermal insulation, acts as a neutron shield in conjunction with the LG. There is a 5 mm gap between the LGs and the filler blocks to provide enough space for thermal expansion without experiencing any stress. See Figure 4.8 for a zoomed-in image of the area around a PMT.

The top part of the AV is the neck area that allows access to the inner detector volume. The neck consists of a cooling coil that is used to cool the LAr by using liquid nitrogen (LN_2). The inner neck has a diameter of 255 mm. At the top of the neck, we have a glove box interface that can be used to insert or extract equipment in a radon-free environment.

A stainless steel shell that holds dry nitrogen gas is then used to house this setup while the shell itself is placed in a cylindrical tank of water with a diameter of 7.8 m. The water tank provides shielding from external radiation sources and is also part of the

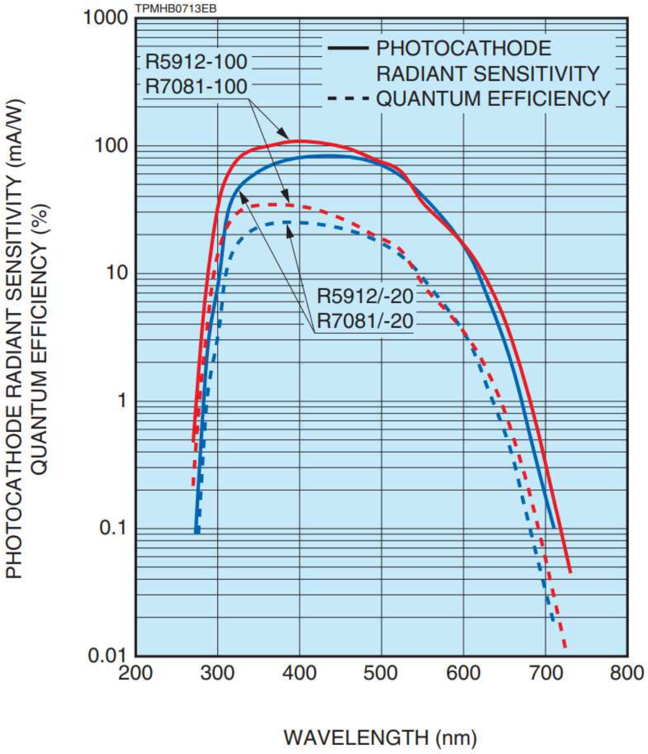

Figure 4.7: The quantum efficiency, in percentage and the photocathode radiant sensitivity, defined as photoelectric current over the incident (mA/W), of R5912-HQE PMT. Image taken from [152].

muon veto system which will be covered later in this section. Note that on 17 August 2016, during the initial fill, we discovered a missing neck seal which caused the LAr to spill and subsequently a contamination of about 100 ppm N_2 leaked into the LAr. We had to completely boil and vent the full 3600 kg of LAr. Since then, the top 30 cm of the detector is not filled with LAr but instead is filled with Gaseous Argon (GAr) [150]. Figure 4.9 shows different stages of the DEAP detector under construction. For a full description of the detector design and construction see Ref [150].

4.6.1 Photomultiplier Tubes

A PhotoMultiplier Tube (PMT) is a sensitive light detector that enables the detection of even a single photon. The inside front face of the PMT is a photocathode surface and when a photon hits this surface, an electron can be emitted through the process of

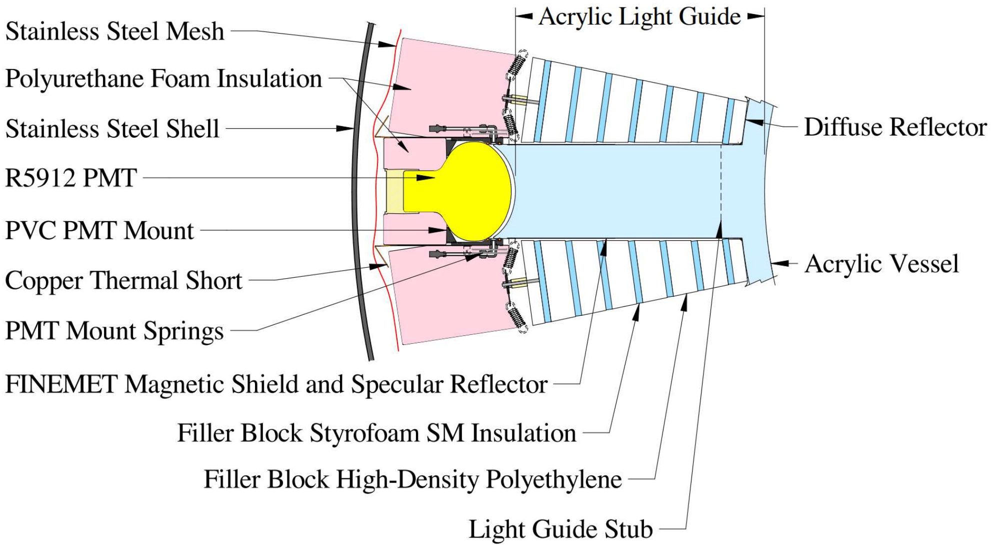

Figure 4.8: A schematic view of the inner components of the DEAP-3600 highlighting the LG, PMT, and filler blocks. Image taken from [150].

photoelectric emission. Inside the PMT, we have an electric field caused by the high voltage, 1500 V to 1900 V, applied to the PMT. The emitted electron, also referred to as the primary electron, is accelerated through vacuum toward a metal plate known as a dynode. Upon hitting the first dynode, the primary electron will create several secondary electrons. There are multiple dynodes inside the PMT and at each one, every electron will create multiple secondary electrons until all of them are collected by the anode plate at the other end of the PMT. This cascade process can normally amplify the signal by a factor of 10^6 to 10^7. PMTs can have up to 19 dynodes where the total amplification of the current can range from 10 to 10^8 [155]. In DEAP, the PMTs have 10 dynodes and the transit time from the cathode to the anode is measured to be 25 ns.

There are a few phenomena that often occur in conjunction with the PMTs generating a pulse; afterpulsing, earlypulsing, Dark Noise (DN), double-pulsing, and late-pulsing. The residual gases in the PMT can be ionized to create positive ions which in return can drift toward the photocathode, emit electrons and undergo collisions, and similar to the process explained above multiply to cause a small-amplitude pulse. This is referred to

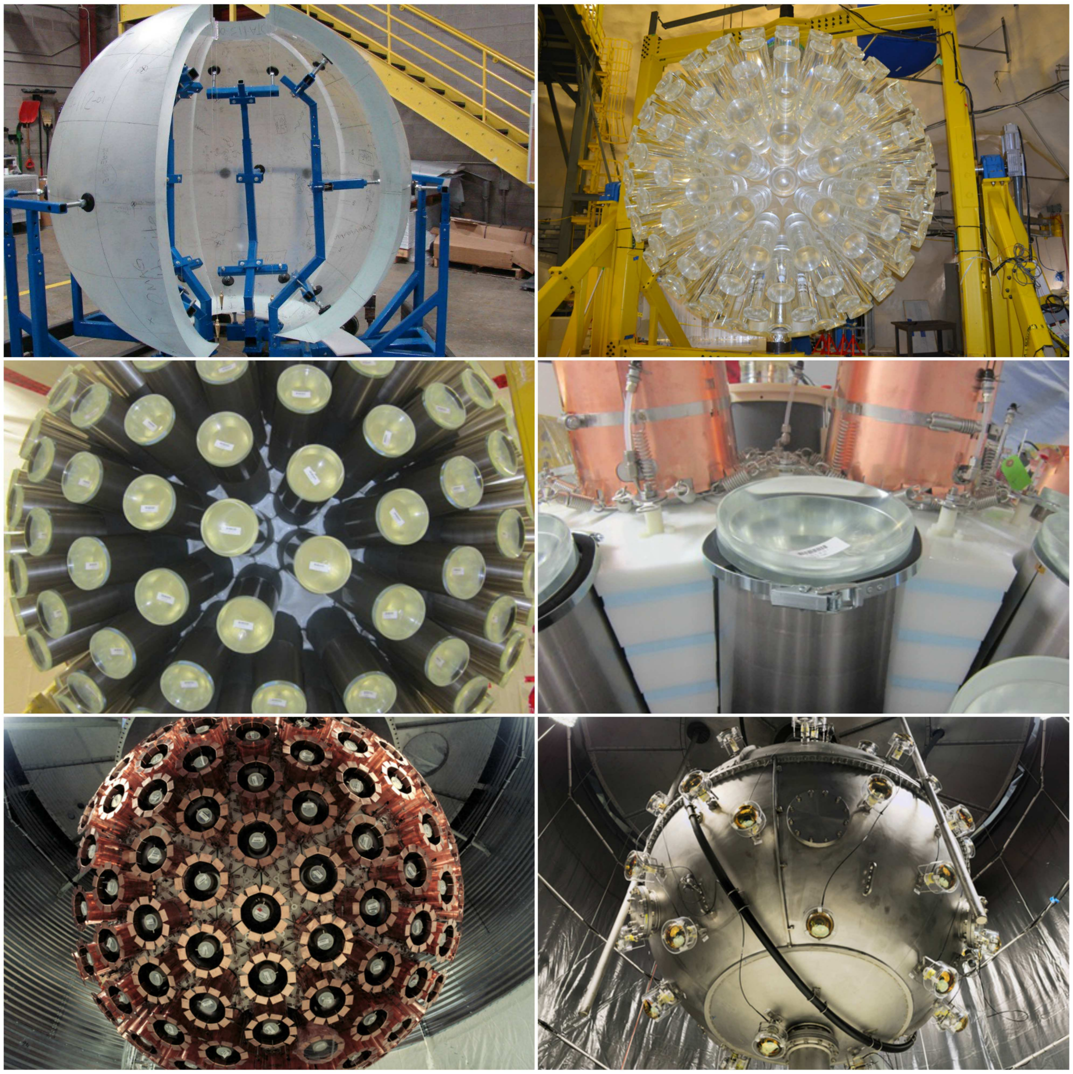

Figure 4.9: A collection of photos showing the DEAP detector in various stages. From top to bottom and left to right: assembling the AV; bonding the LGs to the AV; applying the reflector to the LGs; installing the PMTs, their shielding and the filler blocks; installing the detector inside the water tank; the final steel shell enclosing the AV inside the water tank where the muon veto PMTs are also visible. Image taken from [154].

as afterpulsing, since it often appear after a signal output. These pulses can be delayed up to 10 μs. On the other hand, earlypulsing happens when the photon directly hits the first dynode and releases one electron from the first dynode causing a small-amplitude pulse to happen and no prompt pulse is observed. DN is a random event where the pulse recorded in the PMT is caused by an electron thermally emitted from the cathode. The rate of DN is strongly dependent on the temperature of the PMT. At room temperature, the DEAP PMTs have an average DN rate of 5.80 ± 0.78 kHz[1]. The last case is backscattering pulses. In this scenario, the photoelectron strikes the first dynode and scatters back. If it scatters before losing enough energy to create secondary electrons, it travels almost to the cathode and then back, creating a late pulse with a transit time of up to 2×25 ns. If it generates electrons before scattering, due to the electric field, the electrons will drift back and hit the dynode to create a pulse, hence double-pulsing. The afterpulsing has a probability distribution with mean and RMS of $7.1 \pm 1.8\%$. The probability per photoelectron of double and late pulses are $2.7 \pm 0.2\%$ and $2.3 \pm 0.1\%$, respectively. In our detector, the in-situ measurement of the mean Single PhotoElectron (SPE) charge was performed for all the PMTs where the final measured value was found to be 9.39 ± 0.16 picoCoulomb (pC). The mean SPE charge $\bar{q}$ is related to the applied bias voltage V using:

$$\bar{q} = AV^{\gamma}, \tag{4.5}$$

where A is a normalization factor and the parameter γ needs to be measured where in our detector is found to be 6.9 ± 0.2. For more details and comprehensive plots see Ref [150].

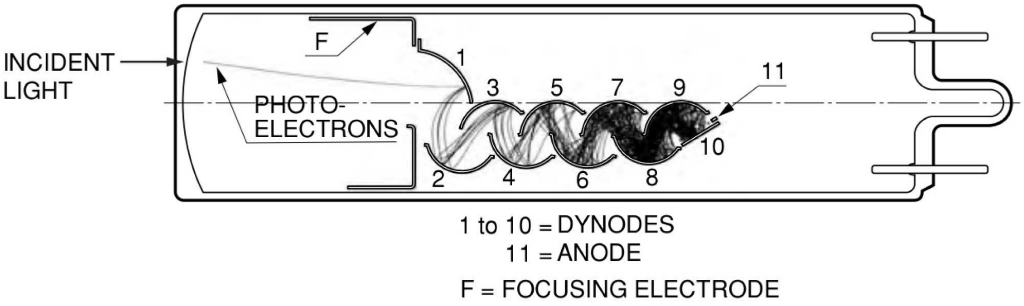

Figure 4.10: A schematic view from Hamamatsu PMT, linear-focused type, showing the process of multiplication of a single electron to many electrons using a chain of dynodes [155].

---

[1] These numbers are the mean and Root Mean Squared (RMS) values over all PMTs.

4.6.2 Veto Systems

DEAP has two main veto systems, the neck veto and the muon veto. We will briefly cover these two here.

Neck Veto System An important background source in DEAP is neck alphas, which will be discussed later in this chapter. Since we have partial light collection from events happening in the neck region, events that could have 40000 qPE[1] in the argon, reconstruct in the energy range near the ROI of the DM search with 80 to 200 qPE. To help identify these events, the bottom 10 cm of the neck is wrapped with wavelength-shifting optical fibres where each fibre is between 2.6 to 3.3 m long. The ends of these fibre optics, in bundles of 50 m, were then coupled to four Hamamatsu-HQE extended green R7600-300 2-inch PMTs, constituting the neck veto system. Other than the PMT type, the other properties of neck PMTs, such as their distance from the centre of the detector and their readout, is the same as the primary PMTs. See Figure 4.11 for a closeup photo of the neck region.

Muon Veto System The bottom right photo in Figure 4.9 shows our detector in the water tank before it is filled. It also shows some outward facing PMTs. The water tank and 48 Hamamatsu R1408 8-inch PMTs, from which only 45 are active, constitute the muon veto system. If a muon from the Earth's atmosphere survives the journey and reaches the lab, the water tank behaves as a water Cherenkov detector. When the muon passes through the water, it will create Cherenkov light that will be collected by the outward-facing veto PMTs.

The main issue with these muons is that when they pass through or near the LAr volume or detector materials, they can create secondary particles like spallation neutrons. When the neutron gets inside the detector, it will cause a nuclear recoil that can mimic a WIMP signal. If a muon signal is detected in the water tank, we will remove any

---

[1] qPE is a variable used in DEAP for measuring the mount of charge in an event or a given PMT and will be covered in more details in the next chapter.

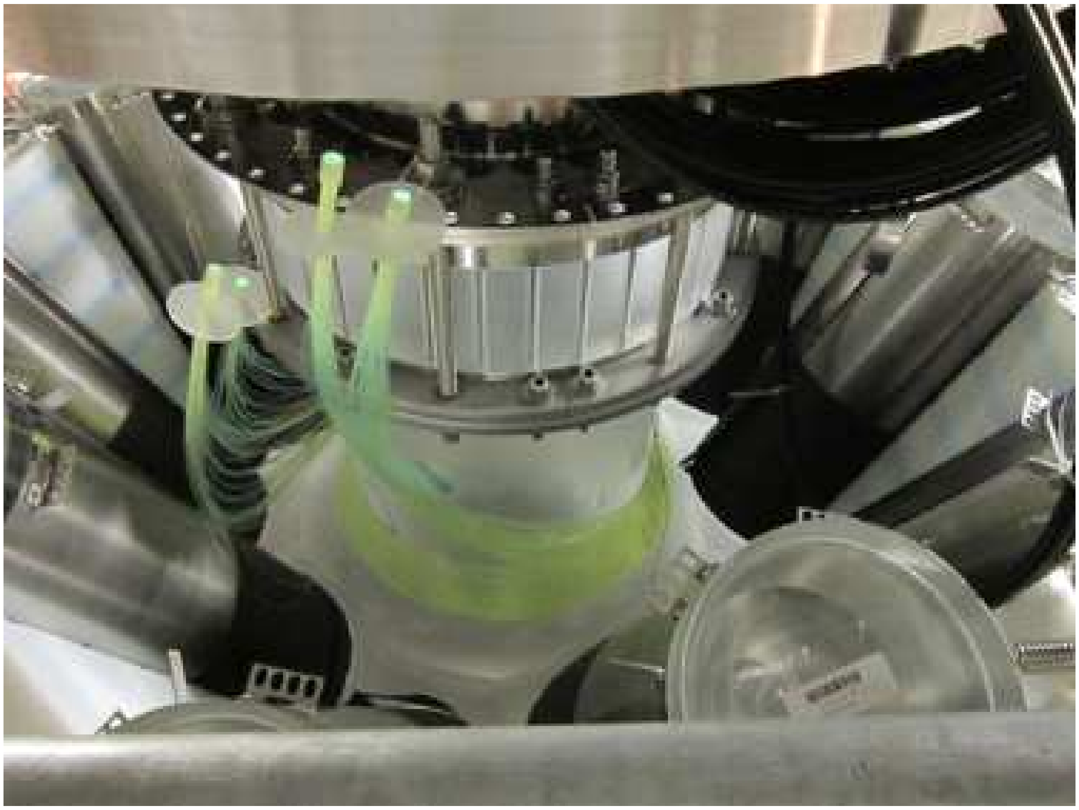

Figure 4.11: The neck region of DEAP, before installing the neck filler blocks, showing the wavelength shifting fibres wrapped around the bottom 10 cm of the neck. Image taken from [150].

data, up to 5 seconds after the detection of the muon signal, to make sure we reject any background signal caused by the muon interaction [156].

4.6.3 Data Acquisition System

Figure 4.12 shows the general architecture of the Data AcQuisition (DAQ) system used in DEAP. All the 255 inner PMTs, the 48 muon veto PMTs, and the 4 neck veto PMTs are connected to the DAQ. The Digitizer and Trigger Module (DTM) is responsible for analyzing the PMT signals and deciding whether or not to trigger an event readout. If a trigger is issued, the trigger signals will be sent to digitizers (CAEN V1720s [157] and V1740s [158]) that are tasked to digitize the PMT information; i.e measuring the charge every 4 ns. The final step would be to read out, filter, and write the digitized information to disk.

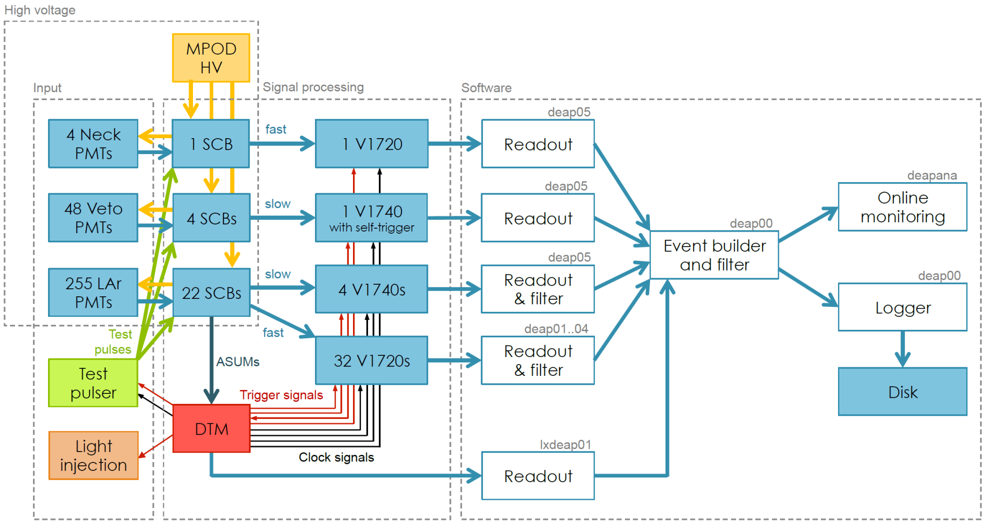

Figure 4.12: A schematic drawing of the DAQ system used in DEAP where the hardware components and software programs are shown as shaded and white boxes, respectively. Image taken from [150].

Signal Conditioning Boards DEAP, through 27 Signal Conditioning Boards (SCBs), uses a WIENER MPOD crate [159] with ISEG high voltage modules [160] to power up all of its PMTs. Each SCB can support up to 12 PMTs. From the 27 SCBs, 22 are reserved for the inner PMTs, 1 for the neck veto PMTs, and 4 for muon veto PMTs. The SCBs decouple the high voltage, protect against high voltage, and shape the PMT signals.

The 12 identical channels on each SCB are used to amplify and shape the PMT signals. Each of these channels has three outputs: a high-gain, a low-gain, and a summing channel. The high signal-to-noise for single photoelectrons is achieved with the high-gain channel that is also used to shape the pulse in a way to better match the 250 Million Sample (MS)/s V1720 digitizer. The pulses that saturate the high-gain channel are handled by the low-gain channel where the amplitude is attenuated by a factor of 10. Unlike the high-gain channel, to better match the 62.5 MS/s V1740 digitizer, the shape of the low-gain pulses are much wider. The Analog SUM (ASUM) for each SCB is created using the 12 summing channels. The 22 ASUM, from the 22 SCBs of the inner detector, are sent to the DTM via a 24-channel differential connector.

Each SCB includes a “test pulse” input, on top of the 12 Safe High Voltage (SHV) inputs from the PMTs. The DTM creates a test pulse and simultaneously sends it to all SCBs through a discriminator and a fan-out board. Then, with a 0.2 ns channel-to-channel delay, each SCB distributes the test pulse to all 12 channels. The timing offsets between different digitizer channels are extracted with this process.

Digitizers The pulses coming from SCB have negative polarity. They are fed in our CAEN V1720 digitizers which are set up so that the baseline, corresponding to zero volts, is approximately 3900 Analog-to-Digital Converter (ADC) bins and −2 volts saturates the digitizer with a value of zero ADC bin. The V1720 channels have a noise level of about 1.2 ADC and the SPE pulses are typically about 50 ADC high. MCX cables connect the high-gain output channels of SCBs to the 250 MS/s CAEN V1720 waveform digitizers[1] where the data can be stored as full waveforms or in Zero Length Encoding (ZLE) mode. Figure 4.13 is an example of an SPE pulse in ZLE mode. When a given number of samples are above an ADC threshold, the ZLE algorithm will save the data. The threshold is 5 ADC bins from the baseline which enables us to record real pulses and limit recording noise fluctuations. Instead of setting the baseline at the maximum of 4096 ADC, we use 3900 ADC so that it will allow us to record overshoots. Also, 20 extra samples, equating to $20 \times 4 = 80$ ns, are recorded before and after the pulse.

Similar to high-gain channels, MCX cables are used to connect low-gain channels to CAEN V1740 waveform digitizers that support 62.5 MS/s. Unlike high-gain channels, the low-gain channels only can record the full waveform, with no ZLE support. These full waveforms can saturate data rates, so we use software to avoid saving unnecessary data. The data reduction will be covered below in section 4.6.4

As can be seen from Figure 4.12, all the muon veto PMTs are connected to V1740 digitizers. These digitizers run in a self-trigger mode which means that the DTM will not analyze the signal from these PMT and instead the digitizer itself decides to issue a trigger based on whether or not there was sufficient activity in the water tank. The 48

---

[1] The V1720 digitizers have 8 channels while V1740 have 64 channels. Both have 12-bit precision corresponding to $2^{12} = 4096$ ADC bins and span a 20 range of input.

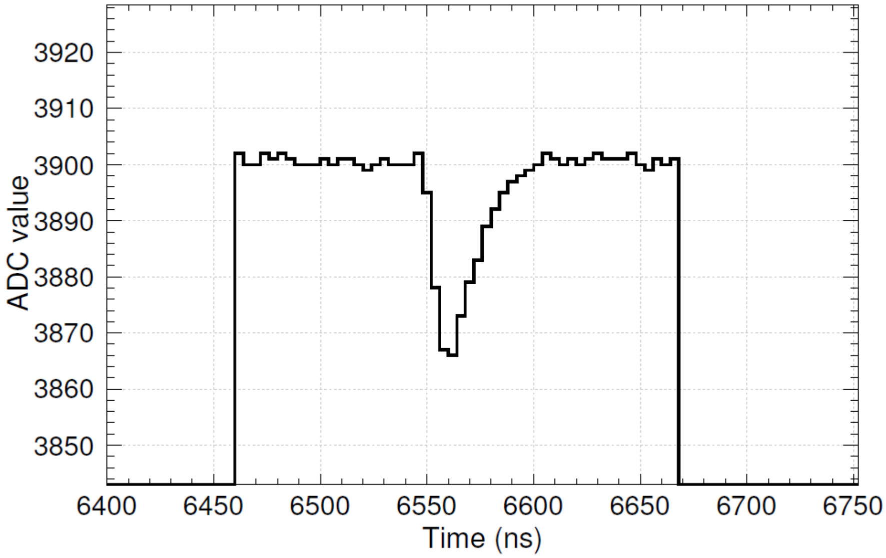

Figure 4.13: An SPE pulse saved in ZLE mode on a V1720 channel where the baseline is at 3900 ADC and the time bins are 4 ns wide. Image taken from [150].

PMTs are broken into 6 groups of 8 PMTs. A group is marked active if any channel in the given group surpasses the threshold by 15 ADC bins. The self-trigger condition is met when three groups are deemed active simultaneously after which a signal is sent to the DTM.

On the other hand, a single V1720 is used for the neck veto PMTs that runs in ZLE mode. This digitizer also handles the signals from tagging PMTs that are used during calibrations with radioactive sources.

To read out the digitizers, DEAP uses optical links using proprietary CAEN A3818 cards [161] where each card can read out eight V1720s, or four V1740s.

DAQ Trigger and Its Efficiency The DTM has different responsibilities including: deciding to issue a trigger, providing a master clock for synchronizing digitizers, triggering both digitizers and external calibration systems, and in case of DAQ getting overwhelmed, the DTM will throttle data collection. A set of “trigger sources” and logical “trigger outputs” form the basis of the trigger system. The trigger sources decide whether to issue a trigger or not by analyzing PMT signals and using the periodic and external triggers while deciding which hardware should be fired is the trigger outputs responsibility. A logical trigger output can decide whether to fire one, several, or even no NIM[1] outputs. A fixed percentage of trigger signals can be ignored, referred to as pre-scaling, by configuring the trigger outputs.

The "physics trigger" is the main trigger algorithm in DEAP in which the 22 ASUMs (from the internal 22 SCBs) are added together, summing all the 255 inner-detector PMTs. The trigger computes two rolling integrals in two windows that have the same start time and are 177 ns and 3100 ns wide referred to as prompt and late windows, respectively. Two variables are then calculated: E_{prompt} which is the total charge in the prompt window and F_{prompt} which is the energy ratio of the prompt window over the late window. Figure 4.14 shows this phase space broken into 6 different regions. Any event in the X region is ignored but each of the other 5 regions count as a separate trigger source. When a physics trigger is issued, a waveform of 16 μs is saved that is 2.5 μs before the trigger and 13.5 μs after the trigger.

DEAP data-taking uses three triggers as its standard trigger setup: the physics trigger, the periodic trigger, and the muon veto self-trigger. Since region C is dominated by ^{39}Ar beta decays, the physics trigger is configured to ignore 99% of the events in this region, a pre-scaling factor of 100. In fact, the end of ^{39}Ar beta decays spectrum sets the lower bound of region E. For regions A, B, D, and E, the digitizers are read out for all events and the summary information consist of time, E_{prompt}, and F_{prompt} are saved for all events if the digitizers are not read out. The ROI for DM search lies inside region B.

The periodic trigger operates at 40 Hz from which 1 Hz is used for injecting test pulses while the rest is used to monitor the PMTs. Lastly, only when the muon veto self-trigger activates, the muon veto PMTs are read out. The rate of the overall trigger is 3200 Hz and the readout of digitizers happens at 500 Hz. There is one last trigger system which is used for daily calibration using LED light injection. The calibration

---

[1] The 12-channel NIM I/O cards have 8 outputs and 4 inputs and are part of the daughterboards of the DTM hardware. See Ref [150] for more information about the hardware pieces.

system is outside the scope of this thesis and will not be covered. See Ref [150] for more information.

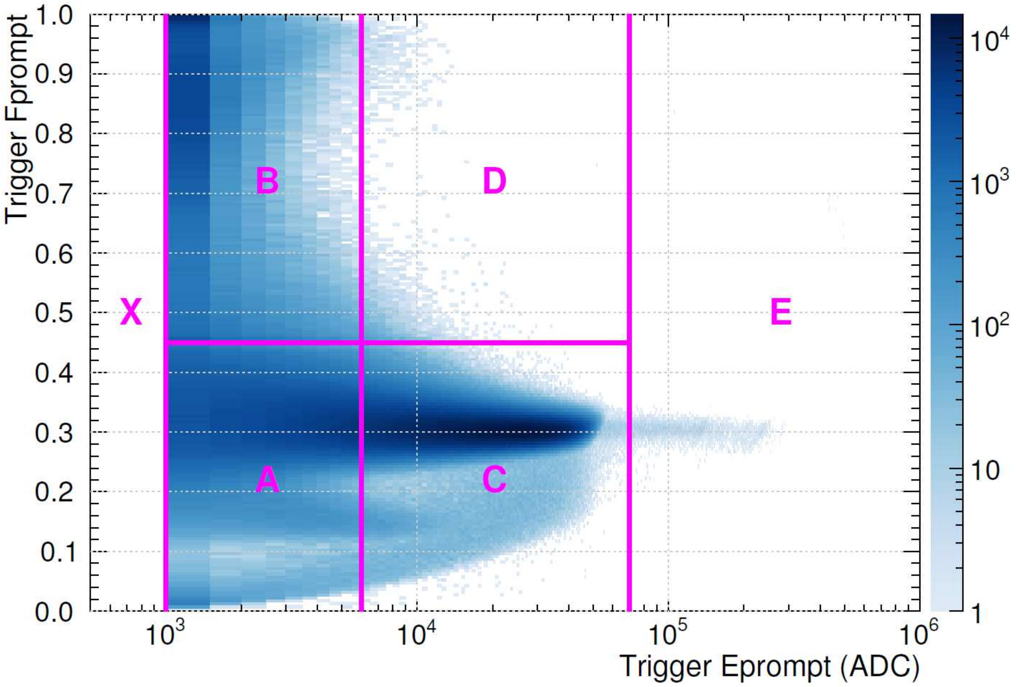

Figure 4.14: The (E_{prompt}, F_{prompt}) phase space for an example taken using the physics trigger without applying any cut. The z-axis is indicative of the number of events. Image taken from [150].

4.6.4 Data Reduction

In DEAP, a software readout is used to collect information from the digitizers and the DTM and filters the unnecessary information. It writes the final collected information to disk as a single event. The information from V1740 is only needed when V1720 digitizers are saturated which happens at about 100 PhotoElectron (PE). In such cases, we use two stages to filter out unnecessary information from V1740. In the first stage, we only rely on the data from V1740. If a waveform does not drop below 3750 ADC, 150 units lower than the 3900 ADC baseline, it will be filtered out. The first stage helps to reduce the amount of data sent to the master computer. This is also where the second filtering stage is applied and any waveform that its corresponding V1720 channel does not go below 500 ADC is removed. With these two stages, we reduce more than 99.9% of V1740 information.

To reduce the amount of written data even further, the V1720 waveforms are also filtered to only save the summary information of the pulses. The summary information is enough to keep a timing resolution of sub-ns around the peak. It will also preserve pulse charge, height, and baseline with its RMS. With these filtering and other compression methods, the data rate is reduced by about three orders of magnitude from 7 GB/s to 6 MB/s.

4.7 Pulse-Shape Discrimination in DEAP-3600

LAr has a great PSD power and the DEAP detector utilizes this feature. DEAP uses the Reactor Analysis Tool (RAT) software framework which is a custom tool that combines Geant4 and ROOT[1]. RAT is used in both analyzing the data, and simulating and analyzing Monte Carlo (MC) simulations. DEAP, through the RAT framework, have different processors and algorithms to reconstruct different characteristics of an event from the raw data collected by the PMTs. An important variable is the total charge of the event. In fact, DEAP has two different algorithms for calculating the charge of each PMT, which will subsequently be summed and calculate the total charge of the event.

The total charge of the event is found by measuring the PE count in a time window of 28 ns before the trigger and up to 10 μs after the trigger[2]. The two algorithms are meant to measure the PE in each PMT. In a simpler method, we sum the PE counts of each PMT to find the total charge of the event, which is referred to as the qPE. In the second method we use Bayesian analysis to find the most probable number of PE that was generated in the LAr. This method is preferred because it will remove the effect of afterpulsing in PMTs. The charge found from this approach is called nSCBayes.

The PSD variable in DEAP exploits the time difference between the singlet and triplet states of LAr and is the ratio of charge in a prompt and late window, Since we

---

[1] ROOT is an object-oriented program and library that is developed by CERN.

[2] These times are relative to calibrated trigger time.

have two methods for calculating the charge, we also have two PSD variables called $\mathrm{F}_{\mathrm{prompt}}$ and $\mathrm{R}_{\mathrm{prompt60Bayes}}$ that are defined as:

$$\begin{aligned}
\mathrm{F}_{\mathrm{prompt}} &= \frac{\int_{t=-28\mathrm{ns}}^{150\mathrm{ns}} \mathrm{qPE}(t)}{\int_{t=-28\mathrm{ns}}^{10\mu\mathrm{s}} \mathrm{qPE}(t)}, \\
\mathrm{R}_{\mathrm{prompt60Bayes}} &= \frac{\int_{t=-28\mathrm{ns}}^{60\mathrm{ns}} \mathrm{nSCBayes}(t)}{\int_{t=-28\mathrm{ns}}^{10\mu\mathrm{s}} \mathrm{nSCBayes}(t)}.
\end{aligned} \tag{4.6}$$

Both charge and PSD variables are used based on the given analysis but for the DM search analysis we use nSCBayes and $\mathrm{R}_{\mathrm{prompt60Bayes}}$, unless stated otherwise.

Other important variables calculated and used by DEAP will be covered in the next chapter when we talk about the data set used for the studies done in this thesis.

4.8 Backgrounds in DEAP

WIMP interactions are rare. Therefore one of the most important topics in DM detector is the complete understanding of contributing backgrounds in the experiment. We need to be sure that normal radioactivity does not fool us and appear as WIMP. In DEAP, we have a great understanding of the possible backgrounds and their contribution to our studies. DEAP was designed and constructed with the goal of less than 0.6 background events during a 3-tonne-year exposure [150]. But this goal cannot be achieved by only using the SNOLAB facility to reduce the muon flux or by using proper materials for shielding, because we still would have many background events scintillating in the detector. To remove these background events and reach our target, we use the properties of LAr, our detector, and the properties of each background type to identify and remove them.

As shown in Figure 4.15, the two major categories of backgrounds are EM events such as ^{39}Ar β-decays and Cherenkov radiation, and nuclear recoil events caused by neutron scatters and α-decays. Each of these background sources will be discussed in more detail in this chapter. If we zoom in the red region of Figure 4.15, Figure 4.16 shows the ROI in PE-$\mathrm{F}_{\mathrm{prompt}}$ space.

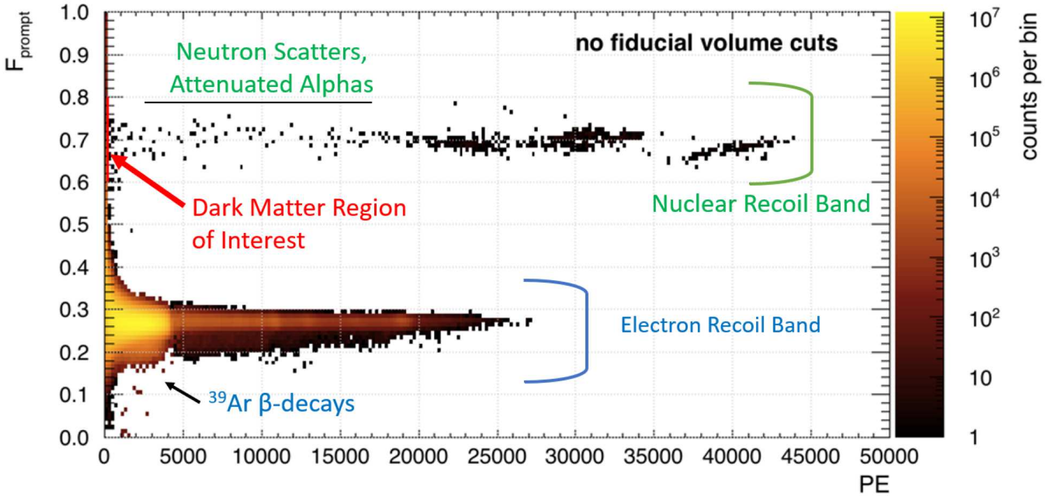

Figure 4.15: PE versus F_{prompt} distribution using 4.4 live-day dataset where the EM and nuclear recoil bands are shown in blue and green respectively. The DM ROI highlighted with red lies in the region of 80-200 PE.

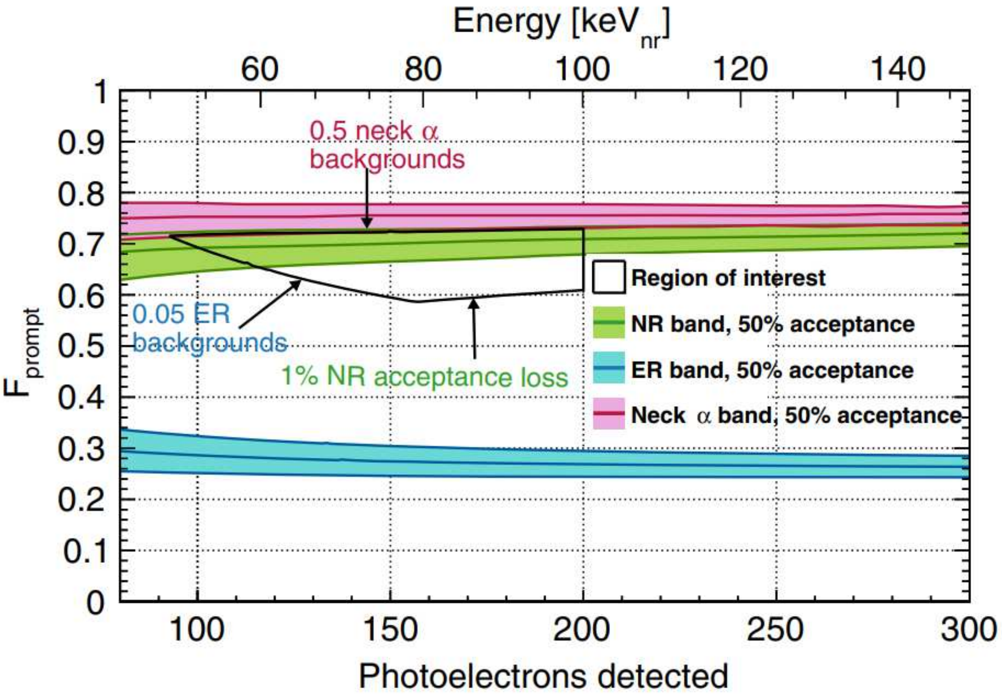

Figure 4.16: The ROI for DM search shown in black where the boundaries are defined by Electron Recoil (ER) (50% of the ER events are in the blue band and 0.05 events in the 223 days move the top boundary of the blue curve to the black region), nuclear recoil (green), and neck alpha (pink) backgrounds. Image taken from [162]. The

4.8.1 ^{39}Ar β Decays

Although EM events come from different sources, see Figure 4.17, they are dominated by ^{39}Ar β-decays that are also the dominant event type in DEAP. The LAr in DEAP is atmospheric argon which has a trace amount of ^{39}Ar isotopes that are unstable and can beta decay to ^{39}K with a half-life of 269 years. The activity of ^{39}Ar in atmospheric argon is 0.95 ± 0.05 Bq/kg [163] that translates to about 2.7×10^{8} ^{39}Ar decays per day.

As can be seen from Figure 4.15, EM events with energies more than ~ 1000 PE can be easily removed using PSD. But at lower energies, the F_{prompt} widens and these events can have higher values of F_{prompt} and leak into the ROI. This widening can happen in two ways. The first way is due to the statistical fluctuations in measuring the F_{prompt} at such low energies where we detect very few photons. The second one is a coincidence event of ^{39}Ar beta decay with a Cherenkov event where the latter has an F_{prompt} of close to one and when combined, they can mimic a WIMP signal. The lower contour of the ROI shown in Figure 4.16 is set to maximize the nuclear recoil acceptance while keeping the leaking EM events within our background budget. As shown in Figure 4.18, at 110 PE, with a nuclear recoil acceptance of 50%, PSD provides a 10^{-9} EM leakage probability.

^{39}Ar is not the only event type responsible for EM band. At energies above 5000 PE, the EM events can be produced by different sources such as: other Ar isotope decays like ^{42}Ar to ^{42}K, and radioisotopes from the PMT glass (e.g ^{208}Ti and ^{214}Bi) and radon gas diffuse in the components of the detector [164]. Due to their high energies, these events do not affect the DM search, see Figure 4.17.

4.8.2 Cherenkov Radiation

When a particle in a medium travels at a speed greater than the group velocity of light in that medium, Cherenkov light is generated. In DEAP, this light can be generated by particles travelling in the acrylic LG. Since they occur in the LG, most of their light is directly sent to the PMT attached to that LG. In addition, the time profile for Cherenkov events is very narrow since the production of light is instantaneous and F_{prompt} should be

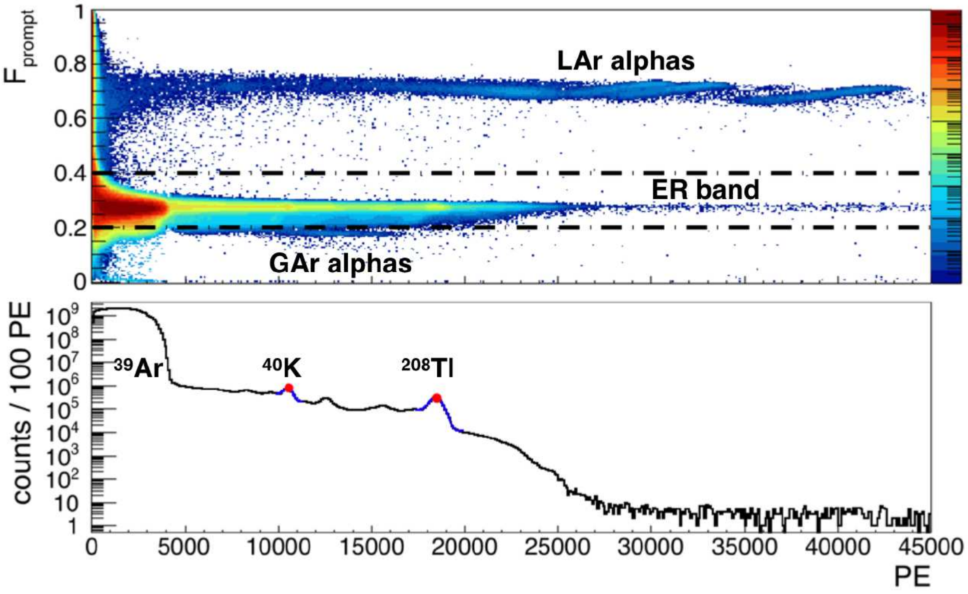

Figure 4.17: Top plot shows the spectrum of PE versus $\mathrm{F_{prompt}}$ for the dataset of 247.2 days after quality checks and a sequence of cuts. The bottom plot shows the contribution of different event types in the EM band. Since the ^{40}K and ^{208}TI energy range are well above the DM ROI, we won't discuss them in detail in this thesis. But ^{39}Ar β-decays can leak into the ROI. Image taken from [164].

close, if not equal, to 1. This is in fact true for most of the Cherenkov events observed in DEAP where a PSD cut would prove to be useful again. A Cherenkov event can happen in coincidence with an ^{39}Ar which results in a single event getting registered with a lower $\mathrm{F_{prompt}}$, bringing it close to the ROI.

To deal with such cases, in the DEAP collaboration we have defined a variable called “fmaxpe” which is the ratio of charge in the brightest PMT to the total charge of the event. Since the scintillation light in LAr is quite isotropic [162]. This cut removes the Cherenkov events that happen in a single LG.

4.8.3 Radiogenic and Cosmogenic Neutrons

Neutrons, similar to WIMPs, are neutral particles and given their source and path, they can cover a big range of energies. Since neutrons cause nuclear recoil, they can mimic a WIMP signal. Based on the source of the neutrons, we can divide them into two

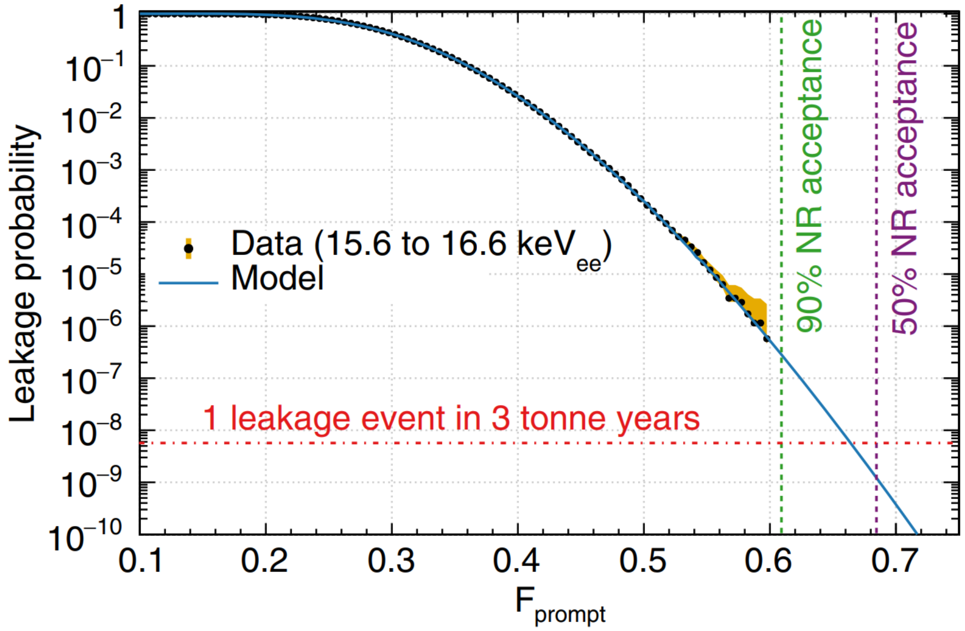

Figure 4.18: Probability of detecting an EM exceeding a specific $\mathrm{F_{prompt}}$ value in the WIMP ROI's lowest 1 $\mathrm{keV_{ee}}$ bin. Vertical lines depict the values above which 90% and 50% of NRs are anticipated to be found. Image taken from [162].

categories, radiogenic neutrons and cosmogenic neutrons.

As the name suggests, the cosmogenic neutrons are produced by cosmic ray interactions and their flux is greatly reduced by the 2 km of rock above our detector. Any muon surviving the journey and creating neutrons outside the detector will be tagged and removed through the coincident muon detection of the muon veto system.

There are two main sources for producing radiogenic neutrons. One source is the spontaneous fission of ^{238}U, and the other is where α-decay of ^{238}U, ^{235}U, and ^{238}Th decay chain induce (α, n) reactions. A trace amount of these isotopes exists in the detector components. The dominant source of the neutron background is the PMT glass followed by polyethylene filler blocks and polystyrene filler foam, both of which are between the LGs. Other sources are the ceramic in the PMT glass, the polyvinyl chloride (PVC) material in the PMT mounts and the neck veto PMTs [162]. DEAP has done detailed studies to understand this background in our detector. Since this background is not the emphasis of this thesis, we won't get into the details and reference the reader to read chapter **VII**, section C. from ref [162]. The conclusion though is that the contribution of neutron backgrounds in the WIMP ROI using the 231-live day results were found to be negligible. The radiogenic and cosmogenic neutron contributions, respectively, were found to be $N_{n,rdg}^{\mathrm{ROI}} = 0.10^{+0.10}_{-0.09}$ and $N_{n,csg}^{\mathrm{ROI}} < 0.11$.

4.8.4 Alphas

Since alphas cause nuclear recoils, they can mimic a WIMP signal. They are one of the most important backgrounds in DEAP and are the emphasis of this thesis. The source of the alpha particles in the DEAP experiment are the radioactive isotopes that exist within the detector and detector components. The main radioisotopes are ^{238}U and ^{232}Th where the decay chain is shown in Figure 4.19. As can be seen from their exceptionally long half-life, these are primordial radioactive elements from the Earth's creation. These isotopes and their daughters are scattered throughout the detector. As such, the high-energy alphas created in these decay chains can appear anywhere in the detector and create nuclear recoil events by depositing their energy to the LAr.

The DEAP detector was designed to minimize the internal and external backgrounds that could mimic a WIMP signal; such as radon and radon progeny within the liquid argon volume, radioactivity for both at the AV or near the inner side of the AV, among other backgrounds discussed previously [150]. Multiple mitigation strategies were employed to minimize the radon background. The cryostat's acrylic material was selected carefully, and the construction of the cryostat and the AV was closely monitored to minimize their exposure to radon and other contaminations. But then the detector components were assembled underground at SNOLAB which exposed the acrylic to the underground lab air. The ^{222}Rn contamination level of the air is about 130 Bq/m^3 [150]. After the AV construction underground, a robotic resurfacer was built to remove radioactive contaminants that had accumulated on the inner acrylic surface due to radon surface deposition and diffusion. The production of the TPB was also closely monitored by the collaboration to reduce the contribution to surface backgrounds from the wavelength-shifting coating used after resurfacing.

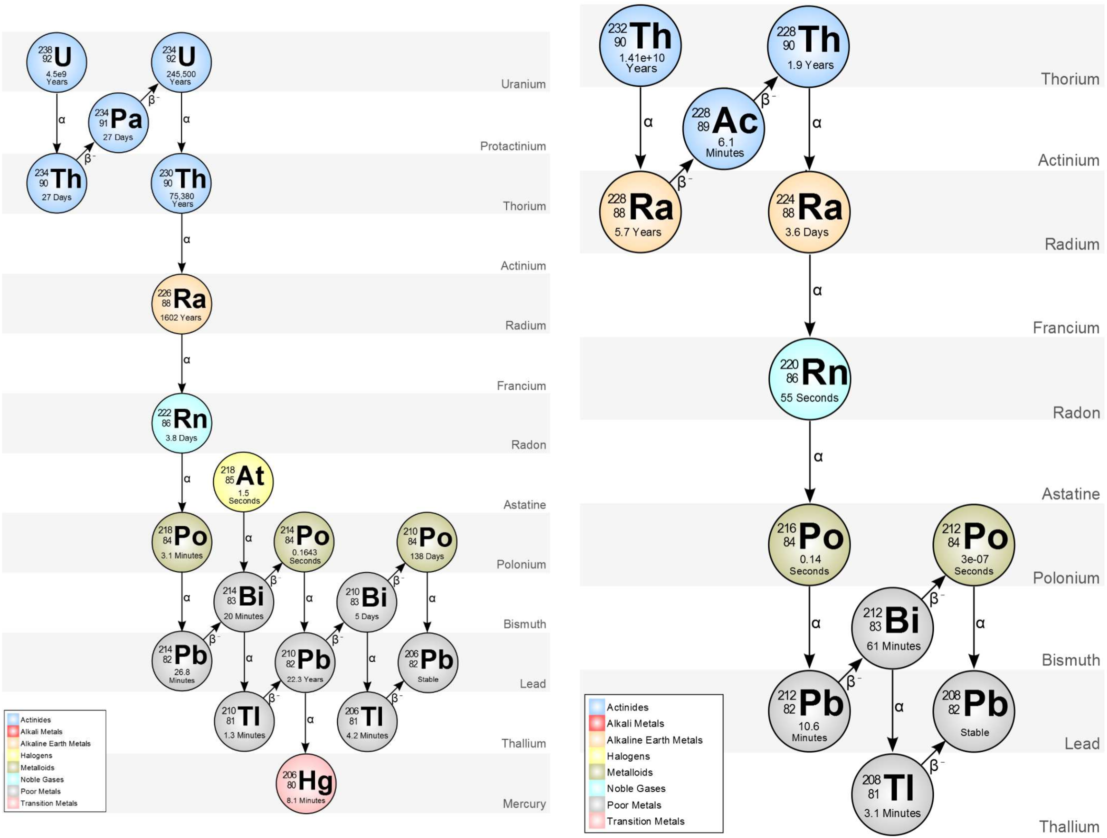

(a) ^{238}U

(b) ^{232}Th

Figure 4.19: Decay chain diagrams of **(a)** ^{238}U and **(b)** ^{232}Th taken from Ref. [165].

The Radon gas ,^{220}Rn and ^{222}Rn, can be created through the decay chain of ^{238}U and ^{232}Th, respectively. The activity of ^{220}Rn and ^{222}Rn in LAr are measured to be 4.3 ± 1.0 nBq/kg and 153 ± 5 nBq/kg, respectively [162]. Since the latter has much higher activity, we will consider the ^{222}Rn nuclei. The short-lived daughters of ^{222}Rn include ^{218}Po and ^{214}Po, while ^{210}Po has a longer half-life. The predominant decay of all the three Po daughter nuclei and the mother Rn is α-decay where they generate a high energy α particle. The energy of these α particles is in the order of a few MeV and when they deposit their energy into the LAr, they create large amounts of scintillation light, pushing the event PE well above the ROI[1]. Figure 4.15 shows these alpha particles at $\mathrm{F_{prompt}} \approx 0.7$ and energies above 20,000 PE.

---

[1] The PE window of the ROI is around 80 to 240 PE.

Although the full energy alpha decays do not pose any challenge for DM analysis, there are cases where we can have attenuated alphas that only deposit a portion of their energy into the LAr bulk and cause a low energy nuclear recoil event near the ROI. The main source of such events are the alpha decays of ^{210}Po happening inside the component material[1]. In this case, the generated alpha will lose some of its energy passing through the material and once it reaches the LAr, it has a much lower energy, creating events near the ROI. These events are also shown in Figure 4.15. There are three cases from which we can get attenuated alpha particles. The first instance is an alpha decay happening within the inner surface of the AV and TPB layer. These events are the main topic of study in this thesis. Another source is the alphas generated in the neck region of the detector where the attenuation is mainly caused by the shadowing caused by the neck flowguide which is made of acrylic. The last case, which poses the most challenging background removal, are α-decays happening inside dust particulates that are scattered throughout the LAr inside the detector. We will discuss each of these instances below in more detail.

TPB Layer and AV Inner Surface

Among the three sources of attenuated alphas, the simplest events for background removal are α-decays happening in the TPB layer and the inner surface of the AV, shown in Figure 4.20. The decays that happen inside the LAr are the ideal case for background removal since the alpha particle will deposit all of its energy inside the LAr and the event energy will be well above the ROI. In the second case, either the alpha particle or the daughter nucleus might enter the scintillation material. But in this case, before entering the LAr, the particles will deposit a portion of their energy in the TPB layer and produce TPB scintillation. This light has an $\mathrm{F}_{\mathrm{prompt}}$ of 0.4 to 0.5. The amount of energy loss can defer based on how deep the initial decay was and how much it had to travel before reaching the LAr; e.g tangential path taken along the TPB layer. The last

---

[1] Note that there are other isotopes in our detector such as Bi and Pb, but the dominant source in DEAP is from ^{210}Po. We will cover these in the next chapter.

scenario is when the decay happens in the AV inner surface in which the alphas will lose most of their energy in both the AV and TPB. The last two cases can create events with low enough PEs to mimic a WIMP signal in the ROI. The best way to deal with these events is a fiducial volume cut to remove events reconstructing near the surface. In fact, one purpose of this thesis is to design a new algorithm for identifying surface alpha events so that we can expand the fiducial volume and improve our signal acceptance while preserving the background budget.

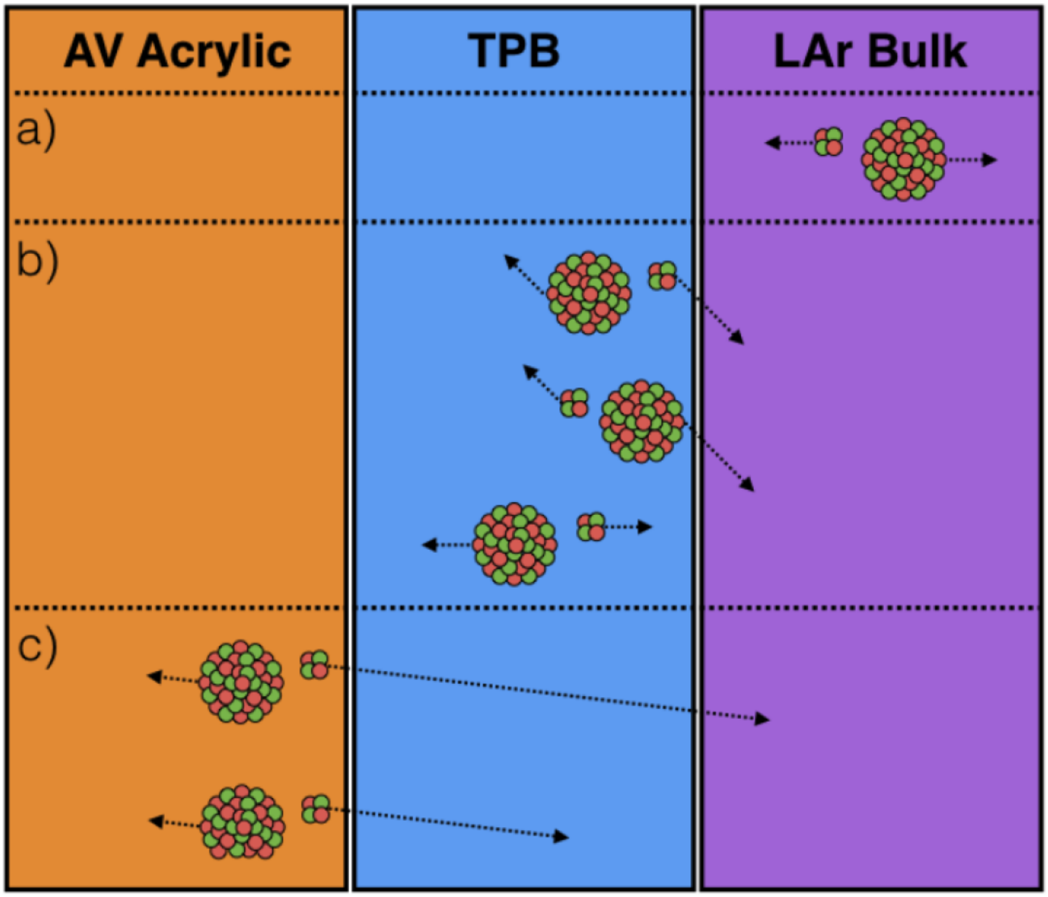

Figure 4.20: Graphical breakdown of ^{210}Po surface alphas. The alpha-decays can happen **(a)** inside the LAr, **(b)** within the TPB layer, and **(c)** inside the AV inner surface. Image courtesy of the DEAP-3600 collaboration.

Acrylic Neck Flowguide Surface

A challenging background in DEAP is the alphas coming from the neck region, which is located at the top of the detector, in the GAr region. The main difference between these alphas compared to those mentioned above is the neck and neck flowguide geometry, shown in Figure 4.21. Although the top of the detector is filled with GAr, simulations show that there is some population of LAr, most probably in the form of a thin film at the flowguide. When the alpha decay of ^{210}Po pass through this LAr film, they scintillate and produce UV light. Since the acrylic in this region is not coated with TPB, a large fraction of the UV light is absorbed by other parts of the acrylic flowguide. The geometry of the neck region can also prevent the light to reach inside the detector to be observed by the PMTs. This process is referred to as shadowing which reduces the number of scintillation photons that reach the PMTs, hence causing low energy alpha events mimicking WIMP signal in the ROI.

Using the 231-live day results, neck events were the dominant background with a share of 0.49 events out of the total budget of 0.62 events. The DEAP collaboration has been developing different methods, including a likelihood approach [166] and machine learning algorithms [167] to mitigate these alpha background events.

Dust Particulate Diffuse in LAr

Based on the alpha model and the 231-live days results published in [124], the DEAP collaboration observed an excess of events in the nuclear recoil band with energies between 5000-20000 PE. Although they behave as an attenuated alpha, the background model was not able to explain the excess data in this region. A proposed explanation was that we have ^{222}Rn contaminated dust particulates diffuse within the LAr bulk. An α-decay could occur inside the dust particle.

From the studies and investigations done by the DEAP collaboration, there are different possibilities of dust particles remaining in the detector:

- Norite dust: Norite dust is the mine dust, from SNOLAB rocks, that has high

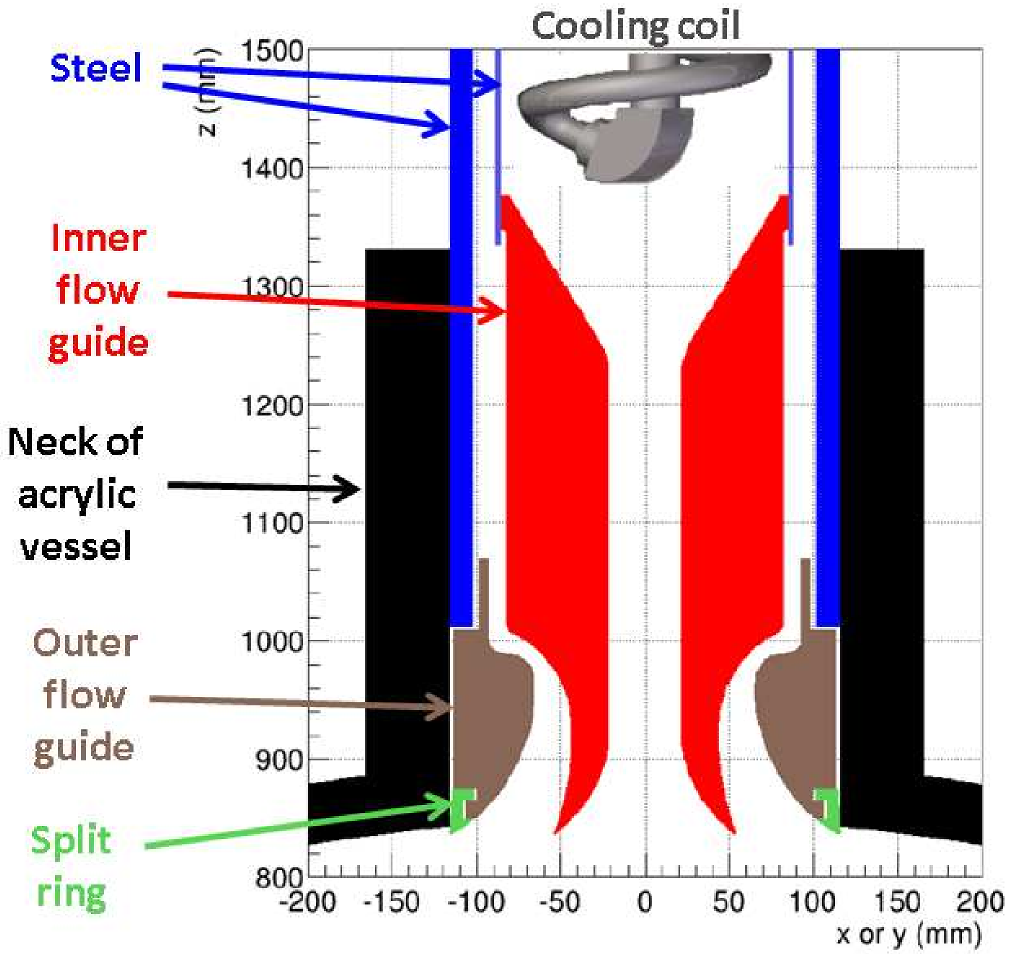

Figure 4.21: The diagram of the geometry of the neck region showing the inner and outer flow guides. Image courtesy of the DEAP-3600 collaboration.

levels of Uranium and Thorium activity. Early SNOLAB investigations show that the lab contains a large amount of norite dust. Norite has a concentration of 1.2×10^{-6} g/g for ^{238}U, and a concentration of 3.3×10^{-6} g/g for ^{232}Th[1]. Using the ^{238}U and ^{232}Th activity of 12.44×10^{3} Bq/(g ^{238}U) and 4.07×10^{3} Bq/(g ^{232}Th), the norite activity translates to 14.9 mBq/g and 13.4 mBq/g for ^{238}U and ^{232}Th, respectively [145].

- Metallic dust: A metal cylinder is used to store cryogenic liquids. In the storage

---

[1] g/g means **x** gram of ^{232}Th or ^{238}U in one gram of norite dust.

tank, metallic surface erosion may take place, generating dust particles. A sub-micron filter was used to fill the acrylic vessel with argon at the time the detector was installed, so no dust particles may be still present in the argon itself. However, to reduce the Radon activities, the AV resurfacing was performed with 10 tonnes of nitrogen purge inside the vessel. For this procedure, a filter of 50 μm pore size was used, allowing deposits of particulates smaller than 50 μm to enter the AV. Using filter paper, the liquid nitrogen was found to contain copper and zinc particle remnants.

- Acrylic powder: Because a thin layer of AV surface, about 0.5 mm, was removed in situ with a resurfacer and washed with water, some acrylic dust may have remained in the AV from the resurfacing residues.

Figure 4.22 shows the process of an attenuated alpha caused by a dust particulate. Before the emitted alpha can reach the LAr, it will lose a portion of its energy by travelling through the dust. Furthermore, the dust particulate itself will block some of the scintillated light and cause shadowings, leading to a heavily attenuated alpha leaking inside the ROI. In fact, given the different possibilities for the dust size and its nature, the dust events can occur in a wide range of PE. Since the dust particulates are uniformly distributed throughout the detector, unlike surface events, a positional cut is not an option which makes the dust alphas the dominant background in the WIMP search.

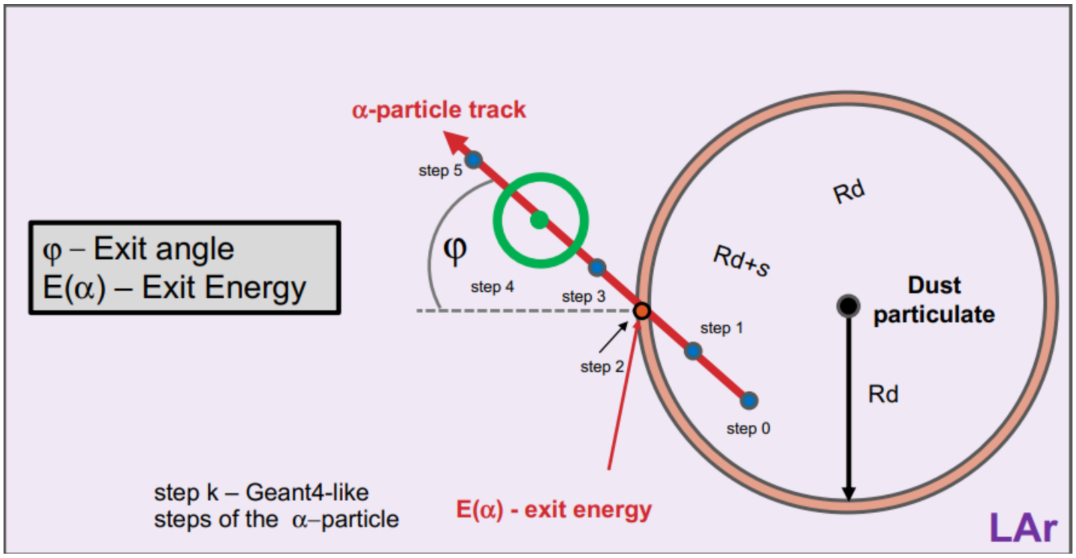

Figure 4.22: A schematic view of an α-decay happening within a dust particulate. The dust is in the LAr. The alpha particle loses most of its energy in the dust material before exiting to the LAr and creating scintillation light. A portion of the scintillation light will also get absorbed by the dust particulate. Image courtesy of DEAP-3600 collaboration.

Chapter 5

Analysis

In this chapter I will cover some of the more important studies that I conducted and had significant impact on the physics analysis of the DEAP collaboration. But before getting into our studies, we need to cover two topics. First, we need to define some of the variables that are commonly used by our collaboration and used throughout this thesis. Secondly, we need to cover the position fitters used in DEAP as finding the position of the interaction is an integral part of almost all of our studies.

The first study, presented in section 5.3, focuses on a study of the time profile in MC simulations and experimental data. This study is crucial for accurately estimating background contributions using MC simulations.

In the second study, section 5.4, we introduce a scintillation likelihood processor designed for RAT. Although the variables investigated in this study did not make it into our final DM search analysis, some of them have been incorporated into the machine learning algorithms used in DEAP.

Dedicated to studying the saturation in PMTs, the third study, section 5.5, proposes a new method to utilize the late light signals for studying alpha quenching factors and determining the Birk's constant. While this study does not directly contribute to the DM search analysis, understanding the position resolution of surface alphas is crucial.

In the fourth study, section 5.7, we introduce a new processor designed to veto surface background events, enabling the expansion of the fiducial volume and improving DM cross-section limits.

The fifth study, section 5.8, investigates Cherenkov background events and introduces a new variable that will be utilized in the next chapter to establish the WIMP-nucleon cross-section limits.

5.1 DEAP Analysis Variables

The only information we have for each event is the set of waveforms collected by the PMTs and measured with digitizers as described in section 4.6.3. These waveforms are analyzed to generate the time and charge of each pulse. This is converted into arrival times for each of the detected photons. A set of reconstruction algorithms determine the position, total charge, and trigger time. Subsequent processing uses these variables and generates hundreds of derived variables. In this section, we will only cover the variables commonly used in our studies and in DEAP. Any specific variable needed for our studies will be discussed separately as needed.

5.1.1 Non-Physics Event Removal Variables

The trigger that generates the event is recorded with two integers which are used to remove non-physics events. These variables are not derived and are only available for data and not MC events.

dtmTrigSrc The first integer is labelled dtmTrigSrc which specifies the trigger source of the event. Bits in this integer are assigned to each of the five energy-F_{prompt} regions shown in Figure 4.14, an external calibration trigger, or the internal pulse generator. The internal pulse generator is a component of a periodic trigger that fires at a frequency of 40 Hz. It causes the DAQ to trigger and record a pulse. one component of the periodic trigger is the Pulse Pattern Generator (PPG) that runs at 1 Hz. The random trigger generates the other 39 samples and is used to monitor the PMTs. The external calibration trigger can come from either of our radioactive calibration sources; AMericium-BEryllium (AmBe) and ^{22}Na. The events matching bit 13, region C in Figure 4.14, are mainly ^{39}Ar beta decays. Due to their high rates, and in order to reduce the file size, we only save the waveform of one such events per 100 of them. In any physics study, we use the bit-wise cut of 0x82 in order to remove non-physical events, matching bits 2 and 8. Table 5.1 summarized the different triggers in DEAP and their corresponding hexadecimal.

Bit	Hex Code	Trigger Source
2	0x2	Internal periodic trigger (PPG event)
8	0x80	External calibration trigger
11	0x400	Low energy, low F_{prompt}
12	0x800	Low energy, high F_{prompt}
13	0x1000	Medium energy, low F_{prompt}
14	0x2000	Medium energy, high F_{prompt}
15	0x4000	High energy, all F_{prompt}
bit-wise cut	0x82	Removes any instances of bits 2 and 8

Table 5.1: Different trigger types used in DEAP.

calcut The second flag used to remove "bad" events is the calcut variable. There are different reasons why an event should be excluded from the analysis, such as a PPG event, a DAQ error, or not being properly calibrated. Table 5.2 shows the list of possible flags and their meaning. The current bit-wise cut is 0x31f8 which removes any events matching bits 3, 4, 5, 6, 7, 8, 12, or 13.

5.1.2 Pile-Up Event Removal Variables

A pile-up event is a case when more than one event occurs within the same trigger window. Since the charge information of the piled-up events will get contaminated, we remove all such events. We have four variables in DEAP designed to deal with pile-up.

subeventN The subeventN variable calculates the number of (sub)events happening within a given 16 μs time window. It separates the single recoil events from instances when we have more than one event within the given 16 μs. In data, we only included events where subeventN is equal to 1, meaning that only a single event was identified

Bit	Hex Code	Description
0	0x1	A V1720 pulse had a bad baseline
1	0x2	A V1720 pulse reached 0 ADC (saturation)
2	0x4	Failed to find a “good” calibrated trigger time
3	0x8	A PPG event (not suitable for physics analysis)
4	0x10	If an event is soon after a PPG event
5	0x20	If a spare V1720 has a pulse (due to PPG or noise)
6	0x40	DAQ was running busy and suppressing readout of digitizers
7	0x80	If trigger and digitizers are out of sync
8	0x100	Event timestamps are appearing out-of-order
9	0x200	There are no digitizers in the event (due to pre-scaling)
10	0x400	Event came from a non-physics trigger source
11	0x800	SQT info used for a non-SPE-like pulse
12	0x1000	SQT info used for a pulse where the charge integral was truncated
13	0x2000	SQT info used for a pulse $>$ 1000 pC
bit-wise cut	0x31f8	Removes any instances of bits 3, 4, 5, 6, 7, 8, 12 and 13

Table 5.2: A list of different calcut flags used in DEAP. Smart QT (SQT) is an algorithm used in the front-end software of the V1720 digitizers to encode waveforms.

by the processor within the trigger window. Figure 5.1 shows a sample event where subeventN was found to be 2.

numEarlyPulses When the DAQ triggers, the numEarlyPulses variable measures how many peaks or sub-peaks happen in the pre-trigger portion of the trigger window. This scenario happens when the tail of a previous event or a fraction of its charge leaks into the current event trigger window. In data, we remove events with numEarlyPulses great than 3. Figure 5.2 shows two sample events with numEarlyPulses greater than 3.

deltaT The time difference between the beginning of two successive events is measured by the delatT variable. In data, we use delatT greater than 20 μs which is 4μs more than the event window. This cut removes many of the events where the light of a previous

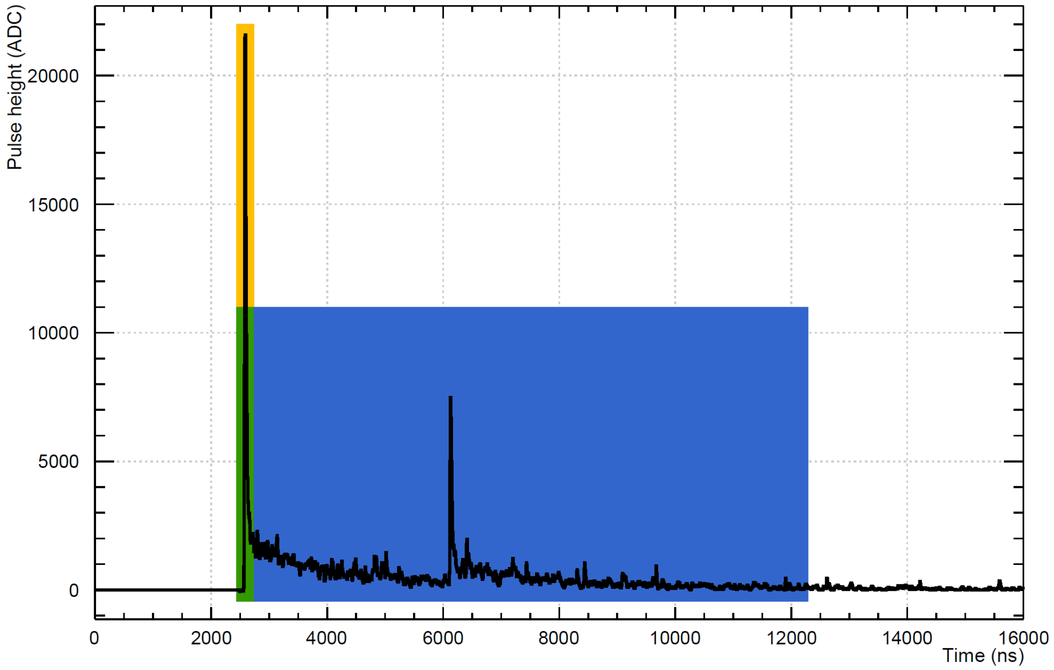

Figure 5.1: An example of pile-up event with subeventN = 2. A second pulse happens within the integration window of the first trigger. This will add to the total charge of the event and change the PSD variable. The prompt and late windows are shown as yellow and blue, respectively. The green area shows the overlap region. Image courtesy of Matthew Dunford.

event contaminates the current event.

eventTime The time of the initial pulse peak of an event is measured by eventTime[1]. A typical event happens around 2500 ns which is set by the hardware and corresponds to the time of the photons that satisfies the hardware trigger. The range used for the data allows triggers between 2250 ns to 2700 ns. The 2250 ns cut is used to remove pre-trigger pileup events which are the charge-tails of previous events continuing into a new event window and causing an early trigger. Similarly, the 2700 ns is to remove events that happen late in the waveform. This is typically from the pileup of events after the primary event. Many of these are in fact caught by the subeventN processor but there are some instances which are not and this cut is a contingency against any

---

[1] We will often refer to this time variable as T0.

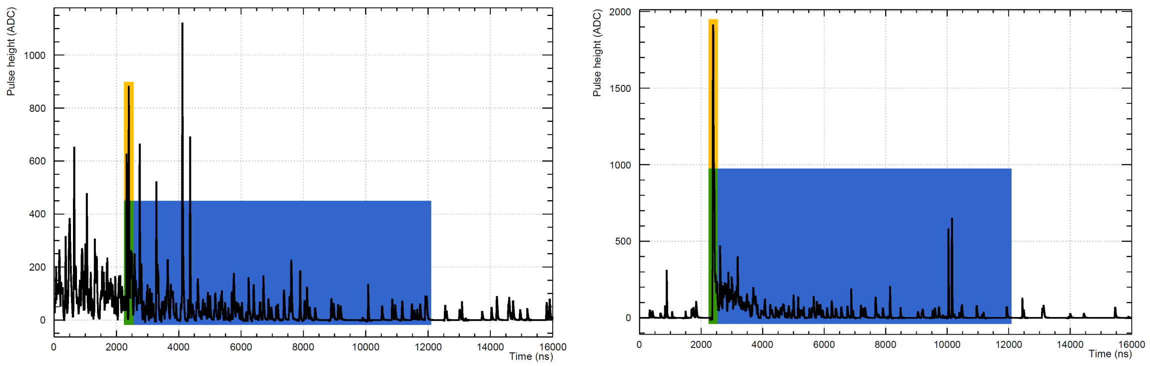

Figure 5.2: Two examples of events with numEarlyPulses great than 3. The prompt and full integration windows are shown in yellow and blue, respectively. The green area is the overlap region of the prompt and late windows. Image courtesy of Matthew Dunford.

inefficiencies associated with subeventN.

The combination of these six variables, shown Table 5.3, is often referred to as low-level cuts. These cuts are designed for data and MC events do not require these events unless special settings are used during the simulations for specific studies.

Cut Variable	Cut value	Purpose
dtmTrigSrc	0x82	Non-physics data removal
calcut	0x31f8	Removes “bad ”events
subeventN	=1	Pile-up removal
numEarlyPulses	<=3	Pile-up removal
deltaT	>20000 (ns)	Pile-up removal
eventTime	2250< T0 <2700 (ns)	Pile-up removal

Table 5.3: A summary of low-level cuts applied to data.

5.1.3 Calculated Variables

As mentioned earlier, for any given event, we can calculate many variables that can be used for different studies and purposes.

fmaxpe The fmaxpe variable is the fraction of the charge in the brightest PMT to the total event charge. fmaxpe is our main variable to remove Cherenkov backgrounds.

neckVetoN The neckVetoN variable measures how many hits were counted in the neck veto PMTs. Thus, the neckVetoN value can be either 0,1,2,3,4. For DM searches we use a cut value of neckVetoN=0; i.e. the event must not have fired any of the neck PMTs.

PE and $\mathbf{F_{prompt}}$ Probably the two most important variables in our studies are the event charge and the PSD variable, as discussed in section 4.7. As a quick reminder, we have two charge variables referred to as qPE and nSCBayes. The qPE variable uses a simpler method which counts the PEs in each PMT while nSCBayes uses Bayesian analysis to remove the effects of afterpulsing. The PSD variable calculated from qPE is called $\mathrm{F_{prompt}}$ while $\mathrm{R_{prompt60Bayes}}$ is calculated from nSCBayes. The full window of both PSD variables is -28 ns to 10μs but the prompt window for $\mathrm{F_{prompt}}$ is -28 ns to 150 ns while $\mathrm{R_{prompt60Bayes}}$ only goes to 60 ns[1]

5.2 Position Fitters

A piece of information of significant importance about any event is its position within the detector. All the information we have from a given event is the photons collected by the PMTs. For figuring out where the interaction took place in the detector we have to find the position through software algorithms. In DEAP, we have two position fitters called TimeFit2 and MBLikelihood (MBL)[2] each of which will be covered below. A third position fitter is being developed which uses a Neural Network approach to find the position of the event.

5.2.1 TimeFit2

TimeFit2 (TF2) is a time-based position fitter. There was a first generation of this fitter called TimeFit, hence the "2" in the latest version of this fitter. TF2 takes advantage

---

[1] We also have a variable called $\mathrm{F_{60}}$ which is a PSD variable calculated from qPE but with a prompt window of -28 ns to 60 ns for charge integration.

[2] Named after Mikhail Batygov, a DEAP collaborator.

of the finite speed of light propagation in LAr. The group velocity of light in LAr is 133 mm/ns for 128 nm UV light and 241 mm/ns for 420 nm visible light, created after interaction with the TPB. TF2 uses an analytical, pre-compiled PDF and only uses the first 40 ns of the pulse information. It calculates the likelihood of an event with time t_0 and test position $\vec{x_0}$ as [124]:

$$\ln \mathcal{L}\left(t_0, \vec{x}_0\right) = \sum_{i=1}^{N_{\mathrm{PE}}} \ln \mathcal{L}^{t \text{ res.}}\left(t_i - t_0; \vec{x}_0, \vec{p}_i\right) \tag{5.1}$$

where t_i is the time when the ith photon was detected by the PMT at position $\vec{p_i}$, and N_{PE} is the number of photons detected in the first 40 ns. The fitter will vary the event time and position, calculates the Negative Log Likelihood (NLL), and move the event time and position towards a direction in the parameter space that gives a smaller NLL value. The output of the algorithm are t_0 and $\vec{x}_0$ that maximized $\ln \mathcal{L}\left(t_0, \vec{x}_0\right)$.

5.2.2 MBLikelihood

The second and more commonly used position fitter is the MBL. Unlike TF2, MBL only relies on the charge distribution of the event and uses the full 10 μs information of the pulse. The MBL fitter uses Nelder-Mead minimization approach to find the best position describing the observed charge distribution. It calculates the likelihood $\mathcal{L}(\vec{x})$ that the event happened at some test position $\vec{x}$ as [124]:

$$\begin{gathered}\ln \mathcal{L}(\vec{x}) = \sum_{i=1}^{N_{\mathrm{PMTs}}} \ln \operatorname{Poisson}\left(q_i; \lambda_i\right), \\ \lambda_i = \lambda_i\left(|\vec{x}|, \frac{\vec{x} \cdot \vec{r}_i}{|\vec{x}|\,|\vec{r}_i|}, q_{\mathrm{total}}\right),\end{gathered} \tag{5.2}$$

where $\operatorname{Poisson}\left(q_i; \lambda_i\right)$ is the Poisson probability of observing q_i PE in PMT$_i$ located at position $\vec{r}_i$. λ_i is the expected number of PE in PMT$_i$. λ_i is a function of the radius of the test position, $|\vec{x}|$, the angle formed between PMT$_i$ and the test position, and the total event charge. λ_i is computed based on MC simulations. For more information on these fitters, see Ref. [124].

Two commonly used variables throughout this thesis are going to be the radius of the event position as found by MBL or TF2. From hereon, we will refer to these two radii as MBLR and TF2R for simplicity.

5.3 Recombination Model Tuning

The time profile in DEAP includes contributions from LAr scintillation, time-of-flight, TPBscintillation, PMT time resolution and response, uncertainties from position reconstruction, and properties of the electronics. Before tuning th MC, the simulated distribution did not match the measured distribution. Since the charge and the PSD are our main variables, both of which are variables based on integral, we were not affected too much by the lack of full agreement in our MC. Based on internal discussions, it was assumed to be improbable/impossible to capture the prompt distribution of pulses in MC. In our first study, we set out to improve the timing resolution of our MC.

As mentioned earlier, LAr has two states, singlet and triplet. A reasonable model for LAr scintillation would be a double-exponential decay model. But in a recent paper, the DEAP collaboration showed that having an intermediate component, first introduced by Hofmann et al. [168], can explain the data better [169]. We refer to this model as the recombination model, where the intensity can be written as:

$$I_{\mathrm{LAr}}(t) = \frac{R_s}{\tau_s} e^{-t/\tau_s} + \frac{1 - R_s - R_t}{(1 + t/\tau_{\mathrm{rec}})^2} \frac{1}{\tau_{\mathrm{rec}}} + \frac{R_t}{\tau_t} e^{-t/\tau_t}, \tag{5.3}$$

where τ_s and τ_t are the singlet and triplet lifetimes of LAr and R_s, and R_t are their corresponding weights. The intermediate component describes the electrons that are ejected out of the immediate reach of their ions' attractive electric fields and they will, after a random walk, re-combine with the ion. τ_{rec} is the characteristic time of the recombination process. Note that the time constants of this model are independent of the event type but the two weights are different for each event type. Also, the weights can be energy-dependent. If the weights are energy-independent, we will refer to the model as Energy Independant Recombination (EIR), and if they are energy dependent we will refer to it as Energy Dependant Recombination (EDR).

Although the new model explained our data better and improved the timing in our MC, there were several covariant parameters in the MC that were not included in the model and we needed to tune these parameters in order to make the waveform in MC match the data.

Another timing response in our detector is the time response of the TPB layer which as shown in Ref. [170] can be written as:

$$I(t)_{\mathrm{TPB}} = I_p(t) + I_d(t), \tag{5.4}$$

where $I_p(t)$ and $I_d(t)$ are the instantaneous intensities of prompt and delayed components of TPB, respectively. $I_p(t)$ is the decay of the short-lived singlet state where:

$$I_p(t) = \frac{N_p}{\tau_S} e^{-t/\tau_S}, \tag{5.5}$$

where τ_S is the life time of the singlet state and N_p is the total integrated intensity of $I_p(t)$. As discussed in Ref [170], to derive the full form of the delayed component $I_d(t)$, we need to take into account the interactions between tightly packed triplet states and their diffusion which makes it too complicated to calculate. Since $I_p(t)$ is the dominant term by orders of magnitude at short time scales $t \sim \tau_S$, the inaccuracies of $I_d(t)$ can be ignored and the simplified version can be written as:

$$I_d(t) = \frac{N_d}{\tau_d} F(t), \tag{5.6}$$

where N_d is the total integrated intensity of $I_d(t)$ and $\tau_d = \int_0^\infty F(t)dt$ is the normalization factor with $F(t)$ defined as:

$$F(t) = \frac{e^{-2t/\tau_T}}{\left\{1 + A\left[\mathrm{Ei}\left(-\frac{t+t_a}{\tau_T}\right) - \mathrm{Ei}\left(-\frac{t_a}{\tau_T}\right)\right]\right\}^2 (1 + t/t_a)}, \tag{5.7}$$

where τ_T is the lifetime of the triplet state. Since we wanted to improve the timing around the peak of the waveform, the time constant variable of interest for us is τ_S. Please refer to Ref. [170] for more information on TPB scintillation and definition of other variables such as A and Ei that are outside the scope of this thesis.

Table 5.4 shows the parameters that were found for the recombination model fitted to DEAP ^{39}Ar data along the values we tuned for MC purposes. But these changes were not enough for MC to agree with the data. We also had to make the following changes for TPB and PMT properties:

- Singlet lifetime of TPB, τ_S, was changed from 8.3 ns to 2.2 ns. This was expected since the early analysis in Ref. [169] did not account for the TPB scintillation time, the PMT response time, variations in time of flight, but included them all in the singlet life time.
- Scattering length of TPB was changed from 3 μm to 2.25 μm.
- The transit time between the cathode and anode plates in the PMT was a Gaussian distribution with a mean of 25 ns and a standard deviation of 1 ns. We reduced the σ to 0.6 ns
- To better capture the late and double pulsing in PMTs, we also increased the time between the regular pulse and the late pulse times by 2.2 ns[1].

Table 5.5 shows the cutflow used for choosing ^{39}Ar events in data where we used the sample run with id 18831, often referred to as a golden run. We also generated two sets of MC samples of ^{39}Ar beta decays. One sample was generated using the double-exponential model and the other used the EDR with all of the updated optical parameters mentioned above.

Figure 5.3 shows the waveform for ^{39}Ar samples for a physics run, the two-exponential model, and the new EDR model. With the changes made, we were able to capture the peak distribution of the waveform and the shoulder at around 50 ns caused by the photo

---

[1] These are arrays of probabilities for different delay times ranging from 24 ns to 60 ns. We did not change the probabilities, but rather shifted the distribution by 2.2 ns. This was empirically done to capture the at around 50 ns caused by late and double pulsing.

Variable	Ref. [169] value	MC tuned value
τ_s (ns)	8.2	2.2
τ_t (ns)	75.5	75.5
τ_{rec} (ns)	1445	1445
R_s	0.3	[0.29-0.22]
R_t	0.71	[0.67-0.73]
1 - R_s - R_t	0.06	[0.04-0.05]

Table 5.4: LAr optical parameters used in the recombination model as described by Equation 5.3. We show the parameters that were found by fitting to data from Ref. [169] and values we tuned for our simulations. Note that, unlike the time constants, the weights are energy-dependent and the values in the table show the range of these values in our MC.

electrons back-scattering off the dynode and travelling back and forth inside the PMTs. For these waveforms, we used both MBL and TF2 position for calculating the time-of-flight. As we can see, the TF2 distribution shows a better improvement over the double-exponential model. Since TF2 relies heavily on the timing of the peak distribution, the fitter performance was also improved by the changes we made, as shown Figure 5.4. Note that the waveforms in this figure are Time of Flight (ToF) corrected where ToF is defined as:

$$ToF = \frac{|\vec{PMT_i} - \vec{x}|}{v_g}, \tag{5.8}$$

where $\vec{PMT_i}$ is a vector from the centre of the detector to PMT$_i$, $\vec{x}$ is the position of the event found by either of MBL or TF2, and $v_g = 133$ mm/ns is the group velocity of photons in LAr.

Also, as shown in Figure 5.5, compared to the double-exponential models, the F$_{\text{prompt}}$ variable at different energies matches that of the data better with the EDR model. We have broken the 100-300 qPE region into bins of 20 qPE. Then we calculate the mean and RMS of the F$_{\text{prompt}}$ distribution for events within the given qPE range. Since we have fewer events at higher energies and have less energy dependence, we increase the

Event Selection	Purpose
dtmTrigSrc&0x82 = 0	Non-physics event removal
calcut&0x31f8 = 0	Non-physics event removal
subeventN = 1	Pile-up event removal
numEarlyPulses <= 3	Pile-up event removal
2250 <= eventTime <= 2700	Pile-up event removal
deltaT > 20000	Pile-up event removal
100 <= qPE <= 4000	^{39}Ar energy range
$0.2 < \mathrm{F}_{\mathrm{prompt}} < 0.4$	^{39}Ar $\mathrm{F}_{\mathrm{prompt}}$ range
$\mathrm{MBL}_Z < 550.0$	Events happen below the LAr fill level

Table 5.5: The cutflow used for selecting ^{39}Ar events in data.

energy binning. The x-axis shows the high-end of the qPE window; e.g. events with charge 100-120 qPE are plotted at x=120.

The main challenge in this study was finding the right parameters and their values to match the time response. Tuning the singlet and triplet weights to match the $\mathrm{F}_{\mathrm{prompt}}$ distribution was then an easy task. Once we tuned the timing responses, we tuned the weights using an EIR model to improve our simulations for NR events, such as alpha decays and ^{40}Ar. For NR, we used EIR model as a first step since there are empirical reasons to believe that the EIR model would be able to explain data but there is an ongoing discussions in DEAP to decide if we need an EDR model for NR events as well.

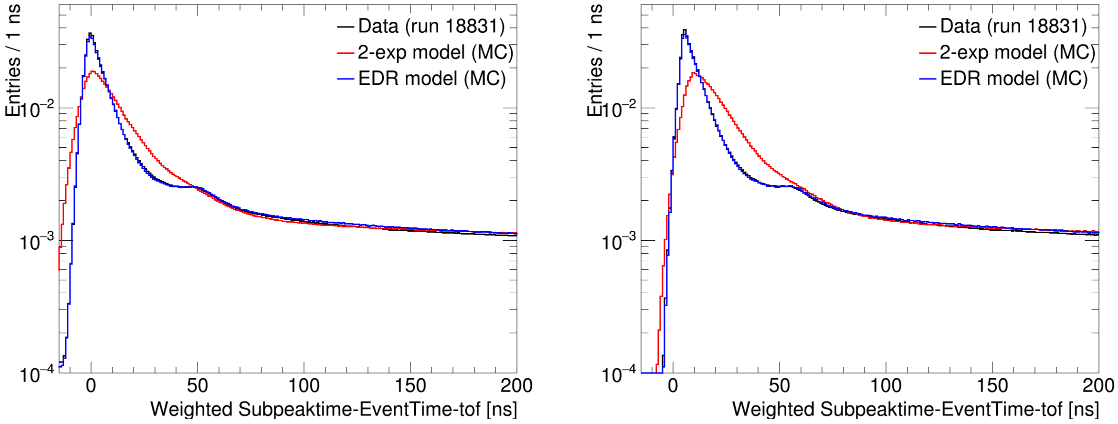

(a) Using MBLikelihood position **(b)** Using TF2 position

Figure 5.3: The waveform of ^{39}Ar obtained from data and those simulated with the double-exponential model and the EDR model. **(a)** shows the waveform using MBL for ToF calculations while **(b)** uses TF2 position. Since the number of events used in each sample could be different, the histograms are scaled such their integral equates to 1 so the shape can be easily. To compare the shapes of the waveforms, they are scaled such that their integral is equal to one.

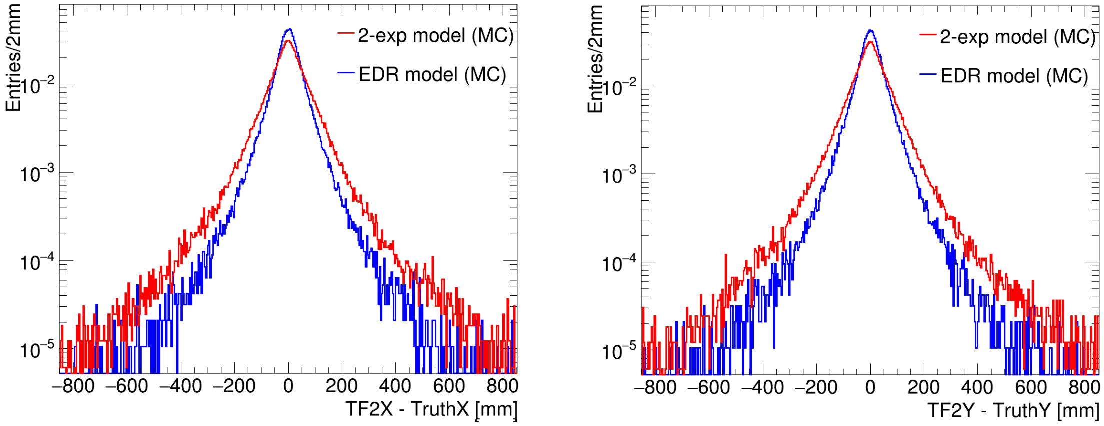

(a) $\mathrm{TF2}_X$ - Truth_X

(b) $\mathrm{TF2}_Y$ - Truth_Y

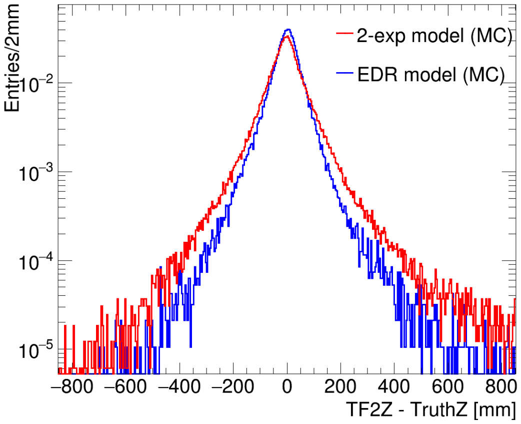

(c) $\mathrm{TF2}_Z$ - Truth_Z

Figure 5.4: The difference between the truth position of events found from MC samples minus the position found by the TF2 algorithm for **(a)** the X position, **(b)** Y position, and **(c)** the Z position. Since the EDR model captures the peak of the waveform better, TF2 also performs better with the updated model.

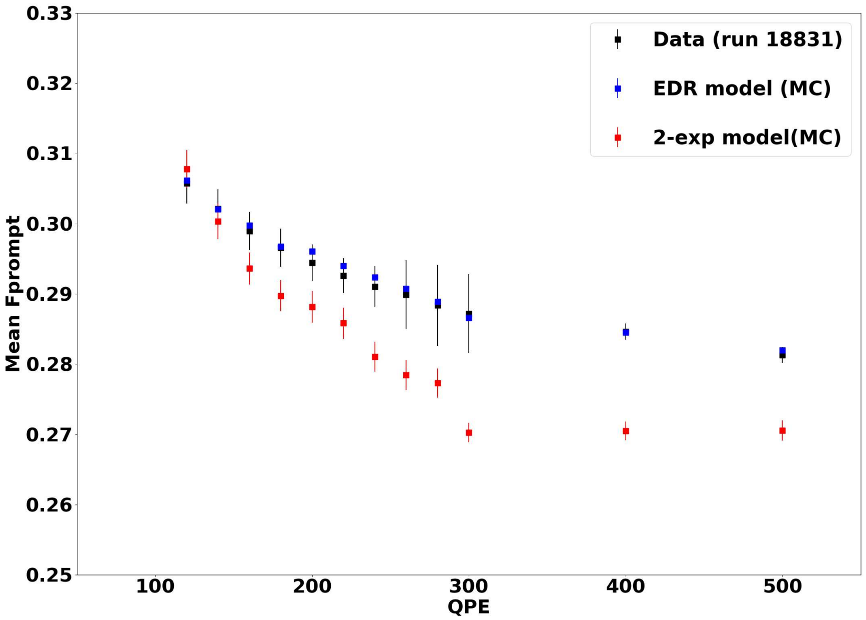

(a) $\mathrm{F_{prompt}}$ vs (low) qPE

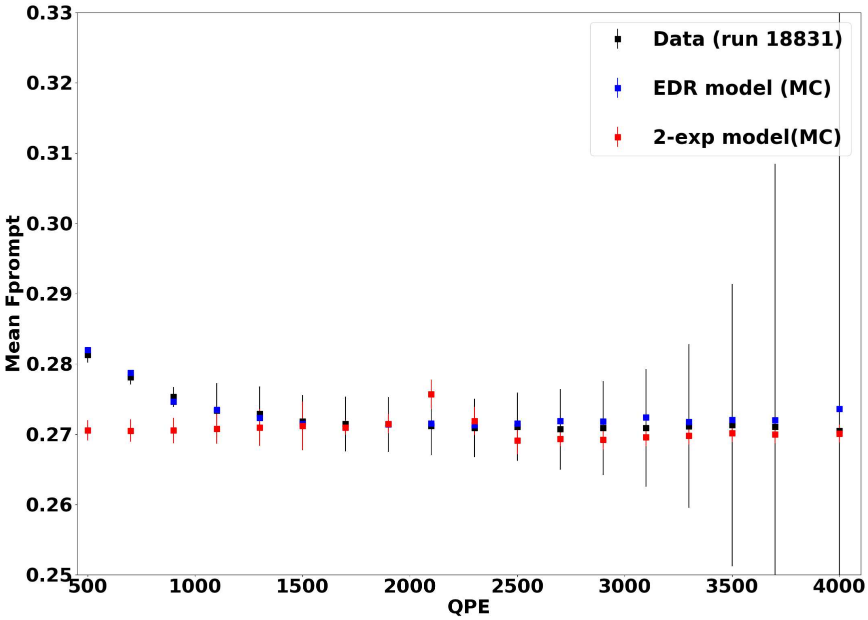

(b) $\mathrm{F_{prompt}}$ vs (high) qPE

Figure 5.5: The mean $\mathrm{F_{prompt}}$ for different qPE energy bins. The error bars are purely statistical. The huge error bars at very high energies are due to lack of statistics at such energies.

5.4 Scintillation Likelihood Processor

During the COVID-19 pandemic, we had to drain the detector but kept the detector running. Analyzing the data with the detector completely filled with GAr revealed something interesting. As can be seen from Figure 5.6 we have a set of events with high F_{prompt} and low energy, qPE<5000. We don't have any physics model implemented in RAT that can explain these events. Cerenkov light is the only high F_{prompt} mechanism that can not generate events in energy more than about 200 qPE. From internal discussions, apparently, similar events were observed during early gas runs and vanished when we ran the detector in a vacuum state.

Similar events were observed in SNO. They were attributed to flashers which are electrostatic discharges inside a PMT, often induced by shaking. Since these events vanished during the vacuum runs, this is not a plausible explanation. But electrostatic discharges inside the detector or the neck region (from static electricity) could look similar and explain the observation of these events. Figure 5.6 shows the full dataset worth 48.5 hours. Note that we have applied the low-level cuts, except the eventTime since these events are not regular scintillation events happening in LAr. We are more interested in the subset of qPE>200, $0.6 < F_{\text{prompt}} < 0.85$ which is near the ROI region. We also require fmaxpe<0.6. The low F_{prompt} high energy events are alpha particles in the GAr and low energy high F_{prompt} are Cherenkov events. The results are shown in Figure 5.7. As we would expect, these events reconstruct near the surface of the detector.

Observing these events gave us the idea of a scintillation likelihood approach, a way to measure how likely the time profile of an event is caused by scintillation in LAr. Not only for discharges events but also other types of events such as neck alphas and neutrons. For each event type, we need to first construct their PDFs.

We describe the time profile of measured scintillation events with the following equa-

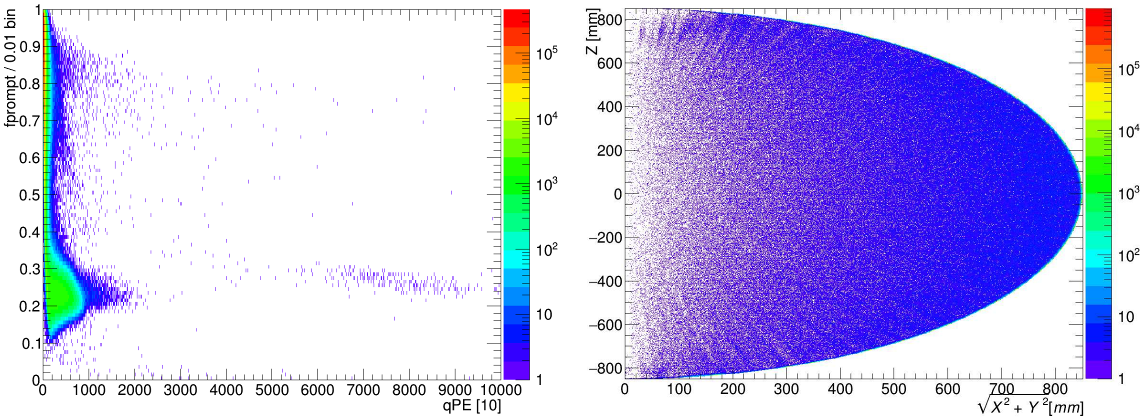

(a) qPE vs $\mathrm{F_{prompt}}$ **(b)** $\sqrt(X^2+Y^2)$ vs Z

Figure 5.6: The **(a)** qPE vs $\mathrm{F_{prompt}}$ and **(b)** event position plot of the events when the detector was filled with GAr.

tion:

$$\begin{aligned} I(t) &= \beta \left(I_{\mathrm{LAr}} * \left(I_{\mathrm{TPB}} * Gauss(0;\sigma_1)\right)\right)(t+t_{\mathrm{offset}}) \\ &\quad + \gamma \left(I_{\mathrm{LAr}} * \left(I_{\mathrm{TPB}} * Gauss(0;\sigma_2)\right)\right)(t+t_{\mathrm{offset}}+t_{\mathrm{delay}})\,. \end{aligned} \tag{5.9}$$

We start with the regular scintillation events, such as ^{39}Ar. We cannot directly use data to construct this PDF, because it has to be used for events with different $\mathrm{F_{prompt}}$ values which would change the shape of the waveform. We will first design a function to simulate the timing response in our detector. Then, we fit this function to our data for which we use low energy ^{39}Ar events[1]. Since our function would have the singlet and triplet ratios as free parameters, we can then interpolate them to construct a new PDF at any given $\mathrm{F_{prompt}}$. Let's start with the LAr scintillation. We can re-write Equation 5.3 as:

$$I_{\mathrm{LAr}}(t) = \frac{R_s}{\tau_s} e^{-t/\tau_s} + \frac{\alpha(1-R_s)}{\left(1+t/\tau_{\mathrm{rec}}\right)^2}\frac{1}{\tau_{\mathrm{rec}}} + \frac{(1-\alpha)\,(1-R_s)}{\tau_t} e^{-t/\tau_t}, \tag{5.10}$$

where we have replaced $1-R_s-R_t$ with αR_t and R_t with $1-R_s$. We have effectively moved the R_t degree of freedom to the new variable α which signifies the portion of the

---

[1] Same cutflow used in Table 5.5, only with limiting qPE<200.

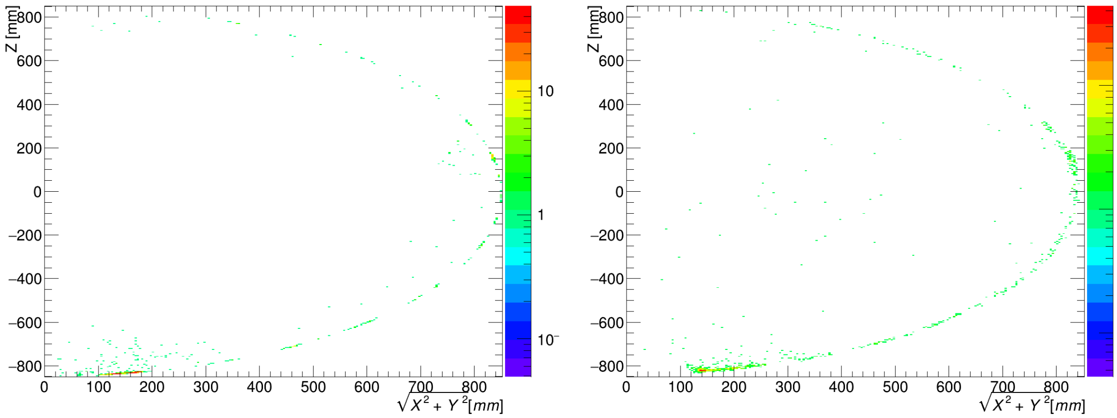

(a) $\sqrt{(X^2+Y^2)}$ vs Z (MBL) **(b)** $\sqrt{(X^2+Y^2)}$ vs Z (TF2)

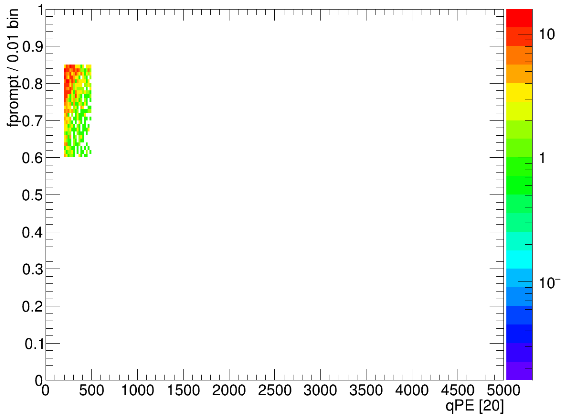

(c) qPE vs $\mathrm{F_{prompt}}$

Figure 5.7: The position plot of the potential discharge events, after applying the cuts, using the **(a)** MBL and **(b)** TF2 fitter. **(c)** shows the qPE vs $\mathrm{F_{prompt}}$.

triplet states that contribute to the recombination term. The second term to consider is TPB short response time:

$$I_{\mathrm{TPB}}(t) = \frac{1}{\tau_S} e^{-t/\tau_S}. \tag{5.11}$$

The last piece is to add a Gaussian distribution which is used to incorporate the time resolution of the PMTs, the uncertainties in the fit-time, differences in ToF in the LG, re-emission time in TPB, and so on. The full-time response would be the convolution of these three functions which we do by integrating over the time domain. Figure 5.8 shows the LAr scintillation time response, convolved with the TPB response, and finally convolved with a Gaussian. This gives us $5 + 1 + 1 = 7$ fit parameters[1].

But as was seen in Figure 5.3, there is a shoulder at around 50-60 ns which is caused by the double and late pulsing in the PMTs. Since these pulses are caused by the same initial photons and not a separate process, we use the same convolution but shift the time in the integrand and also use a separate Gaussian since its standard deviation has to incorporate a wider spread (parameters t_{delay} and σ_2 in Equation 5.9). We then need to sum these two convolutions but each with its own contribution factor, which will add 3 new parameters. We add a last free parameter to allow the function to start at a non-zero time which brings the total free parameters to 11. Figure 5.9 shows the data and our fit. Table 5.6 summarizes the fit variables with their description and the fitted values. Note that the waveform for data was reconstructed using TF2 vertex information.

Parameter	Description	Value
τ_s	Argon Singlet Lifetime	9.206 ± 0.016
τ_t	Argon Triplet Lifetime	1458 ± 0.6
τ_{rec}	Argon Recombination Lifetime	75.5 (fixed)
τ_{S}	Fast TPB Time	2.998 ± 0.016
R_s	Singlet Fraction	0.2157 ± 0.0002
α	Alpha (recombination portion)	0.09529 ± 0.00032
σ_1	First Time Resolution	1.246 ± 0.0009
σ_2	Second Time Resolution	7.147 ± 0.120
t_{delay}	Time Delay	-48.12 ± 0.09
t_{offset}	Time Offset	-0.2662 ± 0.0055
β	Contribution Factor 1	1.917 ± 0.001
γ	Contribution Factor 2	0.006008 ± 0.00056

Table 5.6: The fit parameters, their description and fit values as described by Equation 5.9. All the time constants are in units of ns.

---

[1] 5 parameters come from I_{LAr}, 1 from I_{TPB} and 1 from the Gaussian. We fixed the recombination time constant at $\tau_{\text{rec}} = 75.5$ ns and the mean of the Gaussian set to 0.

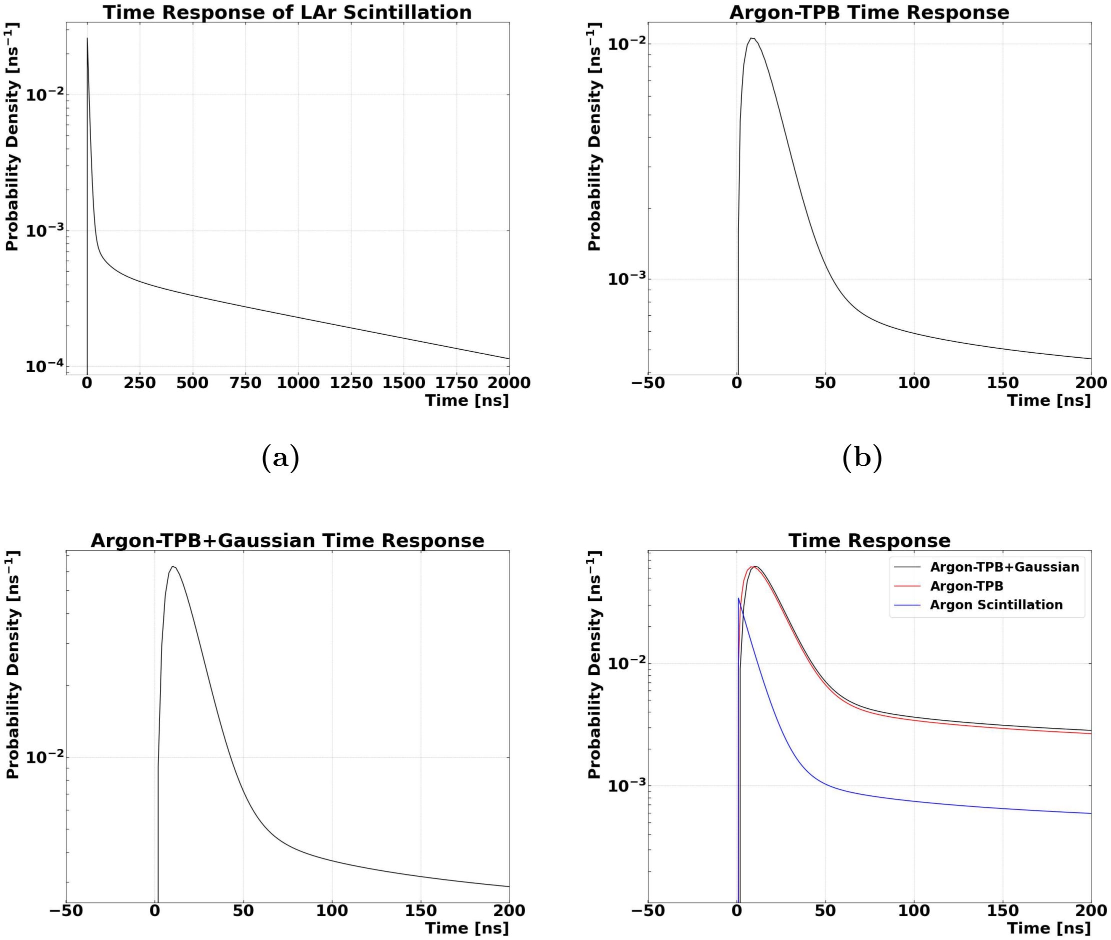

(a) **(b)**

(c) **(d)**

Figure 5.8: The simulated time responses using **(a)** only LAr scintillation, **(b)** LAr scintillation convolved with TPB response, and **(c)** both convolved with a Gaussian function. For a better comparison **(d)** shows all three within the same time window. The mean of the Gaussian is 0 and the standard deviation used here was set 5 to magnify the effect.

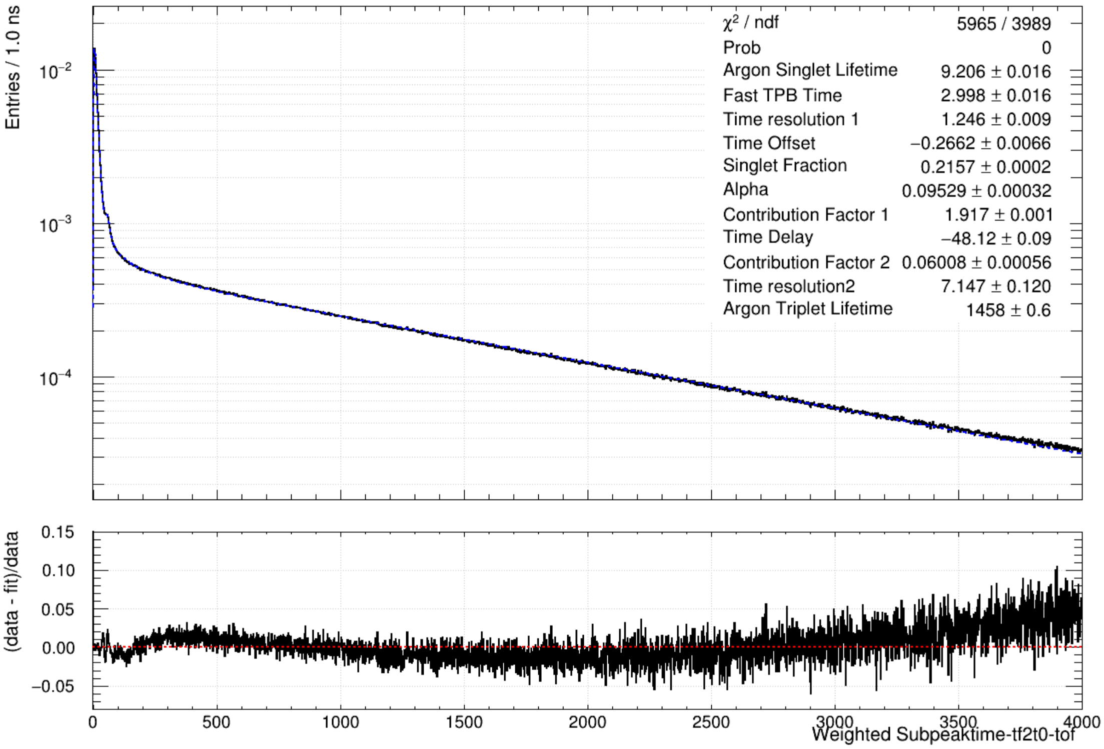

Figure 5.9: ^{39}Ar waveform and the fitted time-response function using the physics data.

We have three more PDFs, shown in Figure 5.10 along with the Argon-TPB response. These PDFs are data-driven and not analytical or based on MC. The three PDFs are as follows:

- Flash: Fast pulses, based on Cerenkov distributions using the AmBe source.
- Neck: Regular physics runs with no external source where we take events with significant charge in the neck region with a modest amount of charge in the detector.
- Neutron: Neutron time distribution, measured with the AmBe source.

Recall that the Argon-TPB response shown here is using ^{39}Ar singlet and triplet ratios. But for each event, we calculate the singlet and triplet factors based on the F_{prompt} value of the event. For each event then, we compare its waveform to the four PDFs we have and calculate their log-likelihood, along with a few other variables. The goal is to identify events that do not look like a regular scintillation in the LAr.

Note that the timing improvements achieved in MC will make the scintillation likelihood processor more reliable when comparing data to MC. Have we had wider-than-data waveforms, it would have made it harder to study the performance of this processor.

We did not come up with any direct cut on any variable from this processor that would improve our results. But there is a Multi-Variable Analysis (MVA) under development by the DEAP collaboration where the scintillation likelihood probability is used and among the top 10 most influential parameters for the machine learning model.

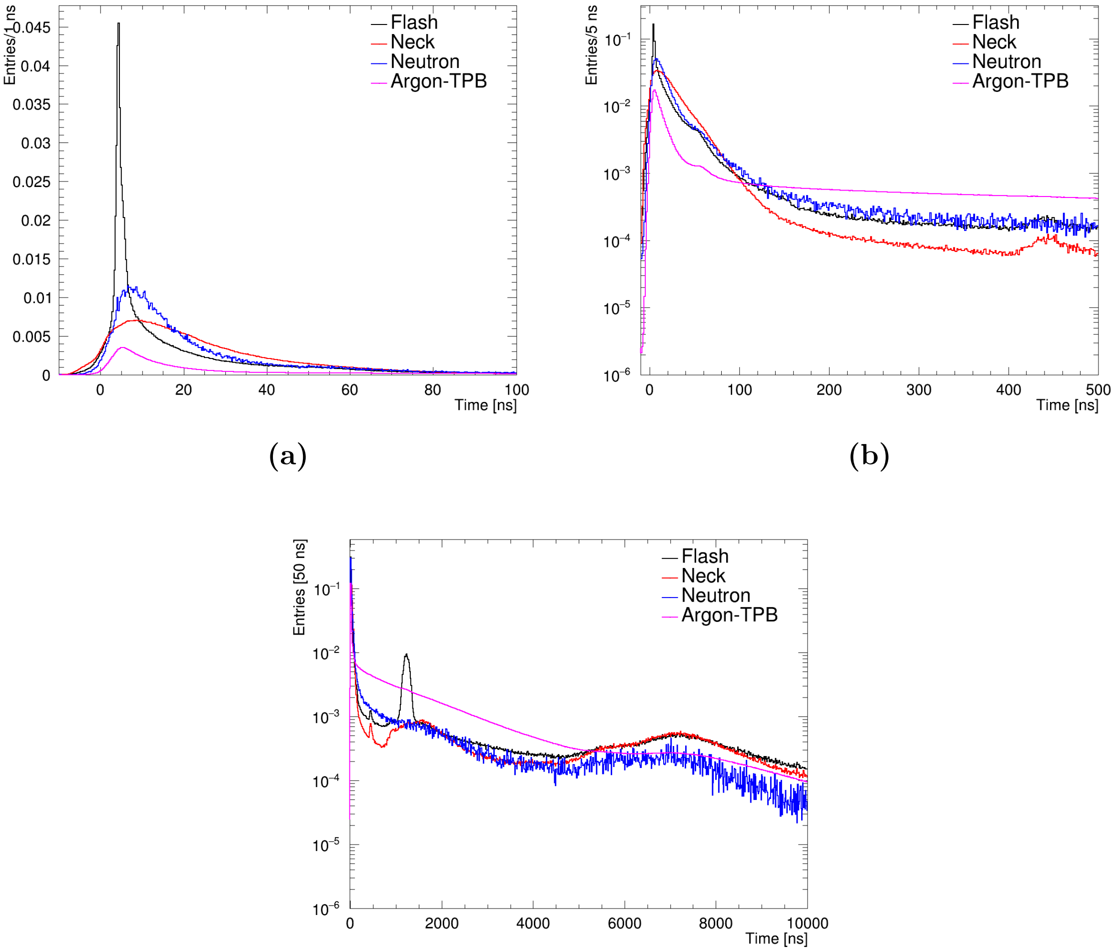

(a)

(b)

(c)

Figure 5.10: All four PDFs used in the scintillation-likelihood processor. **(a)** shows the PDFs in linear-scale and up to 100 ns with bin width of 1 ns, **(b)** shows them in the log-scale and up to 500 ns in bin width of 5 ns, and **(c)** shows them in log-scale for the full 10 μs in bin width of 50 ns. Note that the Argon-TPB PDF shown here uses ^{39}Ar singlet and triplet factors, hence the lower prompt peak compared to other PDFs.

5.5 Late Light and PMT Saturation

Most of the studies done in DEAP, MC in particular, concentrate mainly on low-energy events, since those are the events near the ROI and are of more interest and concern to us. But high energy events are often used to make sure our background models and optical properties implemented in MC can properly explain the observed data. But as we observe around 60 photons strike a PMT within approximately 15 ns we encounter PMT saturation. When a PMT overflows with too many photons over a short time, it can create a nonlinear response in the PMTs, which is proportional to the charge [155]. This dead time will cause the PMT to not register a portion of the charge and we get the wrong amount of charge for the event. Another possible outcome is that if a PMT is hit by too many photons over a very short time, the digitizer will clip and not register the full charge. The clipping is simulated in DEAP but simulating the saturation proved harder to implement. Instead, the collaboration designed a processor called Pulse-Level Saturation Correction (PLSC). The purpose of this processor is to figure out if a saturation has happened in a given PMT and also measure the missing amount of charge and add this missing amount of charge. Although this processor made great corrections, which we will discuss shortly, there is one issue with using it for some studies. We still have the degree of freedom regarding how much charge we want to add; i.e. the peak of the given isotope need to be predetermined. Since we would be proposing a method that does not rely on an arbitrary correction of data, we won't get into the details of how this processor works. But we should note that the PLSC works as intended on data, but simulating the effect of saturation is harder and this processor was not tuned to work on MC. For more information about this processor, see Ref. [171].

The three isotopes that are present in our detector make the direct study of this phenomenon possible. Table 5.7 shows these isotopes and the energy of their α decay. For this study, we will analyze two sets of data and two sets of MC samples. The data we use are physics run without any external source but reprocessed with two different versions of RAT. One dataset uses data processed with RAT version 5.11 and the other dataset uses reprocessed data with RAT version 5.14. The main difference between the two versions is the implementation of PLSC in version 5.14. For clarification, we use data_5.11 and data_5.14 when referring to these two sets of data. The two MC samples are both the simulation of the three isotopes ^{222}Rn, ^{218}Po, and ^{214}Po within the LAr, but with different settings. One MC set of samples will disable the effect of clipping, which would be the ideal case since the PMTs would not get overwhelmed and properly record all the charges, although it would not be a realistic scenario. In these samples, since there is no clipping, there is also no need for enabling the saturation correction. In the second set of MC samples, we enable the effect of clipping but not the saturation correction. We will refer to these MC samples as MC_on_off and MC_off_off, respectively. The first on/off refers to whether the clipping effect was simulated or not and the second part refers to whether the saturation corrected was included in the simulation or not, which for both sets is not included.

Particle	α Energy (keV)
^{222}Rn	5489.48
^{218}Po	6002.55
^{214}Po	7686.82

Table 5.7: The alpha energy of the three main isotopes used in our study. The decay mode of ^{222}Rn and ^{214}Po are 100% to an α daughter particle. α decay of ^{218}Po is at 99.98%. All data is taken from NNDC database.

Figure 5.11 shows the qPE vs. F$_{\text{prompt}}$ data using the two different versions[1]. The three alpha lines are clearly visible here which from left to right are ^{222}Rn, ^{218}Po, and ^{214}Po. The alpha coming from Rn has an energy of 5489 keV which with a LY of approximately 7.3 photons/keV$_{ee}$ and Quenching Factor (QF) of 0.75, it would translate to a qPE of 30,000. As we can see in the data with RAT version 5.11, the events near the centre of the detector show the same amount of charge, but as we get closer to the

---

[1] Note that for this study we have only used the high F$_{\text{prompt}}$ data which requires F$_{\text{prompt}}$ > 0.55

surface, the huge amount of prompt charge will saturate the nearby PMTs and register the wrong qPE. Since this charge is in the prompt light, it will affect the F_{prompt} as well. The PLSC implemented in version 5.14 fixes this issue and the three alpha lines are straight as expected with the F_{prompt} also fixed. Note that in this study we will be using qPE and F_{prompt} as our main variable of study.

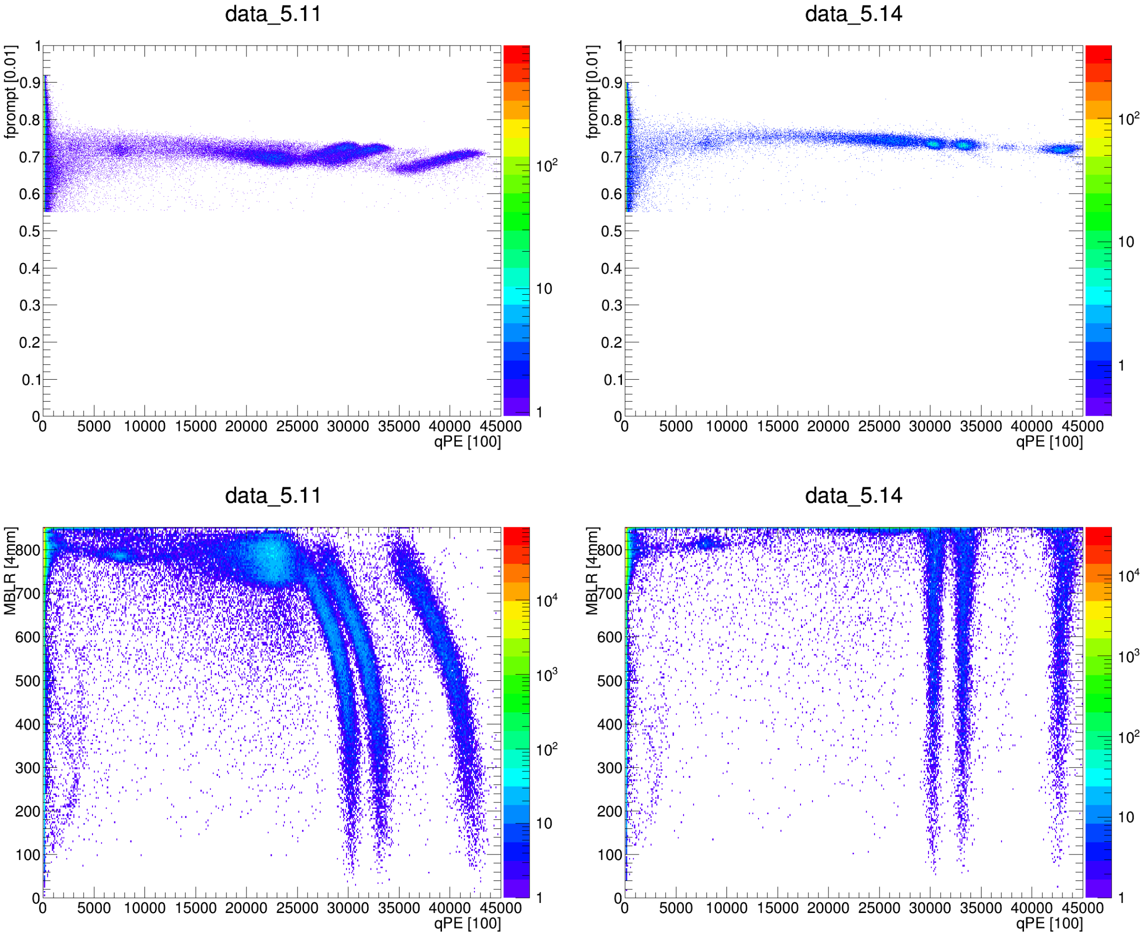

Figure 5.11: The distribution of qPE-F_{prompt} and qPE-MBLR for physics data processed with two different RAT versions; 5.11 and 5.14. The three alpha lines starting at 30,000 qPE from left to right are ^{222}Rn, ^{218}Po, and ^{214}Po. Due to the effects of saturation and clipping, 5.11 shows curved lines caused by missing charges for events near the surface. Data processed with 5.14 corrects this missing charge and forms straight lines. The bulb around 20,000 to 25,000 are the ^{210}Po events.

Figure 5.12 shows the qPE vs F_{prompt} and qPE vs MBLR, similar to what we showed for data. As discussed earlier, the ideal MC sample is the off_off setting where the

PMTs don't get clipped and can record the full qPE, hence the correct F_{prompt} values and straight lines in the qPE-MBLR plot. If we turn the clipping on, we start seeing the MC looking like data. Note that even in our ideal setting of clipping turned off, the nSCBayes vs. MBLR cannot reconstruct the straight lines we expect. We will come back to this point when we talk about alpha quenching factors.

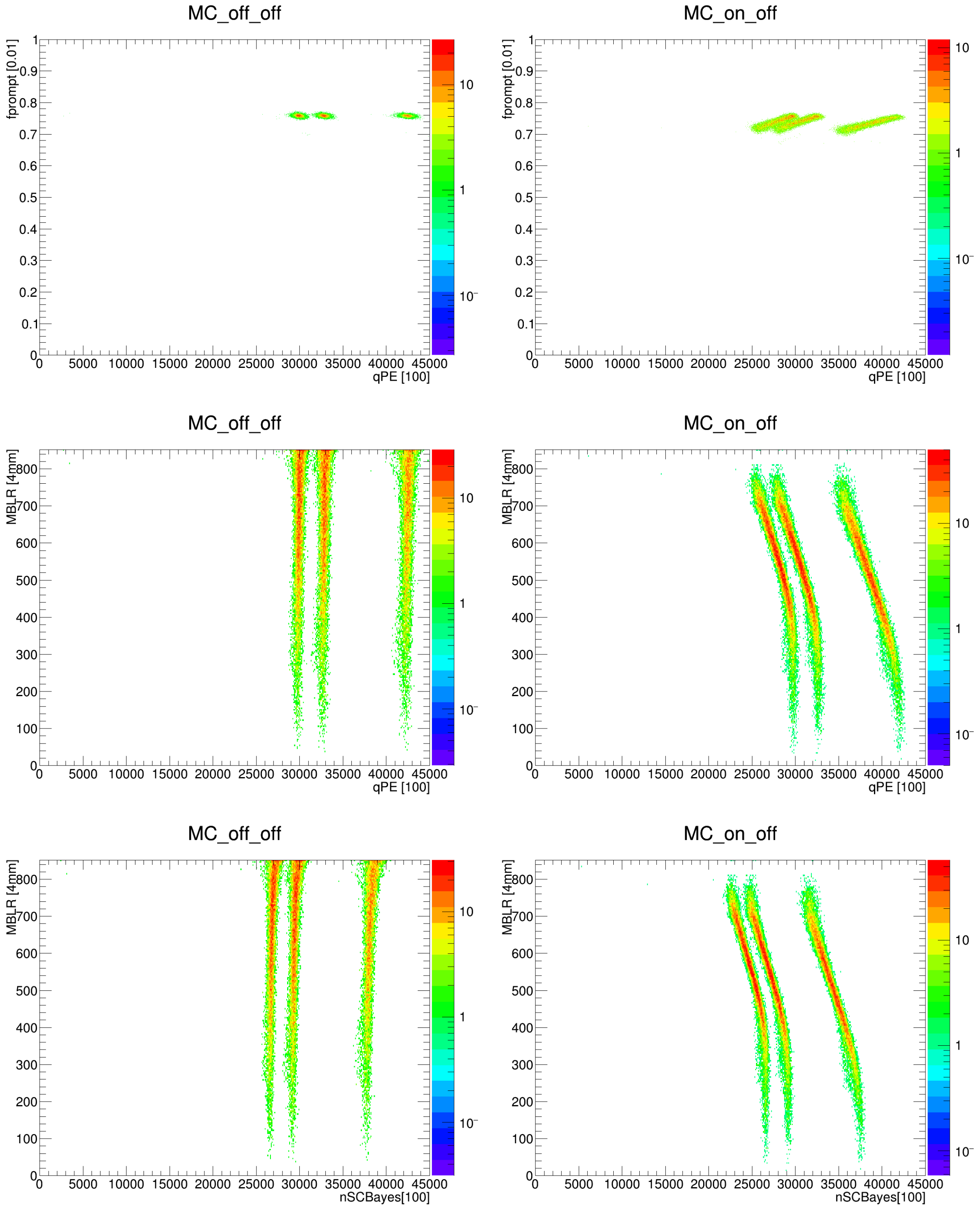

Figure 5.12: qPE vs. F_{prompt} and qPE vs. MBLR for our two sets of MC with off_off setting and on_off. We have also included nSCBayes vs. MBLR for comparison.

5.6 Use of Late Light in DEAP-3600

So far, we have used the full qPE of the event to show the effect of saturation. Since these are NR events, most of the charge is prompt light. Even if we take the lowest alpha line and $F_{\text{prompt}} = 0.7$, we get more than 21,000 qPE hitting the PMTs in a span of about 170 ns. Given these events have very high energies and cause PMT clipping and saturation, instead, we propose using a charge integration that skips the prompt portion of the light. We will refer to this as late light.

First, we need to find the proper integration window. For this, we keep the upper bound of integration fixed at 10 μs but use five different starting times for the lower bound of integration. The five lower bounds of integration are 50, 100, 150, 200, and 250 ns. We will keep using the position vertex found by MBL that uses the full charge information.

Let's first look at our ideal MC samples; i.e. clipping turned off. Figure 5.13 shows the late light qPE vs. MBLR using different lower bounds for charge integration. The numbers on the x-axis highlight the lower bound of charge integration. As expected, with all the different lower bounds, the three alpha lines are straight and distinguishable. Figure 5.14 shows the same plots but with the second MC set of samples where the clipping effect is simulated. We can see that by using late light, we can recover the three straight alpha lines. Lastly, we apply the same procedure to our data, shown in Figure 5.15. Note that we have to use RAT version 5.11 to make sure the artificial correction is not applied to the data. As can be seen, even a lower bound of 50 ns significantly improves the shape of the alpha lines, albeit a very small curvature is still visible. But a lower bound of 200 ns shows an almost perfectly straight line. From now on, late light will refer to the qPE integrated over 200 ns to 10 μs. The same procedure was applied to data with RAT version 5.14, shown in Figure B.1.

Although we had mentioned that nSCBayes is usually the preferred variable, it is tuned toward low-energy events and in these high-energy regions, it cannot be trusted. Figure B.2, Figure B.3, Figure B.4, and Figure B.5 in Appendix B show the MBL reconstructed radius versus late nSCBayes for all four samples. As can be seen, even in the ideal detector setting, the clipping effect turned off, the nSCBayes variable is not capable of reproducing the three alpha lines as straight lines. The same effect is also visible in Figure 5.12 where we had used the full energy of the event. Moreover, although the late light qPE was capable to reproduce the three alpha lines in all four samples, nSCBayes fails in all four samples, especially in data. Now that we have identified a proper integration window for using late light, we can use this information for two separate studies; an MBL position fitter for high energy events and studying the QF.

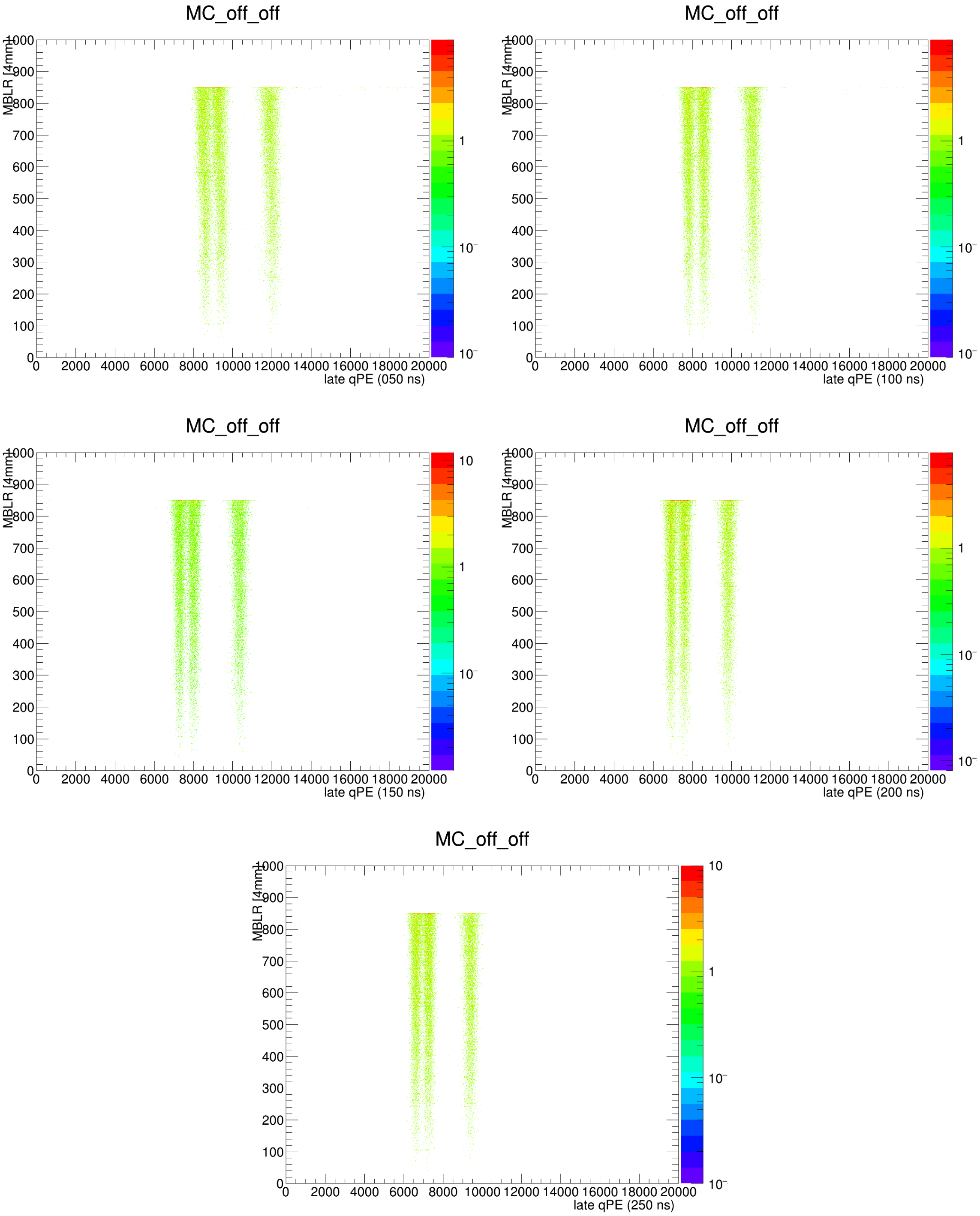

Figure 5.13: Late light qPE vs. MBLR using different lower bounds (50, 100, 150, 200, and 250 ns) for charge integration. The fact that the time windows below 200 ns are wider implies this cut does not remove all saturation. This is the MC samples with both clipping and PLSC turned off.

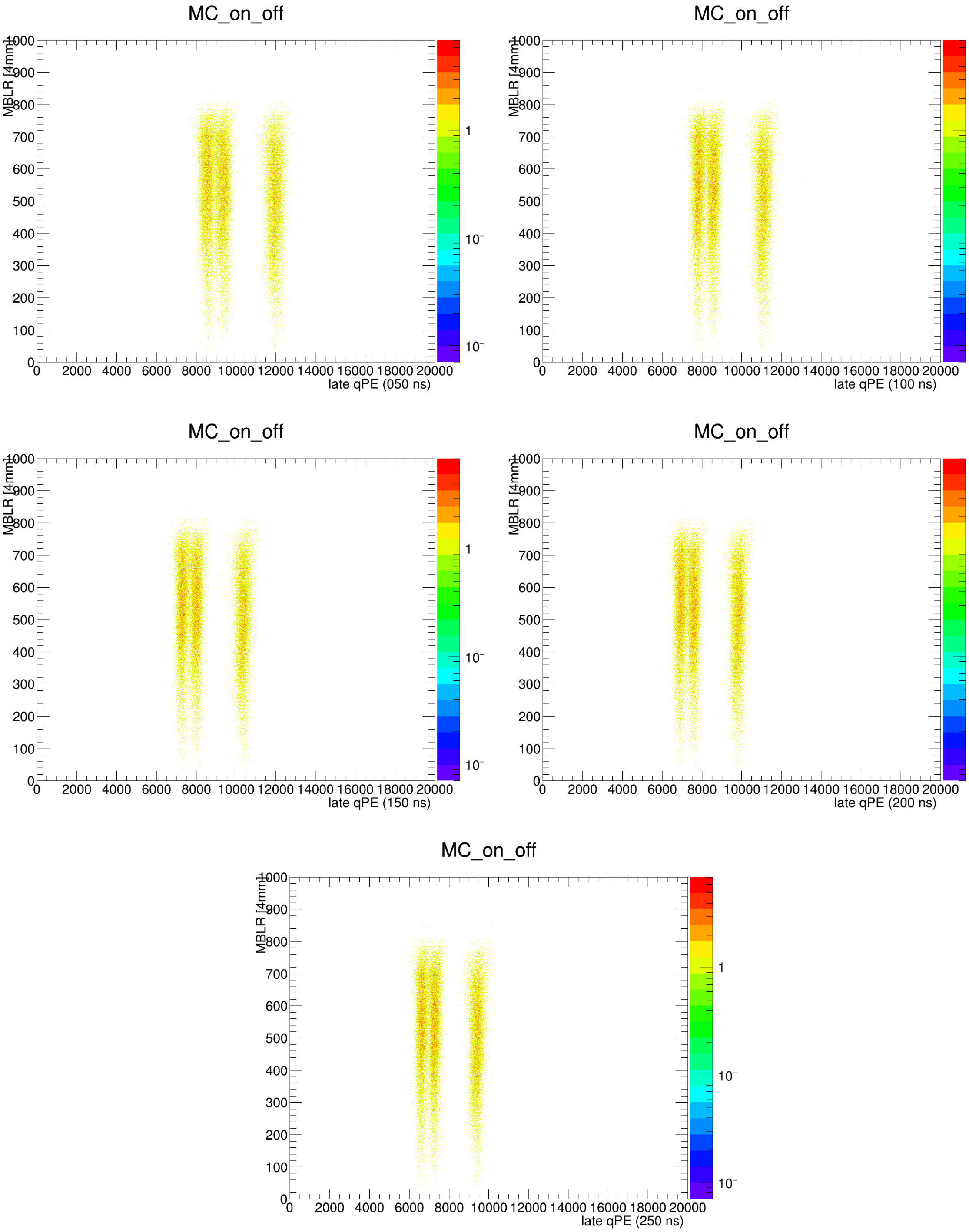

Figure 5.14: Late light qPE vs. MBLR using different lower bounds for charge integration. This is the MC sample with clipping enabled but PLSC disabled.

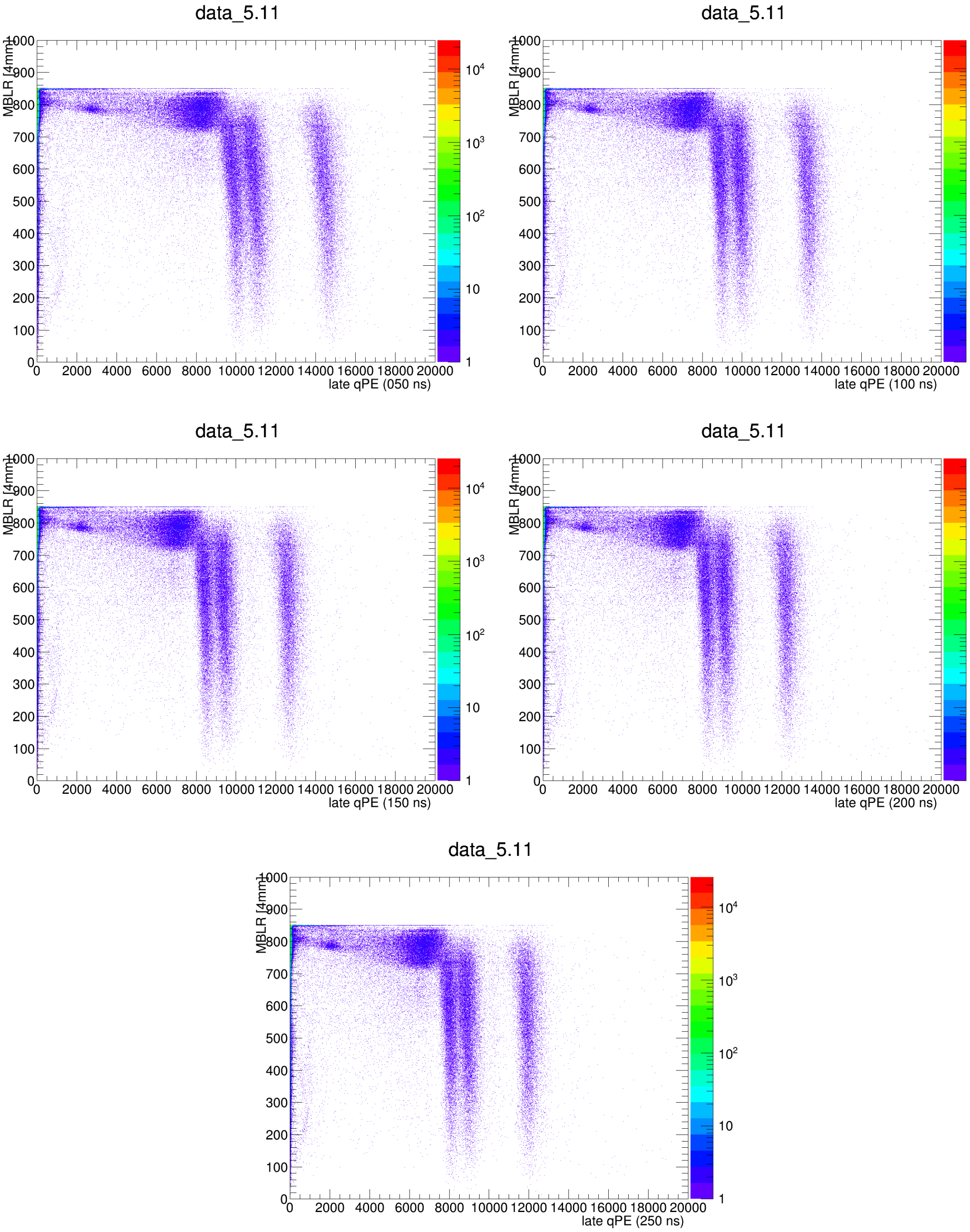

Figure 5.15: Late light qPE vs. MBLR with different lower bounds for charge integration. This is data with rat version 5.11 which does not include PLSC.

5.6.1 Late Light MBL

As mentioned earlier, in DEAP we still have trouble simulating the full effects of clipping and saturation correction. But these effects become important at higher energies. Since the ROI is around qPE$<$ 200, we often sacrifice higher energy event reconstruction to get the backgrounds near the ROI as perfect as possible. In our latest MC models, we tuned some parameters with the assumption of no clipping in the MC to better explain our data at lower energies. But when studying surface alpha events, we realized that MBL position resolution has significantly improved which is not surprising. If we turn the clipping effect off, the nearest PMTs to the event location can record a very high charge without getting clipped which makes it easier for the MBL to reconstruct the event near the surface of the detector. In fact, studying the miss-reconstruction of surface events was the purpose of our study which will be covered in the next section as it is a major portion of our contribution to the DEAP collaboration. However, the non-realistic position resolution of the MBL gave us the idea of using late light. This way, the MC simulation and the position resolution will not be dependent on the simulation settings.

The regular MBL uses the charge information from -28 ns to 10 μs to find the position vertex. Based on the discussion above, we implemented a separate version of MBL, referred to as late light MBL, that uses the charge information from 200 ns to 10 μs. This way, the fitter is safe from the effects of PMT clipping and saturation. Since MBL only uses charge information and does not rely on timing information, removing a portion of the pulse in each PMT will not skew the fitter.

To study this new version of MBL, we simulated full energy ^{210}Po surface samples with two detector settings. One sample uses both clipping and saturation correction disabled while the other sample has both effects simulated. Since these are MC samples and we have access to their true position, we can easily measure the position resolution by plotting the difference between each component of the fitted position vertex and the true position. Figure 5.16 shows the three position components fitted by the two versions of MBL while Figure 5.17 shows the difference in the fitted radius. The latter is of importance for our discussion of leaking surface events. When the clipping is turned off and we have access to all the charge information, the regular MBL performs similarly to the late light MBL. But when we enable the clipping and saturation correction, our new fitter performance is not affected much and performs better. This is another proof of the reliability of using late-light information for high-energy events. Table 5.8 summarized the position resolution of these two fitters as measured by the difference between the truth MC position and the fitted position. The position resolution is measured by the RMS of the histograms.

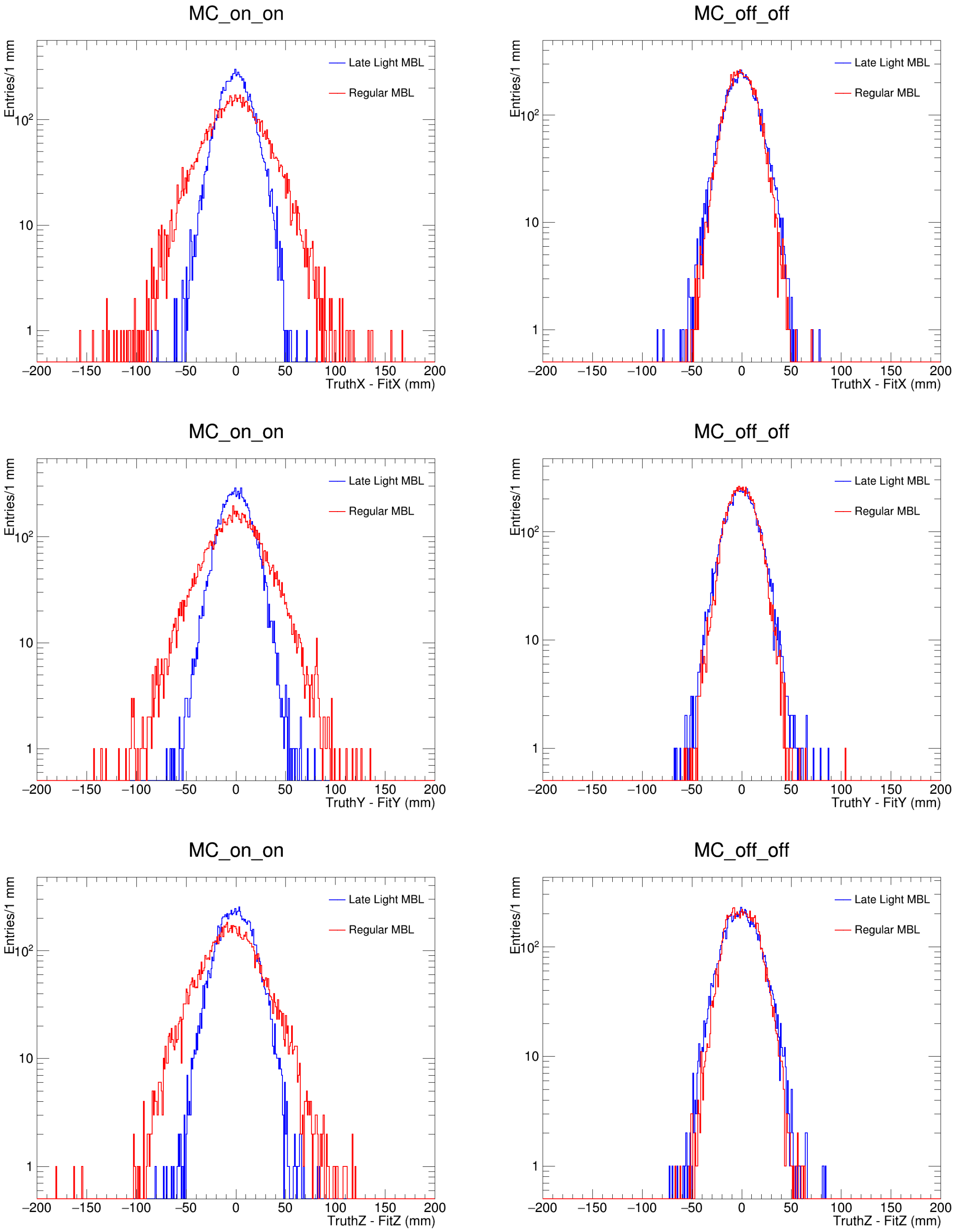

Figure 5.16: Truth position minus regular MBL (red) and late light MBL (blue) using the MC sample. The left column is with clipping and PLSC both enabled and the right column is with both processors disabled. Row 1 to 3 are the X, Y, and Z positions.

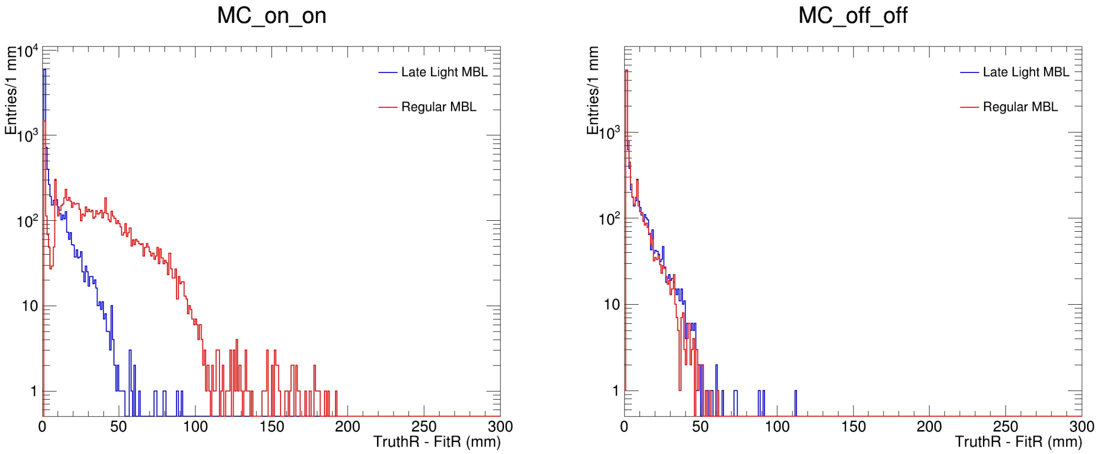

Figure 5.17: Truth radius minus the fitted radius found by the regular MBL (red) and late light MBL (blue).

Sample Setting	Regular MBL(X/Y/Z/R) RMS [mm]	Late Light MBL(X/Y/Z/R) RMS [mm]
MC_off_off	13.8-13.6-15.2-6.7	15.2-15.2-16.8-7.9
MC_on_on	28.2-27.8-27.3-26.1	15.1-15.2-16.8-7.8

Table 5.8: Position resolution of regular MBL and late light MBL for X, Y, Z, and R, variables measured as the RMS of their corresponding histograms.

5.6.2 Alpha Quenching Factors

The more important study that can make use of the late light is measuring the QF in our detector. As we discussed earlier, three sources can contribute to quenching which reduces the observed LY in a noble liquid. When there is an elastic interaction between a noble liquid atomic nucleus and a neutron or WIMP, the recoiling nucleus collides with electrons and nuclei within the detector and loses its energy. This loss of energy happens in two forms; energy transfer to atomic electrons and the kinetic energy of atoms, translational motion. The total rate of energy loss of the recoiling nucleus per unit of distance, dE/dx, is called the stopping power and depends on the medium it is travelling through. The total stopping power, at low energies, is the sum of electronic and nuclear stopping power. The electronic stopping power is the amount of energy lost per unit distance by the recoiling nucleus as a result of electronic excitation and ionization of the noble liquid atoms around it. The nuclear stopping power is defined as the energy loss per unit length caused by atomic collisions that contribute to the kinetic energy (thermal motion) of noble liquid atoms but do not result in internal atom excitation. The ratio of electronic to nuclear stopping power is determined by the recoil energy of the nucleus. At high energies, the electronic stopping power is the dominant form while at lower energies the nuclear stopping power would become the dominant contributor [172].

Assuming that the recoiling nucleus will lose all of its energy within the detector, we can write the total energy loss as [172]:

$$E_R = \eta\left(E_R\right) + \nu\left(E_R\right), \tag{5.12}$$

where η and ν are both a function of the recoil energy E_R and represent the energy losses due to electronic stopping power and nuclear stopping power, respectively. Because only a fraction of the energy lost in electronic excitation or ionization results in the formation of excitons and electron-ion pairs in noble liquids, we can define an ionization energy reduction factor caused by energy losses due to the nuclear stopping power as:

$$f_n\left(E_R\right) \equiv \frac{\eta\left(E_R\right)}{E_R} = \frac{\eta\left(E_R\right)}{\eta\left(E_R\right) + \nu\left(E_R\right)}. \tag{5.13}$$

Since the total stopping power is:

$$\left(\frac{dE}{dx}\right)_{\text{tot}} = \left(\frac{dE}{dx}\right)_{\text{elec}} + \left(\frac{dE}{dx}\right)_{\text{nucl}} \tag{5.14}$$

$f_n\left(E_R\right)$ can be calculated by:

$$f_n\left(E_R\right) = \frac{\int_0^{E_R} (dE/dx)_{\text{elec}} dE}{\int_0^{E_R} \left((dE/dx)_{\text{elec}} + (dE/dx)_{\text{nucl}}\ \right) dE}. \tag{5.15}$$

The integrals above should be computed for each possible recoil energy to represent f_n as a function of recoil energy. Lindhard et al. represented f_n as [172]:

$$f_n = \frac{kg(\varepsilon)}{1 + kg(\varepsilon)}, \tag{5.16}$$

where given a nucleus with atomic number Z, $\varepsilon = 11.5\, E_R\,(keV)\, Z^{-7/3}$, $k = 0.133 Z^{2/3} A^{-1/2}$ where A is the atomic mass, and $g(\varepsilon)$ can be fitted by $g(\varepsilon) = 3\varepsilon^{0.15} + 0.7\varepsilon^{0.6} + \varepsilon$. f_n is often referred to as Lindhard QF.

Two other factors can contribute to the quenching, especially at high ionization density. The bi-excitonic quenching happens when two excited atoms collide with each other before they can form the excimer. This process will prevent the excimer to form by creating an argon in the ground state plus an electron-ion pair ($Ar^* + Ar^* \rightarrow Ar + Ar^+ + e^-$) [129]. Penning ionization is a similar process where two excimers, before emitting the VUV photons, collide with each other and create two ground state argon atoms, an ionized dimer, and an electron ($Ar_2^* + Ar_2^* \rightarrow 2Ar + Ar_2^+ + e^-$) [137]. These two processes are described by the Birk's saturation law that shows the specific fluorescence can be written as [173]:

$$\frac{dS}{dx} = \frac{A\frac{dE}{dx}}{1 + kB\frac{dE}{dx}}, \tag{5.17}$$

where kB is the Birk's constant. A is a proportionality constant representing the fact that the number of excitons and electron-ion pairs created per unit distance is proportional to dE/dx [174]. From Equation 5.17, we can define a quenching factor as [175]:

$$f_l = \frac{1}{1 + kB\frac{dE}{dx}}, \tag{5.18}$$

that is related to nuclear recoil's electronic stopping power dE/dx. So, as suggested by Ref. [175], we can write the total QF as:

$$q_f = f_n \times f_l, \tag{5.19}$$

with the Birk's constant for liquid argon found to be $kB = 7.4 \times 10^{-4} \mathrm{MeV}^{-1}\mathrm{gcm}^{-2}$ [175].

The three alpha lines we have in DEAP enable us to study the QF and check the value of Birk's constant using DEAP data. Another importance of this study is that a different set of QFs can affect our background model of dust particulates.

To find the QF, we need to find the peak energy of each of the three alpha lines. Knowing the initial energy of the emitted alpha, we know how much charge we should theoretically observe in our data. Given that the quenching will reduce the observed amount, the ratio of the two will give us the QF. There was an internal study made by David Gallacher[1] where he used the full energy of the events and also relied on PLSC data, and MC for validation, to find the peak energy of the alpha. To explain our data, they had to fit the Birk's constant and found that $kB = 1.699 \times 10^{-4}\text{MeV}^{-1}$ g cm^{-2} with A also as a free fit parameter and found $A = 0.859$. That study also showed that the fit performed better when using nSCBayes instead of qPE. As we argued earlier, using nSCBayes and full energy information while relying on PLSC both can be bad choices. Although, at the time of writing this thesis, there is another ongoing study that does not rely on PLSC. In that study, our other members are trying to still use the full energy events but using data without any correction and instead use the events that are closer to the centre of the detector and possibly safe from clipping and PMT saturation. But as can be seen from Figure 5.11, the ^{214}Po line, our highest energy alpha line, starts curving at around 300 mm. This is assuming that events near the centre have absolutely no saturation, which is not true since saturation starts at around 60 PE and we have 255 PMTs which translates to events with energies around 15,000 qPE. It could be that events near the centre suffer from relatively the same amount of saturation and no curvature is visible for those events. Instead, we propose using the late light which is much safer from saturation. Although the same argument could be made that we cannot be sure there is no saturation happening, we believe it would be a safer assumption in our case. Figure 5.18 shows the fitted Birk's constant from the first study done by DEAP, where the red triangles represent DEAP alpha energies.

---

[1] He is a former graduate student with DEAP collaboration.

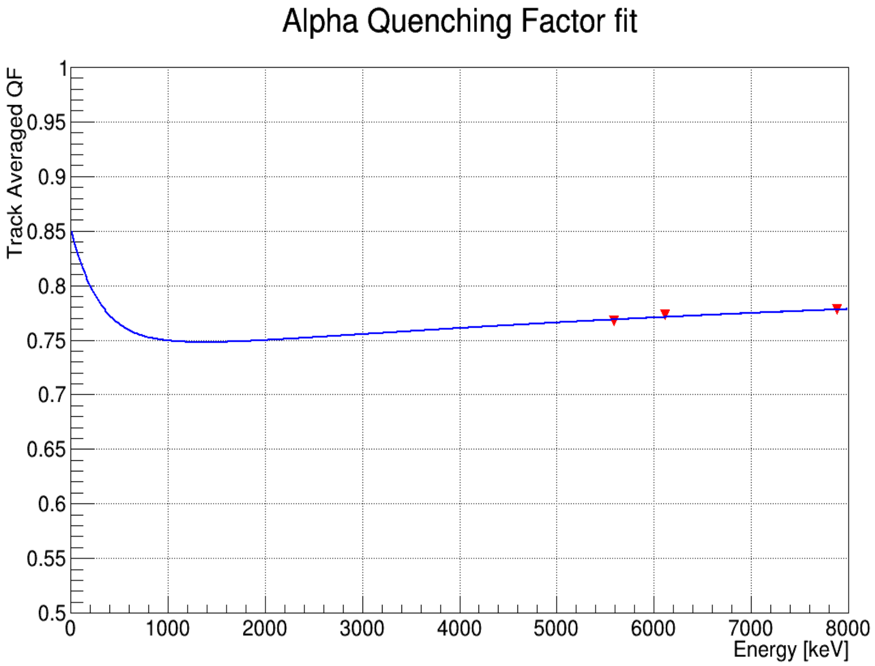

Figure 5.18: Alpha quenching factors found by DEAP collaboration based on nSCBayes and full energy events using DEAP data corrected with the PLSC. Image courtesy of David Gallacher.

Late Light & Quenching Factors

The general definition of quenching factors and light yield were discussed in section 4.3. Let's first take a look at the quenching factors found in previous studies. Figure 5.19 shows the electronic stopping power and the Lindhard nuclear quenching factor calculated by SRIM [176], and the scintillation quenching factor relating scintillation photons to ionization using Birk's law. We have interpolated the stopping power and Lindhard QF for integration purposes. Also, note that Equation 5.18 is the QF at any given energy; i.e. instantaneous QF. Since in data we do not have access to the information of the recoiling nucleus at every step, we have to use a track averaged QF which, at a given staring energy E_0, it is simply the integral of the instantaneous QF from zero to E_0. Something to keep in mind is the curvature seen in Figure 5.19, lower plot, for energies between 5 to 8 MeV compared to the flatness observed in the previous study done by DEAP collaboration shown in Figure 5.18.

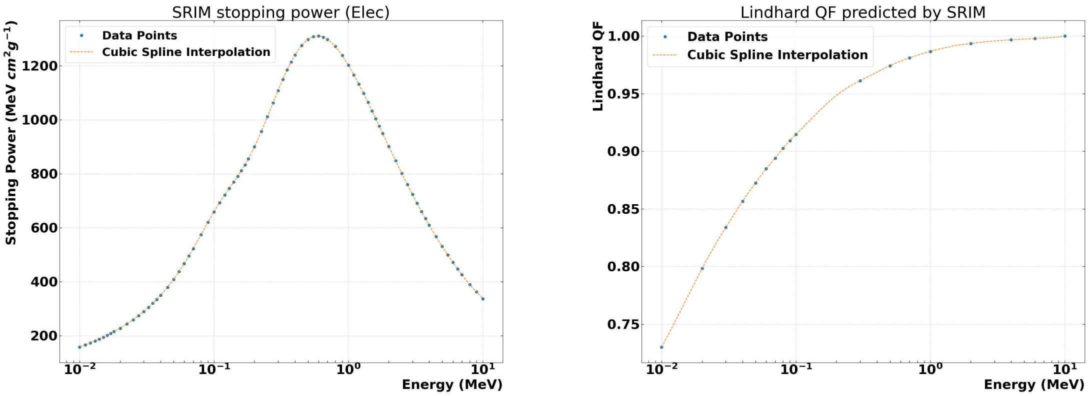

(a) SRIM stopping power

(b) Lindhard QF

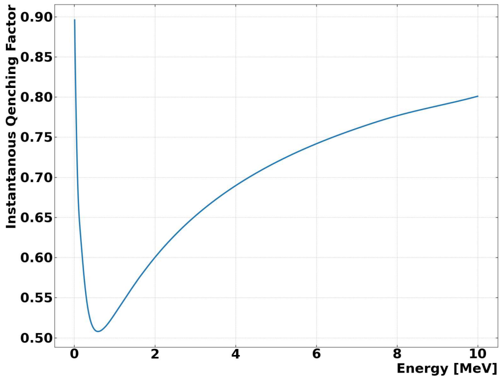

(c) Birk's QF

Figure 5.19: **(a)** the SRIM electronic stopping power, **(b)** Lindhard quenching factors from SRIM, and **(c)** the QF using Birk's law, both instantaneous and track averaged, with a Birk's constant of $kB = 7.4 \times 10^{-4}$ MeV^{-1} g cm^{-2} as a function of energy.

Next, we need to find the peak energy of the three alpha lines and see if they agree with the literature-accepted value of kB. As a reminder, the late light in our study refers to the charge integration over a time window of 200 ns to 10 μs. This makes our charge calculation far away from the peak of the distribution and safe from saturation. First, we need to measure the qPE peak of each alpha line. For this purpose, we fit a Gaussian to the qPE distribution of each alpha line to get the peak value of the qPE. We don't do a full MBLR projection, but rather use three different radius slices: [0-450] mm, [150-600] mm, and [0-650] mm. Although the lines are straight all the way to 800 mm, we will not go above 650 mm to be away from events too close to the surface.

Although we are more interested in studying the data, we include MC samples as a sanity check of our method of study. But note that energies in data and MC for late light could be different since the MC is based on a prior study that has updated the QF values used in our simulations. The results of the fit to both data and MC are shown in Figure 5.20. Table 5.9 summarizes the fit results to data. See Table C.1, and Table C.2 for MC off_off and MC on_off fit results. Note that the three MBLR ranges are consistent and to have more data for our fits, we choose the 0-650 mm range from now on. MC off_off and MC on_off are also consistent compared to each other which gives us more confidence that the 200 ns starting window is safe from clipping and probably saturation.

Particle	MBLR range	Late Light qPE mean ± STD	Late Light LY (PE/keV)
Rn222	0-400	8310 ± 220	1.51 ± 0.04
Po218	0-400	9190 ± 290	1.53 ± 0.05
Po214	0-400	12310 ± 300	1.60 ± 0.04
Rn222	150-600	8270 ± 240	1.51 ± 0.04
Po218	150-600	9140 ± 300	1.52 ± 0.05
Po214	150-600	12270 ± 300	1.60 ± 0.04
Rn222	0-650	8260 ± 250	1.50 ± 0.05
Po218	0-650	9120 ± 310	1.52 ± 0.05
Po214	0-650	12270 ± 310	1.60 ± 0.04

Table 5.9: Results of the Gaussian fit to the three alpha lines with three different MBLR ranges for data. The late light qPE mean and its uncertainty come directly form the Gaussian fit and the late light LY variable is the fitted qPE divided by the corresponding alpha energy.

The next step in our analysis is to calculate the QF of the three alpha lines using Table 5.9 and the MBLR range of 0-650 mm fit results. The qPE values we found from the fits are the late light charge. To find QF, we first need to calculate the total qPE. Let's call the charge variable we have qpe^{200}. Note that usually when we use qpe_{150}, we mean the charge integral from -28 ns to 150 ns. Here we use superscript to highlight the difference such that qpe^{200} means the charge integral from 200 ns to 10 μs. First, we need to calculate qpe^{150}:

$$\mathrm{qpe}^{150} = \frac{\int_{150}^{10000} e^{-t/\tau_t} dt}{\int_{200}^{10000} e^{-t/\tau_t} dt} \times \mathrm{qpe}^{200} = R_t \times \mathrm{qpe}^{200}, \tag{5.20}$$

where $\tau_t = 1458$ ns is the triplet lifetime and $R_t = 1.03493$ is the ratio of the 150 ns to 200 ns late light. Since the lower bounds of the integrals are much greater than the LAr singlet lifetime, we can approximate by only taking the triplet portion. What we need to calculate is the total actual qPE of the event; i.e. no after pulsing effect. The total qPE can be written as:

$$qPE = PL + LL + AP = PL + LL + LY_R \times (PL + LL), \tag{5.21}$$

where PL, LL, and AP stand for Prompt Light, Late Light, and After Pulsing. Note that PL is the charge integral from -28 ns to 150 ns and LL is the charge integral from 150 ns to 10 μs. LY_R is the after pulsing charge ratio found from:

$$LY_R = \frac{\mathrm{LY}_{\mathrm{qPE}} - \mathrm{LY}_{\mathrm{nSCBayes}}}{\mathrm{LY}_{\mathrm{qPE}}} = \frac{7.3 - 6.2}{7.3} = 0.15. \tag{5.22}$$

To find PL, we can write the $\mathrm{F}_{\mathrm{prompt}}$ as:

$$\mathrm{F}_{\mathrm{prompt}} = fp = \frac{PL}{PL + LL + AP} = \frac{PL}{PL + qpe^{150}}, \tag{5.23}$$

from which we can find PL to be:

$$PL = \frac{fp \times qpe^{150}}{1 - fp}. \tag{5.24}$$

Next, we can use qpe^{150} to to find LL:

$$\begin{aligned} \text{qpe}^{150} &= LL + AP = LL + LY_R \times (PL + LL) \rightarrow \\ LL &= \frac{\text{qpe}^{150} - (LY_R \times PL)}{1 + LY_R}. \end{aligned} \tag{5.25}$$

The AP can be calculated as:

$$AP = \text{qpe}^{150} - LL. \tag{5.26}$$

Having found the prompt and late light separated from the after pulsing, the real charge needed for calculating the QF is:

$$\text{qPE}^{\star} = PL + LL. \tag{5.27}$$

Note that $\text{qPE}^{\star}$ is different from regular qPE in the sense that it does not include the after pulsing charge, which makes it similar to nSCBayes in meaning. Having found the total charge we can calculate the quenching factor as:

$$QF = \frac{\text{Measured Energy}}{\text{Deposited Energy}} = \frac{\text{qPE}^{\star}}{\alpha\text{Energy} \times LY} \tag{5.28}$$

where LY= 7.3 photons/keV_{ee} and the α energies were tabulated in Table 5.7. Table 5.10 summarizes the fit values, the late light charge, the total charge and the QF found for each of the three particles.

Figure 5.21 shows the results of our study, compared with the Birk's and Lindhard's models. The current QF array used in the MC is also shown. The main source of the uncertainty in our study is the values used for LY_R and F_{prompt}. We have assumed a 2% uncertainty for each variable. The best agreement was achieved with $LY_R = 0.16$ and $\text{F}_{\text{prompt}} = 0.71$. We would like to point out the relative difference between the three data points we have compared to the values found by the earlier study.

Using the late light, we have shown that the combined Birk's and Lindhard QF

Particle	MBLR range	Late Light qPE mean ± STD	alpha peak (qPE)	QF
Rn222	0-650	8260 ± 250	25420	$0.634^{+0.029}_{-0.033}$
Po218	0-650	9120 ± 310	28080	$0.641^{+0.030}_{-0.033}$
Po214	0-650	12270 ± 310	37770	$0.673^{+0.031}_{-0.035}$

Table 5.10: The alpha peak energies found from the late light calculation explained in the text for data and the corresponding QFs. We have used $LY_R = 0.16$ and $\mathrm{F}_{\mathrm{prompt}} = 0.71$ for best agreement to data. For QF uncertainties, we have assumed a 2% uncertainty in LY_R and $\mathrm{F}_{\mathrm{prompt}}$.

can explain our data with the literature-accepted value of Birk's constant $kB = 7.4 \times 10^{-4}$ MeV^{-1} g cm^{-2} [175]. We do not perform any fit to get a new Birk's constant.

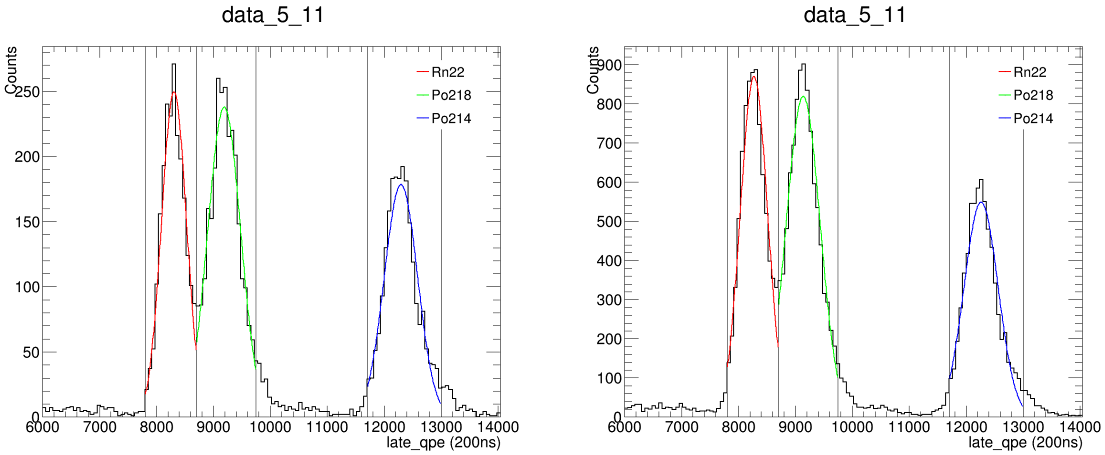

(a) 0 - 400 mm **(b)** 150 - 600 mm

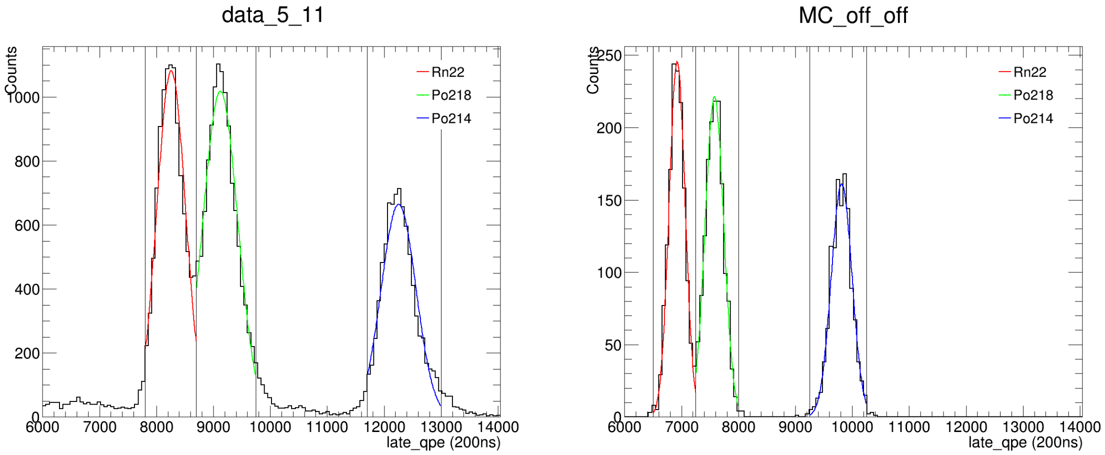

(c) 0 - 650 mm **(d)** 0 - 400 mm

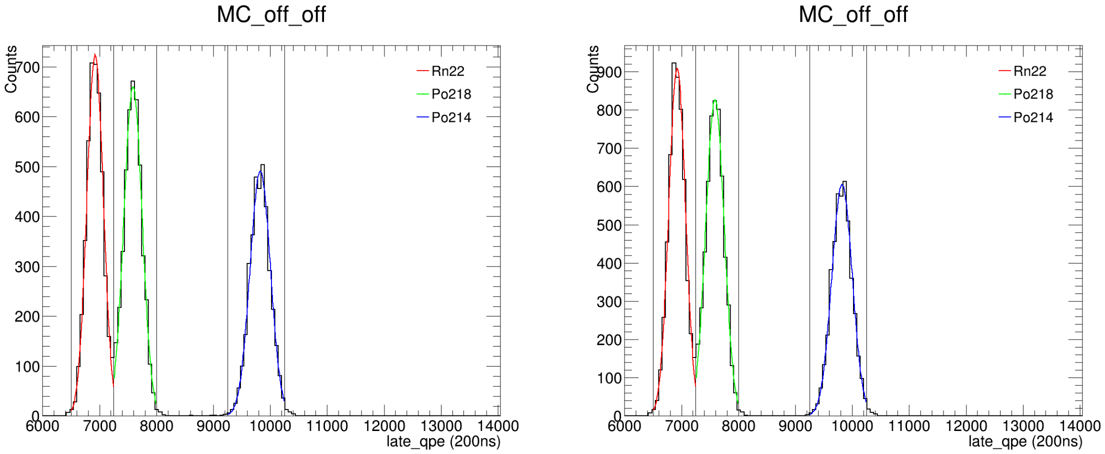

(e) 150 - 600 mm **(f)** 0 - 650 mm

Figure 5.20: Late light qPE projected with three different MBLR ranges for both data (RAT 5.11) and MC sample (off_off setting). The vertical lines show the range used for the Gaussian fits to find the energy peak.

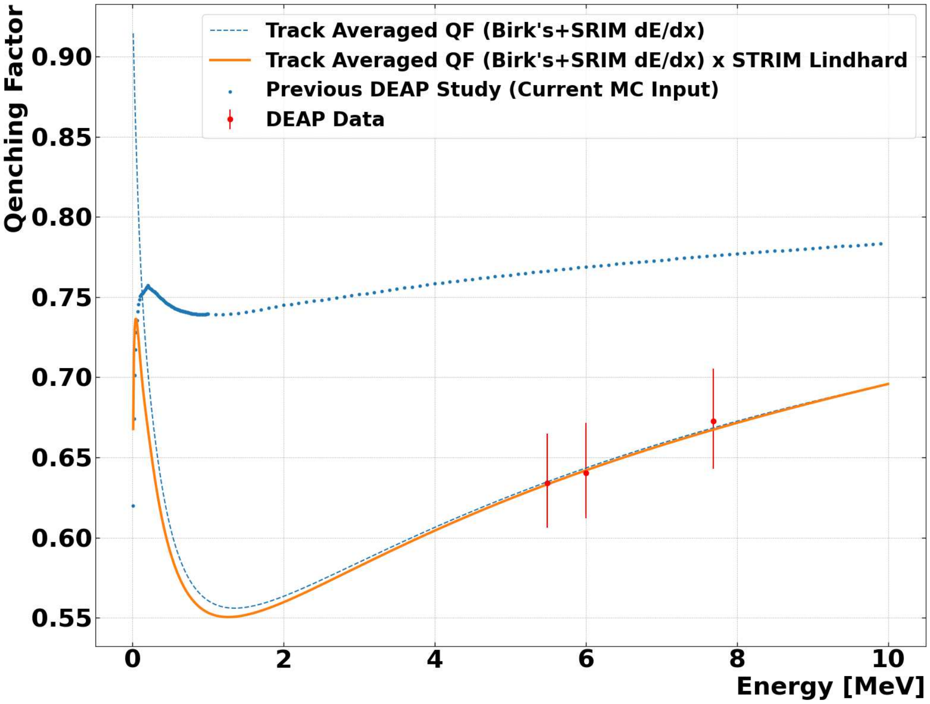

Figure 5.21: Comparing the quenching factor of the combined Birk's QF and Lindhard QF with Birk's constant $kB = 7.4 \times 10^{-4}$ MeV^{-1} g cm^{-2} [175] with DEAP data, and the current QF array used in our MC. $LY_R = 0.16$ and $\mathrm{F}_{\mathrm{prompt}} = 0.71$ were used for achieving the best agreement. For QF uncertainties, we have assumed a 2% uncertainty in LY_R and $\mathrm{F}_{\mathrm{prompt}}$.

5.7 Surface Tagging Algorithm

Probably our most important study is the likelihood approach for identifying surface events. In almost any DM detector, we will have the alpha background from the radioactive isotopes in the detector material. Since these events often reconstruct near the surface of the detector, a fiducial volume cut is often used to mitigate this background. In some cases, like DEAP, the fiducial volume cut is also useful for reducing the neutron background, but the main reason for this cut is the surface background. For example, the fiducial cut in the 2019 paper from DEAP, reduced the contained LAr mass from approximately 3279 kg to 1248 kg [124] while the 2022 results of the LZ experiment reduced the contained xenon mass from 10 tonnes to a fiducial mass of 5.5 tonnes [121][1]. The goal of this study is to be able to identify surface events without relying on a fiducial cut. This will enable us to increase the fiducial mass, hence increasing the signal acceptance and improving the limit on WIMP cross-section. The importance of this study is that it will be applicable to future generations of DEAP-3600 detectors as it is likely to have a surface background.

Alpha surface events, like WIMP interactions, are NR and similar in their physical nature. The major difference is that they happen near or at the surface of the detector. But there is a chance that our position fitter might not be able to accurately find the event position and the surface event would leak inside the detector, hence the fiducial cut. One source of this leakage is pure statistics. Given the position resolution of our fitters, there is a percentage of the surface events that will leak inside the detector. Another reason is the detector configuration during the run and the lack of full PMT coverage.

During the three-year physics data collection, there were runs when some of the PMTs were not operational. In most of the runs, all of PMTs were operational but there have been many runs that we have one, two, or three dead (non-operational) PMTs. In our studies, we found that missing PMTs can increase the leakage if the interaction

---

[1] Note that in the case of DEAP, we also have lost the top 30 cm of the detector due to the neck seal failure, hence 3279 kg instead of the full 3600 kg.

takes place near these dead PMTs.

Also, as mentioned earlier, the PMTs only cover about 76% of the detector surface and there are 11 points around the detector where an area of about 5.3 inches in diameter has no PMT coverage. These areas are referred to as pentagonal gaps. This case is very similar to having a dead PMT and also increases the chance of leakage. Figure 5.22 shows the map of the PMTs in the ϕ-$\cos\theta$ space. The locations of the pentagonal gaps are also highlighted in red. The numbers are just for counting and carry no special meaning. Also, note that the south pole of the detector is connected to a spring support creating a pentagonal gap covering the full range of ϕ. During the design of the detector consideration was given to installing smaller PMTs in the pentagonal gaps but it was decided that it was too complicated.

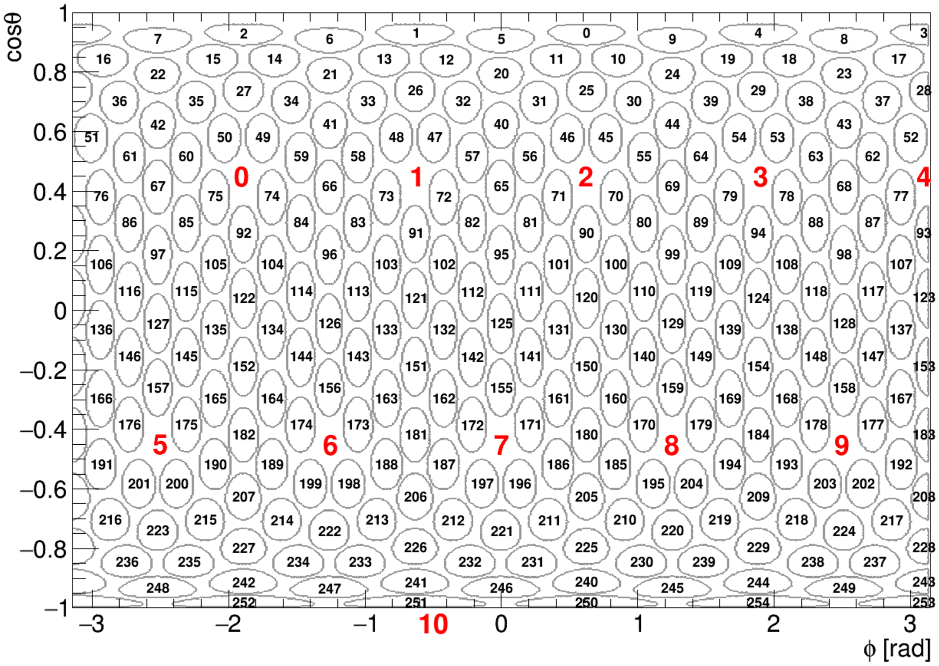

Figure 5.22: Map of the PMT positions in $\cos\theta$ and ϕ space. The numbers in the box represent the PMT id. The pentagonal gaps are highlighted with red numbers. Note that there is a pentagonal caused by the spring support gap at the bottom of the detector that covers the full ϕ range at $\cos\theta = -1$, number 10 in this figure. The top of the detector could also be a pentagonal gap but it is the neck region.

For identifying surface events we use the charge distribution of different event types. In the case of regular surface events, the nearby PMTs will collect most of the light. For regular signal events happening away from the surface, although the nearby PMTs would still collect more light, the amount would be much less and more distributed among all the PMTs. If an event happens in front of a dead PMT, what would have been the brightest PMT, will observe no charge. Lastly, if the event is in front of a pentagonal gap it would look very much like a regular surface event but with the brightest PMTs observing less charge.

The first step would be constructing the Probability Distribution Function (PDF) of these four charge distributions.

- ^{40}Ar: For signal, or ^{40}Ar-like events, we simulated ^{40}Ar samples but only chose those with the truth-radial distance of less than 800 mm.

- Surface α: For regular surface events we simulated ^{210}Po surface alpha events with the nominal detector setting.

- Dead PMTs: We used the same samples as regular surface events but in this case, we would get the truth MC position of the event, find the nearest PMT in the angular distance and move the location of the event to this new spot. Then we subtract the charge of the said PMT from the total charge and recalculate the charge of each PMT. This was done to mitigate the effect of a dead PMT without needing to spend more computational power on new MC samples.

- Pentagonal Gaps: For these events, we first identified the 11 locations around the detector that have the pentagonal gap. Then we simulated low energy α particles in front of each pentagonal gap but only up to 4 inches from the centre of the gap, instead of the full 5.3 inches. This was done to avoid including events happening at the very edge of the gap and skewing the results. Also, we simulated low energy α particles instead of our regular ^{210}Po surface alphas to save on computational power.

Having simulated the required samples, we need to construct the charge distribution. For each event, we find the cosine of the angle between the two vectors formed from the centre of the detector to the event (truth MC) location and from the centre to the PMT$_i$ location. For a given event, we do this for all the 255 PMTs. Then we sort them in the increasing distance and label them from 0-254 with PMT index 0 being the closest one. Each bin in the histogram is then filled with the charge of the PMT. After the charge distribution is made, we scale the histograms such that the integral is equal to 1; i.e. the PDF shows the probability of observing the percentage of the total charge in each PMT based on their angular distance from the event location. To get the expected amount of charge in each PMT, the PDF value should be multiplied by the charge of the event. Figure 5.23 shows the charge distribution for the different event types described above.

Now that we have the expected charge distributions, for each event we do the same exact procedure and create the charge distribution of the event but this time with the fitted position since we cannot rely on the truth MC position when applying this approach to data. Assuming the Poisson statistics:

$$f(k;\lambda) = Pr(X = k) = \frac{\lambda^k}{k!} e^{-\lambda}, \tag{5.29}$$

for each event we calculate the NLL as:

$$NLL = -\sum_{i=0}^{i=254} q_i \ln(\lambda_i) - \lambda_i - \ln(q_i!). \tag{5.30}$$

where q_i is the observed charge in PMT index i and λ_i is the expected charge in said PMT. This NLL should be calculated for each PDF. The PDF that gives the minimum NLL value will determine the event type. This processor is referred to as Surface Tagging Algorithm (STA) and is written in Python language and is now a part of the standard data-reprocessing and MC simulation macros.

5.7.1 MC-Driven Tagging Performance

To measure the performance of this model, we simulated surface and ^{40}Ar events. For the surface events, we used four different detector settings. The first condition is the ideal detector where all PMTs are operational. The other three settings have, one, two, and three dead PMTs. The conditions were chosen based on the actual detector settings when taking physics data. Table 5.11 shows the livetime of each detector setting during the 231-day exposure used in our 2019 paper [124] and the upcoming three-year dataset.

Number of dead PMTs	livetime [days] (first year dataset)	livetime [days] (three-year dataset)
0	156.31	468.68
1	32.96	183.20
2	41.37	129.04
3	0.0	47.57
Total	230.64	828.49

Table 5.11: Livetime of each detector setting based on the number of dead PMTs during the 231-days exposure. Note that we never had three dead PMTs during the first-year dataset, but this condition did happen in the future runs of our three-year dataset.

Let's see how well the STA can identify the surface events and the ^{40}Ar signal events. For this study we simulated four types of ^{210}Po, each with four systematic, based on the number of dead PMTs; from 0 up to 3 dead PMTs. Table 5.12 shows the activity of each sample measured by the DEAP collaboration. Refer to Figure 4.20 for better visualization of these samples. In total, we generated about 62 million events from which 8.4 million have qPE<1000.

Since we want to study the performance of our algorithm in different energy-Fprompt space, and for better visualization, Figure 5.24 shows the blinding strips used by DEAP and the region of interest that was used in our 2019 paper. Although the STA was successfully tested on the full energy surface events, these events are not of particular interest to us because they will not be near the region of interest and an upper charge cut will get rid of them. Since we are calculating likelihoods, the lower the energy of the

Sample	Activity (mBq)
AV Surface	2.51664
AV Bulk	0.31164
TPB Bulk	0.61586
TPB Surface	0.66780

Table 5.12: The activity of each surface α event type measured by the DEAP collaboration. Note that the unreasonable number of digits were copied from another document. These values are probably accurate to the 10 to 20%.

event, the less amount of information we have; hence possibly lowering the efficiency of our algorithm. Table 5.13 shows the performance of our algorithm in different regions of qPE-F_{prompt} space. These numbers are based on using TF2 fitted position but the results obtained from MBL are very similar.

Ideally, we would like to maximize the rejection rate and the signal acceptance rate simultaneously. The rejection rate is measured as the fraction of the number of events that are properly tagged as surface background events. Note that for our purposes, a regular surface event, an event in front of a dead PMT or in front of a pentagonal gap, all count as surface backgrounds; i.e a misidentification of these events, as long as we don't tag them ^{40}Ar-like events, does not count negative toward rejection rate. The acceptance rate, the fifth column, is the number of events from the ^{40}Ar MC samples that are tagged as ^{40}Ar-like events. For now, we have only used the minimum of the four NLL values to tag the events. We have found that for surface events misidentified as ^{40}Ar events, the NLL found from the ^{40}Ar PDF, is very close to the next minimum NLL value. A useful variable to define is the NLL found from the ^{40}Ar PDF minus the next minimum NLL value. Internally, this variable is called NLL_ar40_min. The first choice would be to tag events as ^{40}Ar if NLL_ar40_min<0, which is to say that the NLL found from the ^{40}Ar PDF was, in fact, the minimum value. If we want to tighten the cut to reject more background we use a cut such as NLL_ar40_min<-2. Or we can loosen the cut value to a positive number to keep more of the signal. Later on, this variable will let us favour rejecting more background or increasing the signal acceptance.

Note that in reporting the percentages, the denominator is not the total simulated event but rather the number of events within the identified qPE-$\mathrm{F}_{\mathrm{prompt}}$ region. As an example, if we take the events inside blinding strip 3 with a reconstructed radius of $R < 800$ mm, we have a 99.1% rejection rate while keeping 80% of the signal. The 114 surviving events would translate to 0.227 events per year, from the original 22.80 events had we not applied the STA. The 5 surviving events inside blinding strip 3 would translate to 0.014 events per year which are well within our budget for surface events.

An informative way to visualize these events is by plotting them in their angular distribution with:

$$\begin{aligned} \phi &= \arctan\left(\frac{Y}{X}\right) \\ \cos\theta &= \frac{Z}{\sqrt{X^2+Y^2+Z^2}}. \end{aligned} \tag{5.31}$$

For this visualization, we use their truth MC position to see where the event was originally created. Then we will colour each event based on their tag as found by the STA. Figure 5.25 shows the events in blinding strip 1 and reconstructed radius R<800 mm. Although we have surface events leaking inside the detector from all around the detector, an effect of the fitter position resolution, it is obvious that the majority of them are clustered in front of the pentagonal gaps and simulated dead PMTs. Based on the PDFs shown in Figure 5.23, it could have been expected that regular surface events and events in front of the pentagonal gaps might be misidentified, due to the similarity of their PDFs. But as long as they are tagged as either of the surface events, we can easily veto these events and exclude them as background events.

Cut	raw surface events	survived events (rejection rate %)	raw ^{40}Ar events	survived events (acceptance rate %)
qPE $<$ 1000 & 0.40 $<$ F_{prompt} $<$ 0.92	8398119	3924 (99.95)	485130	329842 (67.99)
Inside strip 1	1083370	199 (99.98)	425409	300835 (70.72)
Inside strip 2	783480	136 (99.98)	322611	229383 (71.1)
Inside strip 3	31092	10 (99.97)	69902	48756 (69.75)
Strip 1 & R<800 mm	12836	114 (99.11)	370608	297299 (80.22)
Strip 1 & R<750 mm	4438	85 (98.08)	296915	272597 (91.81)
Strip 3 & R<800 mm	424	5 (98.82)	60943	48143 (79.0)
Strip 3 & R<750 mm	151	5 (96.69)	48871	43704 (89.43)

Table 5.13: Measuring the performance of the STA in different regions of qPE and F_{prompt}. The fiducial cut is based on the reconstructed position and not the truth MC position.

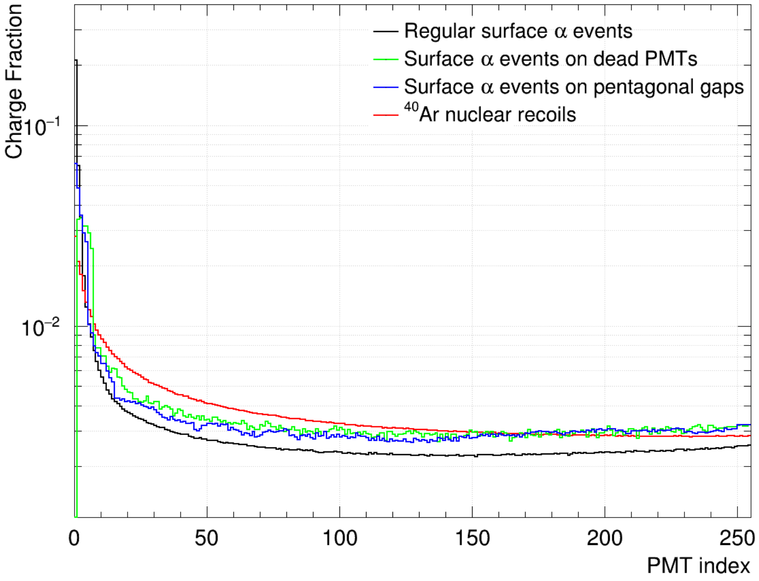

(a) Full PDF

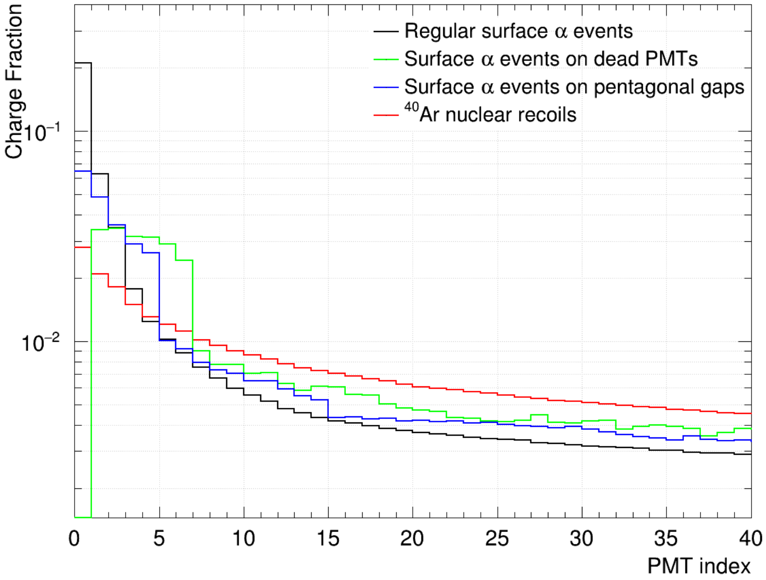

(b) Zoomed-in PDF

Figure 5.23: The charge distribution of the four different event types used in the surface tagging algorithm where **(a)** shows all the 255 PMTs while **(b)** only shows the first 40 bins to highlight the difference in the closest PMTs to the event location.

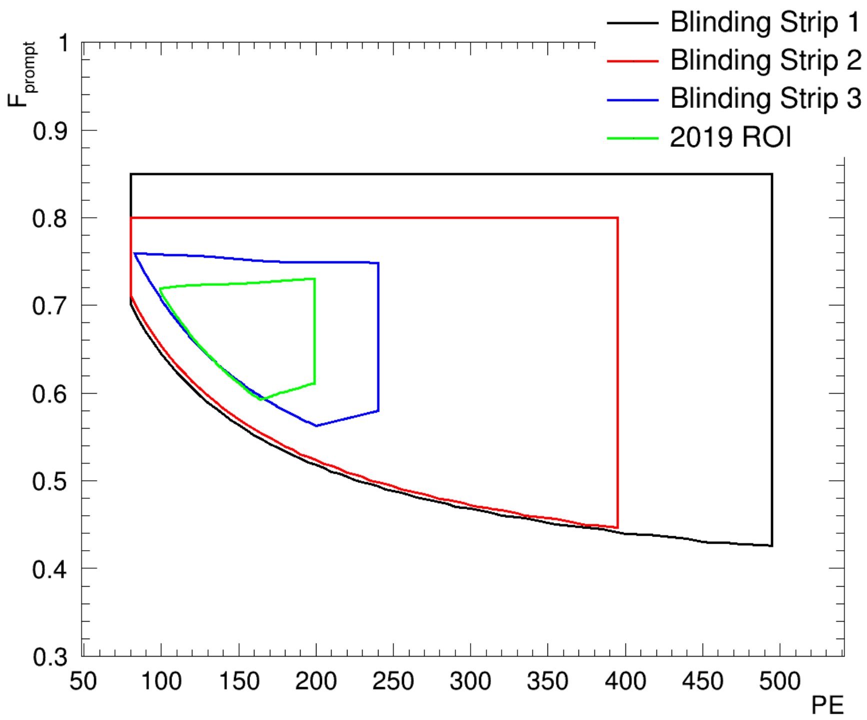

Figure 5.24: The blinding strips and the ROI used in our 2019 paper.

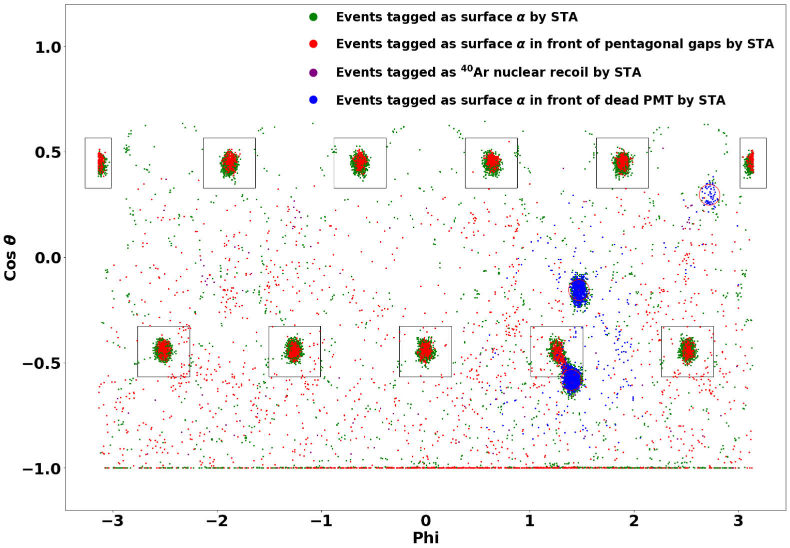

(a) All events

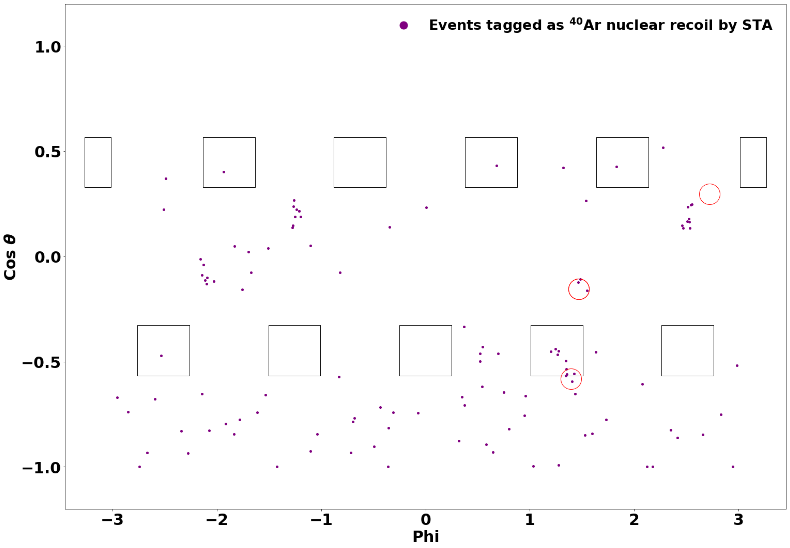

(b) ^{40}Ar-like events

Figure 5.25: **(a)** A plot of the MC surface events inside the blinding strip 3 and fiducial cut of $R < 800$ mm after each event is tagged by our algorithm. The black squares show the region around pentagonal gaps, where the gap at the bottom of the detector is not shown (expands the full ϕ range). The three red circles show the location of the dead PMTs. Neither the dead PMTs nor the pentagonal gap regions are drawn to scale. To better show the performance of our algorithm, the angular position of the events is based on their MC truth position and not the reconstructed position. **(b)** The bottom plot is the same as **(a)**, except we only plot the 144 events that are mistagged as ^{40}Ar-like events. The distribution is not uniform in cosθ and needs to be studied more. But it could be due to the pentagonal gap at the bottom of the detector and the dead PMTs at ϕ>1.

5.7.2 Data-Driven Tagging Performance

There are two main advantages to using MC when studying the STA. Firstly, we know the truth position of the generated event which makes a plot such as Figure 5.25 feasible. Secondly, we can be sure the events used in the study are in fact surface events. Moving to data, one can define a CR but it will always contain a certain amount of contamination. But the downside of only relying on MC is that the MC might not be able to fully capture all the details of the detector such as the details and local variations of the optics. In this section, we will try to measure the performance of the STA in a data-driven method. At the same time, we will pursue two other tasks. As we mentioned before and based on MC results, we can get leakage purely from the position resolution of our fitters. But this leakage can be enhanced due to events happening near a dead PMT or a pentagonal gap. Since the pentagonal gaps always exist in the detector, we cannot directly test the pentagonal gap hypothesis but by choosing the two golden runs of 18831 and 21399, we can test if dead PMTs do in fact cause more leakage. Run 18831 had all the PMTs operational while run 21399 had two dead PMTs. We would expect a higher leakage percentage during run 21399. Given the pentagonal gaps are like a dead PMT with a smaller radius, by extrapolation, we can argue that pentagonal gaps are also a cause of leakage.

Analysis Method

The main challenge when using data is that we do not know the truth position of the event. This is also the problem when in DEAP we try to measure the position resolution in a data-driven method. The approach we take in DEAP is to use a procedure known as SplitEvent. In this method, we perform the position fit of a single event multiple times. The usual number is $nFit = 3$. At the time of writing this thesis, this algorithm is only available using the MBL position fitter, which is referred to as the Multi-MBL fitter. But the same method is being developed for TF2 and the neural-network position fitters.

We will use the default value of $nFit = 3$, meaning that for a given event, we run the MBL fitter three times. Also, note that MBL uses nSCBayes as the charge variable and not qPE. The case of $nFit = 0$ is the same as regular MBL where the full charge information (nSCBayes of the event) is used to fit the position. Let's call this position vector $\vec{x_0}$. For $nFit$ =1 and 2, we randomly choose 25% of the photons in each PMT and perform the fit with the new charge distribution. The total charge is referred to as fitEE1 and fitEE2[1]. This is equivalent to fitting an event with approximately 1/4 of the current event charge. These two events (often referred to as pseudo-events) are independent and their position vector can be denoted as $\vec{x_1}$ and $\vec{x_2}$. For an event with energy fitEE1, the position resolution can be found via $\vec{x_1} - \vec{x_0}$. The same can be used for fit energy fitEE2 where the position resolution can be written as $\vec{x_2} - \vec{x_0}$. Right now, we are not studying the position resolution. Instead, we are interested in surface leakage and the performance of our algorithm in identifying surface events that have leaked inside a given fiducial volume. So, rather than $\vec{x_i}$ we will be working with R_i which is the radial distance of the fitted position from the centre of the detector.

We also developed a C++ version of the STA that can be called from other position fitters instead of a regular RAT processor. This will enable us to study the STA in a data-driven approach. For a given event, we pass the PMT charge distribution and the fitted position of each pseudo-event and calculate the same NLL values explained earlier. Note that since we constructed our PDFs using the qPE variable, we pass the qPE charge distribution of the PMTs and not the nSCBayes used by MBL.

Neither the position fitter nor the STA are dependant on F_{prompt}. This will enable us to study the leakage and tagging performance using ^{39}Ar data. The advantage of using ^{39}Ar data is the higher statistics at energies near the WIMP ROI and lower contamination from other data types such as TPB scintillation events or Cherenkov radiation, were we to use high F_{prompt} events instead. Table 5.14 shows the cutflow used in this study. Note that we require the full-energy position to be reconstructed with $R_0 > 830$ mm where the subscript 0 highlights the full-energy fit and not the pseudo-events. A safer

---

[1] Note that fitEE0 would correspond to nSCBayes of the event.

choice would be taking events even closer to the surface but this would require reprocessing more data only for this study which would require more computational power. We used $R_0 > 830$ mm in favour of increasing the statistics. After applying this cutflow, we also require 80 <fitEE< 200 which is the energy range of the WIMP ROI. We emphasize again that the two pseudo-events, for now, will be treated separately but as we will see, they behave very similarly. With 80 <fitEE< 200, run 18831 has approximately 1.1 M pseudo-events (2.2 M in total) and run 21399 has about 0.56 M pseudo-events.

Event Selection	Purpose
dtmTrigSrc&0x82 = 0	Non-physics event removal
calcut&0x31f8 = 0	Non-physics event removal
subeventN = 1	Pile-up event removal
numEarlyPulses <= 3	Pile-up event removal
2250 <= eventTime <= 2700	Pile-up event removal
deltaT > 20000	Pile-up event removal
$0.1 < \mathrm{F}_{\mathrm{prompt}} < 0.4$	^{39}Ar $\mathrm{F}_{\mathrm{prompt}}$ range
fmaxpe < 0.4	Remove Cherenkov events
$\mathrm{MBL}_Z < 550.0$	Events happen below the LAr fill level
$R_0 > 830$	Events happen near the surface

Table 5.14: The cutflow used for selecting ^{39}Ar events in data for measuring the leakage and the surface tagging performance.

Figure 5.26 shows the leakage percentage (solid lines) and percentage of those events tagged as ^{40}Ar (dashed lines). The dashed lines show the percentage of events surviving the cutflow in a DM search analysis since they are tagged as ^{40}Ar (signal-like). So, assuming surface events such as the case at hand, the lower these curves the better. The blue and red lines use the data from run 18831 corresponding to pseudo-event 1 and 2, respectively. Green and black lines are the same while using run 21399. Note that in run 21399, the STA is vetoing more events. To highlight the percentage of events leaking inside the detector, Figure 5.27 shows the event leakage up to a fiducial volume cut of 800 mm and the relative difference between the two runs where run 21399 clearly has more leakage. As mentioned earlier, in DEAP collaboration these two runs are often referred to as golden physics runs due to the ideal condition of the detector and environment. But run 21399 shows a higher leakage over all fiducial volumes cuts[1]. Using our knowledge from MC simulations, the best explanation is that the higher leakage is caused by dead PMTs. The STA was specifically designed to deal with such events hence its better performance in run 21399. As we push the fiducial volume to around 800 mm, the surface tagging performance between the two runs becomes almost identical and mainly determined by the position resolution of the fitter, overshadowing the effect of dead PMTs and pentagonal gaps. Given the leakage percentage and the percentage of those events tagged as ^{40}Ar, it seems the best fiducial volume cut is somewhere between 780 to 820 mm.

Appendix D shows the leakage (average of the two pseudo-events) of these two runs for each fiducial volume cut but instead broken into energy bins. As expected, since lower charge events have less information, the position reconstruction suffers more.

In conclusion, it is clear that dead PMTs significantly enhance the leakage of surface events and STA successfully removes most of the leaking events as was shown in Table 5.13.

---

[1] Except the 810 and 820 mm cases where the leakage probability is mainly governed by position resolution.

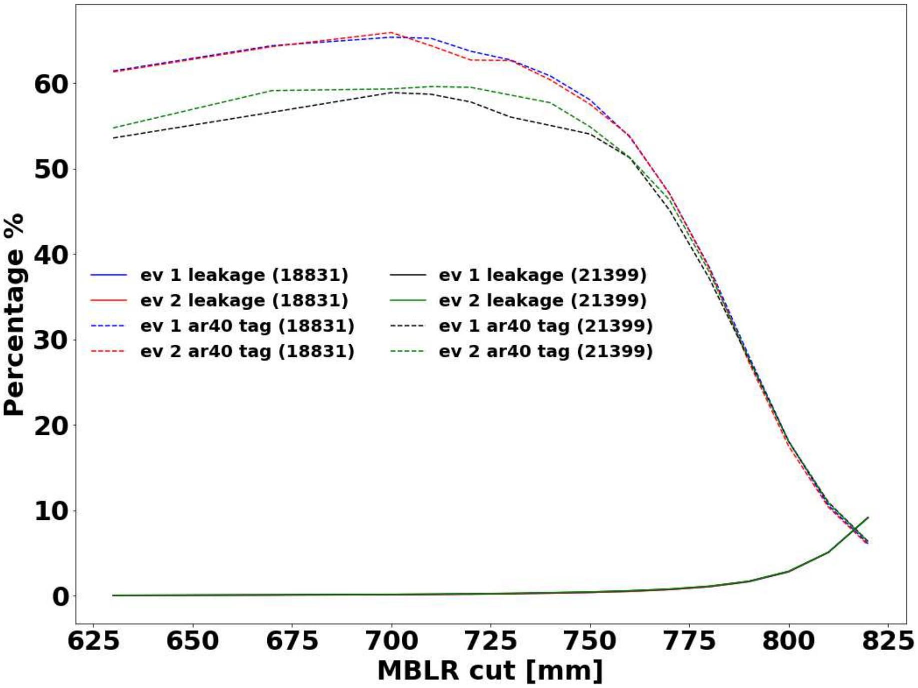

Figure 5.26: The leakage percentage (solid lines) of the pseudo-events using the two golden runs. The dashed lines show the percentage of events tagged as ^{40}Ar events. Note that we want to minimize the dashed lines before the solid lines take off too much; i.e. maximum surface veto with minimal leakage.

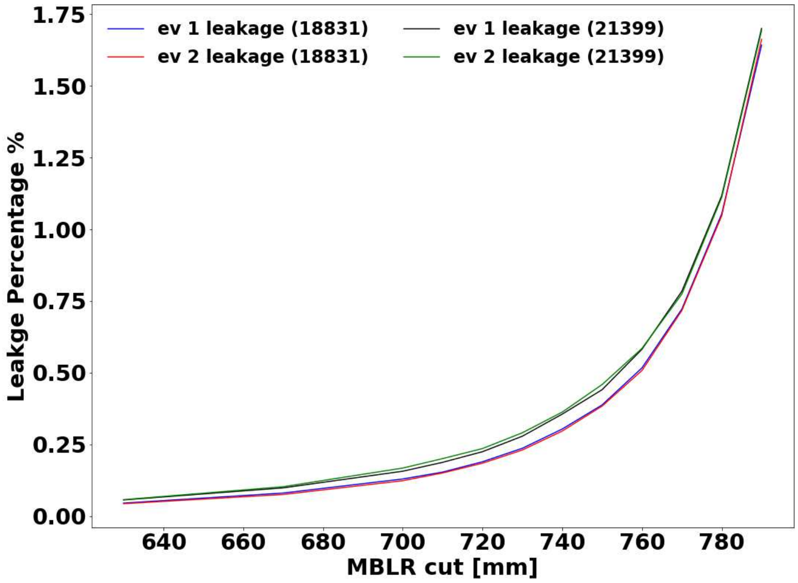

(a) Leakage percentage

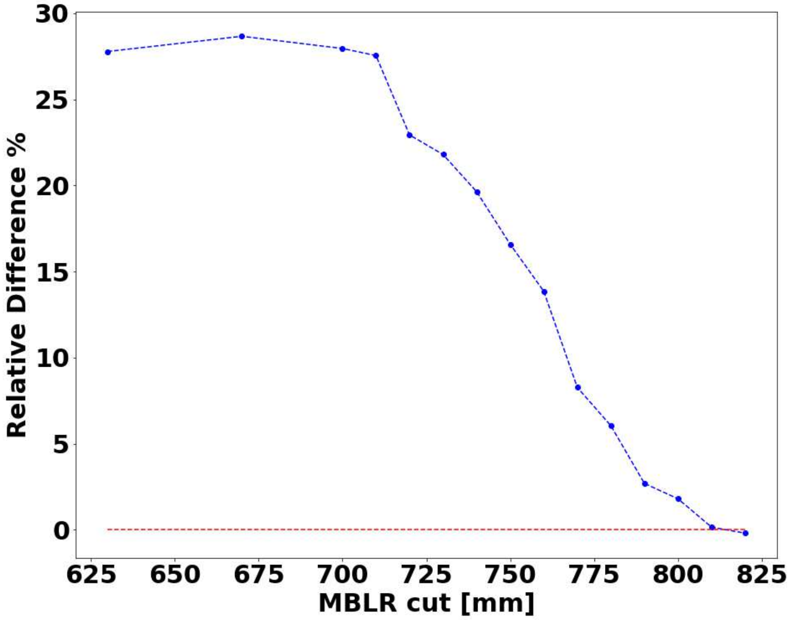

(b) Relative leakage between the two runs

Figure 5.27: **(a)** The leakage percentage using the two golden physics runs. Run 21399 has two dead PMTs and clearly shows an enhanced leakage compared to run 18831. **(b)** Relative difference of leakage between the two runs where we have taken the average leakage between the two pseudo-events. Run 21399 with two dead PMTs and can have up to 30% more leakage at lower radii.

5.8 Double Charge Clusters

For all previous DEAP studies, the Cherenkov background contribution was found to be negligible. This was due to the efficiency of the fmaxpe cut and also the fiducial volume cut. More importantly, we also did not have enough data to interpolate Cherenkov contribution in our background model. As we will see in more detail in the next chapter, we used the data where a ^{232}U source was deployed in the detector to approximate the contribution of Cherenkov events to the expected background events in the ROI. After performing our analysis we saw a huge contribution from the Cherenkov background events, up to 12 events using the first-year dataset with a fiducial volume of 820 mm compared to 3.8 events at 750 mm while the data was showing 19 and 17 events at these radii, respectively. This discrepancy hinted toward the fact that something should be different with the Cherenkov data.

For regular physics data near the centre of the detector, we expect the charge distribution to be uniformly distributed in the PMTs. The LG Cherenkov events are caused by the high energy gamma rays, for example from the ^{232}Th decay, that Compton scatter in the LG and create high energy electrons. Due to their high energy, these electrons will create Cherenkov radiation. As such, for Cherenkov events happening inside a LG, we expect a single very bright PMT, high fmaxpe. While for Cherenkov events happening in the neck or a pentagonal gaps, we expect a cluster of bright PMTs. But on a closer look at the Cherenkov radiation data, we saw that there are often two or more clusters of bright PMTs that are far from each other. This will cause the position fitter to reconstruct the event well within the detector and the surface tagger will also not be able to veto them.

When the detector is in a vacuum state, the high energy electron produced in the LG can leak inside the detector and hit another LG at a different location and cause a second Cherenkov light. This situation would not happen when the detector is filled with LAr since the electron would lose its energy and produce scintillation light. But recall that the top 30 cm of our detector is in a near-vacuum state. So, during regular data collection, such events can also happen. Another possibility is that the electron can move outside the AV and reach another LG causing a secondary Cherenkov radiation without moving into the AV. A situation like this can happen even if the detector is filled with LAr. Besides the electrons, if the gamma ray leaves the original LG before it loses most of its energy, it can pass through the detector and enter another LG, creating a second Cherenkov radiation, even if the detector is filled with LAr. In these instances, we can see two or more cluster of bright PMTs around the detector.

To identify these events and remove them, we pick the six brightest PMTs in the event. First, we require the brightest PMT to have at least 7% of the total charge of the event. This will make sure that the event was near the surface and not originated within the detector. Secondly, we require $q_i/q_0 > 0.3$ and $d_i - d_0 > 600$ mm where i runs over the next five brightest PMTs and $d_i - d_0$ is the distance of the two PMTs on the surface of the detector. Note that for a regular PMT in the detector, 600 mm would exclude the 35 nearest PMTs. section E.2 shows a 3D representation of the detector for a few examples of the Cherenkov events that would be removed or kept by this approach.

We will be covering the background prediction in the next chapter. But with this approach, we remove up to 90% of the Cherenkov events passing the full cutflow. But as mentioned earlier, a double cluster can happen even if the detector is filled with LAr. Since this cut is not dependant on $\mathrm{F_{prompt}}$, we applied the same cut on ^{39}Ar data and ^{40}Ar MC where we ended up removing up to 25% and 13% of the events, respectively.

Chapter 6

Dark matter Analysis Results

Having finalized our new processor and our other studies, in this chapter, we will try to improve the exclusion limits on SI WIMP cross-section. We will first compare our results with the data and cutflow used in our 2019 paper [124] to directly compare the effect of our proposed cutflow and the new surface tagging algorithm. We will then update our results with the three-year open dataset. Note that while the data is taken over three years, we only use open data which corresponds to 386 days of livetime for unblinded analysis. The rest of the data will be unblinded once the DEAP collaboration finalizes the background model.

In this chapter, we will first take a look at the revised cutflow. Next, we will cover the background expectation from different sources and how we estimate their uncertainties. Lastly, we combine this information to set limits on the SI WIMP cross-section.

6.1 New Cutflow

We often break the analysis cutflow into two parts. The low-level cuts are designed to choose appropriate physics data and remove effects such as pile-up. The background removal cuts reduce the number of background events in the WIMP ROI. Table 6.1 and Table 6.2 show the low-level cuts and the background rejection cuts used in our 2019 results [124]. We have 7 cuts mainly designed to reduce neck α background. We have already covered neckVetoN which denotes how many hits were counted in the neck veto PMTs. Another variable is the pulseindexfirstgar (often shortened to PifGAr) which makes sure that the PMT ID of the first three pulses are not looking at the gaseous part of the detector, indicator of events from the neck. Two other variables are the fraction of charge observed in the top two and the bottom three PMT rings. We also have two cuts based on the two position fitters. The two fitters often agree with each other to a high degree except for neck events. The two cuts require consistency between the Z-coordinate and the 3D distance of the two reconstructed positions. We won't cover the details of the study done by DEAP for these cuts, we refer the reader to our last paper for more details [124]. Lastly, we require the events to be in the WIMP ROI defined in the PE-F_{prompt} space, shown in Figure 4.16.

We can break the ROI into three parts. The lower PSD bound between 95-160 PE is designed such that after all the background removal cuts, we expect less than 0.05 EM events leaking to the ROI. The lower bound between 160-200 PE is chosen with a constant 1% NR acceptance loss. The upper PSD bound has a constant 30% NR acceptance loss in each PE bin, designed to keep the expected neck background < 0.5 in the 230 live-day dataset. After 200 PE, we don't expect many WIMP events while it increases the α particle- and neutron-related background events.

In this thesis, we will propose a few changes:

- Remove the PifGAr cut. This cut was mainly designed to have a background-free analysis and costs us 50% of our signal acceptance.
- Remove the requirement that TF2 and MBL reconstruct the same Z-coordinate position, while retaining the cut requiring the two vertices be reasonably close.
- Expand the fiducial volume cut.
- Add the surface tagging (NLL_ar40_min<2) cut. This ensures that the ^{40}Ar PDF is at least as likely as the surface alpha PDF.
- Add the double charge cluster cut.
- Expand the WIMP ROI.

We should mention that all of these changes, except the use STA, have been studied by the collaboration. Some studies have pushed the fiducial volume to 720 mm. We also have a multi-variant analysis (MVA) using a neural net approach designed to remove neck α events with a lower signal loss compared to the cuts we have in place right now. At the time of writing this thesis, the MVA processor is not integrated into RAT and we could not include those results here. Since we are targeting a different background type, these two approaches are independent. We hope to show the advantage of using the STA and expanding the fiducial volume even further. Once the two studies are completed, we can combine them to improve our exclusion curves even more.

Figure 6.1 shows the expanded ROI to reduce the signal loss from 30% to 5% by moving the upper bound of the ROI to 0.78 instead of 0.72. Intermediate regions are also being considered by the collaboration. For the fiducial volume cut, we will consider 6 different values, namely [630, 720, 750, 775, 800, 820] mm to find the best region. Since there have been changes to RAT that can also affect the data, we cannot compare our results directly to that in Ref. [124]. Instead, we repeat that study using the fiducial volume of 630 and using the same cutflow used in that study. This will enable us to directly compare any improvements made by our study.

Event Selection	Purpose
dtmTrigSrc&0x82 = 0	Non-physics event removal
calcut&0x31f8 = 0	Non-physics event removal
subeventN = 1	Pile-up event removal
numEarlyPulses <= 3	Pile-up event removal
2250 <= eventTime <= 2700	Pile-up event removal
deltaT > 20000	Pile-up event removal

Table 6.1: The low-level cuts applied in the DM search analysis to remove non-physics and pile-up events.

Event Selection	Purpose
fmaxpe < 0.4	Remove Cherenkov events
$\mathrm{MBL}_Z < 550.0$	Events are below the LAr fill level
neckVetoN $= 0$	Remove neck α events
Fraction of charge in top two rings less < 0.04	Remove neck α events
Fraction of charge in bottom three rings < 0.10	Remove neck α events
pulseindexfirstgar (PifGar) > 3	Remove neck α events
90% acceptance ΔZ contour	Remove neck α events
85% acceptance 3D distance contour	Remove neck α events
$\mathrm{MBL}_R < 630.0$	Fiducial volume cut to remove surface α events
WIMP ROI	Reduce neck α and EM leakage background

Table 6.2: The background removal cuts applied in the DM search analysis in order to reduce background events in the WIMP ROI.

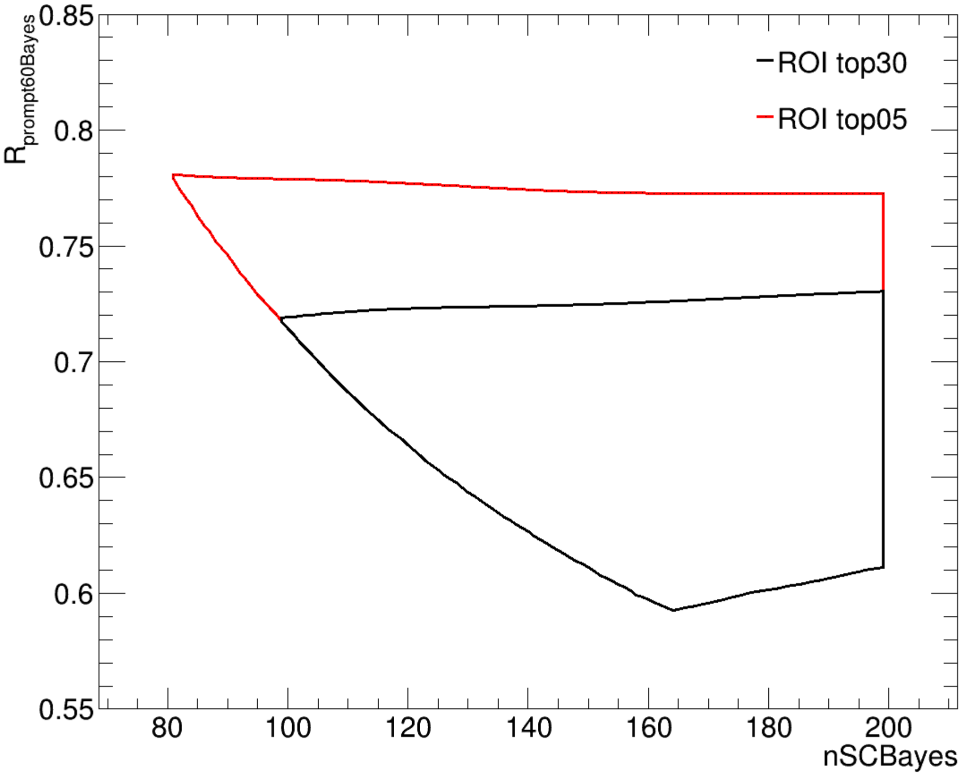

Figure 6.1: Expanding the upper bound of the WIMP ROI to have a 5% signal loss instead of the 30% loss used in previous studies.

6.2 Background Expectation Sources

An integral part of setting limits on the WIMP cross-section is understanding the background model and the number of expected events from different sources. Multiple ongoing studies are trying to even further improve our understanding of our data with the background model we have. In fact, there is an excess of data up to 1000 PE which at the time of writing this thesis, we cannot completely explain. But in the ROI the background expectation is within 1-σ of the observed data enabling us to carry on with our study while the collaboration improves our models.

In this section, we will cover the five sources of background and how we estimate the expected background from each source. In the next section, we will cover the systematic uncertainty of these sources. The neck and dust α background are directly drawn from MC simulations. There are issues with measuring the surface background from MC. So, we approximate this background in a data-driven approach. Simulating Cherenkov events at full statistics is impossible with our computation resources and since we often prefer a data-driven approach, this background will also be drawn from data. The same argument goes for the neutron background where we will be using the results of previous studies since those should still be valid.

In order to find the expected number of background events from MC, we need the trigger rate of each simulated sample. These trigger rates are found by other members of the DEAP collaboration and are not part of our study. We calculate the trigger rates for each background source, such as neck events, by defining a Control Region (CR) in the data where that background is the dominant source and we can reduce contamination from other event types by imposing relevant cuts. Then the simulated samples in MC are fitted to the data to find the trigger rate.

Once we have the trigger rate, we can get the expected number of background events using:

$$N_{\text{background}}^{\text{expected}} = \frac{N_{\text{ROI}}}{N_{\text{triggered}}} \times R \times T_{\text{livetime}}, \tag{6.1}$$

where N_{ROI} is the number of events in the WIMP ROI passing all the cuts applied in the cutflow, $N_{\text{triggered}}$ is the number of triggered events in the simulation[1], R is the trigger rate in Hz and T_{livetime} is the livetime in the data being considered in units of seconds.

The two main T_{livetime} values considered in this thesis will be the 223 and 386 days corresponding to the first-year dataset and the three-year open dataset. Since we are considering different fiducial volumes and different cuts on the STA, we will first cover how we are finding the expected background from each source and then quote the exact number for each cutflow.

6.2.1 Neck α

When simulating neck α background, see Figure 4.21 for the visualization of these locations in the neck region, we simulate three different MC samples:

- Neck, Inner Flowguide Inner Surface (IFIS),
- Neck, Inner Flowguide Outer Surface (IFOS),
- Neck, Outer Flowguide Inner Surface (OFIS).

Each sample, based on the simulated systematic uncertainty has its own trigger rate. We will summarize the latest trigger rates found by the DEAP background group after covering the systematic variations that are often considered in our detector. Once we have the trigger rate, we can get the expected number of background events from Equation 6.1.

Note that the neck α events are also referred to as shadowed α. A shadowed α can mimic a WIMP signal in any detector which in the case of DEAP, the main shadowing of these events happens in the neck region of the detector.

6.2.2 Dust α

For the dust α background, we take a similar approach. Although the dust could be coming from different sources, in DEAP we are considering copper as the main source.

---

[1] Note that number of triggered event is defined as a simulated event with qPE>0 which can be different from the number of simulated events in the macro; not all events are going to trigger the detector.

In our simulation, we simulate dust particulates with a radius of 1, 5, 10, 17, and 25 μm. Same as neck events, each sample will have its trigger rate.

The trigger rates of neck and dust events are summarized in Table E.1 and Table E.2, respectively.

6.2.3 Cherenkov

In previous studies, the Cherenkov background was often taken as negligible since we could remove the majority of these events using the fmaxpe but that only works for LG Cherenkov. Since these events are happening in the LGs, they can be identified as surface events. So, the fiducial volume cut would remove any surviving event. But in our study, we are pushing the fiducial volume to 820 mm which will make this background one of the most important sources in our study. The latest analysis of the Cherenkov data was done in 2023 by Jie Hu, a post-doctoral fellow at the University of Alberta, and the author had no contribution. We have used the result of their study to find the expected number of background events using our proposed cutflow.

We cannot use MC simulations for the Cherenkov background. Luckily, we have a few months' worth of data where the detector was in a vacuum state and a ^{232}U calibration source was deployed enhancing the Cherenkov rate by a factor of 50. We also have runs where the detector was filled with LAr and ^{232}U calibration source was also deployed. In the decay chain of this source, we have 2.6 MeV gamma rays from the ^{208}TI isotope. We break this analysis into two parts:

- Compare LAr data with and without the source being deployed. Since there are residual amounts of ^{232}U in the detector components, this will enable us to compare the relative power of the source by comparing the 2.6 MeV γ rays between the two runs.
- Use the vacuum data with the source deployed to calculate the expected background.

For the second part of this analysis, note that the LAr is transparent and the detector being filled with LAr or being in a vacuum would not affect the Cherenkov events except to the extent it blocks some of the Compton scattered gammas that lead to double Cherenkov events.

The relative power of the source was measured by dividing the integral of the PE distribution in the [14843, 16069] range between the two runs which was found to be 1.998%. This indicates that for 1 event of the 2.6 MeV γ, it takes 1 day for the runs with the ^{232}U source and 50.3 days for the runs without the source. Figure 6.2 shows the PE distribution of the two runs with LAr in the detector.

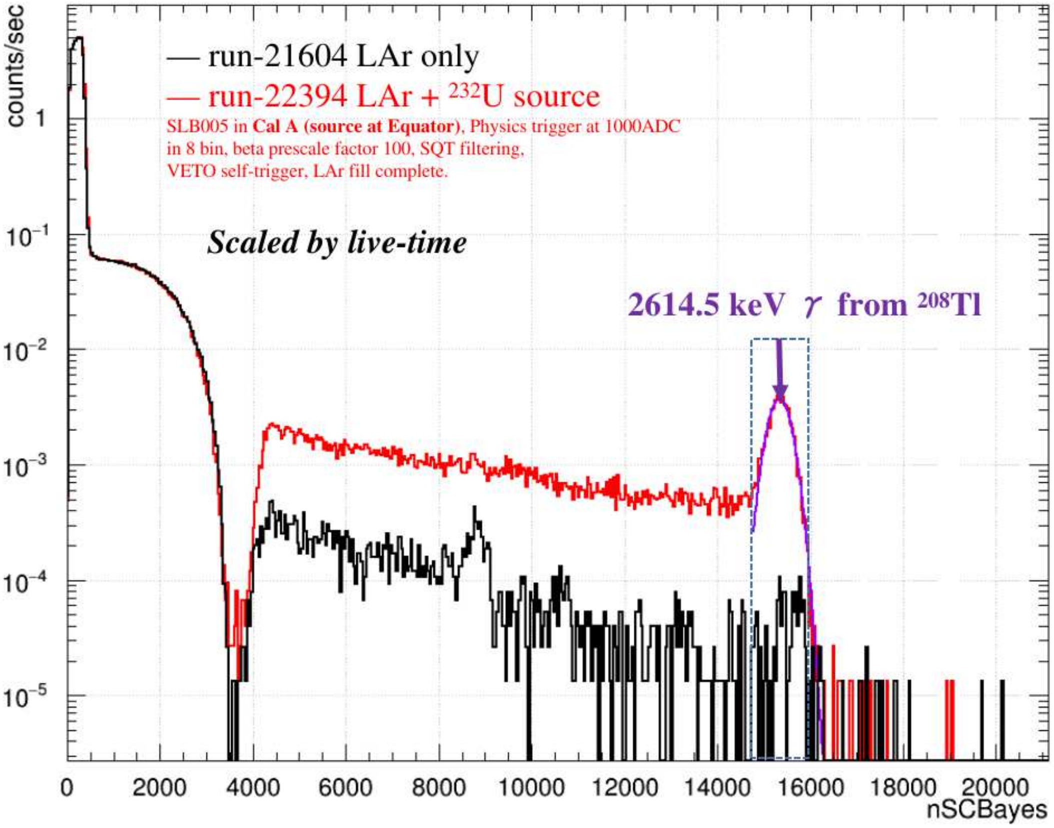

Figure 6.2: PE distribution of two runs where the detector was filled with LAr. The red curve had the ^{232}U calibration source deployed. Plot courtesy of Jie Hu.

Knowing the relative power of the calibration source, we can use the vacuum data to find the expected number of Cherenkov events leaking inside the WIMP ROI. Although we had a few months' worth of data, only 83.53 days were tagged as stable data[1]. We

---

[1] Due to fluctuations in the environment such as the water tank temperature.

also decided to use the same runs suggested by Jie Hu. The 83.53 days have about 2.6 billion events before any cuts are applied. To find the expected number of Cherenkov events we can use:

$$N^{\text{expected}}_{\text{Cherenkov}} = \frac{N_{\text{ROI}}}{50.3} \times \frac{T_{\text{livetime}}}{83.53(days)}, \tag{6.2}$$

where N_{ROI} is again the number of events surviving the full cutflow, 50.3 is the relative power of the calibration source, 83.53 days is the livetime of the vacuum data with the ^{232}U source, and T_{livetime} is the same livetime in the data being considered but for simplicity in units of days rather than seconds.

6.2.4 Neutron

Another background source that will be more important to us due to increasing the fiducial volume is the Neutron background. At the time of writing this thesis, the most accurate study of the neutron background was done by Eric Vazquez in 2018 by considering 16 different sources contributing to the neutron background. The details of that study are outside the scope of this thesis and we only use the final results. The expected number of events was calculated in three different fiducial volumes as shown in Table 6.3. But we cannot use these numbers directly because the cutflow used in our study is different. Eric only considered events with fmaxpe < 0.2, F$_{\text{prompt}} > 0.6$, and a qPE range of 120 to 240 PE. The ^{40}Ar MC samples are the closest simulation we have to a Neutron background that will not burden our computational power. The only difference between neutron recoils and ^{40}Ar (WIMP recoils) is the energy and the position distribution, neither of which affects F$_{\text{prompt}}$.

So, we measure the effect of each cut on the ^{40}Ar samples and apply the same effect to the neutron background. To be conservative in our background expectation, we will ignore the effect of the upper F$_{\text{prompt}}$ bound of the ROI on the neutron background. The ROI we use has a 5% NR loss, so the effect is minimal. Also note that we would be considering different fiducial volumes in our final results and given the limited data from the previous study, we would have to linearly interpolate the expected neutron background at different radial cuts. Figure 6.3 shows the expected number of neutron backgrounds after including the background removal cutflow and applying the effect of the STA. With no fiducial volume, the number of neutron background events can be reduced from 3 events per year to 1 event per year. Note that neutron background is not necessarily a surface background as the neutron can actually interact with the LAr within the detector. Our estimate would be conservative since we did not take into account neutron leakage due to position resolution which the STA was designed to handle.

Fiducial Volume [mm]	Total Events
No cut	5.180 ± 0.792
800	1.594 ± 0.360
550	0.251 ± 0.072

Table 6.3: Number of neutron background events per live-year for no radial cut and two fiducial cuts at 800 and 550 mm in the qPE range of 120 to 240. Results courtesy of Eric Vazquez.

6.2.5 Surface α

The last background source to cover here is the surface α background. At the time of writing this thesis, there is a problem with the MC simulation of surface α events that causes the calculated background from this source to be close to 0. Data clearly shows some background is present. While we are trying to find the issue, for now, we can try to approximate the number of surface α events from physics data and the study of SplitEvent from the previous chapter.

To estimate the surface leakage, we first apply the full cutflow to data except for the fiducial volume and the STA cut. We also know that the majority of the NR events are surface background. For example, in the first year dataset, we have 1341 events in the WIMP ROI from which 1286 (96%) of them reconstruct with MBLR $>$ 840 mm. Although a small percentage of the surviving events are from dust and neck events, to be conservative, we assume all of these events are surface α events. To find the expected number of surface α events leaking inside a given fiducial cut, we can multiply the number of events observed in data by the leakage percentage shown in Figure 5.26 in each PE bin. Note that we had two leakage numbers based on the detector condition. For this study, we take the average of the two graphs as the nominal leakage percentage and the difference as the 1-σ uncertainty. It's noteworthy that for the 1341 events, only 20 events are tagged as ^{40}Ar by the STA. Also, given that we assume all of the surviving events are surface α, this approach is going to give us the upper limit on the contribution from surface events. A more accurate approach would be to subtract the number of expected dust and shadowed α. For now, we will use the upper limit.

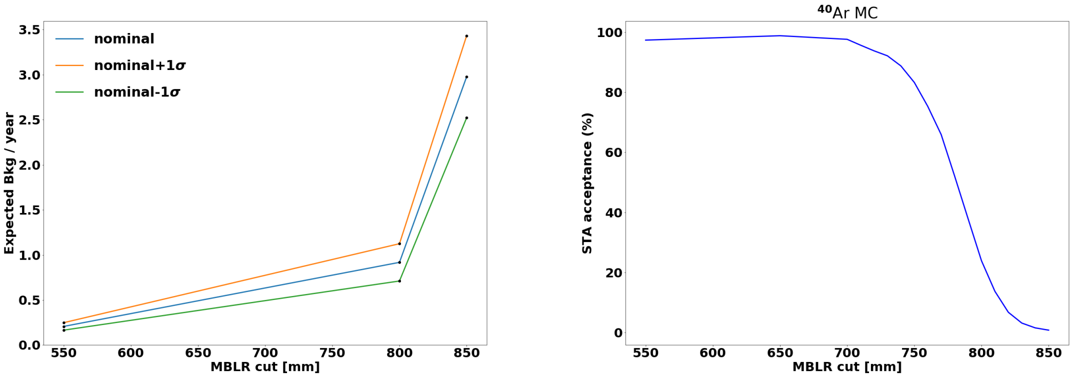

(a) Expected background without STA cut

(b) STA cut efficiency on ^{40}Ar MC

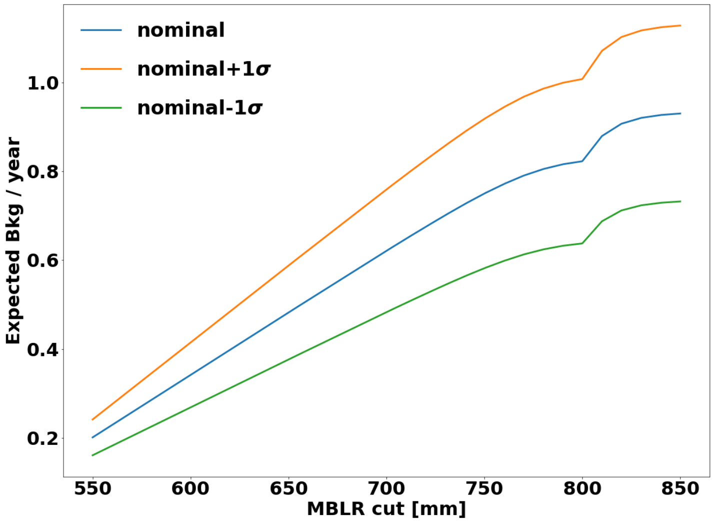

(c) Expected background with STA cut

Figure 6.3: **(a)** shows the number of expected neutron background events within any fiducial volume before applying any STA cut. **(b)** shows the effect of applying the STA cut on ^{40}Ar MC. **(c)** shows the expected neutron background after applying the STA cut.

6.3 MC Background Uncertainty

We have already mentioned how the background uncertainty for neutron and surface α events are derived. For the neck and dust backgrounds, we have relied on MC simulation. In RAT software we have different input parameters controlling different aspects of the simulation such as detector geometry and PMT properties. Some of the input parameters are varied by their 1-σ uncertainty to measure the effect of such variation on the final background count. In DEAP we often consider 8 different variations of the detector condition and optical properties. 6 of these variations are paired systematics, meaning we simulate the $\pm 1\sigma$ variations. This brings the total to 14 simulations for each MC sample. These uncertainties are explained below with their internal abbreviation used in DEAP.

- PMT After-Pulsing (AP^+ and AP^-):
  The AfterPulsing (AP) probability which is a source of noise in the PMTs have an uncertainty of 15%.

- PMT efficiency ($\mathrm{PMT\_eff}^+$ and $\mathrm{PMT\_eff}^-$):
  The quantum efficiency of the PMTs has a 10% uncertainty.

- PMT efficiency smear (PMT_eff_S):
  The efficiency of the PMTs is not constant and has a spread in its nominal value. As such, the efficiency can vary from one PMT to another. To account for this, a spread of 4.5% is randomly applied to all the PMTs.

- Quenching Factor (QF^+ and QF^-):
  The measured QF obtained from the alpha lines are used for the nominal samples and their 1σ value is used for these systematic variations.

- LAr Refractive Index and other optical properties (RI^+ and RI^-):
  The refractive index of LAr has been measured with relatively low uncertainties [177, 178]. In DEAP, the uncertainty of the refractive index and its effect

on the scattering length and the group velocity of photons in LAr is considered a systematic variation.

- TPB Light Yield ($\mathrm{TPB\_LY}^+$ and $\mathrm{TPB\_LY}^-$):
  The LY of the TPB used in DEAP is 882 photons/MeV with a 10% uncertainty [179].

- TPB Scattering Length ($\mathrm{TPB\_SL}^+$ and $\mathrm{TPB\_SL}^-$):
  The thickness of the TPB applied in the detector was 3 μm but the best agreement of MC to data was achieved with a simulated value of 2.25 μm. The actual thickness can be very uneven and the systematic variation in MC considers the TPB thickness to be $2.25^{+2.25}_{-1.125}$ which is scaling the nominal value by a factor of 2 in each direction.

- Disabled PMT 204 (PMT_204):
  For periods of time, we had one or more PMTs turned off. This systematic variation turns off two PMTs with PMT ID 149 and 204.

When we attempt to calculate the exclusion curves, all of these variations should be properly combined into a final expected background and the 1σ uncertainty. section E.1 shows the trigger rate of each systematic variation of each MC sample used in this thesis.

Let's start with the MC systematic variations for the dust and neck simulations. We interpolate MC using the actual distribution of each systematic variation. Thus, the MC simulations only vary the given parameter by exactly 1σ. Given a cutflow, let's call the number of expected background events of a given MC sample using the nominal simulation as n_0. n_i will denote the expected number of events where the ith parameter in the simulation, p_i, was varied by 1σ. Where we able to consider the actual distribution of p_i, n_i would also have a distribution instead of being a single number; i.e. the 1σ of the nominal expected background. But we can still use toy MC to find the distribution of n_i using:

$$n'_i = n_0 + \frac{p'_i - p_{i,0}}{\sigma_i}(n_i - n_0) \tag{6.3}$$

where p'_i is drawn from the Gaussian distribution of p_i with the mean of $p_{i,0}$ and RMS of σ_i. The result is n'_i which is the normal distribution of n_i had we been able to generate thousands of MC simulations. Given enough statistics in the toy MC, the mean of the n'_i distribution will be n_0 and 1σ away from the mean would yield n_i. Note that for systematic variations that involve changing a vector of input parameters, such as QF which is energy dependant, the p'_i is drawn for a Gaussian distribution with $\mu = 0$ and σ=1. As an example, Figure E.3-E.7 show the number of expected background events from the neck and dust samples from each systematic variation using a fiducial volume cut of 820 mm with the updated cutflow using Equation 6.3.

Now that we have an actual distribution of the expected number of background events for each systematic variation, we can once again use toy MC to combine all of these into a single number. To achieve this, we generate millions of toy MC from each systematic distribution and fill a single histogram. We then fit a Gaussian function to this distribution to find the final expected background and its uncertainty for the given source.

6.4 Expected Background & Observed Data

We will be studying different fiducial volume cuts using the updated cutflow mentioned at the beginning of this chapter. Since there have been changes to the RAT software, we will also consider the cutflow used in the 2019 paper [124] to have a direct comparison of our updated study. Table 6.4 shows the expected background from each background source for different fiducial volume cuts. Table 6.5 shows the total number of expected background events and the observed data in the one-year and three-year open datasets corresponding to 230.1 and 380.4 live-days, respectively. Note that we have two fiducial cuts at 630 mm. The row identified with 630* corresponds to the original cutflow and not the updated cutflow proposed in this thesis. As mentioned before, we don't have the best agreement between MC and observed data with the current background model and the DEAP collaboration is working on improving the model. However, the disagreement is not too big to prevent us from studying the benefits of our new STA and the double charge cluster cut.

Note that in Table 6.5, the number of events observed in data does not change as we go from 780 mm to 820 mm. This is because of the STA and double charge cluster cuts. Without these two cuts, the number of events in the 386 live-day dataset would have increased to 44 and 51 events, respectively. All the events that are added by going from 780 mm to 820 mm are removed by the STA and double charge cluster cut.

Fiducial Cut [mm]	Dust	Shadowed α	Neutron	Surface	Cherenkov
630*	0.17 ± 0.54	0.11 ± 0.25	0.31 ± 0.07	0.15 ± 0.07	0.00 ± 0.00
630	4.67 ± 4.40	2.90 ± 1.90	0.09 ± 0.02	0.00 ± 0.00	0.00 ± 0.00
720	7.19 ± 4.19	3.14 ± 2.09	0.14 ± 0.03	0.02 ± 0.00	$0.26^{+0.0}_{-0.26}$
750	7.97 ± 4.11	3.25 ± 2.23	0.16 ± 0.03	0.04 ± 0.01	$0.47^{+0.0}_{-0.47}$
780	8.90 ± 3.84	3.33 ± 2.29	0.17 ± 0.04	0.09 ± 0.01	$1.00^{+0.0}_{-1.00}$
800	8.99 ± 3.79	3.34 ± 2.32	0.18 ± 0.04	0.27 ± 0.01	$1.26^{+0.0}_{-1.26}$
820	8.99 ± 3.76	3.34 ± 2.30	0.31 ± 0.06	1.20 ± 0.06	$1.36^{+0.0}_{-1.36}$

Table 6.4: Expected number of background events from each source at different fiducial volume cuts and the updated cutflow. The first row, 630*, corresponds to the original cutflow used by DEAP.

Fiducial Cut [mm]	Total Background (222.9 days)	Observed Data (222.9 days)	Total Background (386.2 days)	Observed Data (386.2 days)
630*	0.7 ± 0.6	2	1.3 ± 1.0	2
630	7.7 ± 4.8	10	13.3 ± 8.3	14
720	10.5 ± 4.7	13	18.3 ± 8.1	20
750	11.5 ± 4.7	16	19.9 ± 8.1	24
780	12.7 ± 4.5	17	22.0 ± 7.8	25
800	13.0 ± 4.5	17	22.5 ± 7.8	25
820	14.1 ± 4.5	17	24.2 ± 7.8	25

Table 6.5: Total number of expected background and the observed data in the one-year and three-year open datasets corresponding to 222.9 and 386.2 live-days.

6.5 Signal Acceptance & Model Parameters

For calculating the exclusion curves, we use the Maxpatch framework developed by Shawn Westerdale for DEAP collaboration to simulate the WIMP interaction and the detector response. The last two required ingredients for calculating the expected WIMP event rate are the signal acceptance curve and the free parameters of the WIMP and detector model.

We have measured the acceptance using ^{39}Ar data and apply the full cutflow except for the WIMP ROI. This will enable us to have less reliance on MC simulations and also have higher statistics without needing to spend computational resources on MC simulations. Figure 6.4 shows the acceptance curve in each PE bin for the different fiducial volumes using the updated cutflow except for the black curve, 630*, where the original cutflow has been used. Although there is not a huge gain going from 780 mm to 820 mm, given we are not adding any data, it should improve our exclusion curves. Note that acceptance is defined as the ratio of the events passing the cutflow, including the fiducial volume, to the total number of events passing the low-level cuts.

Table 6.6 shows the four free astrophysical parameters in the Maxpatch framework to calculate the velocity profile of the WIMP in the Milky Way. Table 6.7 shows the detector parameters used to describe the response function relating the number of detected PEs to the deposited energy. $<N_{\mathrm{DN}}>$ is the average number of PEs emitted by dark noise and uncorrelated photons, Y_{PE} is the LY, σ^2_{PE} is a resolution scaling factor, and $\sigma^2_{\mathrm{rel,\ LY}}$ explains the difference between the LY and its mean value. The values used in this study are the same as those used in our second paper [124].

Parameter	Model Value
Galactic Escape Velocity ($\mathrm{v_{esc}}$)	544 km/s
Circular Velocity of the Sun ($\mathrm{v_0}$)	220 km/s
Velocity of the Earth ($\mathrm{v_E}$)	230 km/s
WIMP Density	0.3 GeV/cm^3

Table 6.6: The free astrophysical parameters supported by the Maxpatch framework used to calculate the WIMP event rate.

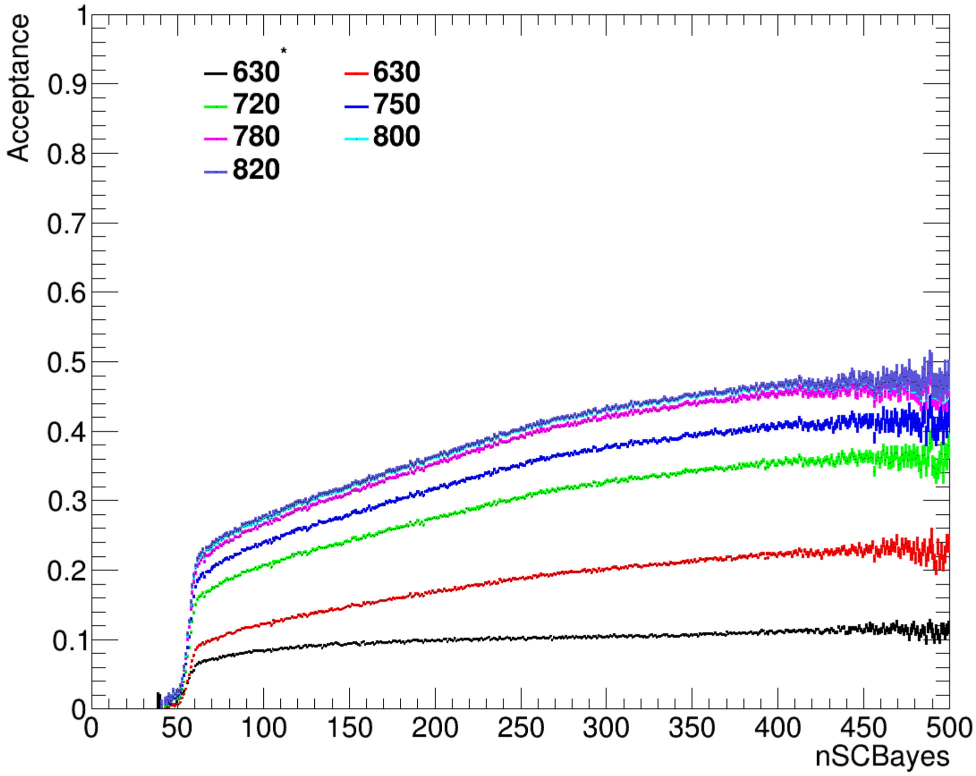

Figure 6.4: The acceptance curves for different fiducial volumes using the updated cutflow in each PE bin, except for the black curve, which uses the original cutflow.

PE mean	$<N_{\mathrm{DN}}>$ 1.1 ±0.2 PE	Y_{PE} 6.1±0.4 PE/keV$_{\mathrm{ee}}$
Resolution	σ^2_{PE} 1.4 ±0.1 PE	$\sigma^2_{\mathrm{rel,\ LY}}$ 0.0004

Table 6.7: The free parameters supported by the Maxpatch framework to model the detector response in detecting PEs.

6.6 Exclusion Curve

Having all the required ingredients, we can set the 90% upper Confidence Level (CL) on the SI WIMP-nucleon cross-section using the frequentist CL$_s$ method which we will briefly explain here. Note that the CL$_s$ approach is a conservative way to set the upper limits. But the DEAP collaboration has also developed a more rigorous Profile Likelihood Ratio (PLR) analysis to improve our limits. In this thesis, we are trying to show the improvement we can get by just expanding the fiducial volume. This should be observed independent of the approach for setting the upper limit. Once the collaboration agrees to the proposed changes, we can improve our limits even further by switching to the PLR analysis.

Let's assume we have a test statistic q that we are going to use to differentiate between the hypothesis that the data comprise a combination of signal and background $(s+b)$, and that which suggests the presence of background only (b), latter often referred to as the null-hypothesis. The two distributions would corresponds to $f\left(q|s+b\right)$ and $f\left(q|b\right)$, respectively. We will talk about the format of the function later. Then the CL$_s$ ratio is defined as:

$$CL_s = \frac{CL_{s+b}}{CL_b} = \frac{p_{s+b}}{1-p_b}, \tag{6.4}$$

where CL_{s+b} is the p-value of the signal+background hypothesis and CL_b is the one minus the p-value of the background-only hypothesis. The p-values are defined as:

$$\begin{aligned} p_{s+b} &= P\left(q \leq q_{obs}|s+b\right) = \int_0^{q_{obs}} f\left(q|s+b\right) dq, \\ 1-p_b &= \int_0^{q_{obs}} f\left(q|b\right) dq, \end{aligned} \tag{6.5}$$

where q_{obs} is the observed value of the test variable. To set an upper CL means to require $CL_s < \alpha$ where α is defined through CL$= 1-\alpha$. In our case of 90% CL, $\alpha = 0.1$.

For a cut-and-count method, the form of the f is usually taken as a Poisson distribution. When using Poisson statistics, to incorporate the effect of the background uncertainty in CL, a common choice is a Gaussian function as described in Ref. [180].

So, Equation 6.5 can be written as:

$$\begin{aligned} CL_{s+b} &= \int_{q=0}^{q_{obs}} \int_{x=0}^{\infty} \text{Poiss}(q \mid x+s) \; \text{Gauss}(x|n_{bkg}, \sigma_{bkg}) \; dx \; dq, \\ CL_{s+b} &= \frac{1}{\sqrt{2\pi}\sigma_{bkg}} \int_{q=0}^{q_{obs}} \int_{x=0}^{\infty} \frac{x^q}{q!} e^{-x} \; e^{-\frac{(x-n_{bkg})^2}{2\sigma_{bkg}^2}} \; dx \; dq, \end{aligned} \tag{6.6}$$

where n_{bkg} and σ_{bkg} correspond to the total expected number of background events and its uncertainty, respectively. Then $1 - p_b$ is the same integral but requiring $s = 0$; i.e $1 - p_b = CL_{s+b}|_{s=0}$.

Figure 6.5 shows the upper 90% CL exclusion curves using 223 and 386 live-days datasets for different fiducial volumes. For comparison, we have shown the curve for the original cutflow used in our 2019 paper [124]. There are a few notable features from these curves to mention.

As we can see from both datasets, increasing the fiducial volume improves our limits, by almost 80% when going from 630 mm to 820 mm. Using the 386 live-days, the original cutflow with a fiducial volume of 630 mm seems to outperform the 750 mm with the updated cutflow. If we look back to Table 6.5, we see that increasing the livetime of the dataset did not add any observed data in the ROI but our background prediction would scale with livetime. This would hugely benefit setting the upper limit. Another point is that the CL_s method has known limitations when dealing with very few number of observed events; one sets limits at levels that have little to no sensitivity. Another problem with using the original cutflow is that the background model would deviate from the observed data at higher radii; for example, the expected background with the original cutflow but the fiducial volume of 720 mm would be 1.7±0.8 events in 223 live-days while the observed data shows 5 events, a difference of more than 4-σ. This would limit our purpose of increasing the fiducial volume. We should note that our 223 live-day result with the original cutflow is different from that which was published in 2019 due to updates to the RAT framework. The 2019 paper [124] result was published under the assumption of no observed events in the ROI while future updates of the software framework added 2 observed events.

Another feature that can be observed is that the gain from pushing the fiducial volume to 820 mm improves with increasing the amount of detector livetime. At the time of writing this thesis, the DEAP collaboration is actively considering a fiducial volume of 720 mm with the PLR analysis. For a WIMP mass of 100 GeV, the 820 mm fiducial volume shows 23% and 32% improvement compared to the 720 mm case for the first-year and the open three-year dataset, respectively. By increasing the livetime by 70%, the gain has improved by almost 50%. The full three-year dataset would increase the livetime by another factor of two which would only improve our results at 820 mm compared to 720 mm.

The main limiting factors to improve the limits set by the DEAP collaboration at any given fiducial volume are the neck and dust background. The new MVA model will enable us to remove the shadowed α background events with minimal cost to our signal acceptance. But the dust background is difficult to remove through the analysis of the data. There is a hardware upgrade planned for DEAP-3600 to remove the dust background. Through the implementation of the MVA analysis, and later on the hardware upgrade, we can expect further improvements that can be gained by increasing the fiducial volume. The number of expected shadowed α events is mostly independent of the fiducial volume. If the hardware upgrade can reduce the dust background, the only limiting factor for expanding the fiducial volume would be the surface background which we are now capable of handling with the STA.

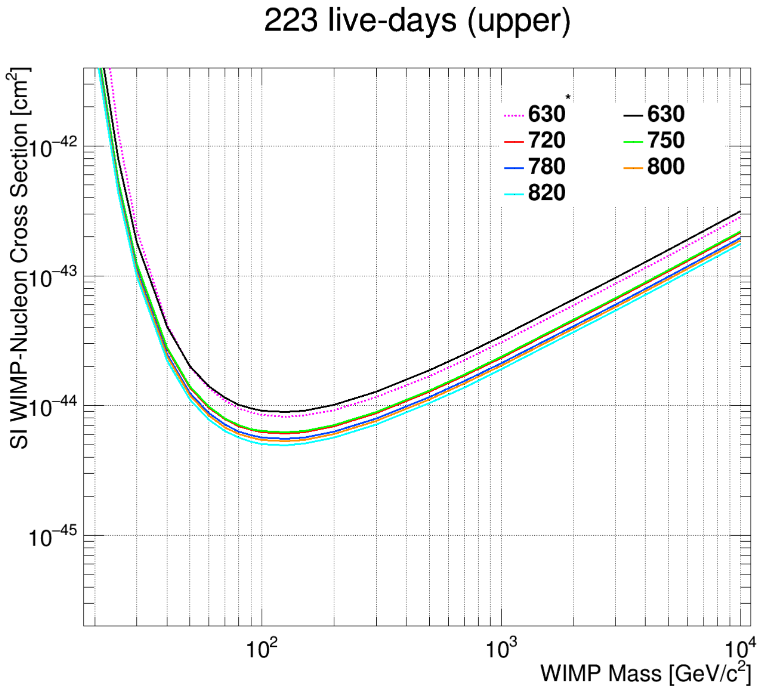

(a) 223 live-days

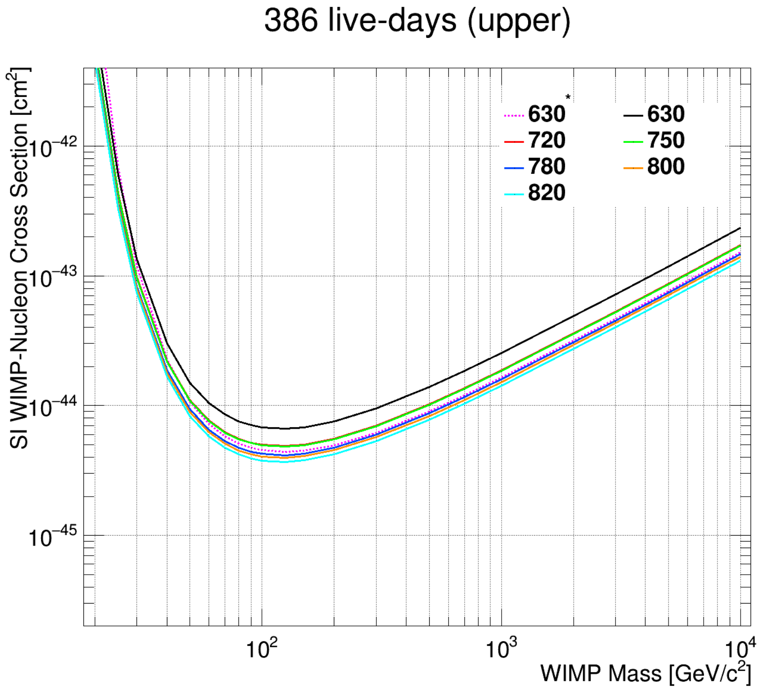

(b) 386 live-days

Figure 6.5: The upper 90% CL for the 6 fiducial volumes studied with the updated cutflow. The results from the original cutflow are also shown for comparison. **(a)** and **(b)** show the results using the 223 and 386 live-days datasets.

6.7 Future Steps

Last but not least, we would like to remind the reader that our purpose was not setting the best exclusion limits using the DEAP-3600 data. Most of the analysis that we showed in this thesis took the conservative route, including the CL_s method used to obtain the upper limits. Our main purpose was to show the feasibility of increasing the fiducial volume for WIMP search analysis, even up to 820 mm, to make the most use of our detector, and possibly future generations of DEAP detector. Here are the most important points the collaboration is working towards:

- Using the MVA analysis to remove shadowed α events.
- Better understanding the Cherenkov background and optimizing the double charge cluster cut further.
- Optimizing the selection of WIMP ROI
- Hardware upgrade to remove dust background and shadowed neck alphas.
- Utilizing the PLR analysis to set the most stringent upper limits.

There is one last point to be made regarding the double charge cluster algorithm that we implemented. The events that are removed by this cut, both in the WIMP ROI and in the ^{39}Ar region, seem to be most compatible with pile-up events. When defining the acceptance, see Figure 6.4, the denominator of the ratio is the number of events passing the pile-up cuts and not the total number of observed events. If the events removed by the double charge cluster cut are in fact mostly pile-up events, we can add an improved version of this cut to identify such events and improve our WIMP acceptance.

Chapter 7

Conclusions

In this thesis, we have shown that the recombination model, although previously thought to be difficult to do, can be tuned to match the time profile of different event types observed in data. We also developed a scintillation likelihood processor that would measure the likelihood of an event being caused by LAr scintillation or other types of phenomena such as discharge events. Although the processor did not make it to our final cutflow, the MVA analysis is making use of this processor to better identify neck events.

Another measurement that the DEAP-3600 is capable of performing is finding the α quenching factors using the three isotopes we see in our detector. We also showed the feasibility of using the late lights in the PMTs to measure the amount of charge from these events to avoid running into problems such as PMT clipping and saturation. This approach is still under review by the collaboration. Also, instead of relying on saturation correction algorithms, we have shown that using the late light will improve our position resolution for events at higher energies that cause PMT saturation.

Our last and main project was to study the leakage of surface events, especially surface α events. We designed and implemented a new processor to perform a likelihood analysis on the charge distribution of different event types and identify those that match the charge distribution of surface events. In our study, we showed that we can expand the fiducial radius used for WIMP search analysis to 820 mm compared to the initial 630 mm used by the collaboration and the updated PLR analysis that was studying a fiducial radius of 720 mm. With a WIMP mass of 100 GeV, the fiducial radius of

820 mm, compared to 720 mm, showed a 23% and 32% improvement using the 223 and 386 live-days datasets, respectively. The gain achieved by increasing the fiducial radius should improve once the collaboration decides to un-blind the full 802 live-days dataset. Finally, we set a limit on the WIMP-nucleon SI cross-section of $3.8 \times 10^{-45}\text{cm}^2$ ($1.4 \times 10^{-44}\text{cm}^2$) for a WIMP mass of 100 GeV/c^2 (1 TeV/c^2) at 90% CL.

References

[1] P. Zyla *et al.*, “Review of Particle Physics,” *PTEP*, vol. 2020, no. 8, p. 083C01, 2020. DOI: `10.1093/ptep/ptaa104` (cit. on pp. 1–3, 17, 24–26).

[2] A. Einstein, “The Foundation of the General Theory of Relativity,” *Annalen Phys.*, vol. 49, no. 7, J.-P. Hsu and D. Fine, Eds., pp. 769–822, 1916. DOI: `10.1002/andp.200590044` (cit. on pp. 1, 5).

[3] D. Baumann. “Cosmology lecture notes.” (), [Online]. Available: `http://cosmology.amsterdam/education/cosmology/` (cit. on pp. 1, 8, 10, 189, 193).

[4] G. Aad *et al.*, “Observation of a new particle in the search for the Standard Model Higgs boson with the ATLAS detector at the LHC,” *Phys. Lett. B*, vol. 716, pp. 1–29, 2012. DOI: `10.1016/j.physletb.2012.08.020`. arXiv: `1207.7214 [hep-ex]` (cit. on p. 3).

[5] G. Aad *et al.*, “Evidence for the spin-0 nature of the Higgs boson using ATLAS data,” *Phys. Lett. B*, vol. 726, pp. 120–144, 2013. DOI: `10.1016/j.physletb.2013.08.026`. arXiv: `1307.1432 [hep-ex]` (cit. on p. 3).

[6] S. Chatrchyan *et al.*, “Observation of a New Boson at a Mass of 125 GeV with the CMS Experiment at the LHC,” *Phys. Lett. B*, vol. 716, pp. 30–61, 2012. DOI: `10.1016/j.physletb.2012.08.021`. arXiv: `1207.7235 [hep-ex]` (cit. on p. 3).

[7] J. D. Lykken, “Beyond the Standard Model,” May 2010. arXiv: `1005.1676 [hep-ph]` (cit. on p. 3).

[8] K. Schwarzschild, “On the gravitational field of a mass point according to Einstein’s theory,” *Sitzungsber. Preuss. Akad. Wiss. Berlin (Math. Phys.)*, vol. 1916, pp. 189–196, 1916. arXiv: `physics/9905030` (cit. on p. 6).

[9] G. Lemaître, “Un Univers homogène de masse constante et de rayon croissant rendant compte de la vitesse radiale des nébuleuses extra-galactiques,” *Annales de la Société Scientifique de Bruxelles*, vol. 47, pp. 49–59, Jan. 1927 (cit. on p. 6).

[10] M. Livio, “Lost in translation: Mystery of the missing text solved,” vol. 479, no. 7372, pp. 171–173, Nov. 2011. DOI: `10.1038/479171a` (cit. on p. 6).

[11] M. Livio and A. G. Riess, “Measuring the Hubble constant,” *Physics Today*, vol. 66, no. 10, p. 41, Jan. 2013. DOI: `10.1063/PT.3.2148` (cit. on p. 6).

[12] E. Hubble, "A Relation between Distance and Radial Velocity among Extra-Galactic Nebulae," *Proceedings of the National Academy of Science*, vol. 15, no. 3, pp. 168–173, Mar. 1929. DOI: 10.1073/pnas.15.3.168 (cit. on p. 6).

[13] S. Perlmutter *et al.*, "Measurements of Ω and Λ from 42 high redshift supernovae," *Astrophys. J.*, vol. 517, pp. 565–586, 1999. DOI: 10.1086/307221. arXiv: astro-ph/9812133 (cit. on p. 7).

[14] A. G. Riess *et al.*, "Observational Evidence from Supernovae for an Accelerating Universe and a Cosmological Constant," vol. 116, no. 3, pp. 1009–1038, Sep. 1998. DOI: 10.1086/300499. arXiv: astro-ph/9805201 [astro-ph] (cit. on p. 7).

[15] A. Einstein, "Die Grundlage der allgemeinen Relativitätstheorie," *Annalen der Physik*, vol. 354, no. 7, pp. 769–822, Jan. 1916. DOI: 10.1002/andp.19163540702 (cit. on p. 7).

[16] F. W. Dyson, A. S. Eddington, and C. Davidson, "A Determination of the Deflection of Light by the Sun's Gravitational Field, from Observations Made at the Total Eclipse of May 29, 1919," *Philosophical Transactions of the Royal Society of London Series A*, vol. 220, pp. 291–333, Jan. 1920. DOI: 10.1098/rsta.1920.0009 (cit. on p. 7).

[17] M. Stanley, "An expedition to heal the wounds of war. The 1919 eclipse and Eddington as Quaker adventurer," *Isis. Journal of the History of Science Society*, vol. 94, no. 1, pp. 57–89, Mar. 2003 (cit. on p. 7).

[18] B. P. Abbott *et al.*, "Observation of Gravitational Waves from a Binary Black Hole Merger," *Phys. Rev. Lett.*, vol. 116, no. 6, p. 061 102, 2016. DOI: 10.1103/PhysRevLett.116.061102. arXiv: 1602.03837 [gr-qc] (cit. on p. 7).

[19] K. Akiyama *et al.*, "First M87 Event Horizon Telescope Results. I. The Shadow of the Supermassive Black Hole," *Astrophys. J.*, vol. 875, no. 1, p. L1, 2019. DOI: 10.3847/2041-8213/ab0ec7. arXiv: 1906.11238 [astro-ph.GA] (cit. on p. 7).

[20] P. A. R. Ade *et al.*, "Planck 2015 results. XIII. Cosmological parameters," *Astron. Astrophys.*, vol. 594, A13, 2016. DOI: 10.1051/0004-6361/201525830. arXiv: 1502.01589 [astro-ph.CO] (cit. on p. 7).

[21] A. G. Riess *et al.*, "Observational evidence from supernovae for an accelerating universe and a cosmological constant," *Astron. J.*, vol. 116, pp. 1009–1038, 1998. DOI: 10.1086/300499. arXiv: astro-ph/9805201 (cit. on pp. 11, 13).

[22] R. J. Adler, B. Casey, and O. C. Jacob, "Vacuum catastrophe: An elementary exposition of the cosmological constant problem," *American Journal of Physics*, vol. 63, no. 7, pp. 620–626, Jul. 1995. DOI: 10.1119/1.17850 (cit. on p. 11).

[23] D. L. Wiltshire, "Exact solution to the averaging problem in cosmology," *Phys. Rev. Lett.*, vol. 99, p. 251 101, 2007. DOI: 10.1103/PhysRevLett.99.251101. arXiv: 0709.0732 [gr-qc] (cit. on p. 11).

[24] M. Ishak *et al.*, "Dark Energy or Apparent Acceleration Due to a Relativistic Cosmological Model More Complex than FLRW?" *Phys. Rev. D*, vol. 78, p. 123 531, 2008, [Erratum: Phys.Rev.D 84, 089902 (2011)]. DOI: `10.1103/PhysRevD.84.089902`. arXiv: `0708.2943 [astro-ph]` (cit. on p. 11).

[25] T. Mattsson, "Dark energy as a mirage," *Gen. Rel. Grav.*, vol. 42, pp. 567–599, 2010. DOI: `10.1007/s10714-009-0873-z`. arXiv: `0711.4264 [astro-ph]` (cit. on p. 11).

[26] J. R. Bond *et al.*, "Dark matter and shocked pancakes," in *Formation and Evolution of Galaxies and Large Structures in the Universe*, J. Audouze and J. Tran Thanh Van, Eds., ser. NATO Advanced Study Institute (ASI) Series C, vol. 117, Jan. 1984, p. 87 (cit. on p. 11).

[27] J. R. Primack and G. R. Blumenthal, "What is the dark matter ? Implications for galaxy formation and particle physics," in *Formation and Evolution of Galaxies and Large Structures in the Universe*, J. Audouze and J. Tran Thanh Van, Eds., ser. NATO Advanced Study Institute (ASI) Series C, vol. 117, Jan. 1984, p. 163 (cit. on pp. 11, 12).

[28] P. J. E. Peebles, "Large-scale background temperature and mass fluctuations due to scale-invariant primeval perturbations," vol. 263, pp. L1–L5, Dec. 1982. DOI: `10.1086/183911` (cit. on p. 12).

[29] J. R. Bond, A. S. Szalay, and M. S. Turner, "Formation of Galaxies in a Gravitino-Dominated Universe," vol. 48, no. 23, pp. 1636–1640, Jun. 1982. DOI: `10.1103/PhysRevLett.48.1636` (cit. on p. 12).

[30] G. R. Blumenthal, H. Pagels, and J. R. Primack, "Galaxy formation by dissipationless particles heavier than neutrinos," vol. 299, no. 5878, pp. 37–38, Sep. 1982. DOI: `10.1038/299037a0` (cit. on p. 12).

[31] G. R. Blumenthal *et al.*, "Formation of galaxies and large-scale structure with cold dark matter.," vol. 311, pp. 517–525, Oct. 1984. DOI: `10.1038/311517a0` (cit. on p. 12).

[32] J. Sommer-Larsen and A. Dolgov, "Formation of disk galaxies: warm dark matter and the angular momentum problem," *Astrophys. J.*, vol. 551, pp. 608–623, 2001. DOI: `10.1086/320211`. arXiv: `astro-ph/9912166` (cit. on p. 12).

[33] C. J. Hogan, "Warm Dark Matter: Clues to Primordial Phase Density from the Structure of Galaxy Halos," in *International School of Astrophysics, Daniel Chalonge: 7th Course: Current Topics in Astrofundamental Physics (A NATO Advanced Study Institute Euroconference)*, Dec. 1999. arXiv: `astro-ph/9912549` (cit. on p. 12).

[34] K. A. Olive and M. S. Turner, "Cosmological bounds on the masses of stable, right-handed neutrinos," vol. 25, no. 1, pp. 213–216, Jan. 1982. DOI: `10.1103/PhysRevD.25.213` (cit. on p. 12).

[35] H. Pagels and J. R. Primack, "Supersymmetry, cosmology, and new physics at teraelectronvolt energies," vol. 48, pp. 223–226, Jan. 1982. DOI: 10.1103/PhysRevLett.48.223 (cit. on p. 12).

[36] A. Kamada, K. T. Inoue, and T. Takahashi, "Constraints on mixed dark matter from anomalous strong lens systems," *Phys. Rev. D*, vol. 94, no. 2, p. 023 522, 2016. DOI: 10.1103/PhysRevD.94.023522. arXiv: 1604.01489 [astro-ph.CO] (cit. on p. 13).

[37] R. H. Wechsler and J. L. Tinker, "The Connection between Galaxies and their Dark Matter Halos," *Ann. Rev. Astron. Astrophys.*, vol. 56, pp. 435–487, 2018. DOI: 10.1146/annurev-astro-081817-051756. arXiv: 1804.03097 [astro-ph.GA] (cit. on p. 13).

[38] J. E. Gunn and I. Gott J. Richard, "On the Infall of Matter Into Clusters of Galaxies and Some Effects on Their Evolution," vol. 176, p. 1, Aug. 1972. DOI: 10.1086/151605 (cit. on p. 13).

[39] J. F. Navarro, C. S. Frenk, and S. D. M. White, "The Structure of cold dark matter halos," *Astrophys. J.*, vol. 462, pp. 563–575, 1996. DOI: 10.1086/177173. arXiv: astro-ph/9508025 (cit. on pp. 13, 14).

[40] A. E. Evrard, C. A. Metzler, and J. F. Navarro, "Mass estimates of X-ray clusters," *Astrophys. J.*, vol. 469, p. 494, 1996. DOI: 10.1086/177798. arXiv: astro-ph/9510058 (cit. on p. 14).

[41] J. F. Navarro, C. S. Frenk, and S. D. M. White, "A Universal density profile from hierarchical clustering," *Astrophys. J.*, vol. 490, pp. 493–508, 1997. DOI: 10.1086/304888. arXiv: astro-ph/9611107 (cit. on p. 14).

[42] N. Okabe *et al.*, "LoCuSS: The Mass Density Profile of Massive Galaxy Clusters at z=0.2," *Astrophys. J. Lett.*, vol. 769, p. L35, 2013. DOI: 10.1088/2041-8205/769/2/L35. arXiv: 1302.2728 [astro-ph.CO].

[43] W. Wang *et al.*, "A weak gravitational lensing recalibration of the scaling relations linking the gas properties of dark haloes to their mass," *Mon. Not. Roy. Astron. Soc.*, vol. 456, no. 3, pp. 2301–2320, 2016. DOI: 10.1093/mnras/stv2809. arXiv: 1509.05784 [astro-ph.CO] (cit. on p. 14).

[44] A. Klypin, H. Zhao, and R. S. Somerville, "Lambda CDM-based models for the Milky Way and M31 I: Dynamical models," *Astrophys. J.*, vol. 573, pp. 597–613, 2002. DOI: 10.1086/340656. arXiv: astro-ph/0110390 (cit. on p. 14).

[45] W. J. G. de Blok, S. S. McGaugh, and V. C. Rubin, "High-Resolution Rotation Curves of Low Surface Brightness Galaxies. II. Mass Models," vol. 122, no. 5, pp. 2396–2427, Nov. 2001. DOI: 10.1086/323450 (cit. on p. 14).

[46] R. Kuzio de Naray and T. Kaufmann, "Recovering cores and cusps in dark matter haloes using mock velocity field observations," vol. 414, no. 4, pp. 3617–3626, Jul. 2011. DOI: 10.1111/j.1365-2966.2011.18656.x. arXiv: 1012.3471 [astro-ph.CO] (cit. on p. 14).

[47] J. F. Navarro, V. R. Eke, and C. S. Frenk, "The cores of dwarf galaxy halos," *Mon. Not. Roy. Astron. Soc.*, vol. 283, pp. L72–L78, 1996. DOI: `10.1093/mnras/283.3.L72`. arXiv: `astro-ph/9610187` (cit. on p. 14).

[48] A. Pontzen and F. Governato, "How supernova feedback turns dark matter cusps into cores," vol. 421, no. 4, pp. 3464–3471, Apr. 2012. DOI: `10.1111/j.1365-2966.2012.20571.x`. arXiv: `1106.0499 [astro-ph.CO]` (cit. on p. 14).

[49] M. R. Lovell *et al.*, "The haloes of bright satellite galaxies in a warm dark matter universe," vol. 420, no. 3, pp. 2318–2324, Mar. 2012. DOI: `10.1111/j.1365-2966.2011.20200.x`. arXiv: `1104.2929 [astro-ph.CO]` (cit. on p. 14).

[50] O. D. Elbert *et al.*, "Core formation in dwarf haloes with self-interacting dark matter: no fine-tuning necessary," *Mon. Not. Roy. Astron. Soc.*, vol. 453, no. 1, pp. 29–37, 2015. DOI: `10.1093/mnras/stv1470`. arXiv: `1412.1477 [astro-ph.GA]` (cit. on p. 14).

[51] K. A. Oman *et al.*, "The unexpected diversity of dwarf galaxy rotation curves," *Mon. Not. Roy. Astron. Soc.*, vol. 452, no. 4, pp. 3650–3665, 2015. DOI: `10.1093/mnras/stv1504`. arXiv: `1504.01437 [astro-ph.GA]` (cit. on p. 14).

[52] B. J. Kavanagh and A. M. Green, "Improved determination of the WIMP mass from direct detection data," *Phys. Rev. D*, vol. 86, p. 065 027, 2012. DOI: `10.1103/PhysRevD.86.065027`. arXiv: `1207.2039 [astro-ph.CO]` (cit. on pp. 15, 34, 40, 41).

[53] G. Jungman, M. Kamionkowski, and K. Griest, "Supersymmetric dark matter," *Physics Reports*, vol. 267, no. 5, pp. 195–373, 1996, ISSN: 0370-1573. DOI: `https://doi.org/10.1016/0370-1573(95)00058-5`. [Online]. Available: `https://www.sciencedirect.com/science/article/pii/0370157395000585` (cit. on p. 15).

[54] A. M. Green, "Astrophysical uncertainties on direct detection experiments," *Mod. Phys. Lett. A*, vol. 27, p. 1 230 004, 2012. DOI: `10.1142/S0217732312300042`. arXiv: `1112.0524 [astro-ph.CO]` (cit. on p. 15).

[55] N. W. Evans, C. A. J. O'Hare, and C. McCabe, "Refinement of the standard halo model for dark matter searches in light of the Gaia Sausage," *Phys. Rev. D*, vol. 99, no. 2, p. 023 012, 2019. DOI: `10.1103/PhysRevD.99.023012`. arXiv: `1810.11468 [astro-ph.GA]` (cit. on pp. 15, 16, 18).

[56] V. Belokurov *et al.*, "Co-formation of the disc and the stellar halo," vol. 478, no. 1, pp. 611–619, Jul. 2018. DOI: `10.1093/mnras/sty982`. arXiv: `1802.03414 [astro-ph.GA]` (cit. on p. 16).

[57] D. Carollo *et al.*, "Two stellar components in the halo of the Milky Way," *Nature*, vol. 450, pp. 1020–1025, 2007. DOI: `10.1038/nature06460`. arXiv: `0706.3005 [astro-ph]` (cit. on p. 16).

[58] G. Myeong *et al.*, "The milky way halo in action space," *The Astrophysical Journal Letters*, vol. 856, no. 2, p. L26, 2018 (cit. on p. 16).

[59] J. T. Mackereth *et al.*, "The origin of accreted stellar halo populations in the Milky Way using APOGEE, Gaia, and the EAGLE simulations," vol. 482, no. 3, pp. 3426–3442, Jan. 2019. DOI: `10.1093/mnras/sty2955`. arXiv: `1808.00968 [astro-ph.GA]` (cit. on p. 16).

[60] A. Helmi *et al.*, "The merger that led to the formation of the Milky Way's inner stellar halo and thick disk," vol. 563, no. 7729, pp. 85–88, Oct. 2018. DOI: `10.1038/s41586-018-0625-x`. arXiv: `1806.06038 [astro-ph.GA]` (cit. on p. 16).

[61] J. D. Kruijssen *et al.*, "The formation and assembly history of the milky way revealed by its globular cluster population," *Monthly Notices of the Royal Astronomical Society*, vol. 486, no. 3, pp. 3180–3202, 2019 (cit. on p. 16).

[62] C. Wegg, O. Gerhard, and M. Bieth, "The gravitational force field of the galaxy measured from the kinematics of rr lyrae in gaia," *Monthly Notices of the Royal Astronomical Society*, vol. 485, pp. 3296–3316, May 2019. DOI: `10.1093/mnras/stz572` (cit. on p. 16).

[63] N. W. Evans *et al.*, "The alignment of the second velocity moment tensor in galaxies," *Monthly Notices of the Royal Astronomical Society*, vol. 456, no. 4, pp. 4506–4523, Jan. 2016, ISSN: 0035-8711. DOI: `10.1093/mnras/stv2729`. eprint: `https://academic.oup.com/mnras/article-pdf/456/4/4506/9378136/stv2729.pdf`. [Online]. Available: `https://doi.org/10.1093/mnras/stv2729` (cit. on p. 16).

[64] G. C. Myeong *et al.*, "The Sausage Globular Clusters," *Astrophys. J. Lett.*, vol. 863, no. 2, p. L28, 2018. DOI: `10.3847/2041-8213/aad7f7`. arXiv: `1805.00453 [astro-ph.GA]` (cit. on p. 16).

[65] N. W. Evans, R. M. Hafner, and P. T. de Zeeuw, "Simple three-integral scale-free galaxy models," *Mon. Not. Roy. Astron. Soc.*, vol. 286, p. 315, 1997. DOI: `10.1093/mnras/286.2.315`. arXiv: `astro-ph/9611162` (cit. on pp. 16, 17).

[66] J. I. Read, "The Local Dark Matter Density," *J. Phys. G*, vol. 41, p. 063 101, 2014. DOI: `10.1088/0954-3899/41/6/063101`. arXiv: `1404.1938 [astro-ph.GA]` (cit. on p. 17).

[67] R. J. J. Grand *et al.*, "The effects of dynamical substructure on Milky Way mass estimates from the high velocity tail of the local stellar halo," *Mon. Not. Roy. Astron. Soc.*, vol. 487, no. 1, pp. L72–L76, 2019. DOI: `10.1093/mnrasl/slz092`. arXiv: `1905.09834 [astro-ph.GA]` (cit. on p. 18).

[68] T. S. van Albada *et al.*, "Distribution of dark matter in the spiral galaxy NGC 3198.," vol. 295, pp. 305–313, Aug. 1985. DOI: `10.1086/163375` (cit. on p. 18).

[69] F. Zwicky, "On the Masses of Nebulae and of Clusters of Nebulae," *apj*, vol. 86, p. 217, Oct. 1937. DOI: `10.1086/143864` (cit. on p. 19).

[70] N. Aghanim *et al.*, "Planck 2018 results. VI. Cosmological parameters," *Astron. Astrophys.*, vol. 641, A6, 2020. DOI: `10.1051/0004-6361/201833910`. arXiv: `1807.06209 [astro-ph.CO]` (cit. on pp. 19, 25).

[71] K. C. Freeman, “On the Disks of Spiral and S0 Galaxies,” *apj*, vol. 160, p. 811, Jun. 1970. DOI: 10.1086/150474 (cit. on p. 19).

[72] V. C. Rubin and J. Ford W. Kent, “Rotation of the Andromeda Nebula from a Spectroscopic Survey of Emission Regions,” *apj*, vol. 159, p. 379, Feb. 1970. DOI: 10.1086/150317 (cit. on p. 19).

[73] V. C. Rubin, J. Ford W. K., and N. Thonnard, “Rotational properties of 21 SC galaxies with a large range of luminosities and radii, from NGC 4605 (R=4kpc) to UGC 2885 (R=122kpc).,” *apj*, vol. 238, pp. 471–487, Jun. 1980. DOI: 10.1086/158003 (cit. on pp. 20, 21).

[74] D. Walsh, R. F. Carswell, and R. J. Weymann, “0957+561 A, B: twin quasistellar objects or gravitational lens?,” vol. 279, pp. 381–384, May 1979. DOI: 10.1038/279381a0 (cit. on p. 22).

[75] D. Clowe *et al.*, “A direct empirical proof of the existence of dark matter,” *Astrophys. J. Lett.*, vol. 648, pp. L109–L113, 2006. DOI: 10.1086/508162. arXiv: astro-ph/0608407 (cit. on p. 23).

[76] N. Aghanim *et al.*, “Planck 2018 results. I. Overview and the cosmological legacy of Planck,” *Astron. Astrophys.*, vol. 641, A1, 2020. DOI: 10.1051/0004-6361/201833880. arXiv: 1807.06205 [astro-ph.CO] (cit. on pp. 24, 25).

[77] D. J. Fixsen, “The temperature of the cosmic microwave background,” *The Astrophysical Journal*, vol. 707, no. 2, 916–920, 2009, ISSN: 1538-4357. DOI: 10.1088/0004-637x/707/2/916. [Online]. Available: http://dx.doi.org/10.1088/0004-637X/707/2/916 (cit. on p. 25).

[78] J. C. Mather *et al.*, “Calibrator design for the cobe far infrared absolute spectrophotometer (firas),” *The Astrophysical Journal*, vol. 512, no. 2, 511–520, 1999, ISSN: 1538-4357. DOI: 10.1086/306805. [Online]. Available: http://dx.doi.org/10.1086/306805 (cit. on p. 25).

[79] Y. Hoffman, H. M. Courtois, and R. B. Tully, “Cosmic Bulk Flow and the Local Motion from Cosmicflows-2,” *Mon. Not. Roy. Astron. Soc.*, vol. 449, no. 4, pp. 4494–4505, 2015. DOI: 10.1093/mnras/stv615. arXiv: 1503.05422 [astro-ph.CO] (cit. on p. 25).

[80] P. A. Oesch *et al.*, “A remarkably luminous galaxy atz= 11.1 measured withhubble space telescopegrism spectroscopy,” *The Astrophysical Journal*, vol. 819, no. 2, p. 129, 2016, ISSN: 1538-4357. DOI: 10.3847/0004-637x/819/2/129. [Online]. Available: http://dx.doi.org/10.3847/0004-637X/819/2/129 (cit. on p. 27).

[81] O. J. Eggen, D. Lynden-Bell, and A. R. Sandage, “Evidence from the motions of old stars that the Galaxy collapsed.,” vol. 136, p. 748, Nov. 1962. DOI: 10.1086/147433 (cit. on p. 27).

[82] M. Milgrom, “A modification of the Newtonian dynamics as a possible alternative to the hidden mass hypothesis.,” vol. 270, pp. 365–370, Jul. 1983. DOI: 10.1086/161130 (cit. on pp. 29–31).

[83] J. D. Bekenstein, “Relativistic gravitation theory for the MOND paradigm,” *Phys. Rev. D*, vol. 70, p. 083 509, 2004, [Erratum: Phys.Rev.D 71, 069901 (2005)]. DOI: `10.1103/PhysRevD.70.083509`. arXiv: `astro-ph/0403694` (cit. on p. 31).

[84] Q. Exirifard, “GravitoMagnetic Force in Modified Newtonian Dynamics,” *JCAP*, vol. 08, p. 046, 2013. DOI: `10.1088/1475-7516/2013/08/046`. arXiv: `1107.2109 [gr-qc]` (cit. on p. 31).

[85] D. S. Graff and K. Freese, “Analysis of a hubble space telescope search for red dwarfs: limits on baryonic matter in the galactic halo,” *Astrophys. J. Lett.*, vol. 456, p. L49, 1996. DOI: `10.1086/309850`. arXiv: `astro-ph/9507097` (cit. on p. 32).

[86] B. Carr, S. Clesse, and J. García-Bellido, “Primordial black holes from the QCD epoch: Linking dark matter, baryogenesis and anthropic selection,” *Mon. Not. Roy. Astron. Soc.*, vol. 501, no. 1, pp. 1426–1439, 2021. DOI: `10.1093/mnras/staa3726`. arXiv: `1904.02129 [astro-ph.CO]` (cit. on p. 32).

[87] A. Boyarsky *et al.*, “Sterile neutrino Dark Matter,” *Prog. Part. Nucl. Phys.*, vol. 104, pp. 1–45, 2019. DOI: `10.1016/j.ppnp.2018.07.004`. arXiv: `1807.07938 [hep-ph]` (cit. on p. 32).

[88] A. M. Green and B. J. Kavanagh, “Primordial black holes as a dark matter candidate,” *Journal of Physics G: Nuclear and Particle Physics*, vol. 48, no. 4, p. 043 001, 2021. DOI: `10.1088/1361-6471/abc534`. [Online]. Available: `https://dx.doi.org/10.1088/1361-6471/abc534` (cit. on p. 32).

[89] R. Essig *et al.*, “Working Group Report: New Light Weakly Coupled Particles,” in *Snowmass 2013: Snowmass on the Mississippi*, Oct. 2013. arXiv: `1311.0029 [hep-ph]` (cit. on p. 32).

[90] G. Jungman, M. Kamionkowski, and K. Griest, “Supersymmetric dark matter,” *Phys. Rept.*, vol. 267, pp. 195–373, 1996. DOI: `10.1016/0370-1573(95)00058-5`. arXiv: `hep-ph/9506380` (cit. on pp. 32, 36, 40–42).

[91] N. Craig, “The State of Supersymmetry after Run I of the LHC,” in *Beyond the Standard Model after the first run of the LHC*, Sep. 2013. arXiv: `1309.0528 [hep-ph]`.

[92] G. ’t Hooft, “Computation of the quantum effects due to a four-dimensional pseudoparticle,” vol. 14, no. 12, pp. 3432–3450, Dec. 1976. DOI: `10.1103/PhysRevD.14.3432` (cit. on p. 33).

[93] M. C. Gonzalez-Garcia and M. Maltoni, “Phenomenology with Massive Neutrinos,” *Phys. Rept.*, vol. 460, pp. 1–129, 2008. DOI: `10.1016/j.physrep.2007.12.004`. arXiv: `0704.1800 [hep-ph]` (cit. on p. 33).

[94] C. A. Baker *et al.*, “An Improved experimental limit on the electric dipole moment of the neutron,” *Phys. Rev. Lett.*, vol. 97, p. 131 801, 2006. DOI: `10.1103/PhysRevLett.97.131801`. arXiv: `hep-ex/0602020` (cit. on p. 33).

[95] F. Wilczek, “Problem of strong P and T invariance in the presence of instantons,” vol. 40, no. 5, pp. 279–282, Jan. 1978. DOI: 10.1103/PhysRevLett.40.279 (cit. on p. 33).

[96] S. Weinberg, “A new light boson?,” vol. 40, no. 4, pp. 223–226, Jan. 1978. DOI: 10.1103/PhysRevLett.40.223 (cit. on p. 33).

[97] D. A. Dicus *et al.*, “Astrophysical bounds on the masses of axions and higgs particles,” *Phys. Rev. D*, vol. 18, pp. 1829–1834, 6 1978. DOI: 10.1103/PhysRevD.18.1829. [Online]. Available: https://link.aps.org/doi/10.1103/PhysRevD.18.1829 (cit. on p. 33).

[98] L. F. Abbott and P. Sikivie, “A cosmological bound on the invisible axion,” *Physics Letters B*, vol. 120, no. 1-3, pp. 133–136, Jan. 1983. DOI: 10.1016/0370-2693(83)90638-X (cit. on p. 34).

[99] J. Preskill, M. B. Wise, and F. Wilczek, “Cosmology of the invisible axion,” *Physics Letters B*, vol. 120, no. 1-3, pp. 127–132, Jan. 1983. DOI: 10.1016/0370-2693(83)90637-8 (cit. on p. 34).

[100] M. Dine and W. Fischler, “The not-so-harmless axion,” *Physics Letters B*, vol. 120, no. 1-3, pp. 137–141, Jan. 1983. DOI: 10.1016/0370-2693(83)90639-1 (cit. on p. 34).

[101] L. Di Luzio *et al.*, “The landscape of QCD axion models,” vol. 870, pp. 1–117, Jul. 2020. DOI: 10.1016/j.physrep.2020.06.002. arXiv: 2003.01100 [hep-ph] (cit. on p. 34).

[102] R. Bernabei *et al.*, “First results from DAMA/LIBRA and the combined results with DAMA/NaI,” *Eur. Phys. J. C*, vol. 56, pp. 333–355, 2008. DOI: 10.1140/epjc/s10052-008-0662-y. arXiv: 0804.2741 [astro-ph] (cit. on p. 34).

[103] C. E. Aalseth *et al.*, “Search for an Annual Modulation in a P-type Point Contact Germanium Dark Matter Detector,” *Phys. Rev. Lett.*, vol. 107, p. 141 301, 2011. DOI: 10.1103/PhysRevLett.107.141301. arXiv: 1106.0650 [astro-ph.CO] (cit. on p. 34).

[104] K. Olive, “Review of particle physics,” *Chinese Physics C*, vol. 38, no. 9, p. 090 001, 2014. DOI: 10.1088/1674-1137/38/9/090001. [Online]. Available: https://doi.org/10.1088/1674-1137/38/9/090001 (cit. on p. 34).

[105] P. J. Fox *et al.*, “Missing Energy Signatures of Dark Matter at the LHC,” *Phys. Rev. D*, vol. 85, p. 056 011, 2012. DOI: 10.1103/PhysRevD.85.056011. arXiv: 1109.4398 [hep-ph] (cit. on p. 35).

[106] G. Bertone and D. Merritt, “Dark matter dynamics and indirect detection,” *Mod. Phys. Lett. A*, vol. 20, p. 1021, 2005. DOI: 10.1142/S0217732305017391. arXiv: astro-ph/0504422 (cit. on p. 35).

[107] G. Bertone, D. Hooper, and J. Silk, “Particle dark matter: Evidence, candidates and constraints,” *Phys. Rept.*, vol. 405, pp. 279–390, 2005. DOI: 10.1016/j.physrep.2004.08.031. arXiv: hep-ph/0404175 (cit. on pp. 35, 36, 41, 42).

[108] B. P. Abbott *et al.*, “Observation of Gravitational Waves from a Binary Black Hole Merger,” *Phys. Rev. Lett.*, vol. 116, no. 6, p. 061 102, 2016. DOI: 10.1103/PhysRevLett.116.061102. arXiv: 1602.03837 [gr-qc] (cit. on p. 36).

[109] S. Bird *et al.*, “Did LIGO detect dark matter?” *Phys. Rev. Lett.*, vol. 116, no. 20, p. 201 301, 2016. DOI: 10.1103/PhysRevLett.116.201301. arXiv: 1603.00464 [astro-ph.CO] (cit. on p. 36).

[110] M. W. Goodman and E. Witten, “Detectability of certain dark-matter candidates,” *Phys. Rev. D*, vol. 31, pp. 3059–3063, 12 1985. DOI: 10.1103/PhysRevD.31.3059. [Online]. Available: https://link.aps.org/doi/10.1103/PhysRevD.31.3059 (cit. on p. 36).

[111] T. Marrodán Undagoitia and L. Rauch, “Dark matter direct-detection experiments,” *J. Phys. G*, vol. 43, no. 1, p. 013 001, 2016. DOI: 10.1088/0954-3899/43/1/013001. arXiv: 1509.08767 [physics.ins-det] (cit. on p. 37).

[112] R. Khatiwada *et al.*, “Axion Dark Matter Experiment: Detailed design and operations,” *Rev. Sci. Instrum.*, vol. 92, no. 12, p. 124 502, 2021. DOI: 10.1063/5.0037857. arXiv: 2010.00169 [astro-ph.IM] (cit. on p. 38).

[113] S. J. Asztalos *et al.*, “SQUID-Based Microwave Cavity Search for Dark-Matter Axions,” vol. 104, no. 4, 041301, p. 041 301, Jan. 2010. DOI: 10.1103/PhysRevLett.104.041301. arXiv: 0910.5914 [astro-ph.CO] (cit. on p. 38).

[114] C. Bartram *et al.*, “Search for Invisible Axion Dark Matter in the 3.3–4.2 μeV Mass Range,” *Phys. Rev. Lett.*, vol. 127, no. 26, p. 261 803, 2021. DOI: 10.1103/PhysRevLett.127.261803. arXiv: 2110.06096 [hep-ex] (cit. on p. 38).

[115] C. Bartram *et al.*, “Dark Matter Axion Search Using a Josephson Traveling Wave Parametric Amplifier,” Oct. 2021. arXiv: 2110.10262 [hep-ex] (cit. on p. 38).

[116] R. Agnese *et al.*, “Improved WIMP-search reach of the CDMS II germanium data,” *Phys. Rev. D*, vol. 92, no. 7, p. 072 003, 2015. DOI: 10.1103/PhysRevD.92.072003. arXiv: 1504.05871 [hep-ex] (cit. on p. 38).

[117] R. Agnese *et al.*, “Nuclear-Recoil Energy Scale in CDMS II Silicon Dark-Matter Detectors,” *Nucl. Instrum. Meth. A*, vol. 905, pp. 71–81, 2018. DOI: 10.1016/j.nima.2018.07.028. arXiv: 1803.02903 [physics.ins-det] (cit. on p. 38).

[118] T. Aralis *et al.*, “Constraints on dark photons and axionlike particles from the SuperCDMS Soudan experiment,” *Phys. Rev. D*, vol. 101, no. 5, p. 052 008, 2020, [Erratum: Phys.Rev.D 103, 039901 (2021)]. DOI: 10.1103/PhysRevD.101.052008. arXiv: 1911.11905 [hep-ex] (cit. on p. 38).

[119] M. F. Albakry *et al.*, “A Strategy for Low-Mass Dark Matter Searches with Cryogenic Detectors in the SuperCDMS SNOLAB Facility,” in *2022 Snowmass Summer Study*, Mar. 2022. arXiv: 2203.08463 [physics.ins-det] (cit. on p. 38).

[120] D. S. Akerib *et al.*, "Projected sensitivity of the LUX-ZEPLIN experiment to the two-neutrino and neutrinoless double β decays of ^{134}Xe," *Phys. Rev. C*, vol. 104, no. 6, p. 065 501, 2021. DOI: `10.1103/PhysRevC.104.065501`. arXiv: `2104.13374 [physics.ins-det]` (cit. on p. 38).

[121] J. Aalbers *et al.*, "First Dark Matter Search Results from the LUX-ZEPLIN (LZ) Experiment," Jul. 2022. arXiv: `2207.03764 [hep-ex]` (cit. on pp. 38, 39, 128).

[122] . [Online]. Available: `http://deap3600.ca/deap-1-protocol/` (cit. on p. 39).

[123] P. A. Amaudruz *et al.*, "First results from the DEAP-3600 dark matter search with argon at SNOLAB," *Phys. Rev. Lett.*, vol. 121, no. 7, p. 071 801, 2018. DOI: `10.1103/PhysRevLett.121.071801`. arXiv: `1707.08042 [astro-ph.CO]` (cit. on p. 40).

[124] R. Ajaj *et al.*, "Search for dark matter with a 231-day exposure of liquid argon using DEAP-3600 at SNOLAB," *Phys. Rev. D*, vol. 100, no. 2, p. 022 004, 2019. DOI: `10.1103/PhysRevD.100.022004`. arXiv: `1902.04048 [astro-ph.CO]` (cit. on pp. 40, 75, 86, 128, 132, 147–149, 162, 164, 167).

[125] P. Adhikari *et al.*, "First direct detection constraints on planck-scale mass dark matter with multiple-scatter signatures using the deap-3600 detector," *Phys. Rev. Lett.*, vol. 128, p. 011 801, 1 2022. DOI: `10.1103/PhysRevLett.128.011801`. [Online]. Available: `https://link.aps.org/doi/10.1103/PhysRevLett.128.011801` (cit. on p. 40).

[126] R. H. Helm, "Inelastic and elastic scattering of 187-mev electrons from selected even-even nuclei," *Phys. Rev.*, vol. 104, pp. 1466–1475, 5 1956. DOI: `10.1103/PhysRev.104.1466`. [Online]. Available: `https://link.aps.org/doi/10.1103/PhysRev.104.1466` (cit. on p. 40).

[127] R. C. Cotta *et al.*, "Dark Matter in the MSSM," *New J. Phys.*, vol. 11, p. 105 026, 2009. DOI: `10.1088/1367-2630/11/10/105026`. arXiv: `0903.4409 [hep-ph]` (cit. on p. 41).

[128] C.-L. Shan, "Determining Ratios of WIMP-Nucleon Cross Sections from Direct Dark Matter Detection Data," *JCAP*, vol. 07, p. 005, 2011. DOI: `10.1088/1475-7516/2011/07/005`. arXiv: `1103.0482 [hep-ph]` (cit. on pp. 41, 42).

[129] A. Hitachi, T. Doke, and A. Mozumder, "Luminescence quenching in liquid argon under charged-particle impact: Relative scintillation yield at different linear energy transfers," *Phys. Rev. B*, vol. 46, pp. 11 463–11 470, 18 1992. DOI: `10.1103/PhysRevB.46.11463`. [Online]. Available: `https://link.aps.org/doi/10.1103/PhysRevB.46.11463` (cit. on pp. 43, 44, 46, 48, 118).

[130] P. Adhikari *et al.*, "Pulse-shape discrimination against low-energy Ar-39 beta decays in liquid argon with 4.5 tonne-years of DEAP-3600 data," *Eur. Phys. J. C*, vol. 81, no. 9, p. 823, 2021. DOI: `10.1140/epjc/s10052-021-09514-w`. arXiv: `2103.12202 [physics.ins-det]` (cit. on p. 43).

[131] D. S. Akerib *et al.*, "Liquid xenon scintillation measurements and pulse shape discrimination in the lux dark matter detector," *Phys. Rev. D*, vol. 97, p. 112 002, 11 2018. DOI: 10.1103/PhysRevD.97.112002. [Online]. Available: https://link.aps.org/doi/10.1103/PhysRevD.97.112002 (cit. on p. 44).

[132] . [Online]. Available: https://www.chemicool.com/elements/xenon.html (cit. on p. 44).

[133] T. Doke *et al.*, "Absolute scintillation yields in liquid argon and xenon for various particles," *Japanese Journal of Applied Physics*, vol. 41, no. Part 1, No. 3A, pp. 1538–1545, 2002. DOI: 10.1143/jjap.41.1538. [Online]. Available: https://doi.org/10.1143/jjap.41.1538 (cit. on pp. 44, 45).

[134] A. Kemp, "Using the profile likelihood method to search for dark matter using the deap-3600 detector.," 2020. [Online]. Available: https://ethos.bl.uk/OrderDetails.do?uin=uk.bl.ethos.855341 (cit. on p. 46).

[135] D. E. Grosjean *et al.*, "Absolute luminescence efficiency of ion-bombarded solid argon," *Phys. Rev. B*, vol. 56, pp. 6975–6981, 11 1997. DOI: 10.1103/PhysRevB.56.6975. [Online]. Available: https://link.aps.org/doi/10.1103/PhysRevB.56.6975 (cit. on p. 46).

[136] J Lindhard, M Scharff, and H. E. Schioett, "Range concepts and heavy ion ranges (notes on atomic collisions, ii)," *Kgl. Danske Videnskab. Selskab. Mat. Fys. Medd.*, vol. 33, Jan. 1963. [Online]. Available: https://www.osti.gov/biblio/4153115 (cit. on p. 46).

[137] O. Şahin *et al.*, "Penning transfer in argon-based gas mixtures," *JINST*, vol. 5, no. 05, P05002, 2010. DOI: 10.1088/1748-0221/5/05/P05002 (cit. on pp. 46, 118).

[138] A. B. Treshchalov and A. A. Lissovskii, "Spectroscopic diagnostics of a pulsed discharge in high-pressure argon," *Quantum Electronics*, vol. 40, no. 3, pp. 234–240, 2010. DOI: 10.1070/qe2010v040n03abeh014243. [Online]. Available: https://doi.org/10.1070/qe2010v040n03abeh014243 (cit. on p. 47).

[139] A. Gedanken *et al.*, "Electronic energy transfer phenomena in rare gases," *The Journal of Chemical Physics*, vol. 57, no. 8, pp. 3456–3469, 1972. DOI: 10.1063/1.1678779. eprint: https://doi.org/10.1063/1.1678779. [Online]. Available: https://doi.org/10.1063/1.1678779 (cit. on p. 47).

[140] K. Katsonis, C. Berenguer, and A. Kaminska, "Argon 4s and 4p excited states atomic data applied in arc-jet modeling," *International Journal of Aerospace Engineering*, vol. 2011, Jan. 2011. DOI: 10.1155/2011/896836 (cit. on pp. 47, 49).

[141] A. Hitachi *et al.*, "Effect of ionization density on the time dependence of luminescence from liquid argon and xenon," *Phys. Rev. B*, vol. 27, 9 1983. DOI: 10.1103/PhysRevB.27.5279. [Online]. Available: https://link.aps.org/doi/10.1103/PhysRevB.27.5279 (cit. on p. 47).

[142] T. Doke *et al.*, “Let dependence of scintillation yields in liquid argon,” *Nuclear Instruments and Methods in Physics Research Section A: Accelerators, Spectrometers, Detectors and Associated Equipment*, vol. 269, no. 1, pp. 291–296, 1988, ISSN: 0168-9002. DOI: `https://doi.org/10.1016/0168-9002(88)90892-3`. [Online]. Available: `https://www.sciencedirect.com/science/article/pii/0168900288908923` (cit. on p. 48).

[143] A. Hitachi *et al.*, “Effect of ionization density on the time dependence of luminescence from liquid argon and xenon,” *Phys. Rev. B*, vol. 27, pp. 5279–5285, 1983. DOI: `10.1103/PhysRevB.27.5279` (cit. on p. 48).

[144] . [Online]. Available: `https://www.snolab.ca/about/about-snolab/` (cit. on pp. 50, 51).

[145] . [Online]. Available: `https://documents.pub/document/snolab-users-snolab-useras-handbook-rev-2-vii-abstract-the-purpose-of-this-handbook.html` (cit. on pp. 50, 51, 76).

[146] P. Urquijo, “Searching for dark matter at the stawell underground physics laboratory,” *EPJ Web of Conferences*, vol. 123, p. 04 002, Jan. 2016. DOI: `10.1051/epjconf/201612304002` (cit. on p. 50).

[147] D.-M. Mei and A. Hime, “Muon-induced background study for underground laboratories,” *Phys. Rev. D*, vol. 73, p. 053 004, 5 2006. DOI: `10.1103/PhysRevD.73.053004`. [Online]. Available: `https://link.aps.org/doi/10.1103/PhysRevD.73.053004` (cit. on p. 50).

[148] “Facility and experiment developments at snolab,” [Online]. Available: `http://www.ba.infn.it/~now/now2014/web-content/TALKS/aMon/Par1/NOW_POCAR.pdf` (cit. on p. 51).

[149] “New experiments with spheres-gas, news-h at snolab," 2019.,” [Online]. Available: `https://news-g.org/news-snolab/` (cit. on p. 51).

[150] P. A. Amaudruz *et al.*, “Design and Construction of the DEAP-3600 Dark Matter Detector,” *Astropart. Phys.*, vol. 108, pp. 1–23, 2019. DOI: `10.1016/j.astropartphys.2018.09.006`. arXiv: `1712.01982 [astro-ph.IM]` (cit. on pp. 51, 52, 54, 55, 57, 59, 60, 62–64, 66, 71).

[151] V. M. Gehman *et al.*, “Fluorescence Efficiency and Visible Re-emission Spectrum of Tetraphenyl Butadiene Films at Extreme Ultraviolet Wavelengths,” *Nucl. Instrum. Meth. A*, vol. 654, pp. 116–121, 2011. DOI: `10.1016/j.nima.2011.06.088`. arXiv: `1104.3259 [astro-ph.IM]` (cit. on pp. 51, 53).

[152] “Hamamatsu r5912 photomultiplier tube datasheet,” [Online]. Available: `https://www.hamamatsu.com/eu/en/product/optical-sensors/pmt/pmt_tube-alone/head-on-type/R5912.html` (cit. on pp. 52, 54).

[153] “Styrofoam^{TM} brand sm extruded polystyrene foam insulation.,” [Online]. Available: `https://www.hsbuild.com/assets/pdfs/BI016_Data%20Sheet.pdf` (cit. on p. 53).

[154] M. G. Dunford, “A search for the neutrinoless double electron capture of ^{36}ar and a measurement of the specific activity of ^{39}ar in atmospheric argon with the deap-3600 detector,” 2018. [Online]. Available: https://curve.carleton.ca/1c0be13f-5b1d-41e5-b763-e0c7e0dbf049 (cit. on p. 56).

[155] “Photomultiplier tubes: Basics and applications,” Third Edition, 2007. [Online]. Available: https://www.hamamatsu.com/content/dam/hamamatsu-photonics/sites/documents/99_SALES_LIBRARY/etd/PMT_handbook_v3aE.pdf (cit. on pp. 55, 57, 103).

[156] D. Mei and A. Hime, “Muon-induced background study for underground laboratories,” *Phys. Rev. D*, vol. 73, p. 053 004, 2006. DOI: 10.1103/PhysRevD.73.053004. arXiv: astro-ph/0512125 (cit. on p. 59).

[157] “Caen, technical information manual: Mod. v1720 8 channel 12 bit 250 ms/s digitizer manual rev. 26.,” [Online]. Available: http://info.phys.tsinghua.edu.cn/enpg/Docs/digi-Device/V1720_REV24.pdf (cit. on p. 59).

[158] “Caen, technical information manual: Mod. v1740 64 channel 12 bit 65 ms/s digitizer manual rev. 17.,” [Online]. Available: https://daq-plone.triumf.ca/HR/VME/CAEN/v1740.pdf/at_download/file (cit. on p. 59).

[159] “Wiener, plein & baus, ltd., mpod lv/hv system startup information.,” [Online]. Available: http://www.phys.utk.edu/expnuclear/LeRIBSS/MPOD_information.pdf (cit. on p. 60).

[160] “Iseg, eds distributor hv modules with common-gnd operators manual.,” [Online]. Available: http://galileo.phys.virginia.edu/research/groups/g-2/Wiener_MPOD_3-0/Manuals%20and%20Doc%20files/ISEG%20Doc/EDS/ED301_3x.pdf (cit. on p. 60).

[161] “Caen, technical information manual: A3818 pci express optical link.,” [Online]. Available: https://cmsdoc.cern.ch/~cschwick/software/distribution/A3818_User_Manual_rev8.pdf (cit. on p. 62).

[162] R. Ajaj *et al.*, “Search for dark matter with a 231-day exposure of liquid argon using deap-3600 at snolab,” *Phys. Rev. D*, vol. 100, p. 022 004, 2 2019. DOI: 10.1103/PhysRevD.100.022004. [Online]. Available: https://link.aps.org/doi/10.1103/PhysRevD.100.022004 (cit. on pp. 67, 69–72).

[163] J. Calvo *et al.*, “Backgrounds and pulse shape discrimination in the ArDM liquid argon TPC,” *Journal of Cosmology and Astroparticle Physics*, vol. 2018, no. 12, pp. 011–011, 2018. DOI: 10.1088/1475-7516/2018/12/011. [Online]. Available: https://doi.org/10.1088/1475-7516/2018/12/011 (cit. on p. 68).

[164] R. Ajaj *et al.*, “Electromagnetic backgrounds and potassium-42 activity in the DEAP-3600 dark matter detector,” *Phys. Rev. D*, vol. 100, no. 7, p. 072 009, 2019. DOI: 10.1103/PhysRevD.100.072009. arXiv: 1905.05811 [nucl-ex] (cit. on pp. 68, 69).

[165] "Berkeley nuclear forensics website. decay chains of u-238 and th-232.," [Online]. Available: https://metadata.berkeley.edu/nuclear-forensics/Decay%20Chains.html (cit. on p. 72).

[166] C. Mielnichuk, "A likelihood ratio algorithm forremoving localized alpha particle backgrounds in the deap-3600 detector," 2017. [Online]. Available: https://era.library.ualberta.ca/items/20cdb83a-3fcc-4f46-b707-736ecdc609e5 (cit. on p. 75).

[167] A. Grobov and A. Ilyasov, "Boosted decision trees approach to neck alpha events discrimination in DEAP-3600 experiment," *Phys. Scripta*, vol. 95, no. 7, L. Bravina *et al.*, Eds., p. 074 007, 2020. DOI: 10.1088/1402-4896/ab8dff. arXiv: 2009.00895 [physics.ins-det] (cit. on p. 75).

[168] M. Hofmann *et al.*, "Ion-beam excitation of liquid argon," *Eur. Phys. J. C*, vol. 73, no. 10, p. 2618, 2013. DOI: 10.1140/epjc/s10052-013-2618-0. arXiv: 1511.07721 [physics.ins-det] (cit. on p. 87).

[169] P. Adhikari *et al.*, "The liquid-argon scintillation pulseshape in DEAP-3600," *Eur. Phys. J. C*, vol. 80, no. 4, p. 303, 2020. DOI: 10.1140/epjc/s10052-020-7789-x. arXiv: 2001.09855 [physics.ins-det] (cit. on pp. 87, 89, 90).

[170] C. Stanford *et al.*, "Surface background suppression in liquid argon dark matter detectors using a newly discovered time component of tetraphenyl-butadiene scintillation," *Phys. Rev. D*, vol. 98, no. 6, p. 062 002, 2018. DOI: 10.1103/PhysRevD.98.062002. arXiv: 1804.06895 [physics.ins-det] (cit. on pp. 88, 89).

[171] J. B. McLaughlin, "Corrections to signal saturation on the deap-3600 dark matter search," 2018. [Online]. Available: https://qspace.library.queensu.ca/handle/1974/24497 (cit. on p. 103).

[172] J Lindhard *et al.*, "Integral equations governing radiation effects. (notes on atomic collisions, iii)," *Kgl. Danske Videnskab., Selskab. Mat. Fys. Medd.*, vol. 33, Jan. 1963. [Online]. Available: https://www.osti.gov/biblio/4701226 (cit. on pp. 117, 118).

[173] J. B. Birks, "Scintillations from organic crystals: Specific fluorescence and relative response to different radiations," *Proceedings of the Physical Society. Section A*, vol. 64, no. 10, p. 874, 1951. DOI: 10.1088/0370-1298/64/10/303. [Online]. Available: https://dx.doi.org/10.1088/0370-1298/64/10/303 (cit. on p. 118).

[174] S. Kubota *et al.*, "Evidence of the existence of exciton states in liquid argon and exciton-enhanced ionization from xenon doping," *Phys. Rev. B*, vol. 13, 4 1976. DOI: 10.1103/PhysRevB.13.1649. [Online]. Available: https://link.aps.org/doi/10.1103/PhysRevB.13.1649 (cit. on p. 118).

[175] D. M. Mei *et al.*, “A Model of Nuclear Recoil Scintillation Efficiency in Noble Liquids,” *Astropart. Phys.*, vol. 30, pp. 12–17, 2008. DOI: `10.1016/j.astropartphys.2008.06.001`. arXiv: `0712.2470 [nucl-ex]` (cit. on pp. 118, 125, 127).

[176] J. F. Ziegler, M. Ziegler, and J. Biersack, “Srim – the stopping and range of ions in matter (2010),” *Nuclear Instruments and Methods in Physics Research Section B: Beam Interactions with Materials and Atoms*, vol. 268, no. 11, pp. 1818–1823, 2010, 19th International Conference on Ion Beam Analysis, ISSN: 0168-583X. DOI: `https://doi.org/10.1016/j.nimb.2010.02.091`. [Online]. Available: `https://www.sciencedirect.com/science/article/pii/S0168583X10001862` (cit. on p. 120).

[177] E. Grace and J. A. Nikkel, “Index of refraction, Rayleigh scattering length, and Sellmeier coefficients in solid and liquid argon and xenon,” *Nucl. Instrum. Meth. A*, vol. 867, pp. 204–208, 2017. DOI: `10.1016/j.nima.2017.06.031`. arXiv: `1502.04213 [physics.ins-det]` (cit. on p. 160).

[178] M. Babicz *et al.*, “Propagation of scintillation light in liquid argon,” *Journal of Instrumentation*, vol. 15, no. 03, p. C03035, 2020. DOI: `10.1088/1748-0221/15/03/C03035`. [Online]. Available: `https://dx.doi.org/10.1088/1748-0221/15/03/C03035` (cit. on p. 160).

[179] T. Pollmann, M. Boulay, and M. Kuźniak, “Scintillation of thin tetraphenyl butadiene films under alpha particle excitation,” *Nuclear Instruments and Methods in Physics Research Section A: Accelerators, Spectrometers, Detectors and Associated Equipment*, vol. 635, no. 1, pp. 127–130, 2011. DOI: `10.1016/j.nima.2011.01.045`. [Online]. Available: `https://doi.org/10.1016%2Fj.nima.2011.01.045` (cit. on p. 161).

[180] J. Conrad *et al.*, “Including systematic uncertainties in confidence interval construction for Poisson statistics,” *Phys. Rev. D*, vol. 67, p. 012 002, 2003. DOI: `10.1103/PhysRevD.67.012002`. arXiv: `hep-ex/0202013` (cit. on p. 166).

Appendix A

WIMP Miracle

In this chapter we will cover the WIMP miracle from the cosmological point of view following [3]. But before we start, we need to learn about two terms; freeze-out and relic density. In simple terms, when the universe is small and hot enough, each particle and it's antiparticle can cause creation and annihilation. If the universe gets big enough, the particle and antiparticle will be far enough that the annihilation will stop. If the universe gets cold enough, then the creation of the particle-antiparticle pair is not energy-wise favourable anymore. When both conditions are satisfied, we say that the particle has frozen-out (decoupled from the thermal bath). And since the number density won't change much anymore, the density is also called the relic density of the particle.

A.1 Boltzmann Equation

There are very useful and interesting information about the universe in equilibrium in chapter three of Baumann lectures [3]. But for our case, we are actually interested in beyond the equilibrium, for which we need the Boltzmann equation. If we have no interactions, the evolution of the number density of a particle species i can be written as:

$$\frac{dn_i}{dt} + 3\frac{\dot{a}}{a}n_i = 0. \tag{A.1}$$

The above equation should be simple to understand. Assuming non-interactive particles, the number of particles in a fixed volume $V \propto a^3$ is constant and it falls with $1/a^3$ if the volume is expanding. Now, let's try adding the interaction term:

$$\frac{1}{a^3}\frac{d(n_i a^3)}{dt} = C_i[\{n_j\}]. \tag{A.2}$$

Equation A.2 is the Boltzmann equation where the where the C_i is the collision term and depends on the specific interaction that one is considering. Interactions involving three or more particles are very unlikely and considering the two particle interaction would suffice for our purpose. This would include the single-particle decay and two-particle scatterings and annihilation. The simple form of this type of interaction can be written as:

$$1 + 2 \leftrightarrows 3 + 4. \tag{A.3}$$

Let's assume that particle 1 is of interest and we want to follow its number density. The rate of change in n_1 (number density of particle 1) depends on its production rate $(1+2 \leftarrow 3+4)$ and its annihilation rate $(1+2 \rightarrow 3+4)$. Equation A.2 can then be written as:

$$\frac{1}{a^3}\frac{d(n_1 a^3)}{dt} = -\alpha n_1 n_2 + \beta n_3 n_4, \tag{A.4}$$

where α quantifies the destruction rate while β quantifies the production rate. α should obviously be related to the cross-section and the cross-section can also depend on the relative velocity of the involved particles (particle 1 and 2 hear). So, we use $\alpha = <\sigma v>$ which is the thermally averaged cross-section. For finding β we use the fact that the LHS is zero at equilibrium. So:

$$\beta = (\frac{n_1 n_2}{n_3 n_4})_{\text{eq}}\alpha, \tag{A.5}$$

where n_i^{eq} is the number density of particle i at equilibrium. We can rewrite the Boltzmann equation:

$$\frac{1}{a^3}\frac{d(n_1 a^3)}{dt} = -<\sigma v> \left[n_1 n_2 - \left(\frac{n_1 n_2}{n_3 n_4}\right)_{\text{eq}} n_3 n_4 \right]. \tag{A.6}$$

We can make this equation even more intuitive if we substitute some variables. The rate of particle interaction can be written as $\Gamma \equiv n\sigma v$. Instead of number density we can use the number of particles in a comoving volume, $N_i = \frac{n_i}{s}$, where $s = S/V \propto a^{-3}$ is the entropy density[1]. Also, recall that $H = \frac{1}{a}\frac{da}{dt}$. So:

$$\begin{gathered}\frac{1}{a^3 n_1 s}\frac{d(N_1 s a^3)}{dt} = -n_2<\sigma v>s\left[1 - \left(\frac{N_1 N_2}{N_3 N_4}\right)_{\text{eq}}\frac{N_3 N_4}{N_1 N_2}\right],\\ \frac{1}{N_1}\frac{dN_1}{da}\frac{da}{dt} = \frac{1}{N_1}\frac{d\ln N_1}{d\ln a}\frac{N}{a}\frac{da}{dt} = \frac{d\ln N_1}{d\ln a}H,\end{gathered} \tag{A.7}$$

which leads to

$$\frac{d\ln N_1}{d\ln a} = -\frac{\Gamma_1}{H}\left[1 - \left(\frac{N_1 N_2}{N_3 N_4}\right)_{\text{eq}}\frac{N_3 N_4}{N_1 N_2}\right]. \tag{A.8}$$

Note that $\Gamma_1 = n_2<\sigma v>$, since the interaction rate of particle 1 depends on the number density of particle 2. Equation A.8 will be used to understand the WIMP miracle but let's first take a look at the RHS. The $\frac{\Gamma_1}{H}$ encodes the interaction efficiency while the term inside the brackets shows the deviation from equilibrium (note the $1 - \ldots$ format). Let's assume two cases. Firstly when $\Gamma_1 \gg H$, we can see that the system will be pushed toward equilibrium. Assuming other particles are near their equilibrium, if we start with $N_i \gg N^{\text{eq}}$, then the RHS is negative and particle 1 will be annihilated until

---

[1] In cosmology using conservation of Entropy is more useful than, for example, conservation of energy.

it gets close to a stable state. On the other hand, if we start with $N^{\text{eq}} \gg N_i$, then the RHS becomes positive and particle 1 gets produced until it reaches equilibrium again. But if the Hubble radius become bigger than the interaction rate, $\Gamma_1 < H$, the RHS will become suppressed which means N_1 will approach its relic density which is a constant density.

A.2 Dark Matter Relic and WIMP Miracle

In this section we want to solve Equation A.8 for DM to find out when the freeze-out happened and what is the relic density of DM. But we need to make some assumptions about DM to be able to this. Firstly, we will consider WIMP as our DM. We also assume a heavy[1] DM particle X and its antiparticle $\bar{X}$ can annihilate and produce two light particles of SM:

$$X + \bar{X} \leftrightarrow l + \bar{l}, \tag{A.9}$$

where $\bar{l}$ is the antiparticle of l. Assuming that the light particle are coupled to the cosmic plasma, they will always maintain their equilibrium density $n_l = n_l^{\text{eq}}$. The last assumption would be that the density of X and $\bar{X}$ is initially symmetric, so $n_X = n_{\bar{X}}$. Then we can write the Boltzmann equation for the DM as:

$$\frac{dN_X}{dt} = -s{<}\sigma v{>} \left[N_X^2 - (N_X^{\text{eq}})^2\right]. \tag{A.10}$$

The more interesting dynamics happen when the temperature is close to the mass of the particle, $T \sim M_X$, where M_X is the mass of the DM particle. So defining

$$x \equiv \frac{M_X}{T}, \tag{A.11}$$

as our new measure of time, we can rewrite the Boltzmann equation in terms of x. To rewrite the derivative we need:

$$\frac{dx}{dt} = \frac{d}{dt}\left(\frac{M_X}{T}\right) = -\frac{1}{T}\frac{dT}{dt}x \simeq Hx, \tag{A.12}$$

where it is assumed that $T \propto a^{-1}$. This is a correct assumption if the freeze-out happens early enough that the universe is still radiation dominant ($a \propto t^{1/2}$). Before writing the final equation, we need to take a small side track to replace the entropy density, s, with constants to simplify the Boltzmann equation.

For the sake of time and space, we won't get into the details but one can write the total entropy density for a collection of particle species as:

$$s = \sum_i \frac{\rho_i + P_i}{T_i} \equiv \frac{2\pi^2}{45} g_\star(T)\, T^3, \tag{A.13}$$

---

[1] In most DM arguments, heavy and massive are not in comparison to any specific mass, but rather stand opposed to being massless.

where $g_\star$ is the "effective number of relativistic degrees of freedom" which is a function of time[1]. Given that we assumed that no other particle is decoupling from the plasma, $g_\star$ would be constant for our case here. Also, since we are considering a radiation dominant universe we can note that $H \propto t \propto a^2 \propto T^{-2}$. Using the definition of x, we can write $H = H\left(M_X\right)/x^2$. So:

$$\begin{aligned}
\frac{dN_X}{dt} &= \frac{dN_X}{dx}\frac{dx}{dt} = \frac{dN_X}{dx}Hx = -s{<}\sigma v{>}\left[N_X^2 - (N_X^{\rm eq})^2\right], \\
\frac{dN_X}{dx} &= -\frac{2\pi^2}{45}g_\star\left(\frac{M_X}{x}\right)^3\frac{1}{Hx}{<}\sigma v{>}\left[N_X^2 - (N_X^{\rm eq})^2\right], \\
&= -\frac{2\pi^2}{45}g_\star\frac{M_X^3{<}\sigma v{>}}{H\left(M_X\right)}\frac{1}{x^2}\left[N_X^2 - (N_X^{\rm eq})^2\right], \\
&= -\frac{\lambda}{x^2}\left[N_X^2 - (N_X^{\rm eq})^2\right], \\
\lambda &\equiv \frac{2\pi^2}{45}g_\star s\frac{M_X^3{<}\sigma v{>}}{H(M_X)},
\end{aligned} \tag{A.14}$$

where all the constant are collected in the new variable λ. The argument that λ is a constant is still a good approximation for even more fundamental theories of WIMP. Even with λ being a constant, Equation A.14 does not have an analytical solution but one can solve it numerically, as can be seen in Figure A.1. Before moving on the the actual miracle, let's take a look at Equation A.14 with its numerical solution. The early universe, $x < 1$, is a hot plasma and as expected we get $N_X \approx N_X^{\rm eq}$. As the the universe expands and cools down, $x \gg 1$, the equilibrium abundance will become exponentially suppressed. But as the universe gets bigger, the particle-antiparticle pairs cannot find each other that frequently to maintain the equilibrium and the freeze-out happens. This final density, the relic abundance is what we are interested in. We will show this abundance as $N_X^\infty \equiv N_X(x = \infty)$.

At very late times we can assume that $N_X \gg N_X^{\rm eq}$ and thus we can drop the latter from the Boltzmann equation we derived:

$$\frac{dN_X}{dx} \simeq -\frac{\lambda N_X^2}{x^2} \qquad (x > x_f). \tag{A.15}$$

To find N_X^∞ we need to take the integral of this equation from x_f to ∞:

$$\frac{1}{N_X^\infty} - \frac{1}{N_X^f} = \frac{\lambda}{x_f}, \tag{A.16}$$

where $N_X^f \equiv N_X(x = x_f)$. To simplify this even more, we can safely assume that

---

[1] The evolution of $g_\star$ and its relevance to the decoupling of SM particle from the cosmic plasma is an interesting topic that I recommend the reader to read. See, for example, section 3.2 of Daniel Baumann lecture notes on Cosmology.

$N_X^f \gg N_X^\infty$. The final analytical form will become

$$N_X^\infty \simeq \frac{x_f}{\lambda}. \tag{A.17}$$

We started with the assumption that λ is a constant. The only unknown variable to find N_X is x_f, the freeze-out temperature or time. But as we can see from Figure A.1, for $\lambda = 10^5$, the freeze-out happens around $x_f \sim 10$ and for $\lambda = 10^{10}$, the freeze-out takes place at around $x \sim 30$; five orders of magnitude change in λ only changes x_f by a factor of three. So, using $x_f \sim 10$ would be a safe approximation for our upcoming argument.

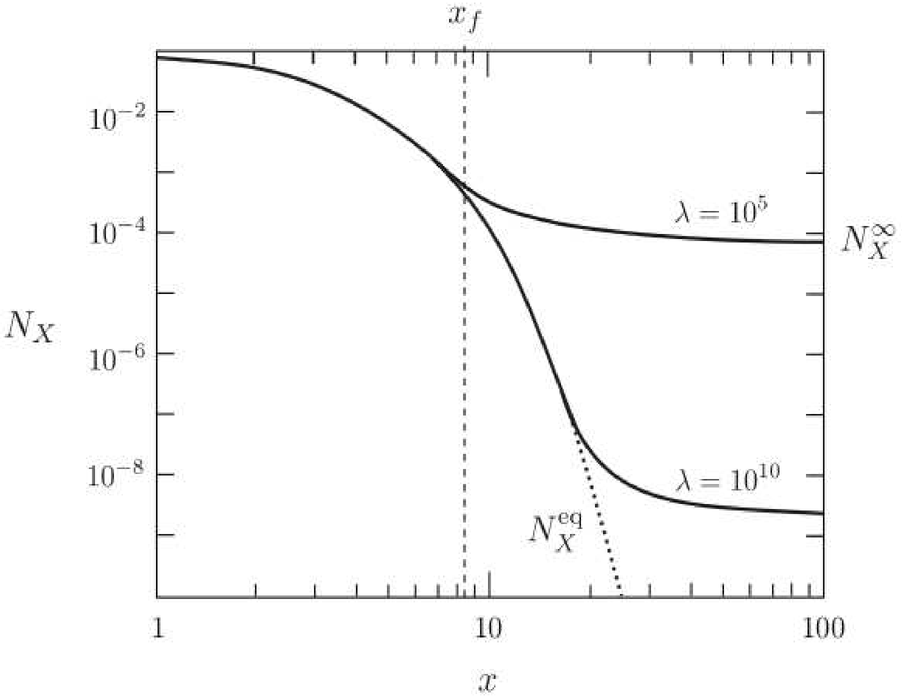

Figure A.1: . Image taken from [3].

WIMP Miracle

We have all the required ingredients to see what the WIMP miracle actually means. We would want to find the relationship between the freeze-out abundance of the relic DM, N_X^∞, to today's density of DM which is denoted as Ω_X. Using the dimensionless density parameter $\Omega \equiv \frac{\rho}{\rho_c}$ and recalling that in cosmology we denote the current value of a variable using a 0 subscript:

$$\Omega_X \equiv \frac{\rho_{X,0}}{\rho_{\mathrm{crit},0}} = \frac{M_X n_{X,0}}{3M_{\mathrm{pl}}^2 H_0^2} = \frac{M_X N_{X,0} s_0}{3M_{\mathrm{pl}}^2 H_0^2} = M_X N_X^\infty \frac{s_0}{3M_{\mathrm{pl}}^2 H_0^2}, \tag{A.18}$$

where $M_{\mathrm{pl}} = \sqrt{\frac{\hbar c}{8\pi G}}$ is the Planck mass and we have used the fact that after freeze-out the number of WIMPs will be conserved and $N_{X,0} = N_X^\infty$. From the section above we can replace N_X^∞ with x_f/λ and $s_0 \equiv s(T_0)$. So:

$$\Omega_X = \frac{H(M_X)}{M_X^2} \frac{x_f}{<\sigma v>} \frac{g_{\star S}(T_0)}{g_{\star S}(M_X)} \frac{T_0^3}{3M_{\mathrm{pl}}^2 H_0^2}, \tag{A.19}$$

where Equation A.13 and Equation A.14 are used. The last thing we would like to replace is the $H(M_X)$. Again, this would be unnecessary details but if we use the fact that $T \propto g_\star^{-1/3} a^{-1}$, then we can write:

$$H = \frac{1}{a}\frac{da}{dt} \simeq \left(\frac{\rho_r}{3M_{\mathrm{pl}}^2}\right)^{1/2} \simeq \frac{\pi}{3}\left(\frac{g_\star}{10}\right)^{1/2} \frac{T^2}{M_{\mathrm{pl}}}. \tag{A.20}$$

Putting this back in the equation above, we get:

$$\Omega_X = \frac{\pi}{9} \frac{x_f}{<\sigma v>} \left(\frac{g_\star(M_X)}{10}\right)^{1/2} \frac{g_{\star S}(T_0)}{g_{\star S}(M_X)} \frac{T_0^3}{M_{\mathrm{pl}}^3 H_0^2}, \tag{A.21}$$

and we can finally replace the constant values (e.g $g_{\star S}(T_0) = 3.91$) and use $g_{\star S}(M_X) = g_\star(M_X)$[1] which gives us:

$$\Omega_X h^2 \sim 0.1 \left(\frac{x_f}{10}\right) \left(\frac{10}{g_\star(M_X)}\right)^{1/2} \frac{10^{-8}\mathrm{GeV}^{-2}}{<\sigma v>}. \tag{A.22}$$

For this to reproduce the observed density of DM today, we should have:

$$\sqrt{<\sigma v>} \sim 10^{-4}\mathrm{GeV}^{-1} \sim \sqrt{G_F}. \tag{A.23}$$

Equation A.23 is the WIMP miracle. If you are having a hard time seeing the miracle , here is the idea. We began the argument by postulating a new particle. The thermal relic of this particle can give the right amount of DM abundance with a cross-section that is characteristic of the weak interaction.

---

[1] Note that for particle species in thermal equilibrium we have $g_{\star S}^{th} = g_\star^{th}$.

Appendix B

nSCBayes Saturation and Late Light

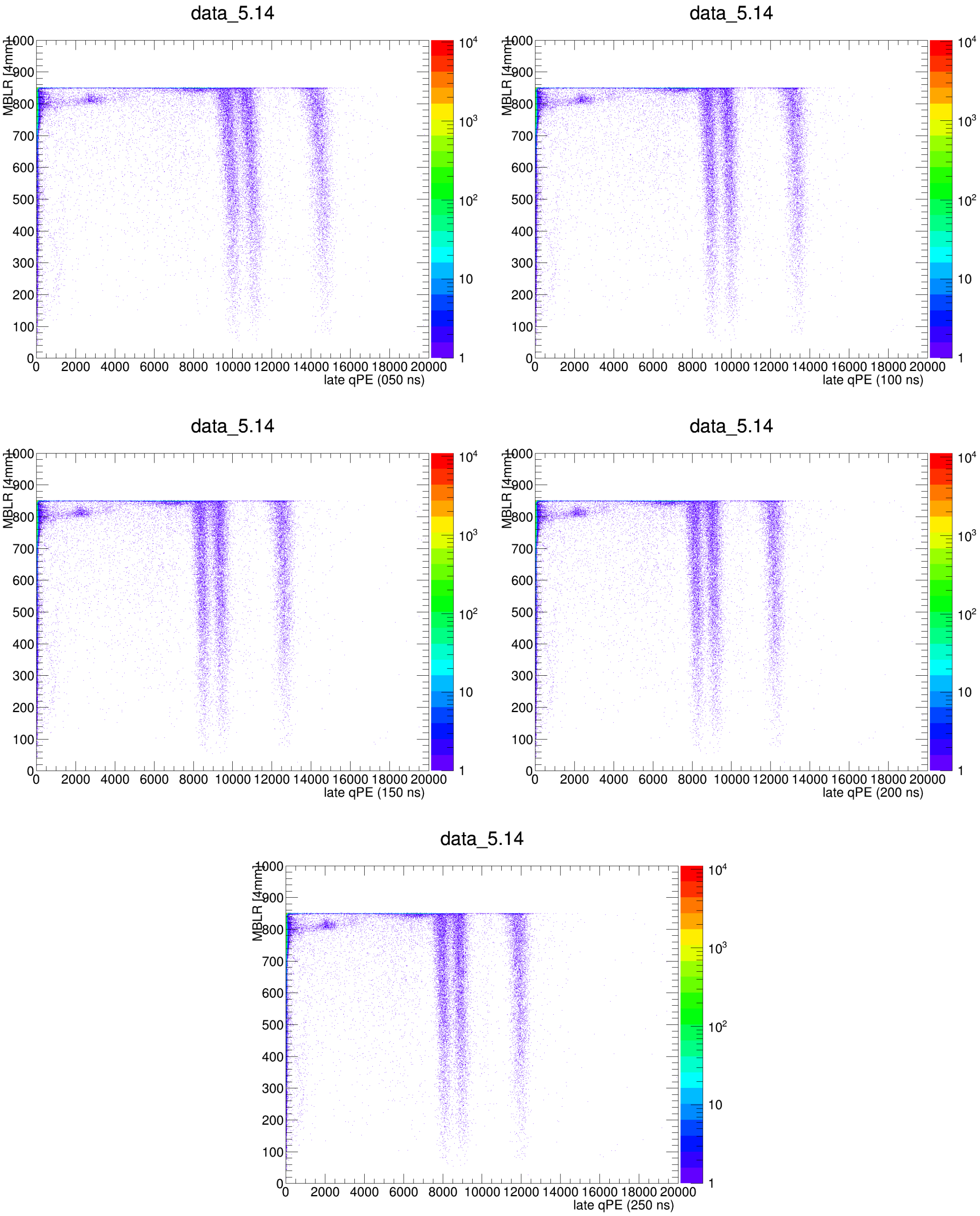

Figure B.1: Late light qPE vs. MBLR with different lower bound for charge integration. This is data with rat version 5.14 which includes the PLSC.

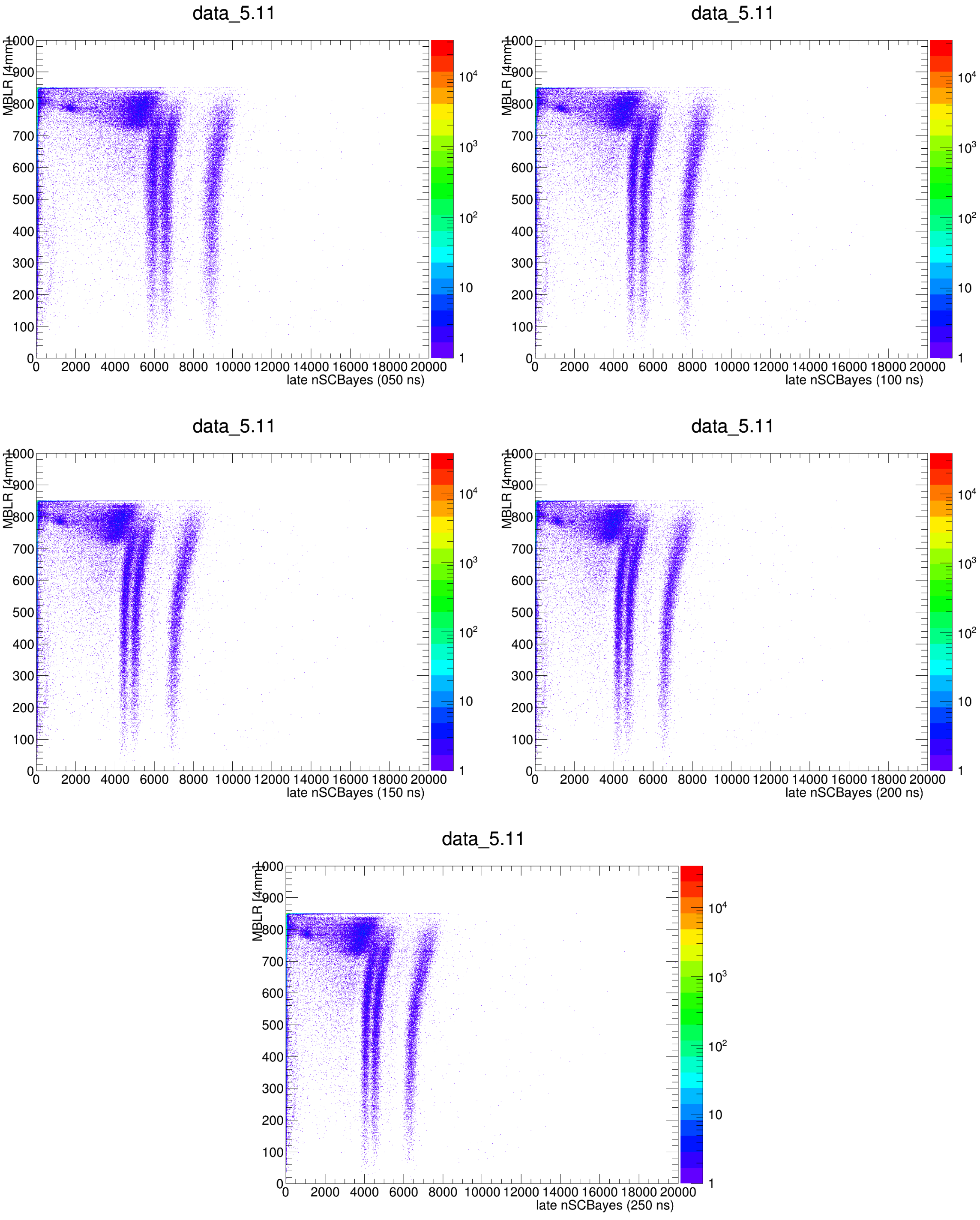

Figure B.2: Late light nSCBayes vs. MBLR with different lower bound for charge integration. This is data with rat version 5.11 which does not include PLSC.

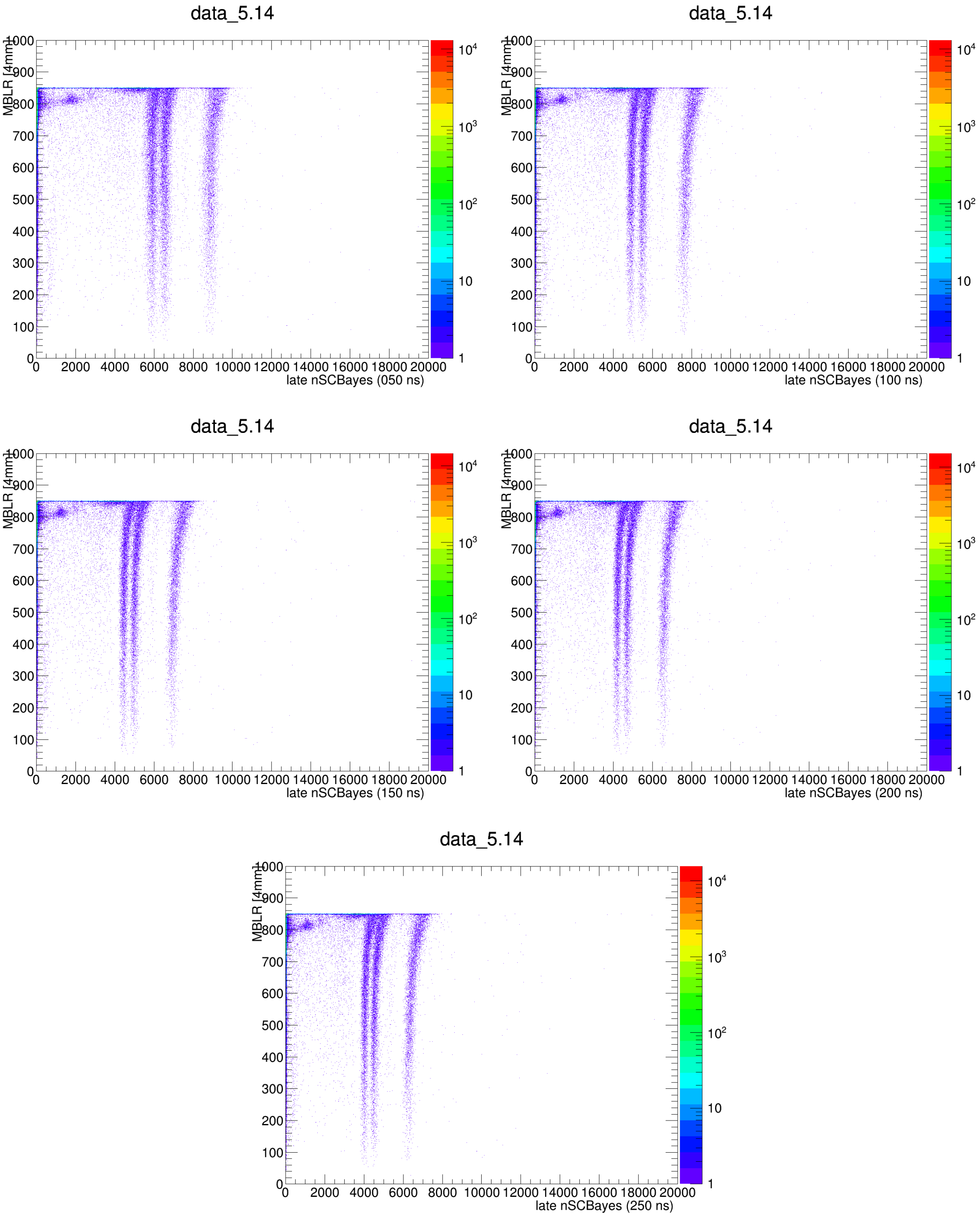

Figure B.3: Late light nSCBayes vs. MBLR with different lower bound for charge integration. This is data with rat version 5.14 which includes the PLSC.

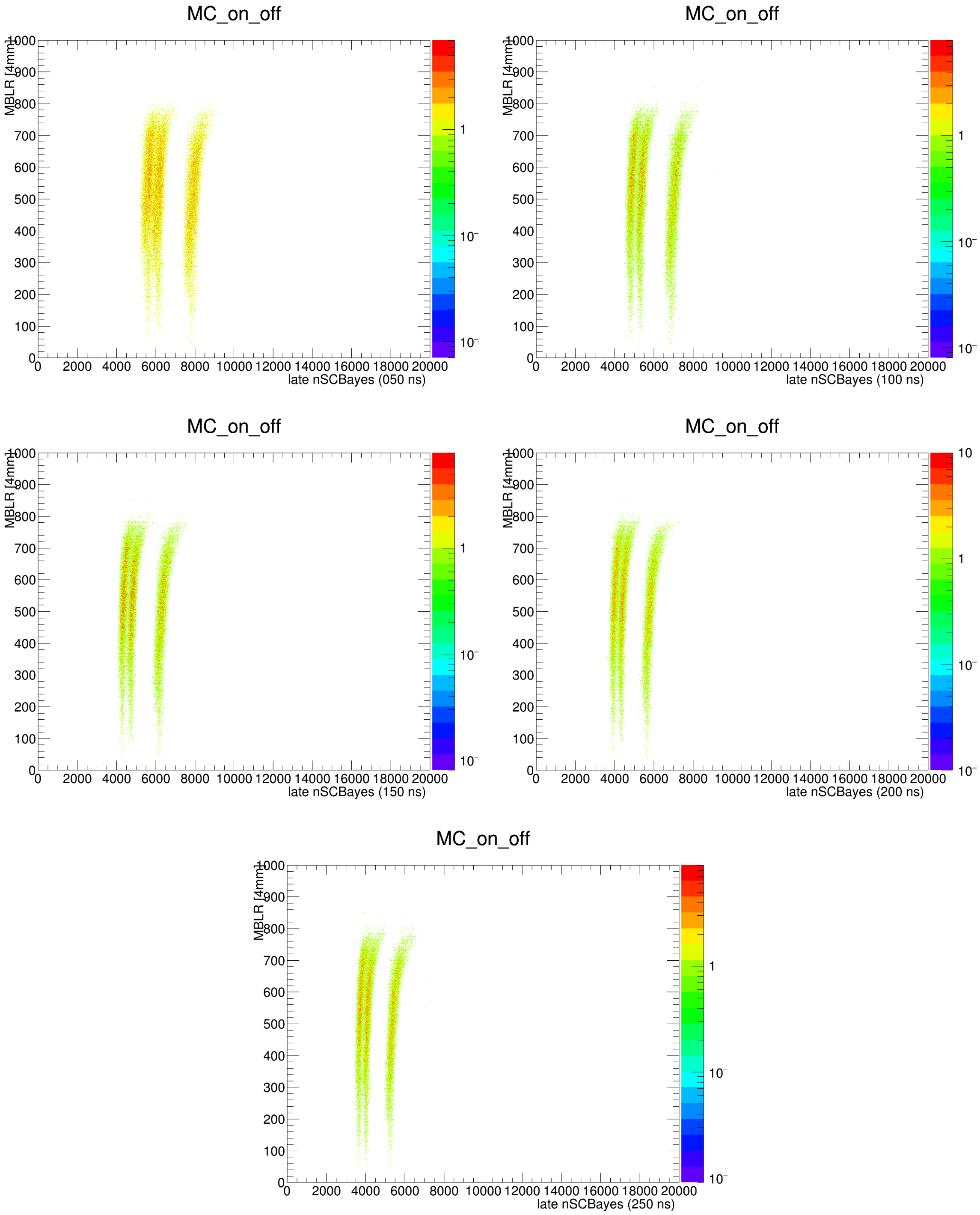

Figure B.4: Late light nSCBayes vs. MBLR with different lower bound for charge integration. This is the MC samples with clipping turned on and PLSC turned off.

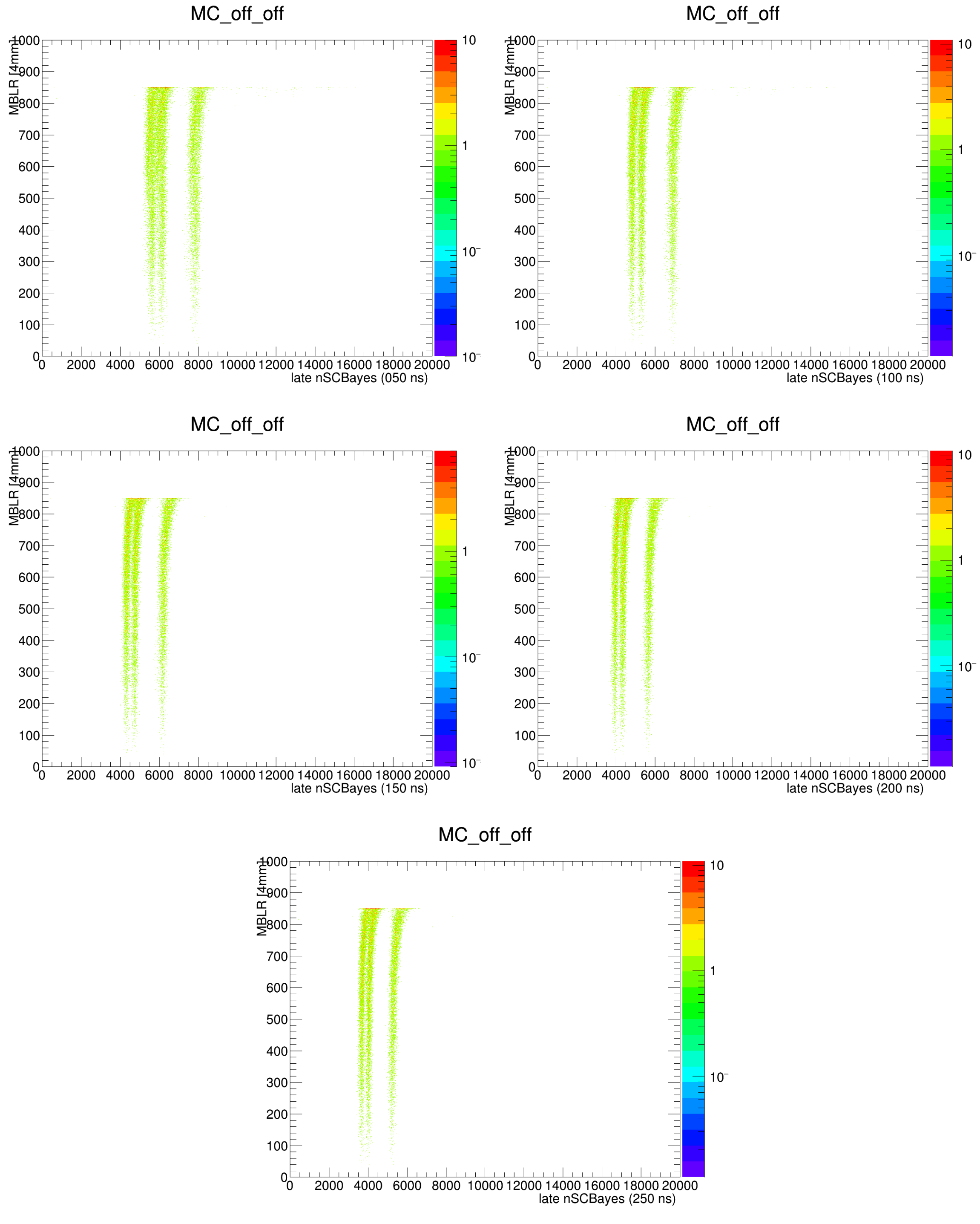
MC_off_off

MC_off_off

MC_off_off

MC_off_off

MC_off_off

Figure B.5: Late light nSCBayes vs. MBLR with different lower bound for charge integration. This is the MC samples with both clipping and PLSC turned off.

Appendix C

Monte Carlo Quenching Factor

Particle	MBLR range	Late Light qPE mean ± STD	Late Light LY (PE/keV)
Rn222	0-400	6922.4 ± 140.5	1.26
Po218	0-400	7577.5 ± 163.0	1.26
Po214	0-400	9812.5 ± 181.8	1.28
Rn222	150-600	6922.0 ± 144.7	1.26
Po218	150-600	7587.2 ± 160.3	1.26
Po214	150-600	9822.9 ± 178.7	1.28
Rn222	0-650	6922.3 ± 146.1	1.26
Po218	0-650	7586.2 ± 161.8	1.26
Po214	0-650	9819.3 ± 179.5	1.28

Table C.1: Results of the Gaussian fit to the three alpha lines with three different MBLR ranges for MC off_off. The late light LY variable is the fitted qPE divided by the corresponding alpha energy.

Particle	MBLR range	Late Light qPE mean ± STD	Late Light LY (PE/keV)
Rn222	0-400	6908.79 ± 154.6	1.26
Po218	0-400	7570.14 ± 155.3	1.26
Po214	0-400	9784.19 ± 179.0	1.27
Rn222	150-600	6924.55 ± 155.9	1.26
Po218	150-600	7587.73 ± 161.7	1.26
Po214	150-600	9814.35 ± 185.5	1.28
Rn222	0-650	6927.68 ± 158.2	1.26
Po218	0-650	7588.55 ± 165.7	1.26
Po214	0-650	9816.41 ± 189.7	1.28

Table C.2: Results of the Gaussian fit to the three alpha lines with three different MBLR ranges for MC on_off. The late light LY variable is the fitted qPE divided by the corresponding alpha energy.

Appendix D

Event Leakage

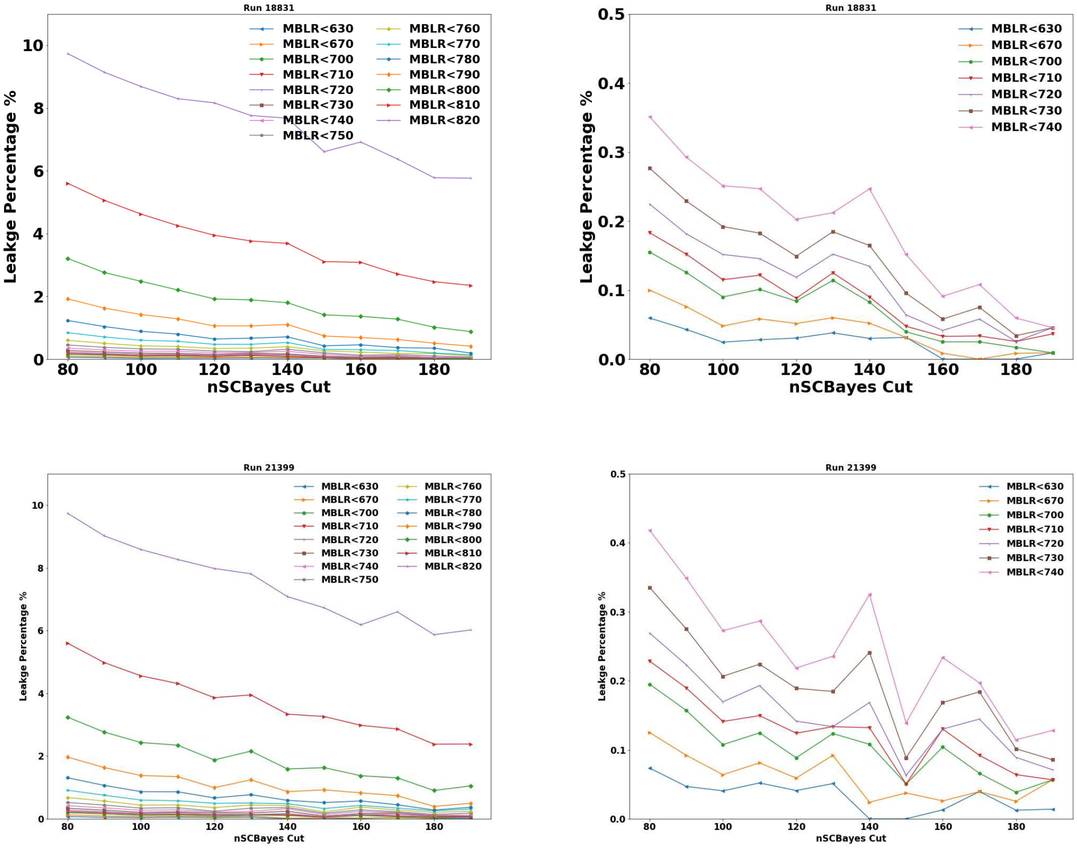

Figure D.1: Event leakage using the SplitEvent procedure for different fiducial volume cuts broken into different energy bins. As expected, lower energy events, due to their low charge information, have a higher leakage. Top row uses run 18831 and bottom row uses run 21399. The non-smooth behaviour is due to lower statistics at lower energies and lower fiducial volume cut, but the general trend remains the same; higher leakage probability for lower energy events.

Appendix E

Background Expectation Material

E.1 Neck & Dust Rates

Trigger rates of neck and dust MC samples for each of the systematic variation.

Systematic	Nominal	AP^{-}	AP^{+}	PMT_204	PMT_eff^{-}
IFIS [μHz]	13.97	14.35	14.07	14.69	17.04
IFOS [μHz]	19.06	19.56	19.80	20.65	24.85
OFIS [μHz]	23.24	23.50	23.46	23.05	21.44

Systematic	PMT_eff^{+}	PMT_eff_S	QF^{-}	QF^{+}	RI^{-}
IFIS [μHz]	13.76	14.30	18.06	14.27	14.28
IFOS [μHz]	20.07	19.65	23.84	18.97	18.65
OFIS [μHz]	23.99	22.78	22.64	23.12	23.05

Systematic	RI^{+}	TPB_LY^{-}	TPB_LY^{+}	TPB_SL^{-}	TPB_SL^{+}
IFIS [μHz]	15.07	13.64	13.79	18.54	14.21
IFOS [μHz]	21.43	20.07	20.14	20.45	19.45
OFIS [μHz]	23.92	24.06	24.01	17.35	25.00

Table E.1: Neck alpha trigger rates for each of the Inner Flowguide Inner Surface (IFIS), Inner Flowguide Outer Surface (IFOS), and Outer Flowguide Inner Surface (OFIS) for the 15 systematic variations and the nominal sample. Data courtesy of DEAP collaboration.

Dust Sample	Trigger Rate [Hz]
TPB-1	1.26e-04
TPB-5	5.12e-05
TPB-10	5.42e-05
TPB-17	5.72e-05
TPB-25	5.54e-05

Table E.2: Dust alpha trigger rates for each of the dust particulate size. The dust samples are not coated with any TPB. Data courtesy of DEAP collaboration.

E.2 Cherenkov Charge Cluster 3D View

The DEAP collaboration has a GUI to visualize an event in the detector. In the following figures, the left part is the 3D representation of the detector where the hexagon are the location of the PMTs that have fired, upper right portion shows the amount of charge observed in the PMTs and the lower right shows the PMT positions in the $\cos\theta$-ϕ space. The red hexagon is the brightest PMT in the event and the red squares, drawn by us, shows the location of the second, or third cluster, that we would not expect to happen for a Cherenkov event if the detector is filled with LAr

Figure E.1 shows and example of a regular Cherenkov event where we have one bright PMT while Figure E.2 shows a few example of seeing two or three cluster of PMTs with a high portion of charge.

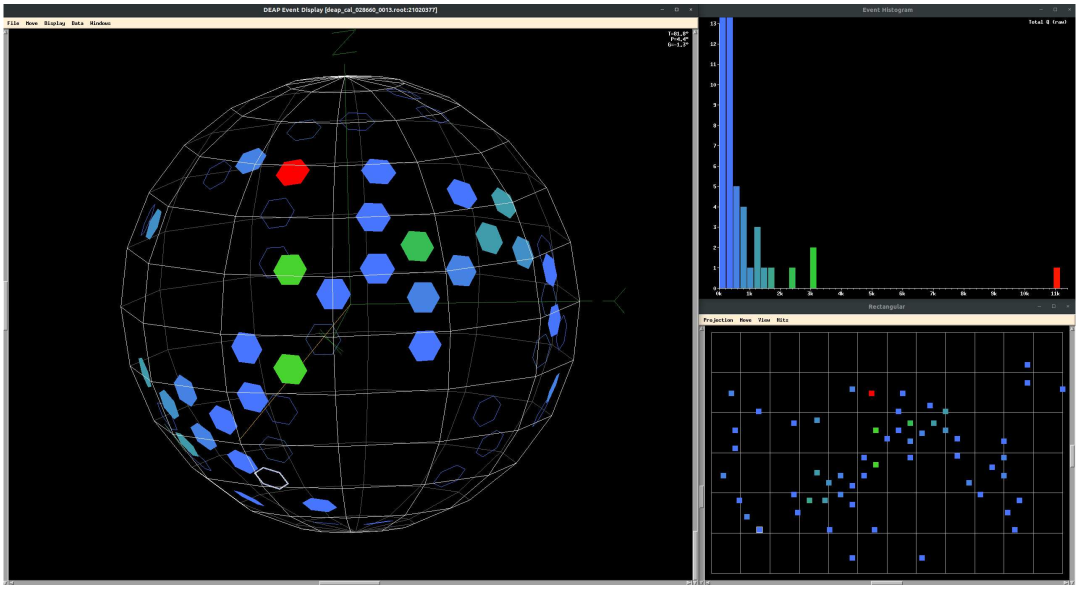

Figure E.1: A regular Cherenkov event with a single bright PMT.

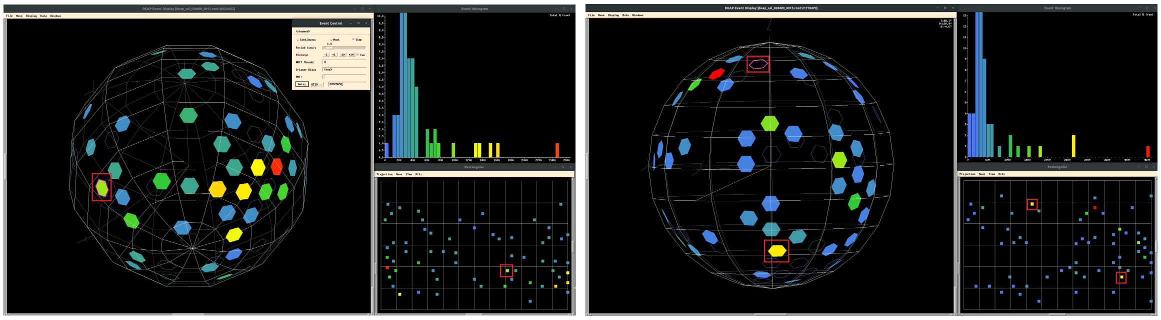

(a) event 1

(b) event 2

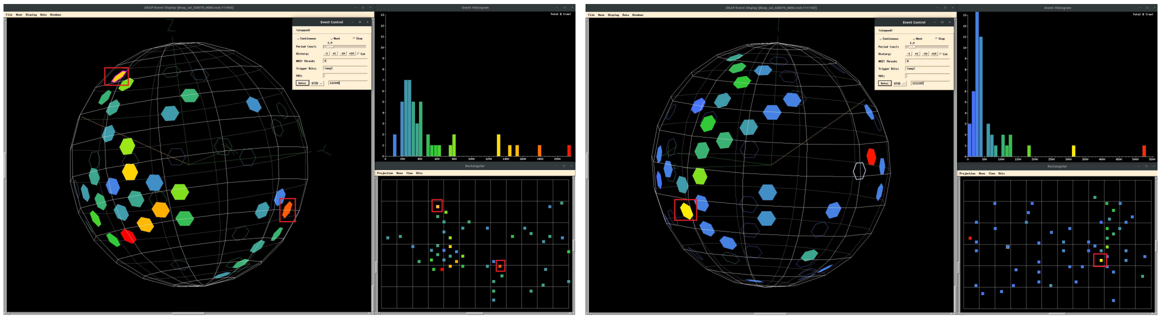

(c) event 3

(d) event 4

Figure E.2: Four examples of Cherenkov events where we have two or three cluster of bright PMTs. These event would not happen very often if the detector was filled with LAr. This is an indication of the electron leaking inside the detector and hitting another LG causing a second Cherenkov event.

E.3 Background Uncertainty

Figure E.3-E.7 show the number of expected background events from the neck and dust using a fiducial volume cut of 820 mm with the updated cutflow from each systematic variation using Equation 6.3 and assuming first-year dataset. Each sample is made of 1M toy MC and assumes 230.1 days of data taking, corresponding to the first-year dataset.

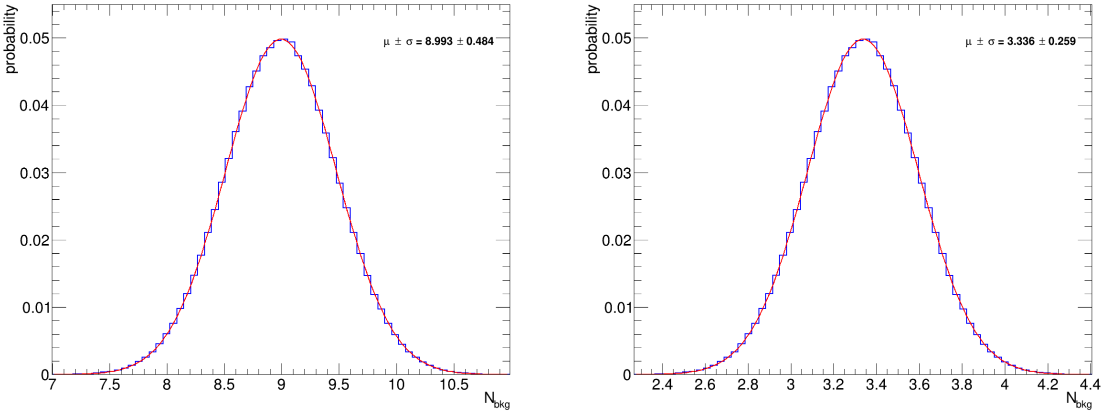

(a) dust afterpulsing_DOWN **(b)** neck afterpulsing_DOWN

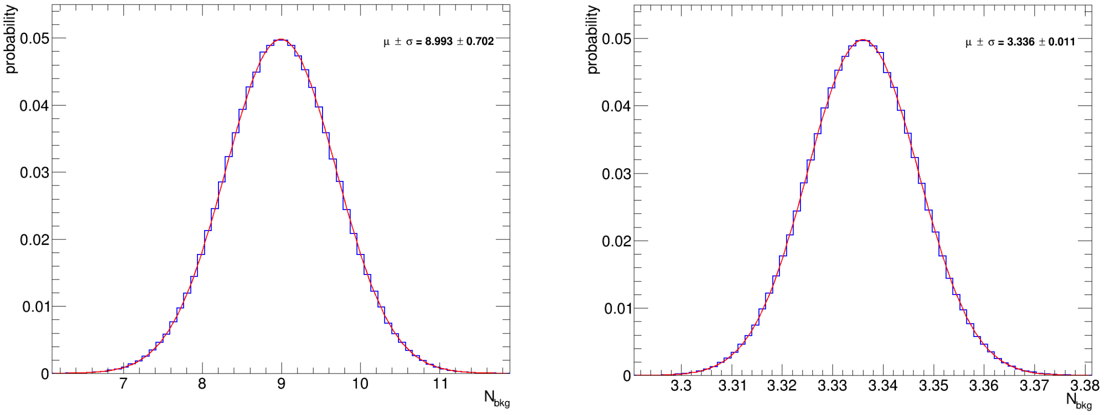

(c) dust afterpulsing_UP **(d)** neck afterpulsing_UP

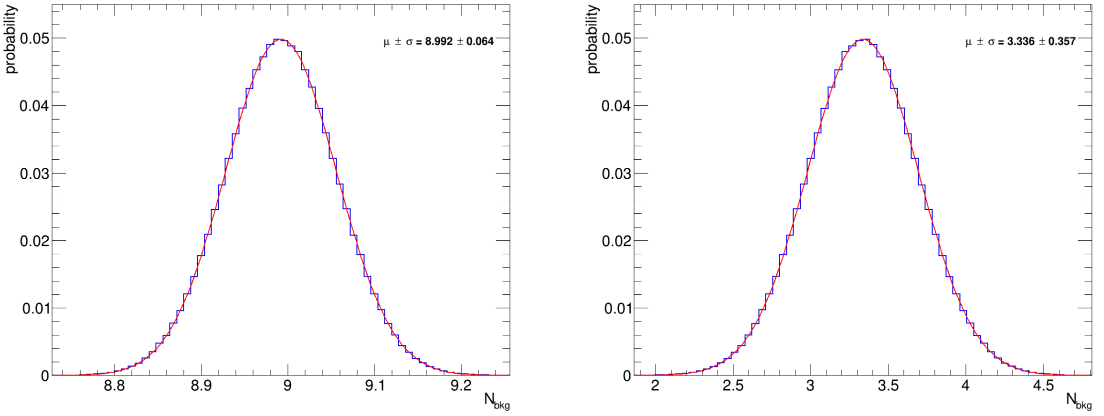

(e) dust pmt_204_OFF **(f)** neck pmt_204_OFF

Figure E.3: Expected number of neck and dust background events using afterpulsing_DOWN, afterpulsing_UP, and pmt_204_OFF systematic variations.

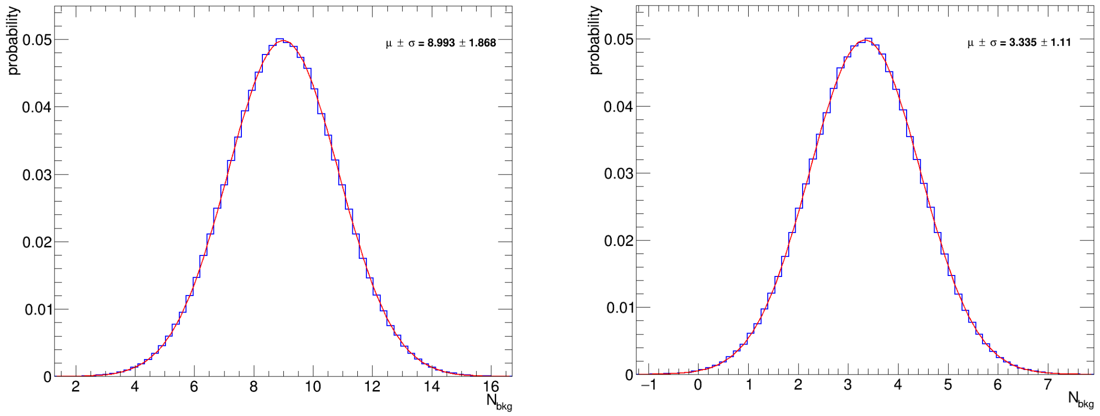

(a) dust pmt_efficiency_DOWN

(b) neck pmt_efficiency_DOWN

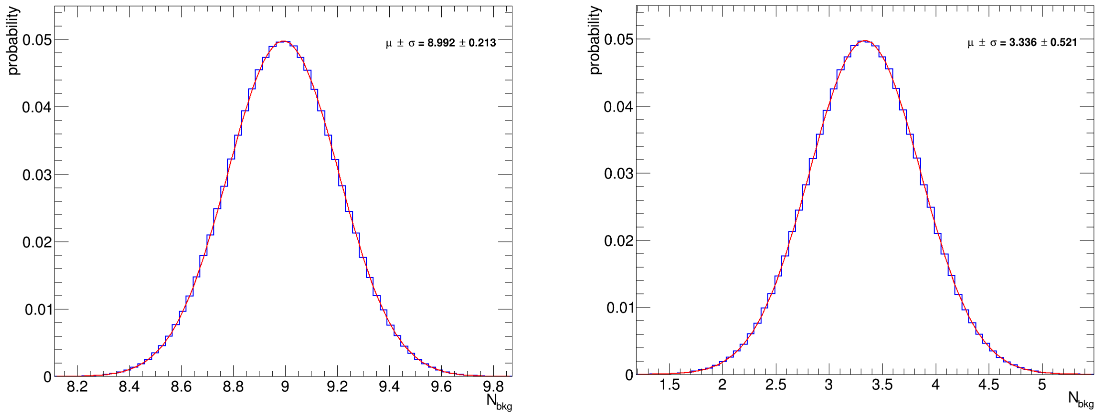

(c) dust pmt_efficiency_UP

(d) neck pmt_efficiency_UP

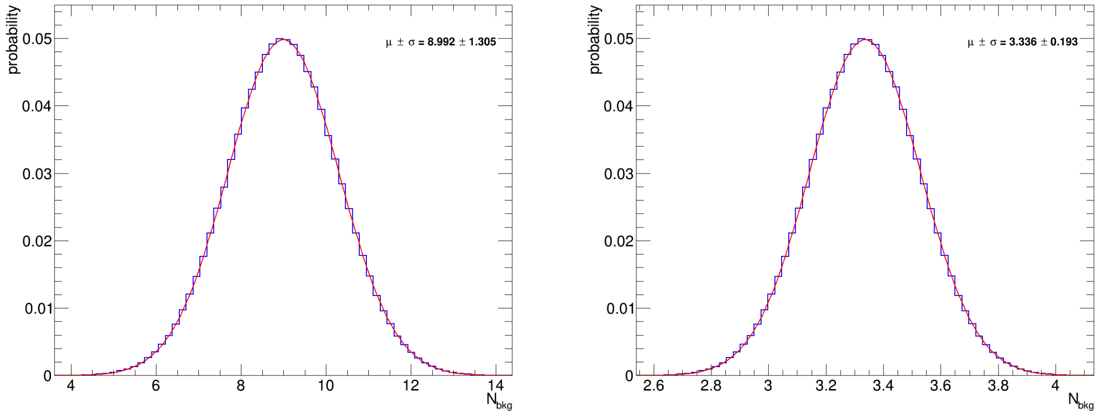

(e) dust pmt_efficiency_SMEAR

(f) neck pmt_efficiency_SMEAR

Figure E.4: Expected number of neck and dust background events using pmt_efficiency_DOWN, pmt_efficiency_UP, and pmt_efficiency_SMEAR systematic variations.

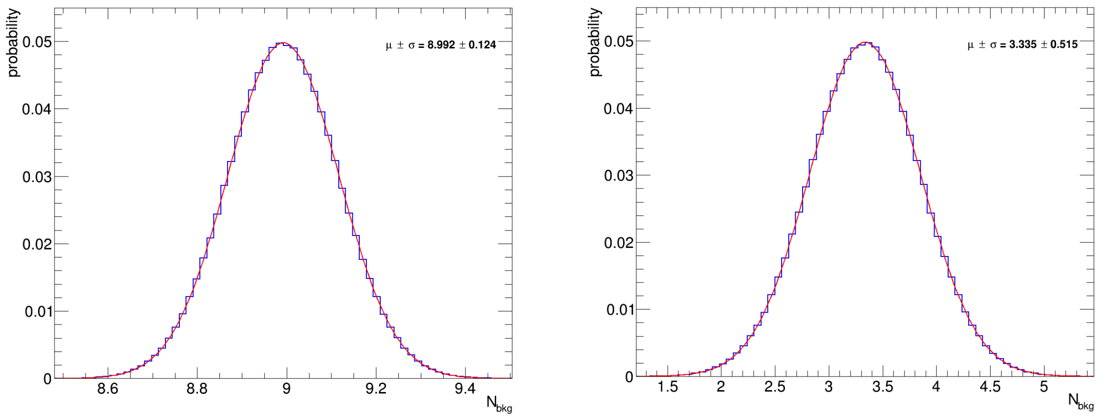

(a) dust quenching_factor_DOWN **(b)** neck quenching_factor_DOWN

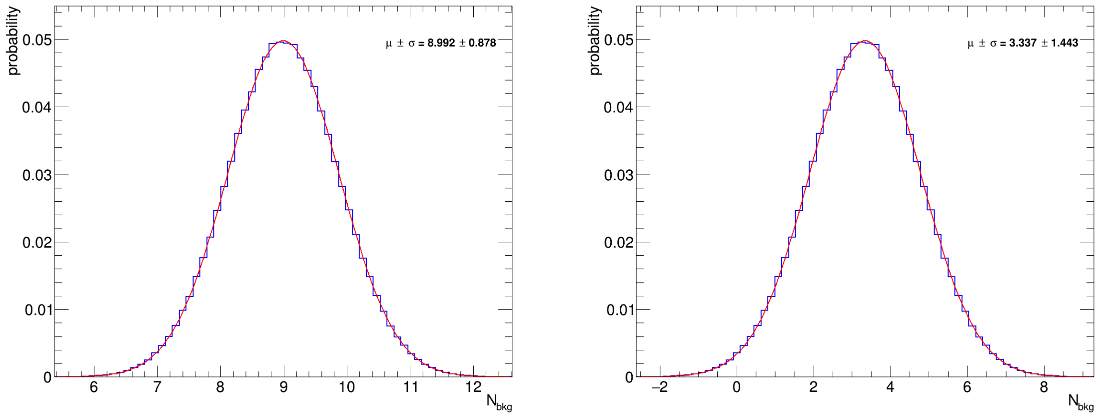

(c) dust quenching_factor_UP **(d)** neck quenching_factor_UP

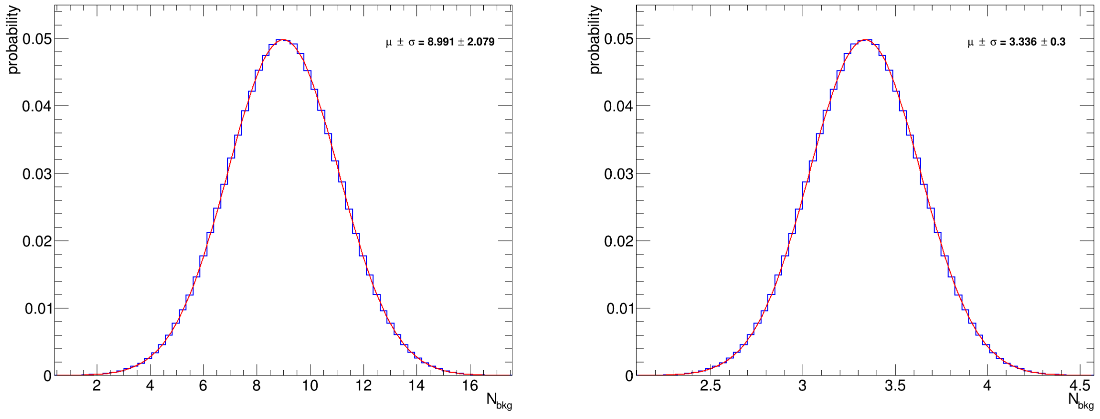

(e) dust refractive_index_DOWN **(f)** neck refractive_index_DOWN

Figure E.5: Expected number of neck and dust background events using quenching_factor_DOWN, quenching_factor_UP, and refractive_index_DOWN systematic variations.

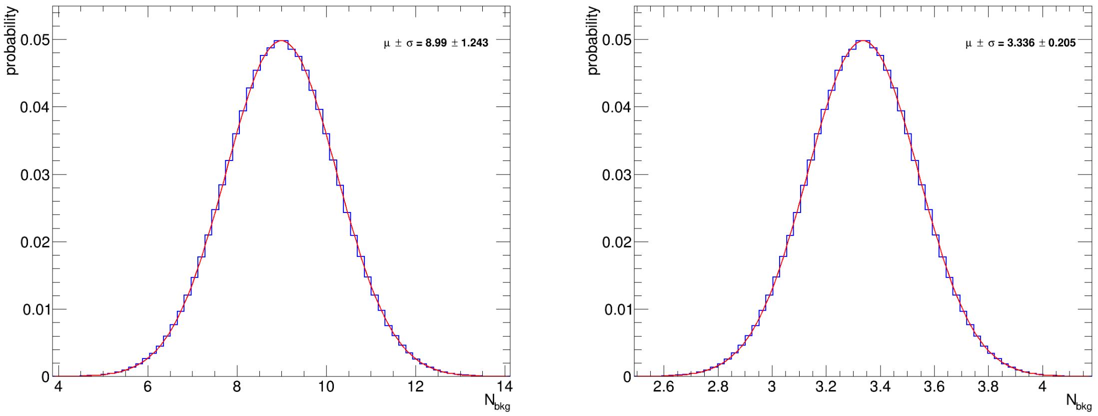

(a) dust refractive_index_UP **(b)** neck refractive_index_UP

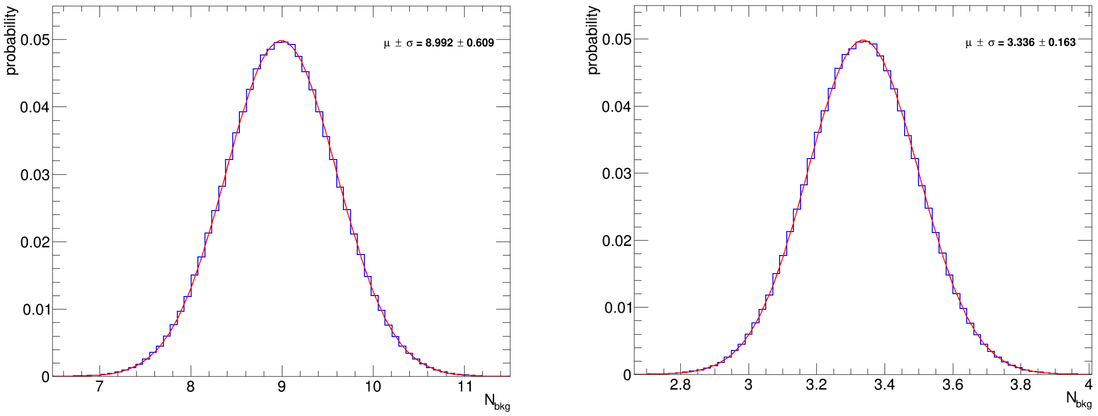

(c) dust tpb_ly_DOWN **(d)** neck tpb_ly_DOWN

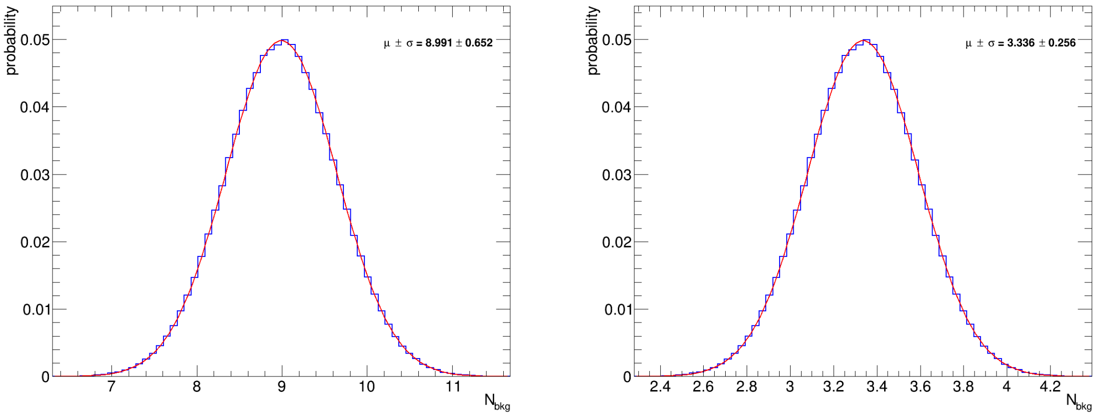

(e) dust tpb_ly_UP **(f)** neck tpb_ly_UP

Figure E.6: Expected number of neck and dust background events using refractive_index_UP, tpb_ly_DOWN, and tpb_ly_UP systematic variations.

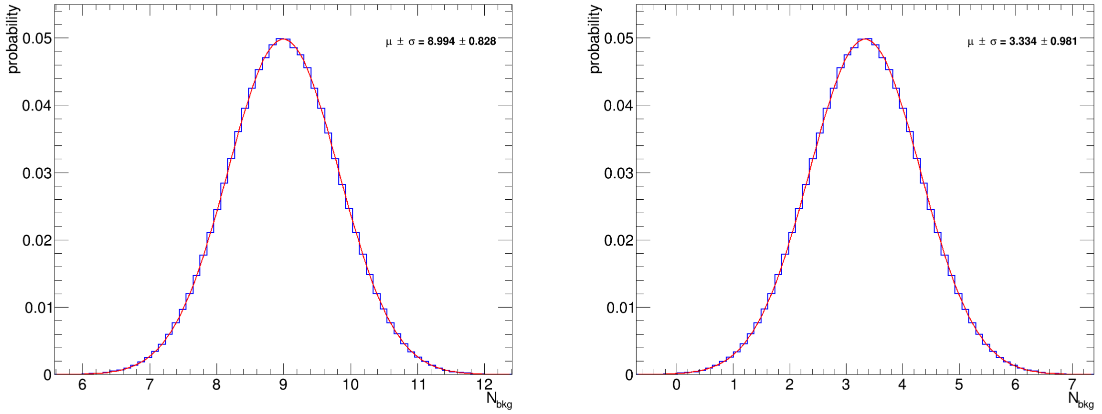

(a) dust tpb_scattering_length_DOWN **(b)** neck tpb_scattering_length_DOWN

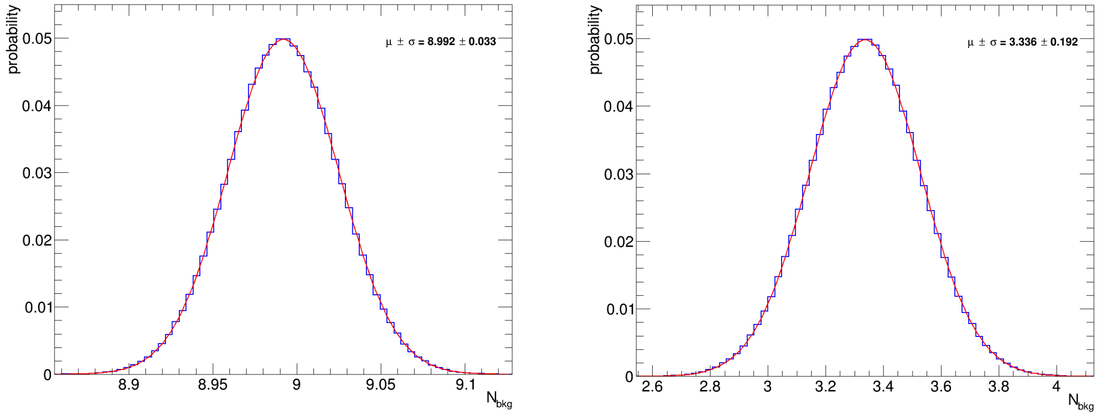

(c) dust tpb_scattering_length_UP **(d)** neck tpb_scattering_length_UP

Figure E.7: Expected number of neck and dust background events using tpb_scattering_length_DOWN and tpb_scattering_length_UP systematic variations.

E.4 Total Background

Figure E.8-E.10 show the total number of background events using the original cutflow and the updated cutflow at different fiducial volume cuts for both the first-year and three-year dataset. Each sample is made of 10M toy MC samples. Note that when calculating the exclusion curves, we eliminate negative numbers and re-normalize the distribution.

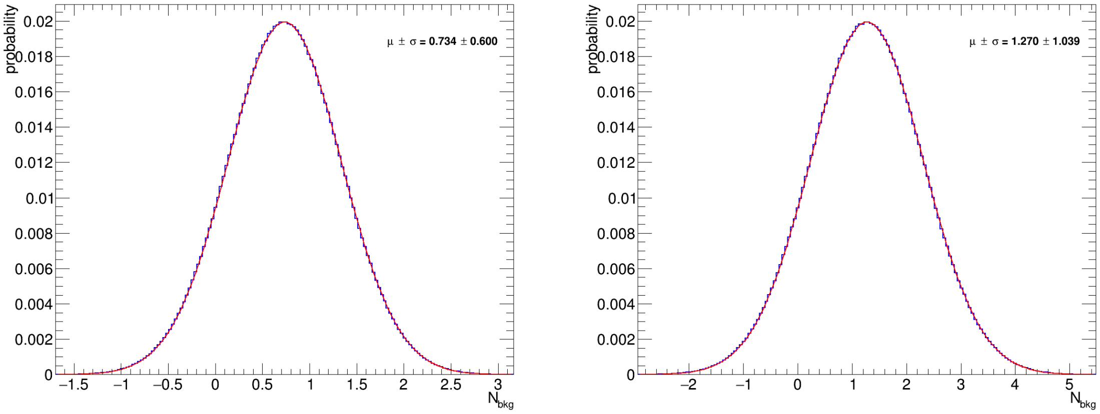

(a) first-year dataset **(b)** three-year dataset

Figure E.8: Total number of expected background events **(a)** assuming the first-year dataset and the **(b)** the three-year dataset using the original cutflow used by DEAP. The fiducial volume is 630 mm

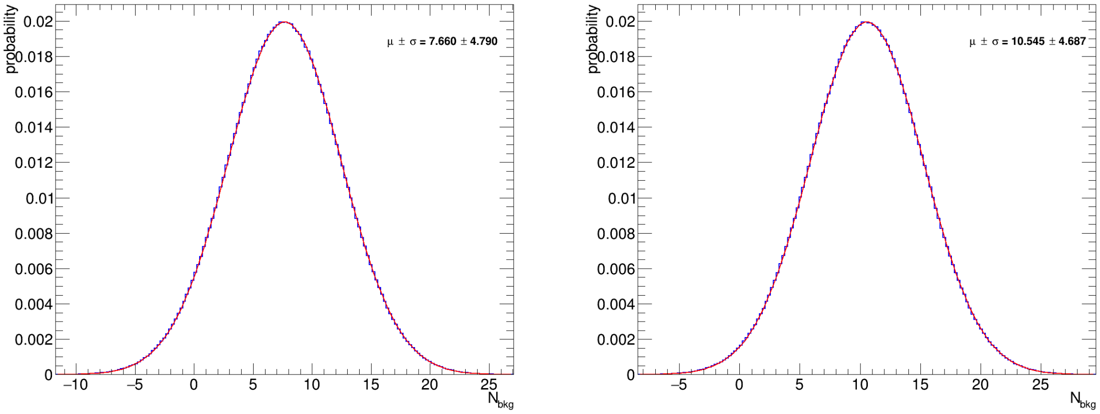

(a) 630 mm

(b) 720 mm

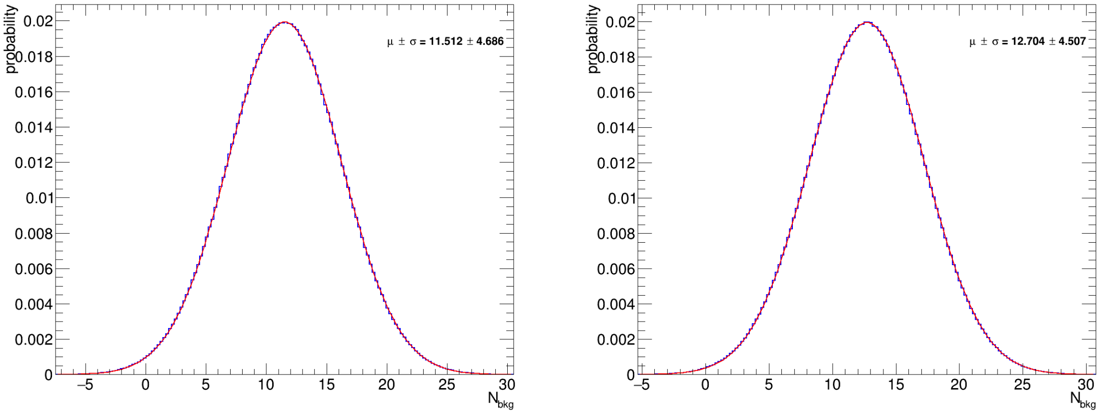

(c) 750 mm

(d) 780 mm

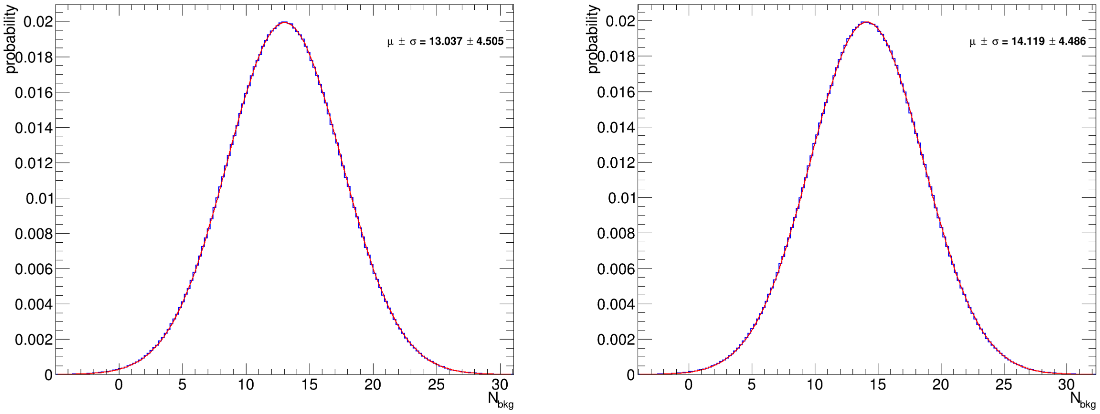

(e) 800 mm

(f) 820 mm

Figure E.9: Total number of expected background events with the updated cutflow proposed in this thesis and assuming the first-year dataset for different fiducial volume cuts.

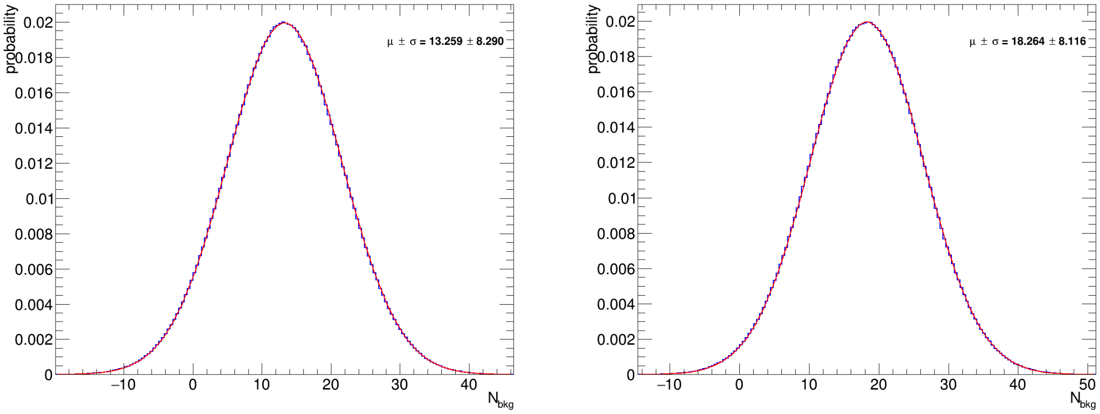

(a) 630 mm **(b)** 720 mm

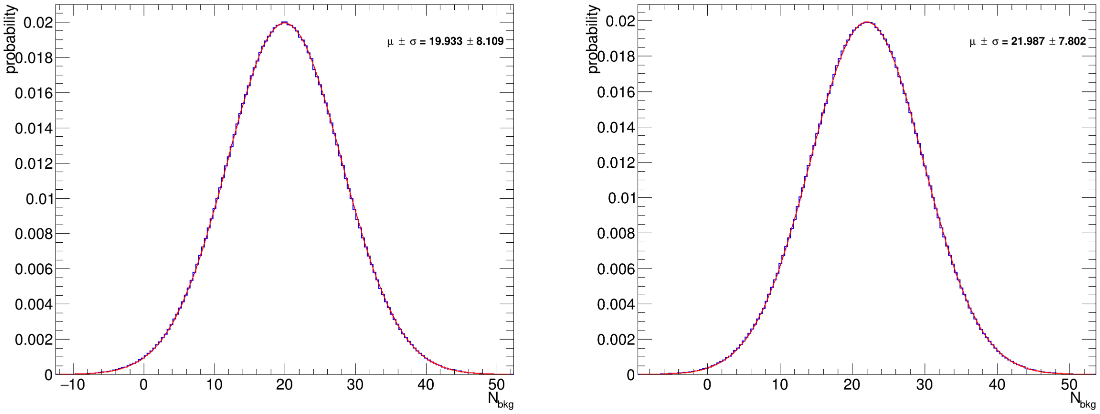

(c) 750 mm **(d)** 780 mm

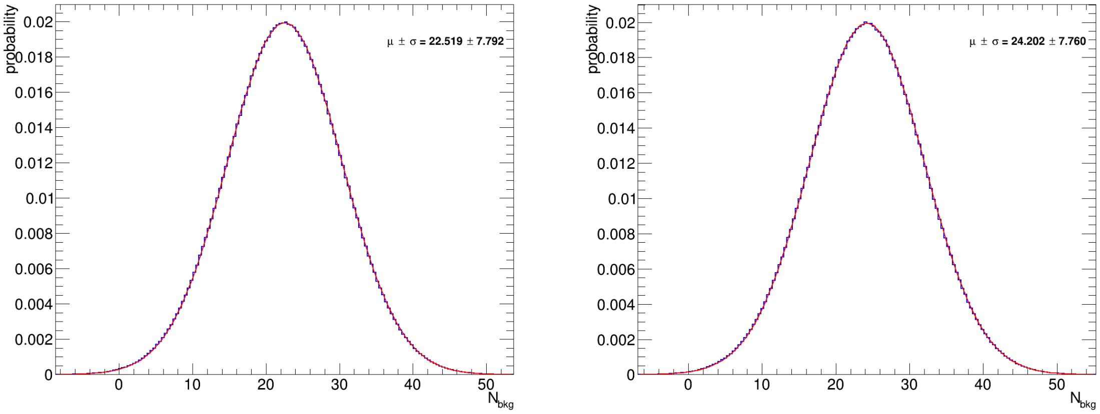

(e) 800 mm **(f)** 820 mm

Figure E.10: Total number of expected background events with the updated cutflow proposed in this thesis and assuming the three-year dataset for different fiducial volume cuts.

Appendix F

Extra Exclusion Curves

Figure F.1 shows the exclusion curves for the upper, median, and lower limits for the 223 and 386 live-days. To obtain the upper, median, and lower limits we used $\alpha < 0.10$, $\alpha < 0.50$, and $\alpha < 0.90$, respectively.

F.1 Upper, Median, and Lower Curves

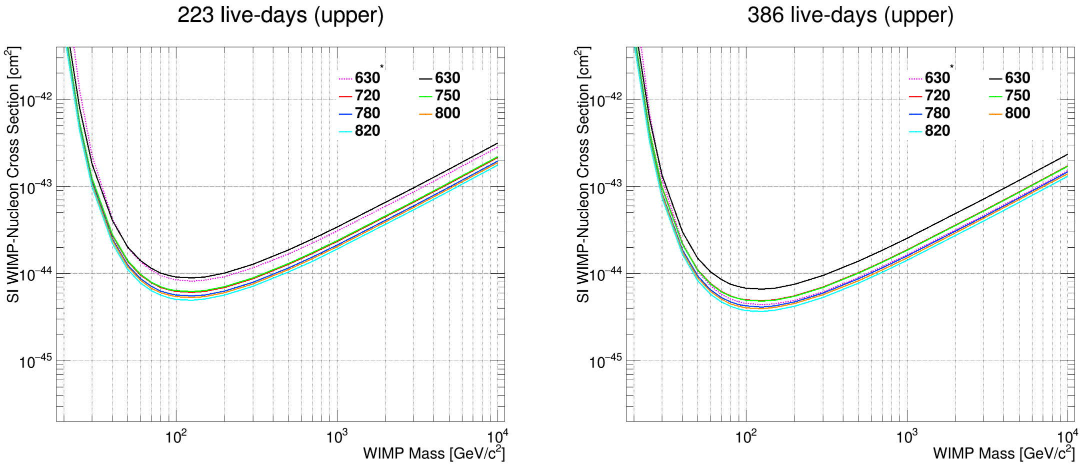

(a) Upper Limit **(b)** Upper Limit

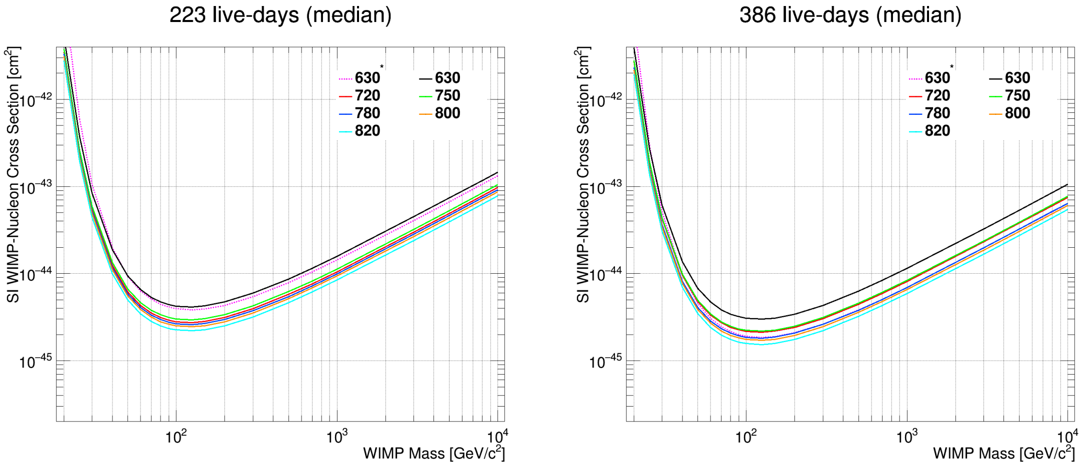

(c) Median Limit **(d)** Median Limit

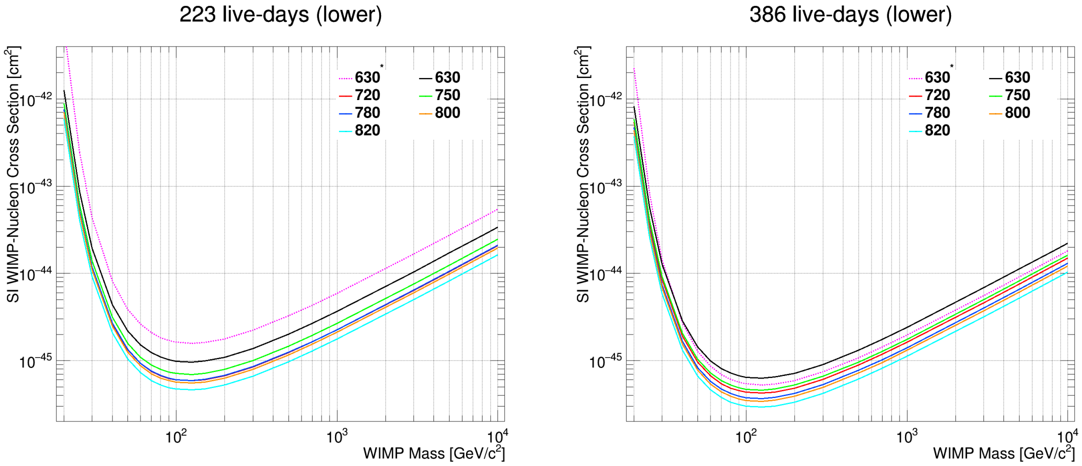

(e) Lower Limit **(f)** Lower Limit

Figure F.1: From top row to the bottom row, the upper, median, and lower 90% CL for the 6 fiducial volumes studied with the updated cutflow. The left column uses the 223 live-days dataset and the right column uses the 386 live-days dataset.

F.2 Tagged Events

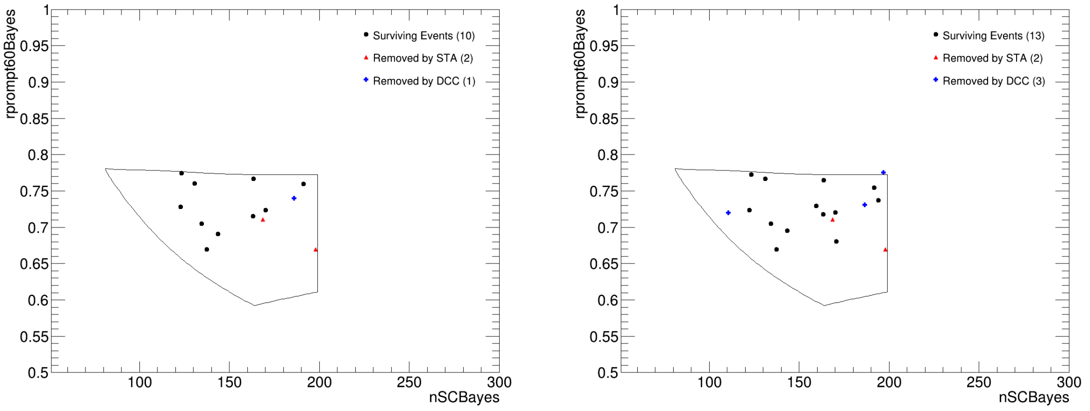

(a) 630 mm **(b)** 720 mm

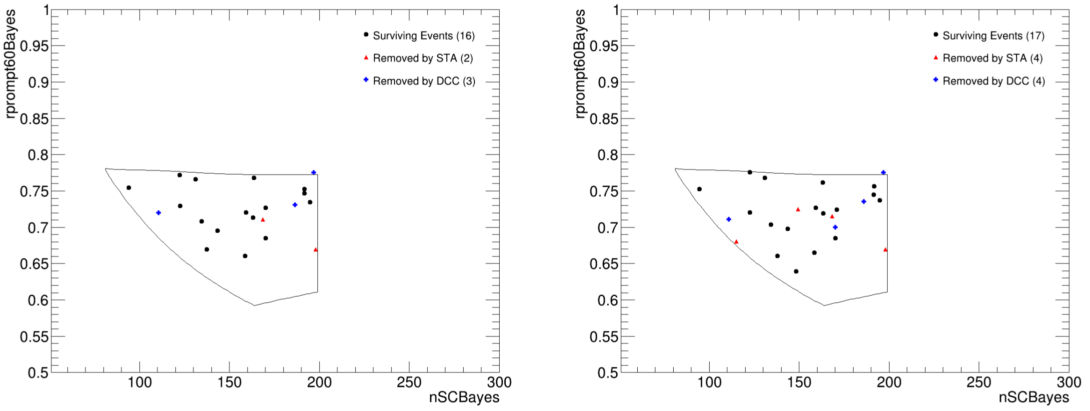

(c) 750 mm **(d)** 780 mm

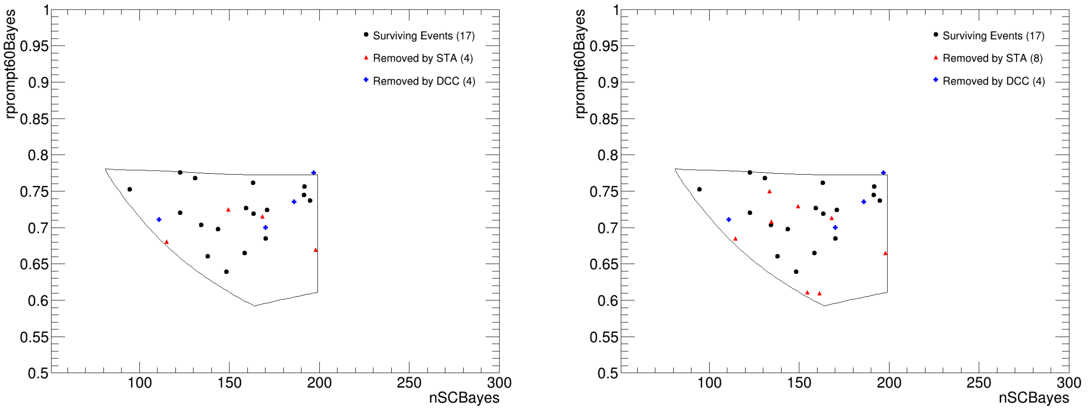

(e) 800 mm **(f)** 820 mm

Figure F.2: The events that survive the full cutflow and the events that were tagged and removed by the STA and the Double Charge Cluster (DCC) cut for different fiducial volumes are shown in the nSCBayes-$R_{\mathrm{prompt60Bayes}}$ space using the 223 live-days dataset. The numbers in parenthesis in the legend show the number of events in each category. The black box is the WIMP ROI used in this thesis.

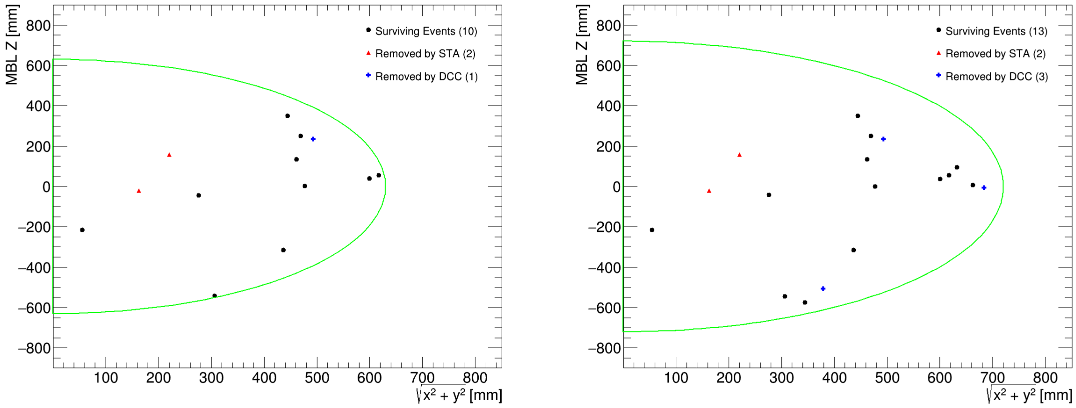

(a) 630 mm **(b)** 720 mm

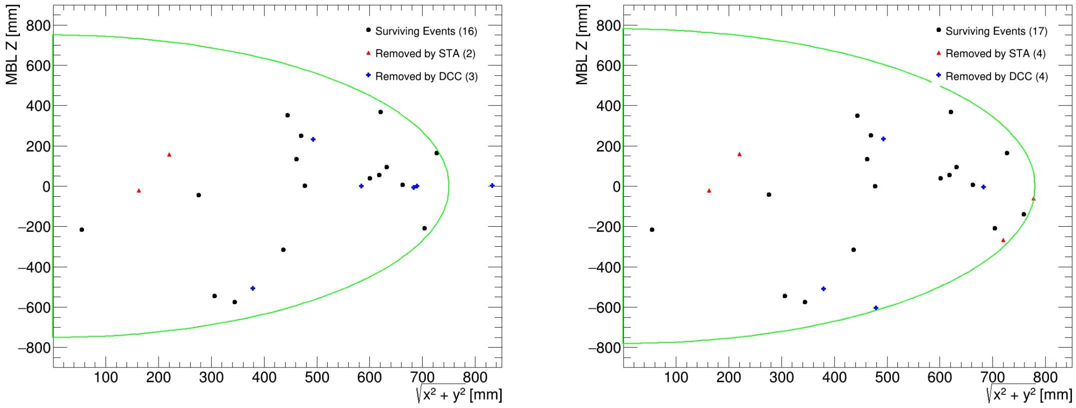

(c) 750 mm **(d)** 780 mm

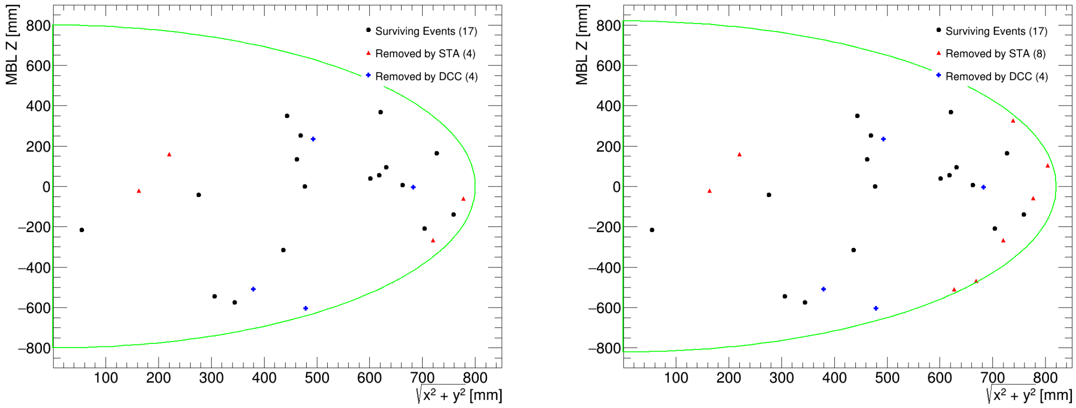

(e) 800 mm **(f)** 820 mm

Figure F.3: The events that survive the full cutflow and the events that were tagged and removed by the STA and the Double Charge Cluster (DCC) cut for different fiducial volumes are shown in the spacial ρ-Z space (MBL fitter) using the 223 live-days dataset. The numbers in parenthesis in the legend show the number of events in each category. The green line highlights the fiducial boundary.

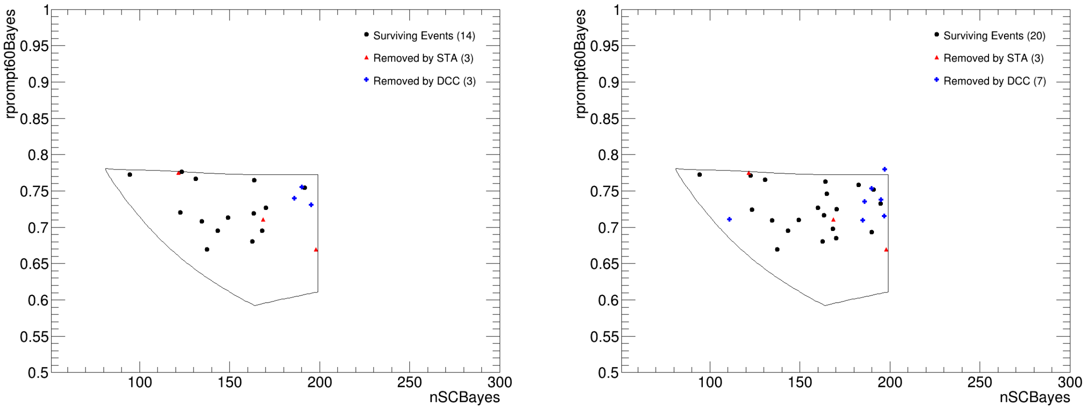

(a) 630 mm **(b)** 720 mm

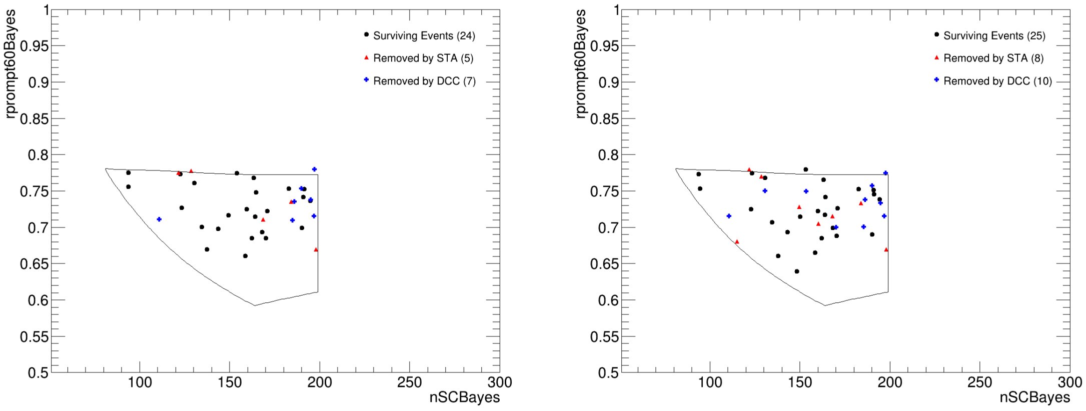

(c) 750 mm **(d)** 780 mm

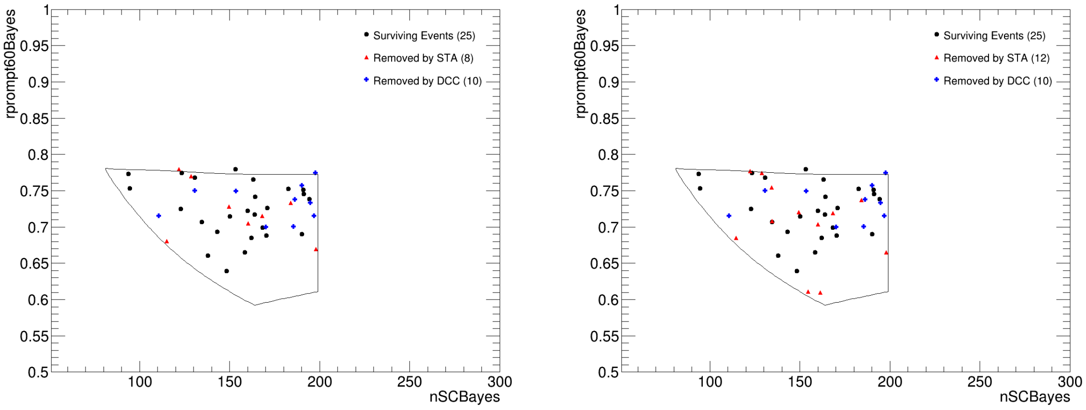

(e) 800 mm **(f)** 820 mm

Figure F.4: The events that survive the full cutflow and the events that were tagged and removed by the STA and the Double Charge Cluster (DCC) cut for different fiducial volumes are shown in the nSCBayes-$R_{\text{prompt60Bayes}}$ space using the 386 live-days dataset. The numbers in parenthesis in the legend show the number of events in each category. The black box is the WIMP ROI used in this thesis.

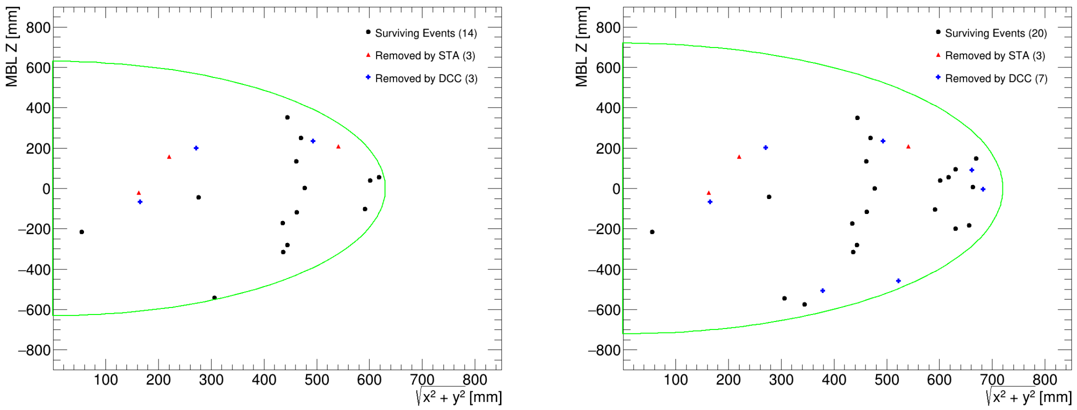

(a) 630 mm **(b)** 720 mm

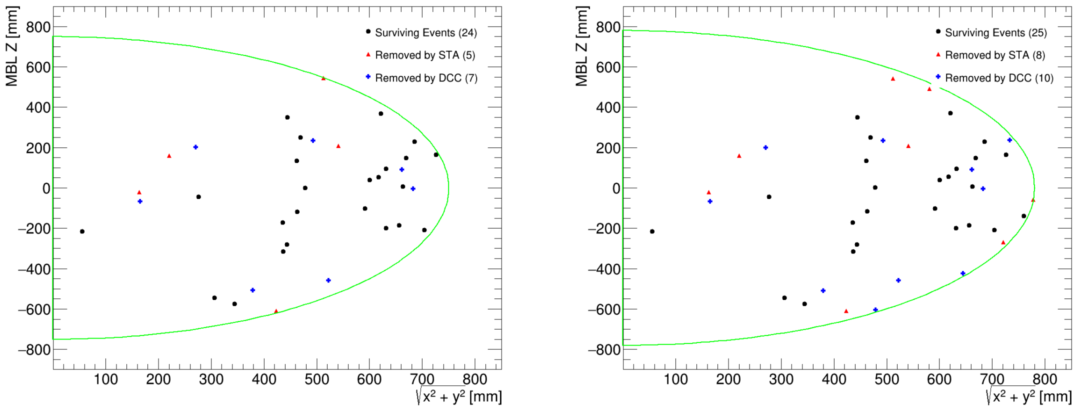

(c) 750 mm **(d)** 780 mm

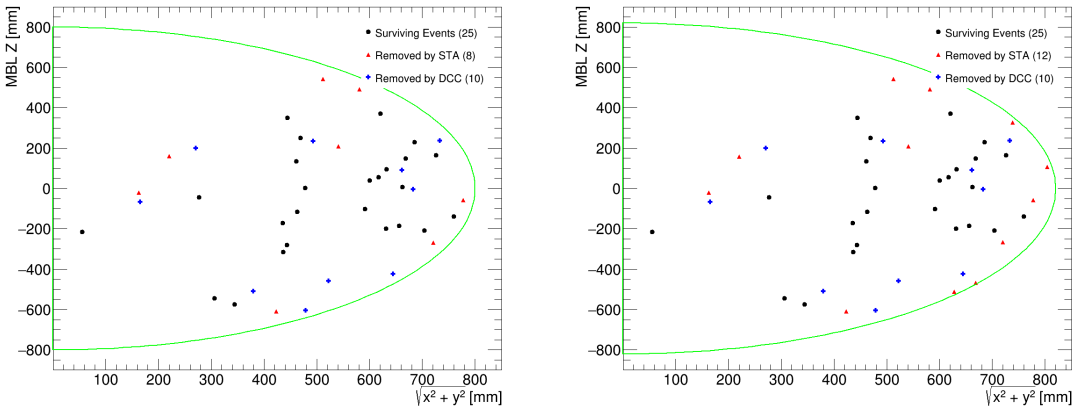

(e) 800 mm **(f)** 820 mm

Figure F.5: The events that survive the full cutflow and the events that were tagged and removed by the STA and the Double Charge Cluster (DCC) cut for different fiducial volumes are shown in the spacial ρ-Z space (MBL fitter) using the 386 live-days dataset. The numbers in parenthesis in the legend show the number of events in each category. The green line highlights the fiducial boundary.